Nano-electronic Devices Using Two-dimensional and Phase Change Materials

Syed Ghazi Sarwat

Supervised by Professor Harish Bhaskaran & Dr Jan Mol

Department of Materials

St Cross College

University of Oxford

A thesis submitted for the degree of

Doctor of Philosophy

"This thesis is yet another punctuation mark in the indefinite book of nature

to Sabiha Nazli Naqvi, Sarwat Ali, Prince Sabahut Ali and Syed Farheen Sarwat,

who paved the way

Abstract

This thesis describes nanoscale devices utilizing phase change and two-dimensional materials. The fundamentals, modeling, chip design, nano-fabrication process, measurement setups and experimental results of such devices are discussed.

In the first example, a graphene-nano-gap phase change memory device concept is proposed, in which a phase change material bridges graphene electrodes that are spaced sub-1 nm apart. These devices are fabricated using a lithography-free self-alignment technique. The manufacture and metrology of such devices are studied, with a demonstration of a Kelvin Probe Microscopy based approach for in-situ imaging. Such devices enable ultra-scaled memory cells for energy efficient operation. Scaling limit of such devices are studied and an intrinsic gap length is found below which carbon filamentation overwhelms resistive switching in the phase change material.

The second example features the study of electronic properties of two-dimensional materials under external perturbation, such as strain. A new approach based on Kelvin Probe Microscopy is demonstrated to overcome the limitations (materials, resolution and substrate effects) of commonly used optical spectroscopy tools, and reveals strain-driven changes in the work functions, including junction potentials in ultrathin heterostructures. A device concept termed strain-effect transistor is proposed wherein two-dimensional materials can be strained cyclically by the reversible amorphous-crystalline phase transition in the underlying phase change material. Crucially, a chalcogenide glass with high volume changes is explored for this application. The volume changes in the material are observed to complement changes in optical properties and are further exploited for a demonstration of solid-state reflective displays and tunable photonic resonators.

The third example reveals the light-matter interaction in low dimensional phase change materials using graphene nano-gaps and crossbar nanoscale devices. Contrary to the existing understanding of these interactions, the complex interplay of three independent mechanisms, viz. photoconductive, photo induced-crystallization and photo-induced-thermoelectric effects, are observed to govern the photoresponse of the material. Significant photovoltaic effects are observed in such devices, which might lead to phase change devices for photonic applications being potentially self-powered. The photodetection bandwidth and photo-responsivity are observed to be tunable based on the state of the phase change material, enabling the development of tunable photodetectors. Finally, the concept of a spiking photodetector is introduced that utilizes the strong-light matter coupling in chalcogenide glasses. Such devices could be used in the development of artificial retinas.

Acknowledgments

This thesis is a testament of not just only my academic success but also my growth into a matured and self-aware individual. I have come to realize quite strongly that the key to progression in work is intertwined with progression in life and that this is profoundly determined by the people that surround us. On that note, I am indebted and grateful to the beautiful people who supported, inspired and influenced this journey of DPhil; for making this the best years of my life so far.

Harish (Prof Harish Bhaskaran), thank you for being a good supervisor. Thank you for kindling my scientific curiosity and for providing the freedom to explore it. You have whipped me into not just a better researcher but equally a confident individual. Jan (Dr. Jan Mol), thank you for being there when I most needed supervision. You were in fact pivotal in introducing me to the field of nano-electronics. Once again, my deepest gratitude to you both for accepting me two and a half years ago and bringing me to this stage of successful completion.

My colleagues Carlos, Eugene, Gerardo, James, Merce, Nathan, Nick, Nhlakanipho, Pascal, Peiman, Sarolta, Xuan, Yingqiu, Zengguang for their invaluable support, friendship, and good moments- this thesis is our success, thank you. Extra special thanks to Ben Porter, Zengguang Cheng, Gerardo Rodriguez, Nathan Youngblood and Peiman Hosseini for their patience in getting me started with the field. Paul Pattinson and Radka Chakalova, as with hundred others, were the unsung heroes of this thesis. Cleanrooms were particularly nice to work-in because of the friendly atmosphere they have created. Thank you IT support (Paul, Rob, and Chris) for making sure I had little to worry when the computers broke, and to other officials in the department for easing this journey. My humblest gratitude to Yingqiu and Nhlakanipho, for being there at all times. You were the pillars for this thesis and my happy stay in Oxfordshire- I cannot thank you both enough. To all my other friends in Oxfordshire- Krish, Naganand, Sue, Thomas, Claudius, Sandoko and others (I am sorry if I have missed listing you), thank you for taking care of me and for the hang outs when I needed them most.

My sincere acknowledgments to my other academic mentors who seeded this journey- Dr. K R Ravi, Late Dr. Baldev Raj, Dr. Joysurya Basu, Dr. B S Murty, and Dr. Vijayalakshmi Mureleedharan- you all are and will be an integral part of my research career. A huge gratitude to the Felix Scholarship that made this dream reality. No action or word can express how grateful I am and will be eternally for the opportunity you gave me to study at Oxford. A big thank you to St Cross College and the University of Oxford for supporting my DPhil and making this journey

so very pleasant. I also want to extend my gratitude to Prof Chris Grovenor, whose meticulous examination styled the thesis the way it is.

Last but most importantly, a heartfelt thanks to the shareholders of this thesis: my parents (Dr. Syeda Sabiha Nazli Naqvi and Sarwat Ali) and siblings (Prince Sabahut Ali and Syed Farheen Sarwat). You have been one amazing family. Where ever I have been and whatever I have achieved, is merely a translation of your support, blessings and undeterred love. I love you all. Ya Allah, thank you for making me who I am today.

I also want to take a moment and say thank you to you too, the reader, for taking this dissertation off the shelf and giving it a read. I would like to remind myself and you the reader that this thesis was written during a time that marked in some ways the dawn of irreversible effects of climate change and wildlife decline, and when the world leaders turned blind eye to growing hatred and terrorism. This thesis, unfortunately, does little to address these concerns; regardless a place like Oxford, which is overly diverse has sufficiently motivated me to steer my research interests and civic responsibility in contributing to solving these grave issues.

Syed Ghazi Sarwat
Oxfordshire, UK
11.06.2018

Table of Contents

CHAPTER 1: Literature Review and Thesis Overview

(A part of this chapter has been published: Syed Ghazi Sarwat, 2017, 33, 1890-1906, Materials Science and Technology)

Literature Review and Thesis Overview

1.1 Motivation

The extent to which data computation and storage platforms like computers, mobile phones, image sensors, media players etc. have pervaded our lives is truly remarkable. These machines work on silicon-transistor based integrated circuits, which deploy electric charges to process and store data. Research on this charge-based technology occupies a unique position in academia and industry, both working towards enhancing the data processing speeds and storage capacities. Seemingly, these characteristics are best achieved through tweaking materials' properties and device miniaturization, which is scaling down the dimensions of the functional units like the transistors, so that their number, hence density on a single package, is increased. A state-of-the-art chip as of today carries as many as 19 billion transistors. However, for the first time, chip making industries are uncertain about further miniaturization. It is convincingly shown and pointed-out in the ITRS (International Technology Roadmap for Semiconductors) that current silicon technology will not be commensurate with future computation and storage requirements[1,2]. This is famously referred to as the end of Moore's law[3] –that stated doubling of the number of transistors every 18 months starting in 1965- and is primarily owing to the increased fabrication costs, power consumption and irresolvable atomic scale challenges which will arise from further miniaturization.

Therefore, the search for beyond silicon-based electronic and optoelectronic technologies is in full swing. Crucially, the research focus is in two co-dependent directions. The first focus is on alternate data-storage and computational platforms, which could beat current scaling limits, as well as overcome the von-Neumann bottleneck[4]. The von-Neumann bottleneck is a severe limitation on the processing speed of the computers that arises due to the bottleneck on shuttling the data to and fro between the memories and processors. The second focus is on the material science and discovery of newer materials that could offer an improved portfolio of properties,

which could not only enhance the performance limits of current technologies but also aid in the development of the emerging platforms.

This thesis focusses on phase change and two-dimensional materials that are uniquely suited for both, emerging as well as for current charge-based technologies and for novel device applications and concepts. Phase change materials lay the foundations for phase change memories that advance the performance standards of current platforms through the entirely distinct mode of device operation, including facilitation of brain-inspired computers. Two-dimensional materials enable enhanced device performance through their remarkable electronic and optical properties; graphene, for example, has two orders of magnitude higher carrier mobility than silicon and molybdenum disulfide, for example, has an order of magnitude higher photon-absorption in the visible spectra than silicon[5–7].

1.1.1 Two-dimensional Materials

Most materials that we see around us are three dimensional in their geometry, meaning they have length, width, and height. A two-dimensional material is a material that as correctly phrased is two-dimensional- it lacks a dimension, which is height. From an electron's perspective, it can be best thought as a sheet of paper. Unlike paper, however, a two-dimensional material is atomic thick (~10000 times thinner) and more functional i.e. can conduct electricity and heat, which is at the heart of modern electronic and optoelectronic technologies. Being only atom thick also make two-dimensional materials transparent in the visible spectra and enable tunability in their electronic and optical properties through electrostatic modulation of the carrier -density and -type. Crucially, two-dimensional materials are more suited for wearable and flexible applications due to the above traits and for the ability to flex and conform due to their two-dimensional geometry.

The experimental discovery of the first two-dimensional material in 2004, called graphene (see Figure 1A), which is a single sheet (~0.35 nm) of carbon atoms covalently bonded to each

other in hexagons (sp^2 co-ordination), led not to just a Nobel Prize (2010) but also laid the grounds for the discovery of many more two-dimensional materials. The fact that two-dimensional materials exist, and moreover, are stable under ambient conditions is amazing by itself. According to the Mermin-Wagner theorem[5], there should be no long-range order in two dimensions; and thus, dislocations should appear in two-dimensional crystals at any finite temperature and long-wavelength bending fluctuations due to thermal excitation of phonons should result in crumbling of the material. This effect however as we know today is suppressed by atomic scale rippling through anharmonic (nonlinear) coupling between bending and stretching vibrational modes, but is an excellent example of how nature never fails to surprise us. Over 1000 layered materials have been realized so far and more being explored, especially through first principle calculations[8]. They have been classified into 23 families based on their chemical structures; of which most are metals/Weyl metals, 161 have bandgaps in the visible regime of the solar radiation, while only 26 are insulating (band gaps greater than 5 eV). Graphene is famously termed as the wonder material for its remarkable material properties, for example, for the given dimension, graphene is: the stiffest (stiffer than diamond) and the strongest material ever measured (~130 GPa), the best conductor of heat (better than diamond) and electricity (1000 times better than copper), the most stretchable and pliable material (up to 21 % elongation) and has the largest surface area (~3000 m^2 per gram)[5,9]. However, despite hosting such impressive properties, graphene remains less suited for applications that revolve around semiconductors, -transistors, image sensors, light emitting diodes etc- because it lacks an intrinsic bandgap. Although a bandgap can be induced externally in graphene through high strain, electric field or sub-10 nm scaling, such approaches are energy intensive and less practicable on-chip[10]. Other forms of two-dimensional materials that have an intrinsic bandgap are therefore being more actively explored (see Figure 1).

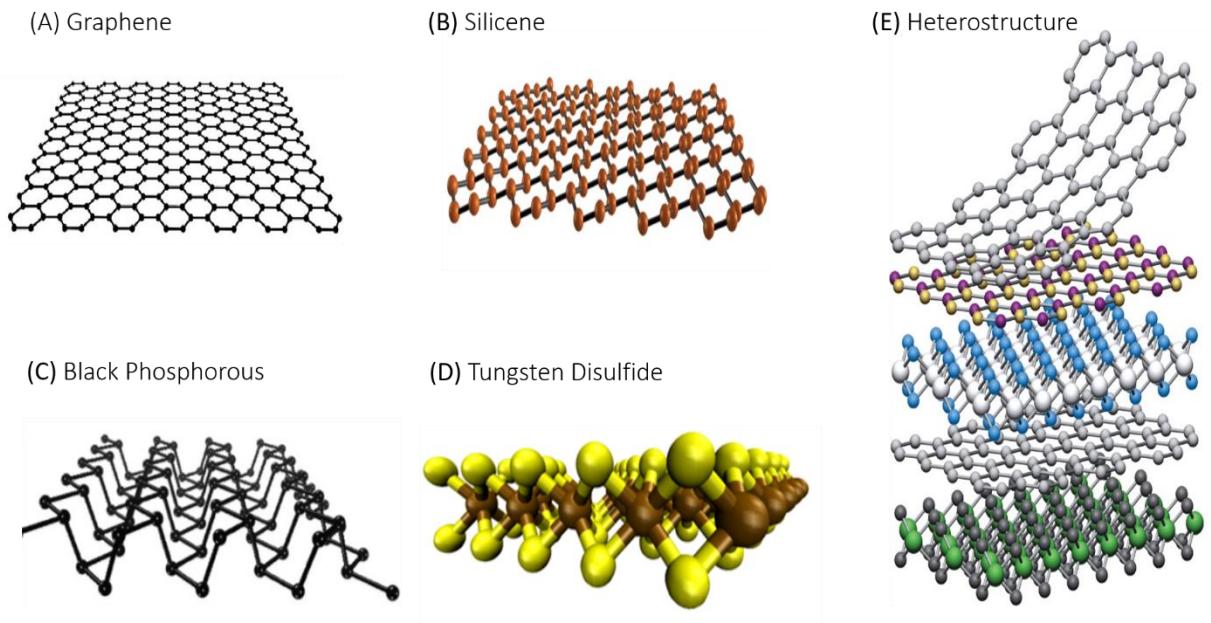

Figure 1. **Different forms of two-dimensional materials**. Lattice structures of commonly used and researched two-dimensional materials. (A) sp^2 graphene (figure reproduced from[11]), (B) sp^2 silicene (figure reproduced from[12]) and (C) sp^3 black phosphorous (figure reproduced from[13]), all have a hexagonal lattice structure, with differences not only in the chemistry of atoms but also in the nature of bonds. (D) Transition metal dichalcogenides unlike previous examples are three atoms thick (figure reproduced from[14]). (E) Different two-dimensional materials can be stacked atop each other to form van der Waal's heterostructure[15] (figure reproduced from[15]).

Of these, transition metal dichalcogenides based two-dimensional materials such as tungsten disulfide (WS_2), phosphorus-based black phosphorus, silicon-based silicene, and hexagonal boron nitride have been mostly applied for device applications, which span from high performing field effect transistors to light emitting diodes, to high-speed photodetectors and artificial synapses. From the standpoint of the applications, two-dimensional materials are broadly categorized based on their bandgaps[6,16]. For example, TMDCs such as tungsten disulfide (WS_2) is demonstrated for photodetectors and light emitting diodes in the visible spectra of radiation, black phosphorus and silicene on the other hand as photodetectors and lasers for optical-communication, while large bandgap materials such as hexagonal boron nitride as insulating substrates/encapsulations and tunneling barriers (see Figure 2). Graphene, on the other hand, is being intensively researched for interconnects and electrodes applications due to its intrinsic high-breakdown current density ($\sim 10^8$ A/cm^2) that is comparable to state-of-the-art carbon

nanotubes and its tunability on nature/magnitude of the junctions it forms on contacting other functional materials[6,7,17–19]. In most cases such devices outperform conventional platforms. For example, transistors based on two-dimensional materials show threshold switching slopes close to the thermodynamic limit (74 mV/decade)[20] while also enabling large operational bandwidths (6 GHz)[21]. Photodetectors based on two-dimensional materials show very high photoresponsivity ~10^7 A/W, although generally limited on photodetection bandwidth[22]. Overall, their ultrathin form factor and accompanying material properties make two-dimensional materials one of the most promising candidates for beyond silicon technologies.

Commonly used two-dimensional materials have the hexagonal lattice structure, with differences not only in the chemistry of atoms but also in the nature of bonds. In graphene, the carbon atoms are packed densely in a regular 'chicken-wire' pattern. In silicene, atoms are twisted, while in black phosphorous the lattice takes a puckered structure. Transition metal dichalcogenides on the other hand are three atoms thick, with the transition metal sandwiched between two chalcogenide atoms. For device applications (see Figure 1E), two-dimensional materials are commonly stacked over each other in a variety of different combinations, from both material and geometry standpoints, to form nanometre thin van der Waals heterostructures[17,19]. In such heterostructures graphene is mostly used as the transparent electrode while other two-dimensional materials as active units; for example in an image sensor, photo-generation of carriers occurs in the active layer while the charge collection at the electrodes. A distinctive feature of van der Waals heterostructures is that in contrast to thin films based heterostructures (Physics Nobel Prize in 2000), such heterostructures intrinsically carry high-quality interfaces and do not suffer from lattice mismatch issues due to the absence of dangling bonds. In essence, this enables realization of high carrier mobilities, atomically sharp junctions and observation of elusive quantum effects such as Klein Tunnelling and electron gas confinement[5,16].

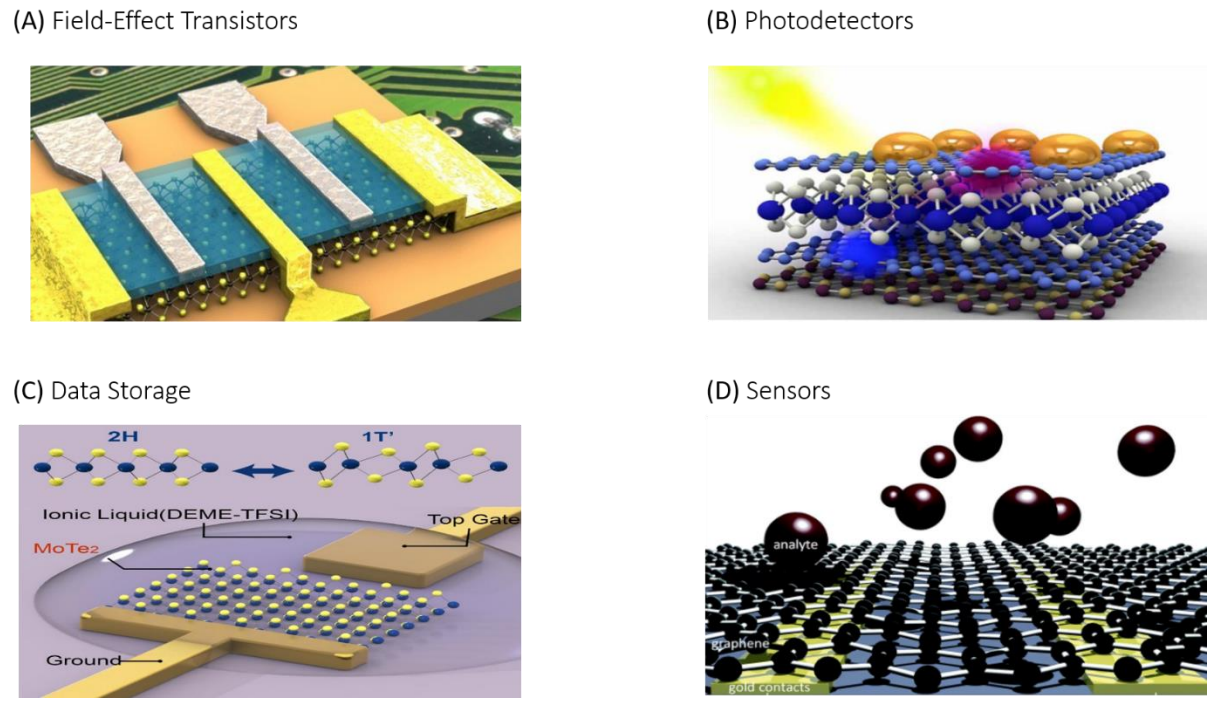

Figure 2. **Some device applications of two-dimensional materials**. (A) A field-effect transistor based on single layer MoS_2 with a top and bottom gate configuration (figure reproduced from[20]). (B) A photodetector based on the heterostructure configuration of graphene, WS_2, and hBN, where WS_2 is the active unit[22]. (C) A non-volatile data storage (memory) device based on electrostatically induced phase transition (2H to IT') in $MoTe_2$[23–25] (figure reproduced from[23]). (D) An illustration of a biochemical sensor based on graphene oxide. Electronic properties of graphene and graphene oxide are sensitive to adsorbents; a property that has been harnessed for single molecule and protein detection[26] (figure reproduced from[26]).

Along with these, one remarkable capability that two-dimensional materials offer is the creation of artificial materials: materials that would otherwise with certain confidence be absent in nature. Derivatives of graphene, such as fluorine functionalized graphene and van der Waals heterostructures. To this end, the greatest challenge perhaps in the commercialization of two-dimensional materials for electronic and optoelectronic technologies has been their economic and large scale CMOS (complementary metal-oxide semiconductor) compatible manufacturability. Synthesis based on mechanical exfoliation of bulk samples using pressure-sensitive (such as scotch) tape and solvents is the most routinely used method to produce two-dimensional materials. This approach produces the highest quality materials (see Figure 3A) but suffers from the inability to scale-up. The throughput of such an approach is poor and the

maximum crystal size of an isolated two-dimensional material is typically ~20 μm (in width). Furthermore, the technique is limited by its inherent stochasticity in controlling the number of exfoliated layers. Several other methods to synthesize two-dimensional materials have therefore been explored (see Figure 3B and 3C), of which chemical vapor deposition (CVD) synthesis is most commonly used for reasons that it enables large-scale synthesis (~100 meters long graphene sheet for example) and strict control and freedom on the number of layers and doping, respectively[27,28]. In this thesis CVD grown two-dimensional materials were used (see Appendix 1 for the recipes). However, CVD grown materials, while offering good material quality, fall short on quality compared with the exfoliated counterparts. For example, carrier mobilities are generally downgraded by 1-3 order of magnitudes in CVD grown materials; the origin of which is attributed to defects and contamination during growth and transfer[18,29,30]. Regardless, CVD setups can further be fitted in an industrial grade roll to roll system for large productions.

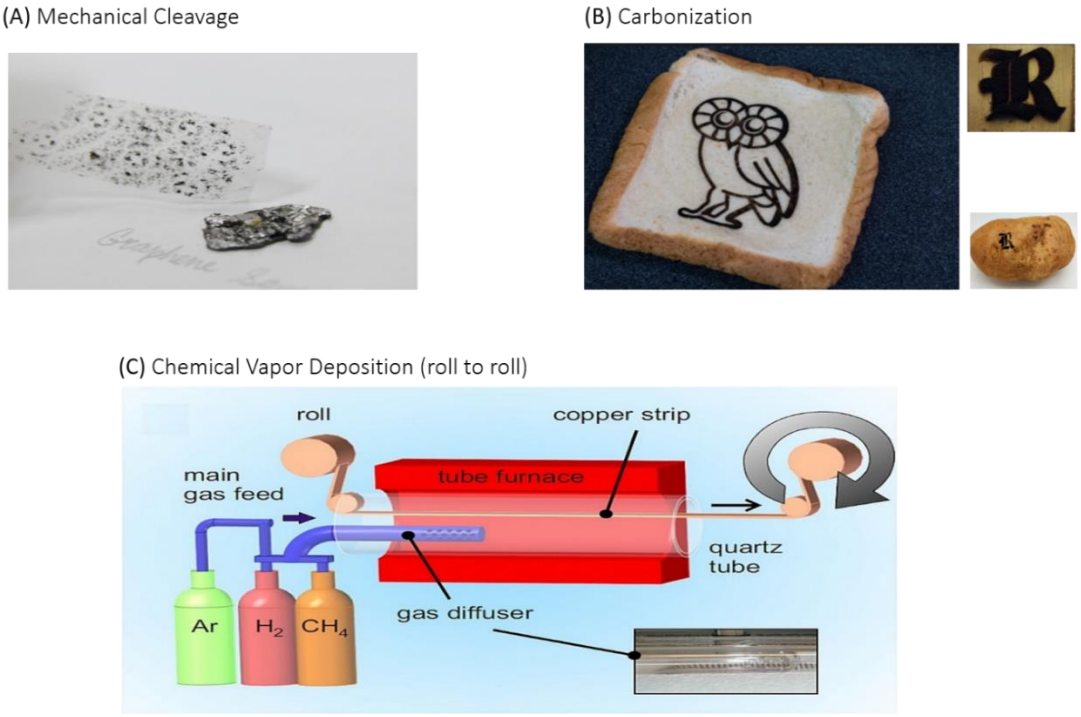

Figure 3. **Illustration of common synthesis methods**. (A) The mechanical cleavage method[31] uses pressure-sensitive tape to peel monolayers from bulk crystals through breaking interlayer van der Waals interaction (figure reproduced from[31]). (B) The carbonization method[32] uses high power lasers to break carbon source (such as bread/wood/potato) into various forms of carbon, of which graphene is one. Such a method can enable direct writing of graphene on structures. (C) Chemical vapor deposition method uses vaporization of precursors to produce two-dimensional materials at the wafer scale. Addition of a roll-to-roll system to the deposition furnace[33] enables large-scale throughput (figure reproduced from[38]).

Because two-dimensional materials are ultrathin structures, their metrology is a demanding task. For instance, most often atomic force microscopy (AFM) is coupled with optical spectroscopy techniques such as Raman spectroscopy and photoluminescence in determining the thicknesses of these materials. Optical spectroscopy techniques also enable the study of bandgaps[34,35], strain effects[36], inter-layer coupling[35,37], catalysis[38] and more, making them undeniably the leading candidates for characterization of two-dimensional materials. More commonly, characterization techniques for two-dimensional materials also serve as test-beds and tools for studying material properties under perturbed states and for fabrication (see Figure 4). For example, cantilevers in atomic force microscopy can be used to indent two-dimensional materials[39], thereby opening bandgaps in them and/or causing phase transformations. Similarly,

lasers in optical spectroscopy systems can be used for direct synthesis and pattern witting of two-dimensional materials[32,40].

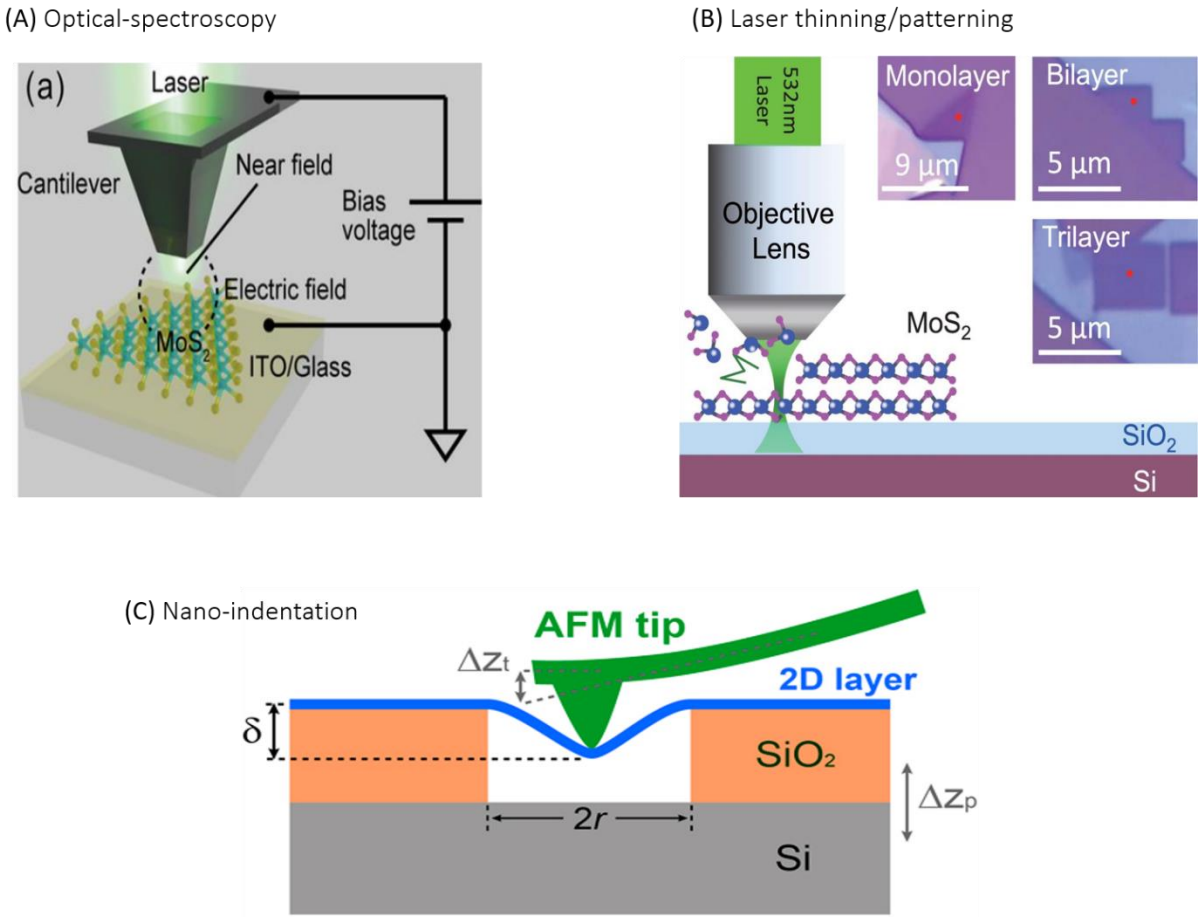

Figure 4. **Some characterization techniques**. (A) Optical spectroscopy techniques[41] such as Raman spectroscopy and Photoluminescence use optical excitation such as lasers in studying the electronic and optical properties of the materials. (B) Laser thinning utilizes a setup similar to optical spectroscopy but uses high laser powers[40] to post-process two-dimensional materials, such as patterning them for device applications. (C) Nanoindentation techniques are used in the characterization of the mechanical properties of two-dimensional materials, such as determining their fracture strength and toughness. Atomic Force Microscopes are most commonly used for such nanoscale measurements[39](figure reproduced from[23]).

1.1.2 Phase Change Materials

Materials that offer tuneable properties on-demand are at the forefront of many emerging electronic and optoelectronic technologies. One example of such materials are the chalcogenide phase change materials (PCMs). PCMs, in broadest of the definitions, refer to materials whose solid-structural phase can be switched between at least two stable states -amorphous and

crystalline-, at ultrahigh speeds (~ 0.1 ns) and with high cyclability (> 10^{11}) using heat, which can be induced either electrically or optically[42,43]. PCMs are at the heart of optical (DVDs/Blu-ray) and electronic (phase change memory and storage class memories– SCMs) data storage, both of which exploit the vastly contrasting properties of optical refractive index and electrical conductivity between the amorphous and crystalline states (see Figure 5A). Figure 5B illustrates the electrical switching characteristics of PCMs. During crystallization, it is thought that the Joule heating heats the material above its glass transition temperature[44] into a conductive crystalline state. Whereas for amorphization, Joule heating induced from fast electrical pulses take the material beyond its melting point, and subsequent quenching produces an amorphous volume that has a greater resistivity.

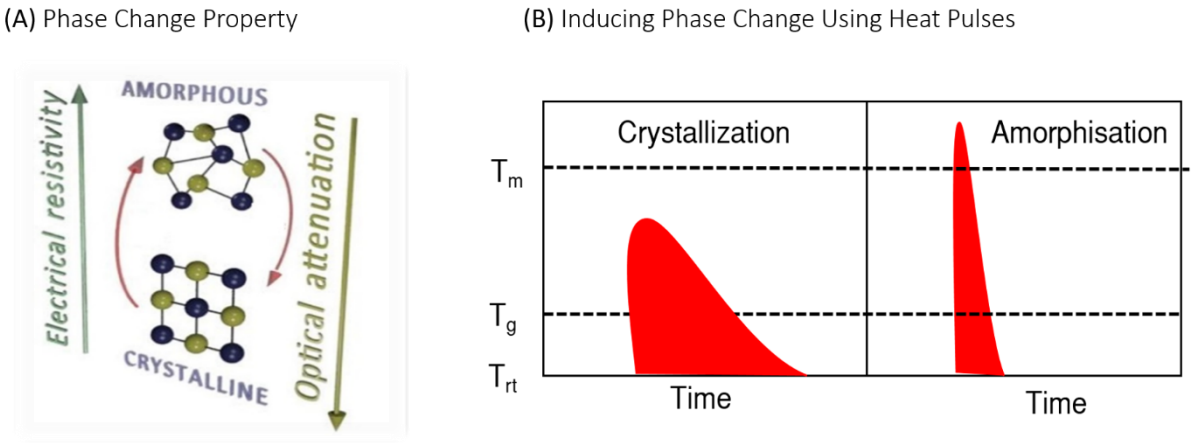

Figure 5. **Switching characteristics of phase change materials**. (A) Schematic illustrating the amorphous (disordered atomic arrangement) to crystalline (ordered atomic arrangement) phase transformation. Electrical resistivity declines while the optical absorption increases from the reversible amorphous to crystalline phase transformation. (B) Such phase transformations can be induced through subjecting a phase change material to heat pulses (either optical or electrical or both). Crystallization is achieved by heating the material above its glass transition temperature and letting it gradually cool down. Amorphization is achieved by heating of the material above its melting temperature followed by rapid quenching.

The first materials[45] to have revealed phase change effects on electrical and optical stimulus were $Ti_{48}As_{30}Si_{12}Ge_{10}$ (in 1968) and $Ti_{81}Ge_{15}Sb_2S_2$ (in 1971), respectively. Since then many new PCMs have been reported. Interestingly, however, the chalcogenides, particularly combinations

of tellurium (Te) with germanium (Ge) and antimony (Sb), have always been the center of focus. Observational work[43,44] on optical switching at speeds sub-50 ns in alloys like $Ge_4Sb_2Te_4$ and $Ge_2Sb_2Te_5$ (GST) could be regarded as the seed for this interest in chalcogenides. As of today, the most widely studied systems lie on or in the vicinity of a pseudo binary line that joins the stoichiometric compounds Sb_2Te_3 and GeTe in the ternary phase diagram of Ge-Sb-Te, as illustrated in Figure 6A. Among these, the alloy[43,44] $Ge_2Sb_2Te_5$ (GST) has the best match of properties; fast crystallization/amorphization rates, amorphous phase stability, endurance limit and excellent contrast between the two states, and therefore has garnered greatest attention. Indeed, in this thesis, GST is mostly used for device applications. Systems constituting Figure 6A, and many others that belong to the chalcogenides family, are broadly classified into two types; nucleation dominated, and growth dominated alloys[46,47], depending on mechanism they follow for crystallization. Classical thermodynamics defines two conjugate stages towards phase transformation; nucleation followed by growth. Depending upon which among these exercise dominant control over the phase transformation process, chalcogenides are differentiated into two types- nucleation dominated (see Figure 6B) and growth dominated (see Figure 6C).

Crystallization by nucleation occurs via formation of nuclei at random locations within the bulk of the phase change material[48]. Upon a temperature rise, these nuclei grow, dilating until they impinge each other. This is when complete crystallization occurs. Examples of nucleation dominated phase change materials[44] include $Ge_2Sb_2Te_5$ (GST), $Ge_2Sb_2Te_6$ and $Ge_4Sb_2Te_4$. Such materials, with their nucleation rate greater than their growth rates, are fast crystallizing[48], and hence undergo crystallization in few nanoseconds. This tendency make nucleation dominated materials the ideal candidates for electrically driven memory since they allow maximization of the clock frequency that drives the processor. A growth-dominated phase change material crystallizes at a growth rate greater than the nucleation rate[46]. This essentially means that only a few nuclei precipitate during annealing of the amorphous volume, among which just one (single nucleus)

tends to grow at the cost of others in achieving crystallization[49]. This process is characterized by directional transformation, which is saying that a nucleus precipitates preferably at the crystalline-amorphous interface, and grows into the bulk of the amorphous volume. Thin specimens are therefore easier to recrystallize, or alternatively, small amorphous regions crystallize faster than larger amorphous regions. Materials which show growth-dominated crystallization include[43,44] Ag and In doped SbTe (AIST), GeSb, GeSnSb, and $Ge_3Sb_6Te_5$. These materials are well-suited for optical data storage, since smaller regions are switched. It is thought that at the nanoscale the process for a single nucleas to grow and modify the material properties is faster than for multiple nuclei to nucleate and coalesce, due to the high crystal growth velocity in such material systems. In the absence of an interface, crystallization or SET takes longer, owing to the increased activation energy for crystal nucleation.

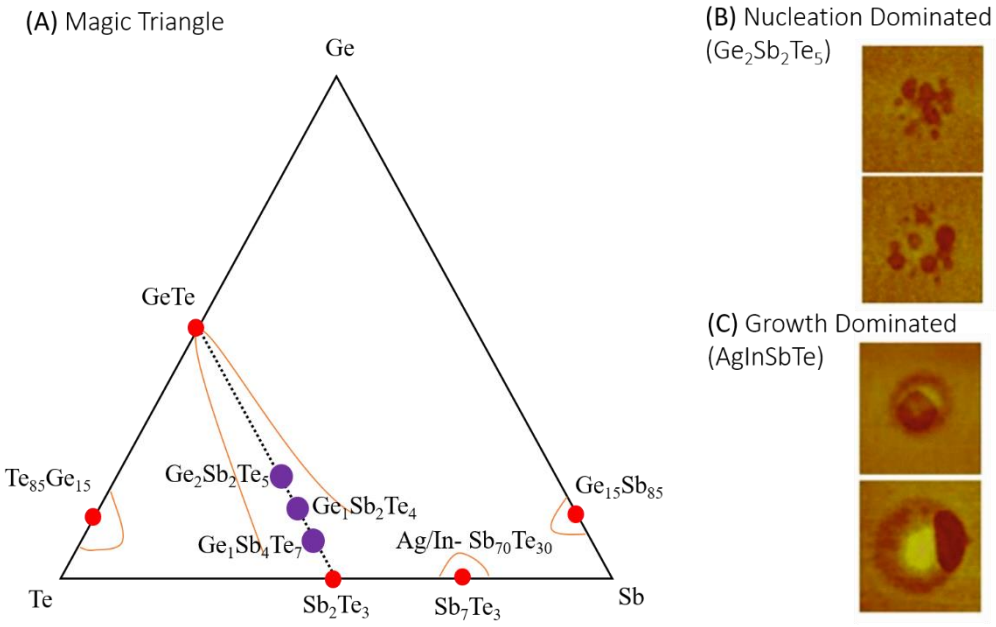

Figure 6. **Different forms of phase change materials**. (A) Ge-Te-Sb ternary phase diagram highlighting various phase change alloys. Most studied and commercialized compositions are on the dotted line (tie-line) that connects the GeTe and Sb_2Te_3 compounds. The materials on the diagram can broadly be classified into (B) nucleation dominated materials, in which homogenous nucleation (dark brown regions in the atomic force micrographs) of the crystalline phase occurs and (C) growth dominated materials, in which heterogeneous nucleation of the crystalline phase occur at the interfaces.

Bulk growth dominated materials quite behind the nucleation dominated materials when it comes to the crystallization rate, which is crucial for data storage applications. Reflectance studies have shown that the crystallization speed in AIST can be 100 times slower than GST[47]. Doping or addition of foreign elements (dopants) is a common practice in altering the PCM properties. Dopants are typically added in unfixed amounts, as long as the original crystal structure and crystallization mechanism remains unaltered. Because the dopant concentration could take large values (sub-15 at%)[50], the term doping is often substituted by alloying in the context of phase change materials. Dopants generally include N, C, O, Ga, Ge, Ag, In, Ga, and Sn[42,50,51]. Nitrogen-doped alloys are a current research focus, due to ease of fabrication[51]. Studies reveal that in GST nitrogen and carbon dopants increase the crystallization temperature of the alloy as well as the activation energy required the for solid to solid phase transformation between the crystalline states (FCC to HCP). These effects are understood to emerge from decreased grain size and suppressed grain growth of the alloy due to presence of the dopants at the vacancy sites, where they bond covalently with Ge and Te, and at the grain boundaries, where they segregate as clusters[52].

Interestingly, the switching mechanism between the amorphous-crystalline phase transformations remains elusive. The vastly contrasting properties between the amorphous and crystalline states, particularly optical is proposed to be resultant of not only changes in atomic structure as with conventional materials but also changes in the type of the chemical bonding between atoms. It is believed, although not satisfactorily confirmed, that in the amorphous phase (disordered atomic arrangement), covalent bonding dominates, where mutual sharing of electrons between neighboring atoms occurs, while in the crystalline state a less common type of bonding called resonance bonding occurs. In resonance bonding, the electrons are delocalized, i.e. continuously resonating between atoms.

In the crystalline state of GST[51,53], Ge takes octahedral coordination with Sb and Te, while in the amorphous phase it bonds with tetrahedral coordination (see Figure 7A and 7B). The process of flipping between these coordination states is termed umbrella flip. It is speculated that the umbrella flip mechanism enables the fast switching speed in phase change materials since atoms move only by atomic distances during switching. Figure 7A illustrates the umbrella flip mechanism at a unit cell level. However, on the contrary to several prior studies, recent experimental and simulation results have suggested that this is not strictly the case; within the amorphous phase, both six-fold and four-fold coordination can co-exist. Furthermore, for GST nanowires, the mechanism of umbrella-flip does not apply. Switching is demonstrated to be a result of the degree of dislocation mobilization and accumulation[54]. It is worth noting that the stable crystalline atomic structure is seldom achieved in practice during device application owing to constrained kinetics. For instance, GST based devices typically switch between a distorted and metastable rocksalt structure and amorphous states; although the stable crystalline form has hexagonal symmetry. The electrical resistivity measurements of the as-deposited GST thin films as a function of temperature show two abrupt drops[53]. The first drop (by two orders of magnitude) occurs at ~150 ^{0}C from the nucleation of the crystalline rocksalt phase, and the second (again by two orders of magnitude) from the phase transformation the rocksalt structure into the hexagonal phase at ~300 ^{0}C. The thermal conductivity of the as-deposited film also increases by an order of magnitude from the crystallization of the hexagonal phase. Typically, a crystalline phase is also characterized by a significant number of vacancies. For example, the GST ($Ge_2Sb_2Te_5$) alloy shows 25 % vacant sites per unit cell (the stoichiometry of GST is, therefore, $Ge_{22}Sb_{22}Te_{55}$). The origin of vacancies in GST has been understood through quantum chemical calculations. Explanations claim that vacancies are needed in order to annihilate antibonding interactions between Ge-Te and Ge-Sb bonds, thus stabilizing the crystalline phase[51]. Additionally, unit cells with vacancies get distorted through the Peierls distortion[55]. Such crystal lattice distortions are believed to

further stabilize the crystalline phase[43] that results in faster crystallization. Furthermore, some compositions of phase change materials, such as GST show metal to insulator transitons[50,53]. For example, the room temperature resistance of crystalline $Ge_1Sb_2Te_4$ decreases by a factor of ~400 from increasing the temperature from 150 °C to 350 °C.

While there is no definitive proof for Joule heating driven switching, it is the most widely adopted explanation for the switching behaviour in electronic devices. For this mechanism to hold, another mechanism termed threshold switching is invoked to explain the surge in the current carrying capacity of the otherwise resistive amorphous state. Threshold switching is not a unique feature of chalcogenides, it has also been observed in amorphous silicon[56], transition metal oxides[57], and amorphous pnictides[58]. Threshold switching has been explained by a variety of models[59–61], each giving a nice fit to the experimental data[59]. However, one can also gain an insight into it from a materials science perceptive[46,47]. From this standpoint, it is defined as the external stimulus field and/or heat required, which converts sub-critical nuclei in the amorphous matrix into super-critical nuclei, which grow until they impinge each other, forming conductive crystalline pathways. Atomic force micrographs in Figure 6B and 6C show how nuclei evolve in a phase change materials. From a physics outlook, it is best understood from voltage-current instability[50,58,59,62]. At sub-threshold fields ($< V_{th}$), the trapped electrons, which are a result of the short-range disorder, defects such as dangling bonds, and/or impurities in the amorphous matrix, and placed within the bandgap mobilize owing to the gained momenta. Such high energy electrons hop between other trap states thereby giving net conductivity. This field dependent conductivity is termed the Poole-Frenkel mechanism[15] and is demonstrated in Figure 7C. Without an external field, the trapped electron needs to overcome a large barrier in order to become mobile. Application of an external field changes the shape of this barrier, consequently decreasing the barrier height and facilitating thermal emission of electrons. Conduction is dependent on the inter-trap distance; increasing with decreased distance.

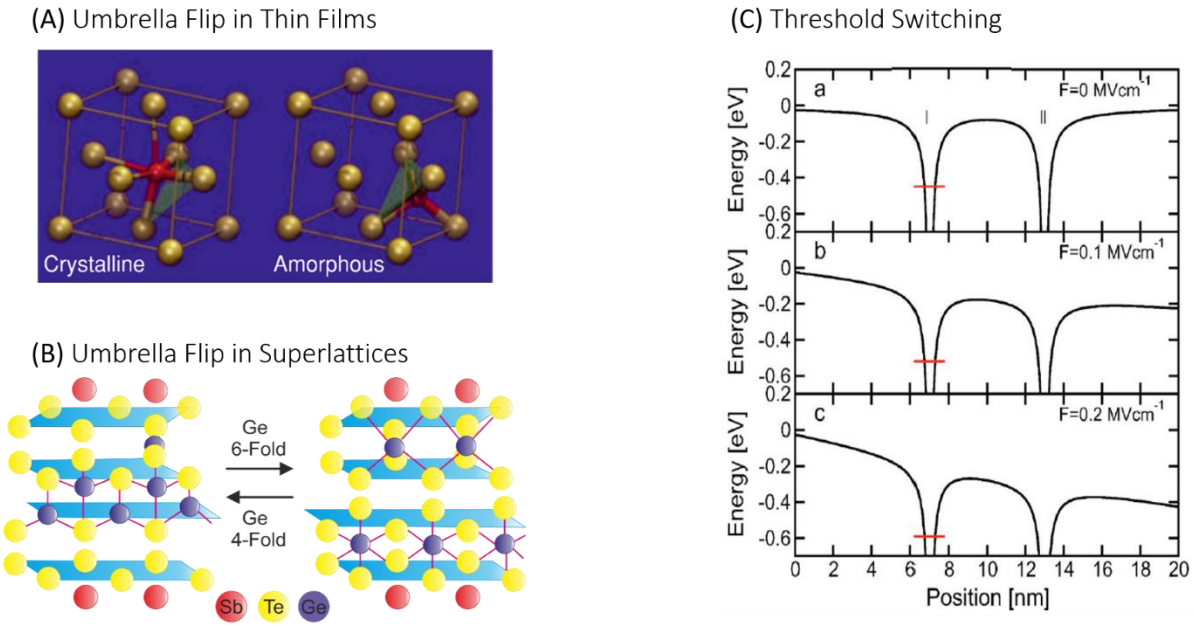

Figure 7. **Switching mechanism**. (A) In the umbrella flip model (shown for GeTe), the Ge atoms atom hops from an octahedral position to a tetrahedral position across the (111) plane during amorphization. The thicker lines represent the strong covalent bonds, and thinner lines represent the weaker bonds[51]. (B) In a superlattice structure, Ge atom hops across the van der Waals region between epitaxial GeTe and Sb_2Te_3 layers, during phase transformation[63]. (C) An illustration explaining the threshold switching phenomenon. Note the downwards sloping behavior with an increase in the field strength (a to c), which is representative of barrier lowering that enables Poole–Frenkel conduction. This field-dependent barrier height reduction is responsible for sub-threshold current that results in Joule heating[59].

Nevertheless, it is indeed surprising that despite these uncertainties in the material's understanding, PCMs remain successfully commercialized for optical (DVD/Blue-ray) data storage, less successfully for electronic data storage, and of interest in emerging applications such as phase change displays, neuromorphic computing, metasurfaces, smart windows and more (see Figure 8). In optical data storage disc, the phase change is driven in a phase change material thin film using a laser, and data (bits) is associated with the reflectivity levels of patterned regions. In electronic data storage applications, the phase change is driven in a phase change material thin film using Joule heating, and data (bits) is associated with the resistance levels of programmed cells[48,64]. In neuromorphic computing, a phase change material is used to emulate either the synapses (junctions between two neurons) and/or the cell membrane. Using either can enable non-von Neumann computing (in-memory computing) or has been demonstrated on both

electronic and photonic platforms[65,66]. Integrated photonic memory (using light for data programming) has been realized by evanescently coupling light to phase change material to both read and write data[67]. In phase change displays, the reflectivity change from phase transformation is utilized to generate color change (for example, a pixel is designed to reflect green in the amorphous state, which on switching becomes blue). Phase change displays can achieve scalability and pixel writing speeds much higher than conventional technologies[68]. Smart windows[69] based on phase change materials utilizes the changes in the light transmission ability to filter certain wavelengths in a reversible, yet non-volatile manner (for example, in one state of the phase change material infrared can be blocked, thus enabling temperature control). Crucially, phase change based technologies are rapidly advancing not only because they offer enhanced device performance, but also because phase change materials mitigate the need for re-inventing the fabrication wheel: phase change materials are already well-studied and mass produced for optical data storage for nearly five decades, thereby enabling manufacturability know-how and infrastructure transfer for other emerging technologies.

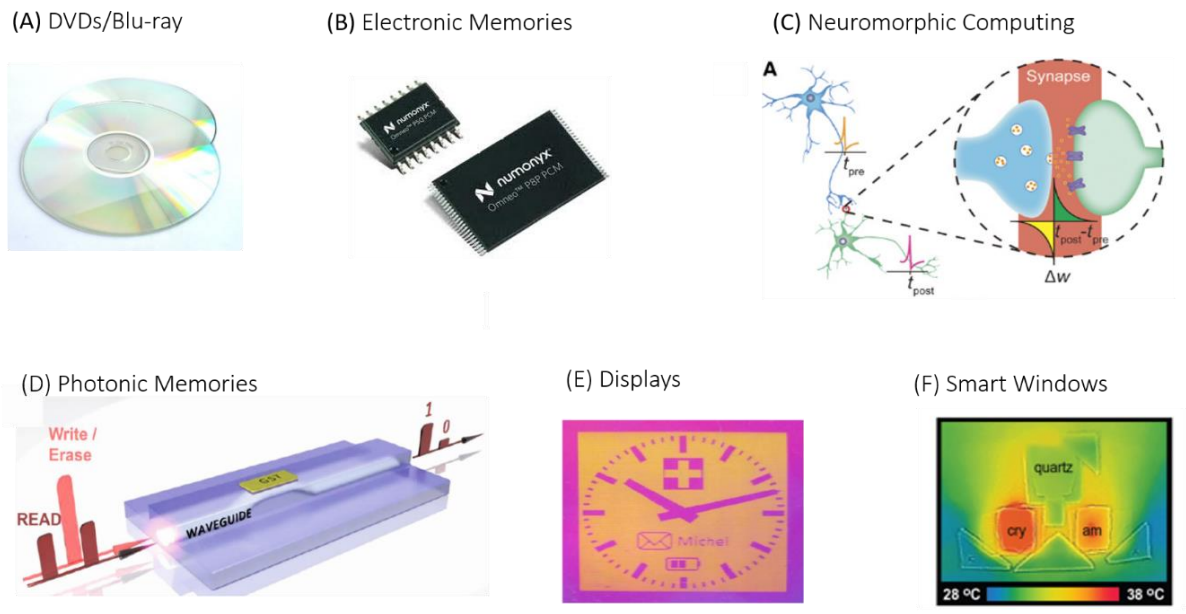

Figure 8. **Device applications**. (A) In DVDs/Blu-ray disc the phase change is driven using a laser (figure reproduced from[70]). (B) In electronic data storage applications, the phase change is driven using Joule heating, (the figure is a Micron(R) product and is reproduced from[71]). (C) In neuromorphic computing, a phase change material emulates neural circuits (figure reproduced from[66]). (D) In integrated photonic memory, light is used to both read and write data in the phase change material (figure reproduced from[67]). (E) In phase change displays, the reflectivity change from phase transformation is utilized to generate color change (figure reproduced from[72]). (F) In smart windows, the modulation in the light transmission from the phase change is used to filter certain wavelengths, such as infrared.

1.1.3 Devices from Two-dimensional and Phase Change Materials

Both two-dimensional and phase change materials share a rather interesting discovery history. The first phase change material to have been discovered but sadly little known and seldom cited was bulk Molybdenum disulfide (MoS_2) in the early 1900s[43], which is a transitional metal chalcogenide and today's most intensively studied two-dimensional material. More recently, other forms of two-dimensional materials have demonstrated characteristics of phase change materials, opening new prospects for device applications. However, these are different from traditional phase change materials that I have so far discussed, in that they switch from one solid crystalline state to others, and not necessarily by an electric field.

Nevertheless, combining the better of these two remarkable materials in their existing forms can enable many imminent efficient technological-platforms. For example, if phase change

memory is to truly compete against current silicon charge-based technology as it is currently touted to[44,64,73], its current device architecture may not suffice because the high programming electrical power has presented a challenge to realize low energy consumption operation. Therefore a considerable amount of research has been put into optimizing material's compositional design and device's geometrical and electrical architectures. Over the years, it has become clear that scaling down the physical volume of the phase change material and its contact area with the electrodes is key to enhancing the device performance. Smaller sized devices would require less heating, hence energy consumption for switching and undergo crystallization and amorphization of a larger volume fraction, thereby decreasing elemental segregation which is the major cause for device failure[48,74,75]. Therefore, there is increased interest in developing devices with ultra-scaled volume. Intuitively the limit to scaling-down is achieving the size of a single unit cell. Figure 9 illustrates the switching energy required to cause the crystalline-to-amorphous transition, which is the most energy-intensive process because the material needs to be melted. Energy consumption falls linearly (in log scale) as the interfacial area gets smaller. Indeed, the state-of-art devices have been achieved through combining low dimensional materials that provide atomic-scale contact areas, such as contacting one dimensional and two-dimensional electrodes with phase change materials.

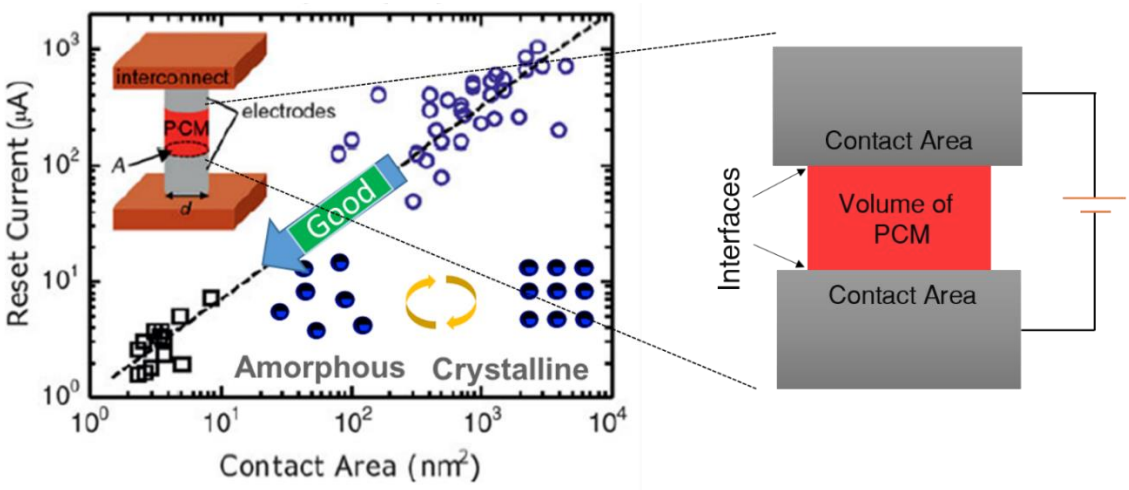

Figure 9. **Scaling Behaviour of phase change memories**. Required current for amorphization as a function of the contact area in phase change memory cells. Amorphization is 40-80 % times more power expensive process than crystallization; naturally, the devices would become more energy efficient if the amorphization power expense is reduced. Devices making lesser contact with the electrodes are more energy efficient.

As I have mentioned earlier, PCM powered memory devices are challenged by high energy consumption. One of the breakthrough discoveries to have fostered the possibility of sub-femto joules energy consumption per bit came in the form of nano-gap electrodes. Nano-gaps is a structure where two electrodes are separated from each other by a few nanometres (typically sub-100 nm). Carbon nanotubes based nano-gap electrodes have been used to create efficient nano-gap phase change memory devices (see Figure 10). Ultra-low currents and voltages and switching energy as little sub-100 fJ switching energy have been demonstrated using carbon nanotubes electrodes spaced 20-30 nm apart spaced[76,77]. Although these experiments demonstrate the possibility of low power switching, carbon nanotubes are difficult to integrate into large scale lithography processes. More recently nano-gap electrodes based on graphene have been demonstrated. The power requirements for such devices are similar to those of carbon nanotubes, and graphene electrodes can more readily be fabricated and integrated. Such low energy consumption in both cases is due to a reduced interfacial contact area (nanotubes are sub-5 nm in diameter while graphene is 0.35 nm in thickness), and the reduced volume of the PCM. Because a reduced volume is switched between amorphous and crystalline states, nano-gap

electrodes have enabled significantly lower programming power (~2.6 μW) compared to the conventional phase change memory cells that require programming power of the order of ~1 mW[76,77]. This figure can be further reduced to ~0.1 μW using device optimization and proper instrumental and control. Crucially, the ultimate-scaling limit is to switch PCMs at the single-unit cell volume, which can be achieved using nano-gaps that are spaced sub-2nm apart. Indeed, studying this scaling limit is one of the themes of this thesis.

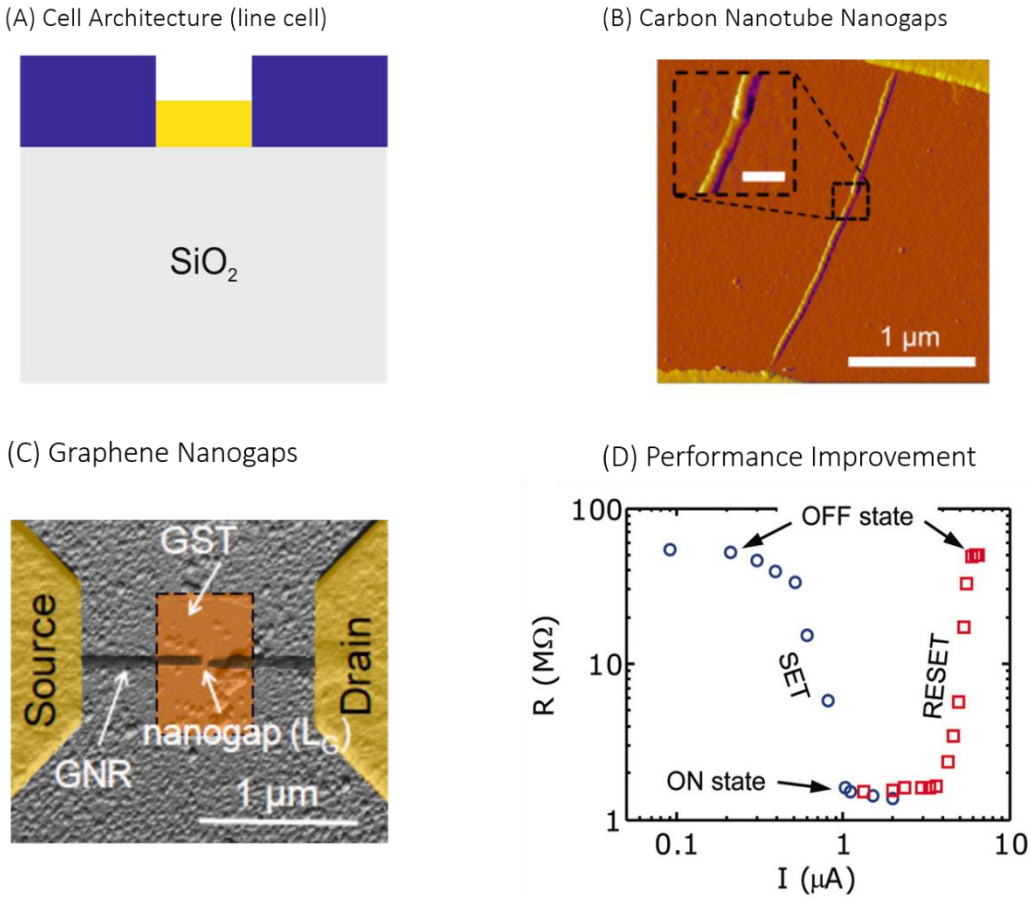

Figure 10. **Nano-gap phase change memories**. (A) Schematic illustrating line-cell architecture of a memory device. (B) An atomic force micrograph of a carbon nanotube nano-gap device, where the gap is bridged by GST. (C) A scanning electron micrograph of a graphene nano-gap device[76] (figure reproduced from[76]). Use of graphene enables lithography control and large scale manufacture[78](figure reproduced from[78]). (D) Experimental data illustrating the performance enhancement in the form of current required to cause phase transformations between amorphous-crystalline states[77](figure reproduced from[77]).

Another example of utilizing two-dimensional materials for efficient phase change memory devices is in the form of the thermal layers or interfacial engineering (see Figure 11). Thermal layers are heat isolating layers and can strongly influence the crystallization kinetics of the

PCM[79,80], and thus, regulate the switching power. Graphene can be the ideal thermal layer for its anisotropic thermal properties i.e. thermal conductivity a function of the crystallographic direction. Graphene has very high in-plane thermal conductivity but equally poor out-of-plane conductivity. This allows graphene to laterally confine heat. Indeed a 40 % decrease in the current requirement for amorphization of the crystalline phase has been reported[79] in commercially used phase change memory cells using graphene thermal layers; thereby paving the way for energy efficient devices. Moreover, graphene as a thermal layer is also speculated to improve endurance limits, as it can significantly reduce the atomic diffusions (migration/segregation), which generally occurs into conventional metallic contacts.

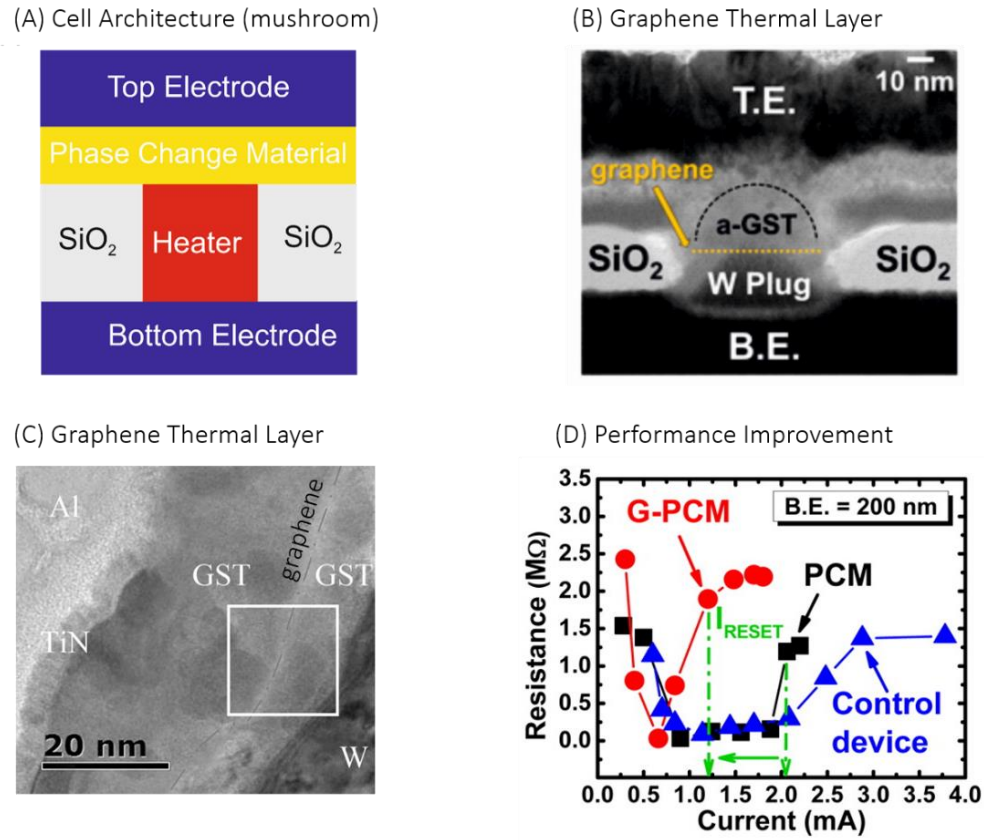

Figure 11. **Graphene thermal layer based memories**. (A) Schematic illustrating a mushroom cell architecture of a phase change memory cell. Such a cell design enables high device density and is currently the commercially used design. A heater enables heat confinement hence energy efficient cell operation. (B) A transmission electron micrograph of a mushroom cell with a graphene layer between the phase change material (GST) and the heater[79] (figure reproduced from[79]). (C) A mushroom cell with the upgrade of placing graphene not in direct contact with the heater, instead in between the phase change material films (GST)[80] (figure reproduced from[80]). (D) Data illustrating performance enhancement (decrease in the current required to cause amorphization of the device[79]). Control device is a mushroom cell without graphene layer.

While these are just two demonstrations, the prospect of combining the better of these two materials can enable many more efficient technology platforms, such as photodetectors, computing, and zero-power radio frequency switches.

1.2 Layout of this thesis

In the current chapter, I have laid the motivation behind the construction of this thesis. I have reviewed the literature towards providing the fundamental understanding and current research status of phase change materials and two-dimensional in the context of nanoscale

functional devices. In the 2nd chapter, I detail the fabrication and characterization methodologies, including the electrical circuitries, which I have used for the manufacture and development of phase change and two-dimensional based nano-scale devices. In the 3rd chapter, I describe the fabrication, metrology and scaling limits of graphene nano-gaps: a relatively new device concept based on graphene nano-electrodes that enables contacting nanoscale objects and therefore defines the ultimate form of device scaling. I use feedback electroburning to fabricate such devices with controlled gap sizes and illustrate a new approach based on Kelvin Probe Microscopy to image them. I then apply this device concept in contacting nanocrystals of phase change material in the fabrication of highly energy efficient phase change memory devices that compare with the state-of-the-art using a lithography-free self-alignment approach. I then report that for gaps approaching 1 nm the switching is dominated by carbon chain formation, creating a fundamental scaling limit for potential devices. In the 4th chapter, I illustrate the effect of strain on two-dimensional materials as I make attempts to translate the phase change memory devices demonstrated in Chapter 3 onto flexible substrates. I demonstrate a new strain characterization technique based on Kelvin Probe Microscopy using ultrathin graphene/transition metal di-chalcogenides (WS_2) heterostructures as a demonstrator system. This technique overcomes the limitations (materials, resolution and substrate effects) of commonly used optical spectroscopy tools, and reveals strain-driven changes in the work function and junction potentials. I show that graphene's work function is strongly modulated, and hence its electronic properties also change. I also propose two new device concepts that use strain effects; a strain-effect transistor in which reversible strain is used in the two-dimensional material from volume changes during the amorphous-crystalline transition in phase change materials and low loss color changing films for smart devices, such as solid-state displays. For these applications, I explore Ge doped Se chalcogenide glasses. In the 5th chapter, I study the photoconductivity mechanism in phase change materials, reporting observations that are in some aspects contrary to the literature. I

report an unprecedented photo-response and a photo-voltaic behavior of significant magnitude in both the crystalline and amorphous states of the phase change material, and study the effect of device geometry and electrodes on the photo-behavior. I demonstrate applications of non-volatile photo-detectors with photo-responsivity and bandwidth tuneability. I then showcase a novel photodetector concept using phase change materials that mimic the working of a retina. These devices enable large dynamic range and scaling limits.

1.3 Statement of Originality

This thesis is an original contribution written entirely by the author. It contains original literature review and novel findings and procedures, all carried-out during a period of nine academic terms, as a part of the DPhil study at the University of Oxford. It is also emphasized that the author carried-out, under the supervisors watch and guidance, mostly independently, all the steps of device fabrication, electrical and material characterization, and manuscripts writing.

1.4 Key Contribution and New Science

The main findings of this thesis- exploring new devices concepts and functionalities using phase change and two-dimensional materials, with relevant mention of fundamentals and procedures are described in Chapters 2-5. The key results and new science presented throughout this manuscript include:

- Experimental and modeling studies of nano-gap formation via feedback controlled electroburning in graphene ribbons, with the demonstration of a technique that enables the metrology of the nano-gap electrodes. The first illustration of the scaling-limits of graphene nano-gap electrodes using low-power and self-aligned phase change memory cells as demonstrator devices.
- Illustration of a new approach for characterization of strain induced effects in ultrathin materials at the nanoscale using Kelvin probe microscopy. Demonstration of an optoelectronic framework for smart devices, such as solid-state displays and photonic resonators, using opto-structural changes in chalcogenide glasses.

- The very first quantitative results of the photoresponse of phase change materials in their three technologically relevant states: amorphous, electrically-switched crystalline and thermally-annealed crystalline, using nanoscale crossbar devices. Key findings include unprecedented photoconductivity, control over photo-thermal and photo-conductive effects, and a significant photovoltaic effect.
- A proof-of-concept demonstration of spiking detectors using chalcogenide glasses and graphene nano-gaps, and their applicability for construction of artificial retinas.

CHAPTER 2: Methodologies and Characterization Tools

Methodologies and Characterization Tools

A key element to this thesis is the fabrication and characterization of nano and microscale devices, of various architectures and designs. The fabrication was in part carried-out in ambient room conditions and partly in class 10,000 cleanrooms. A flow chart describing a general process flow for device fabrication is illustrated in Figure 12.

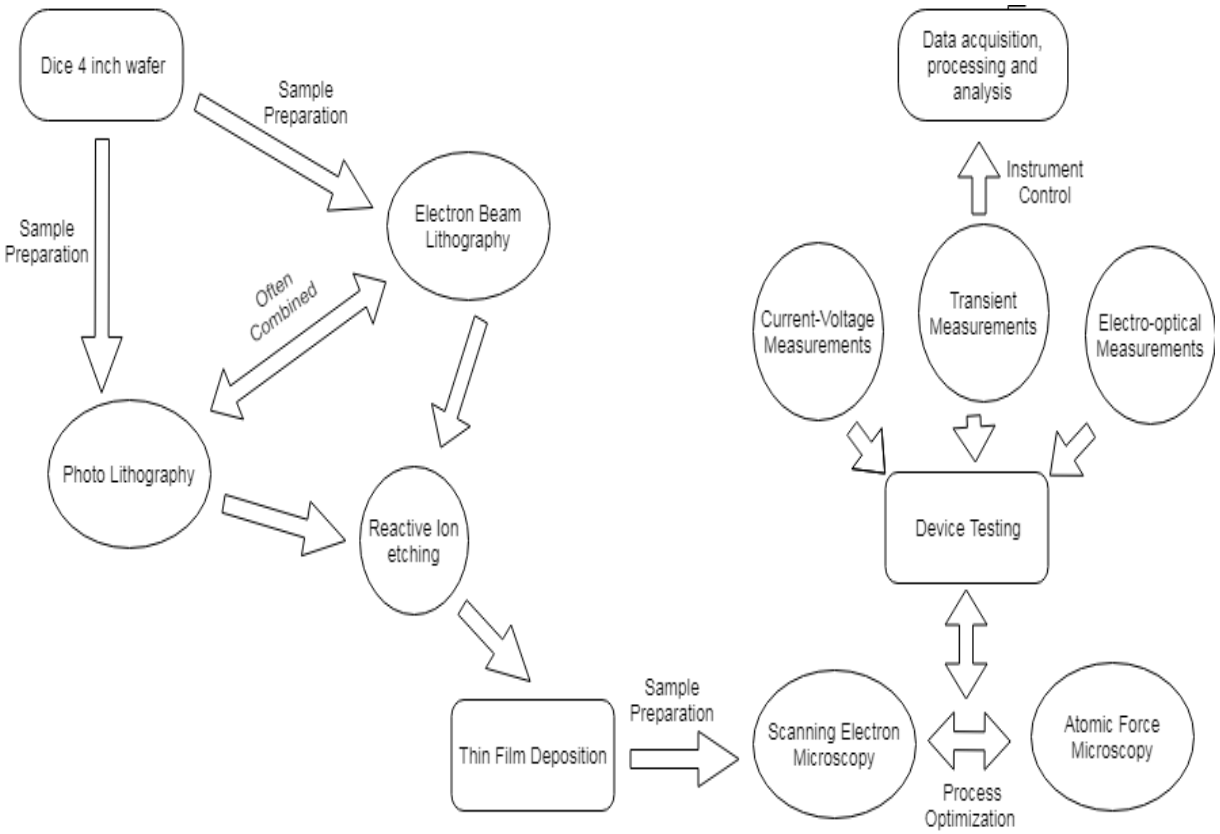

Figure 12. **Experimentation flow chart**. A flow diagram illustrating device fabrication and characterization methodology. Device fabrications were primarily carried-out using standard lithography tools using self-optimized recipes in class 10000 cleanrooms. At every stage of fabrication, device imaging was carried-out using scanning electron microscopy and atomic force microscopy. Device characterizations were carried-out in-house using custom built electrical setups and remotely controlled instruments.

2.1 Device Fabrication

Following are short descriptions of various tools and equipment used, mostly as a trained-independent user.

2.1.1. Lithography Techniques:

Photo-lithography:

Photolithography[81–83], also termed optical lithography uses light (UV) to transfer a geometric pattern from a photomask (in my case made on a borosilicate glass substrate using chrome) to a light-sensitive chemical photoresist that is coated on the substrate (silicon wafers) using spin-coating. Lithography was carried-out on a mask aligner under contact-mode operation and enabled feature sizes reaching ~2 μm. A positive photoresist (S1813) was most commonly used after selection and optimization of the most suitable recipe (2 mins baking at 120 °C, 8-20 seconds exposure time/30-60 seconds development in MIBK developer/30-60 seconds reaction termination in isopropanol). For better lift-off, an image reversal methodology was used using AZ5214E resist (90 seconds baked at 100 °C, UV exposure 1.7 seconds, 115 seconds bake at 119 °C, flood exposure for 50 seconds, 20-25 seconds development in AZ726 MIF, and 60 seconds rinsing in water). Customized masks were ordered from JD Photonics and few of them were self-etched using nitric acid and ammonium nitrate solution for process ease.

Electron Beam Lithography:

Electron beam lithography[82–84], also termed e-beam lithography uses the wave nature of electrons to transfer a geometric pattern from a digitally crafted design (using AutoCAD and K-layout software) to a beam-sensitive chemical "resist" that is coated on the substrate (silicon wafers). Lithography was carried-out on a JEOL-5500FS and enabled feature sizes reaching ~50 nm. Both positive (PMMA/CSAR) and negative resists (m-AN) was used after selection and optimization of the most suitable recipe (PMMA: 2 mins baking at 180 °C, exposure of 600-650 μC/cm^2, 45 seconds development in MIBK developer, 30-60 seconds reaction termination in isopropanol and distilled water. CSAR: 3 mins baking at 150 °C, exposure of 160-180 uC/cm^2, 33 seconds development in A6000 developer, 30-60 seconds reaction termination in isopropanol and distilled water. m-AN: 1 min 30 seconds baking at 90 °C, exposure of 180 μC/cm^2, 45

seconds development in MIBK developer, 30-60 seconds reaction termination in distilled water, cleaning in m-REM 600 solution). Devices on flexible substrates were patterned through spin-coating water soluble and electrically conducting Espacer layer on the baked resists.

Thin-Film Deposition:

Thermal Evaporation:

Thermal evaporation[83,84] is the simplest of the physical vapor deposition techniques. Crucially, material either existing as strips or as pellets in a ceramic boat is heated in a vacuum chamber until its surface atoms have sufficient energy to escape the surface and deposit on the wafer (silicon wafer). Most commonly gold and chromium were thermally evaporated on silicon wafer (Pressure = 2e-6 bar, Current = 56 mA for Au and 75 mA for Cr, Rate = 0.2-0.3 nm/sec). Chromium served as an adhesive layer for the gold, which was used to make electrical connections to the nanoscale devices.

Sputter-Deposition:

Sputter deposition[83–85] is another example of physical vapor deposition method in which a high-purity source material (called a cathode or target, which is the material to be deposited) is subjected to a gas plasma (argon for example). The energetic atoms in this plasma collide with the target material and though momentum-transfer knock off the atoms which then travel to the substrate (silicon wafer for example) and condense into a thin film). Sputter-deposition was carried-out in a Nordioko system operated under RF mode. A list of targets characterized is presented in Appendix 2.

Etching:

Reactive Ion Etching:

Reactive ion etching (RIE) is a plasma process in which excited species etch the substrate (silicon wafer for example) in a low-pressure chamber (etching occurs commonly due to the interplay of chemically active species and energetic ion bombardment)[82,83]. In reactive ion-etching

the ion bombardment is directional, making the process anisotropic, with reduced lateral etch rate, resulting in vertical (or nearly vertical) sidewalls. This process was carried-out on an Oxford Instruments machine and was commonly used to etch SiO_2 using either double layer PMMA, maN or CSAR resist after selection and optimization of the most suitable recipe (CHF_3=50 sccm, Ar=10 sccm, O_2=2 sccm, Power=100 W, Rate = 21 nm/min).

Spontaneous Etching:

Spontaneous etching is a plasma process[82–84] in which the excited species etch the substrate or coated thin films in a non-directional manner. In this thesis, spontaneous etching was most commonly used to clean substrates and etch graphene ribbons that were patterned using m-AN resist, after the selection and optimization of the most suitable recipe (Pressure=4e-3 bar, Power=60W, Time=45-60 seconds).

2.2 Device Characterization Tools

2.2.2 Microscopy

Scanning Electron Microscopy:

A scanning electron microscope[86] (SEM) uses a focused electron beam generated from a gun that is either thermally excited or field emitted to scan over a surface of interest and gathers the excited secondary electrons from the substrate to create an image. SEM was mostly used for topography and imaging purposes and carried-out on Hitachi (thermal-gun) or Zeiss N-Vision (field-emission gun) platforms.

Focussed Ion Beam Milling:

Focused ion beam milling, also known as FIB[87], is a technique that uses focused ion beam which can directly modify or mill the specimen surface, via the sputtering process. This process is used to section devices and prepare them for subsequent transmission electron microscopy. In order to avoid back-sputtering of thin films on our devices, FIB was carried-out with carefully optimized parameters (FIB column voltage: 30 kV and course milling current: 6nA

and 3 nA/fine milling current: 1.5 nA/imaging current 40 nA/depositions: 100 nm electron deposited amorphous carbon/ 100 nm electron deposited tungsten/1 μm Ga ion (FIB) deposited tungsten)

Transmission Electron Microscopy:

Transmission Electron Microscopy[86] (TEM) uses a form of the electron microscope in which an image is derived from electrons which have passed through the specimen, unlike the scanning microscope where electrons scattered from the top-surface are used to form images. TEM can reach a very high resolution, down to single-atom level. Here, TEM, adopted on ARM-200F and Jeol 2100-F platforms, was used to image thin films and their compositions were analyzed using the in-built energy-dispersive X-ray spectrometers.

Atomic Force Microscopy:

Atomic force microscopy[88] (AFM), is a form of scanning probe microscopy in which a cantilever with a sharp-tip (typically < 20 nm apex diameter) is systematically scanned over a sample surface to produce a nanometre-resolution map of the surface topography. AFM is typically carried-out in contact mode, where the tip is in direct contact with the surface and its relative displacement gives the feature size and height or in tapping mode (non-contact), where the sample is mechanically excited and is brought closer to the surface such that it feels the van-der Waal interaction. In this thesis, both these modes were commonly used on an MFP3D machine in addition to some advanced modes such Kelvin probe microscopy (here, a voltage is applied between the tip and sample in non-contact mode to measure the work function of the sample), and conductive atomic force microscopy (here, a voltage is applied between the tip and sample in contact mode to measure the local resistance of the sample).

2.2.3 Spectroscopy

Raman Spectroscopy:

When light is scattered by matter, almost all of the scattering is an elastic process (Rayleigh scattering) and there is no change in energy. However, a very small percentage of scattering is an inelastic process, thus a fraction of the scattered light has different energies from incident light, which is a function of the molecular vibrations and crystal structures of the specimen under test. Raman spectroscopy[89] is commonly used to characterize the chemical composition and structure of a sample using this principle. In this thesis, a Horiba LabRaman machine was used for Raman spectroscopy, especially for identifying and quantifying (number of layers) in chemical vapor grown two-dimensional materials.

Photoluminescence Spectroscopy:

Photoluminescence Spectroscopy[90] (PL) is another optical spectroscopy technique; however it does not use the vibrational modes like Raman to characterize a material, instead the material's luminescence. When light incident onto a matter is absorbed it excites the electrons to higher energy states. These electrons then relax to the ground states either through radiative or non-radiative recombination processes, with the former resulting to the photo-luminescence effect that gives a fingerprint of the specimen under test. In this thesis, PL was carried-out on a Horiba LabRamam machine for studying strain-induced effects in chemical vapor grown two-dimensional materials.

Ellipsometry:

The technique of ellipsometry[91] enables the measurement of the refractive index (both the real (n) and imaginary parts (k)) and the thickness of thin films. The measurement relies on the fact that a linearly polarized light undergoes a change both in amplitude and phase upon reflection from a thin film interface, the degree of which commonly corresponds to the refractive index of the thin film. The reflected light is elliptically polarized and contains useful parameters

which can enable measurements of the material's properties: such as surface roughness, grain size, composition and more. An ellipsometer can be used to measure layers as thin as 1 nm to layers which are several microns thick. In this thesis, ellipsometry (performed on a J.A.Woollam machine) was used to determine the refractive indices of thin films that were sputter-deposited on silicon wafers.

2.3 Custom-Built Setups

Electrical Characterization:

Electrical characterizations were carried-out in-house. Typically device characterization included standard current-voltage, gate sweep, pulsed current-voltage, feedback controlled electroburning and transient measurements, which were carried-out using self-made instrument controls using LabView. Electrical noise (electromagnetic interference and cross talk) was minimized by (a) performing measurements in a custom built Faraday cage, (b) integrating data capture at the line frequency (50 Hz) and (c) using printed circuit boards (PCM) with a metallic back plate coating. Standard 50-Ohm co-axial and SMA cables were used to make electrical connections to the PCB.

Figure 13 and 14 illustrate sketches of electrical and optical circuitry used in this thesis, which perform the above-listed measurements (associated programming for instrument control and data analysis is provided in Appendix 3). Figure 15 shows schematics and optical pictures of self-built setups for optoelectronic measurements.

Measurement circuitry:

Electrical and optoelectronic measurements were carried-out using in-house equipment (Keithley 2400, Keithley 2614B, Tektronix AFG000C, Teledyne Lecroy WaveSurfer Oscilloscope, Keysight B15000 Semiconductor Analyser, AdWIN Gold II microcontroller, Femto DLPCA-200 Amplifier, SRS 570 Amplifier and Cascade Summit Probstation).

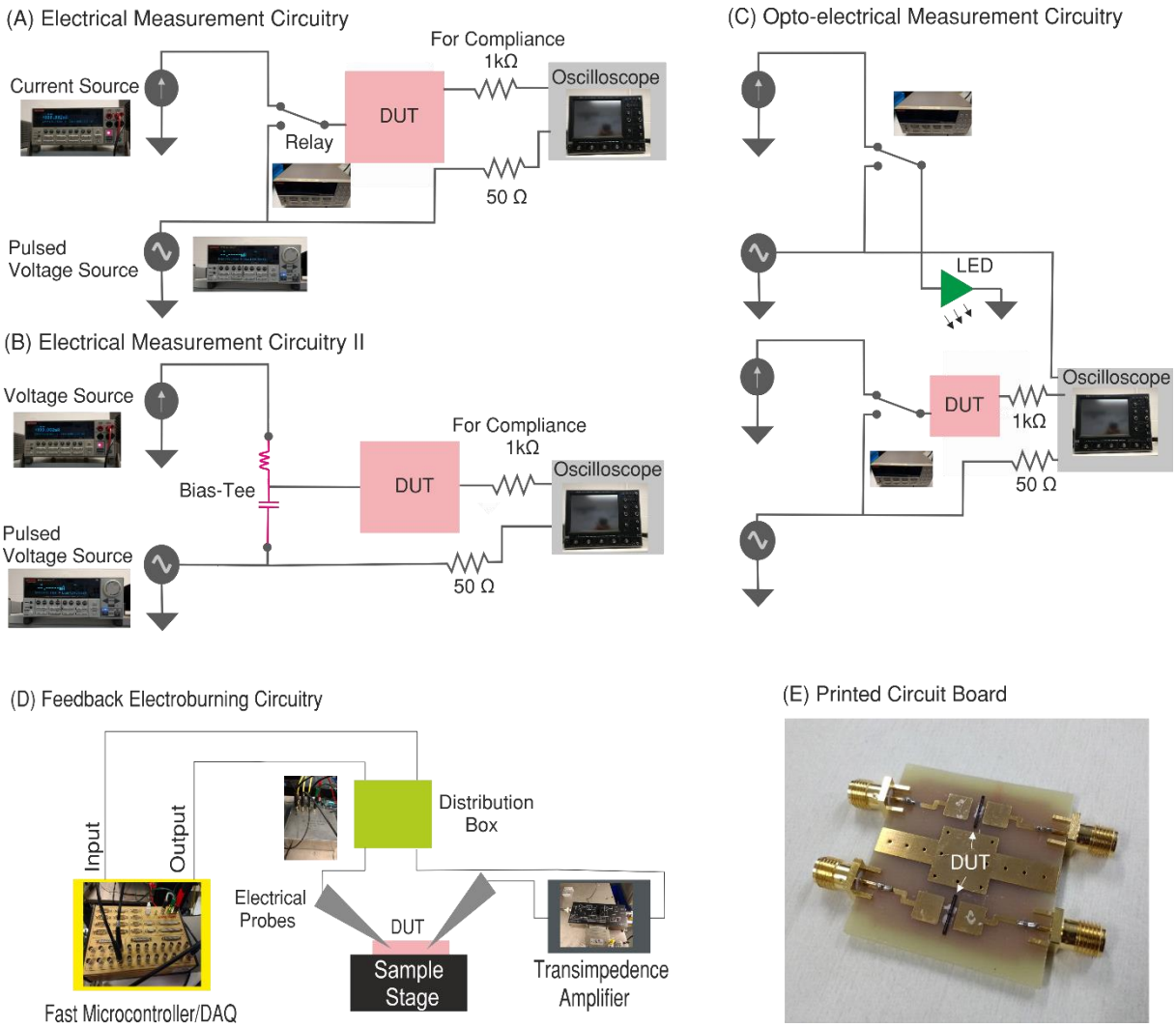

Figure 13. **Measurement Circuitry**. (A and B) Schematics of the circuits adopted for electronic switching experiments of phase change materials in Chapter 3 and Chapter 5. (C) A simplified circuit for similar experiments used in Chapter 3 and Chapter 5. (D) Sketch of the circuitry for feedback controlled electroburning experiments in Chapter 3. These measurements were done on a CASCADE Summit probstation using an ADwin-Gold microcontroller. (E) Optical Image of a custom-built printed circuit board. Connections to the DUT were made with 1% silicon/aluminium wires bonded using a wedge wire bonder.

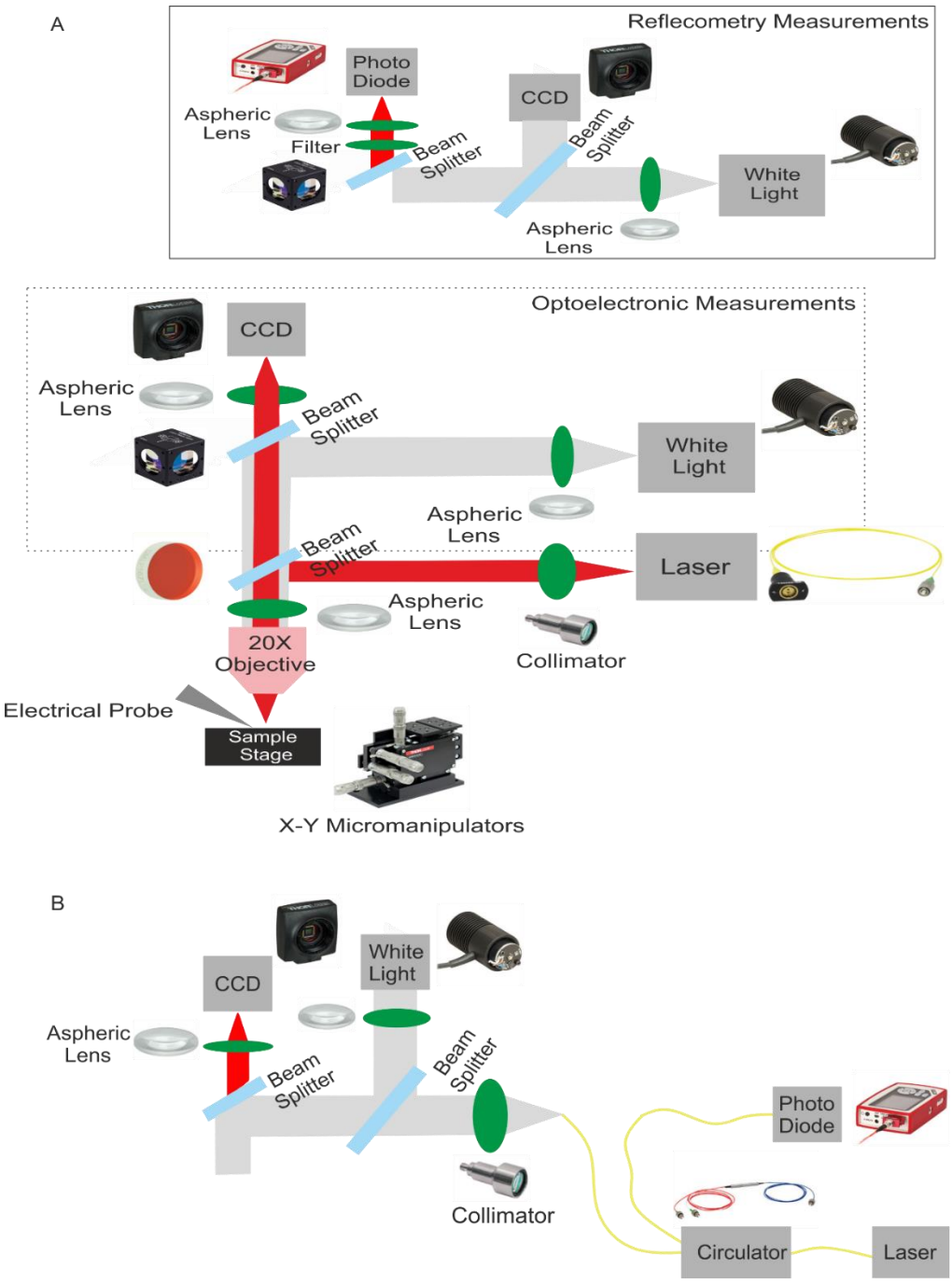

Figure 14. **Illustration of the custom-built setups**. (A) A schematic of the setup for optoelectronic (electrical and optical) characterization of phase change memory devices. The setup can be modified for reflectometry and laser switching measurements by replacing and re-arranging the components in the region highlighted by the dashed box with the components shown in the top panel. (B) A schematic of the setup exclusively used for reflectometry measurements. Most components were purchased from Thorlabs and assembled in-house.

(A) High Bandwidth Low Noise Probstation

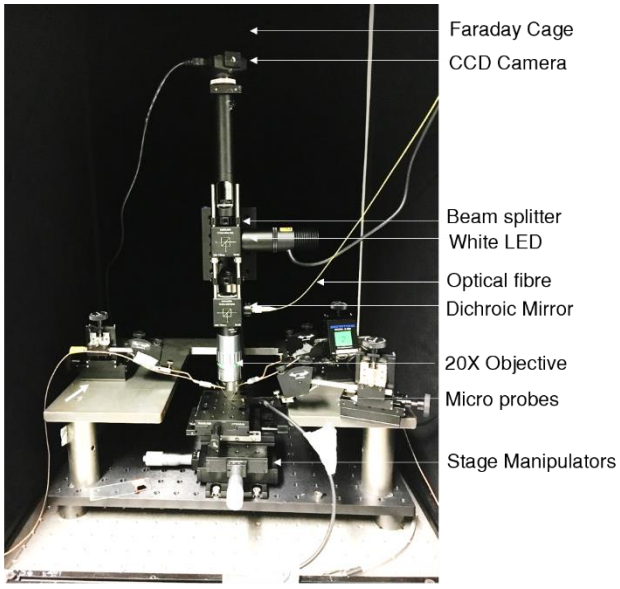

The Probestation was placed on an optical table for damping vibrations and the Strain Driver was fitted into a Atomic Force Microscope

(B) Strain Driver for Two Dimensional Materials

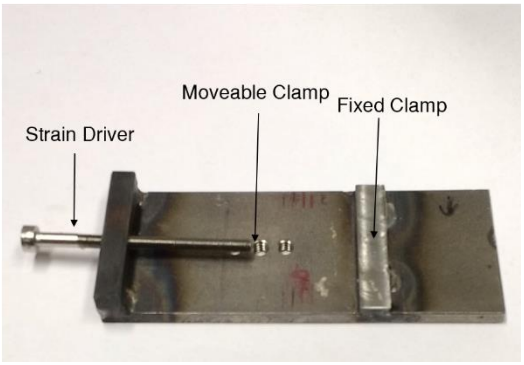

Figure 15. **Custom Built Setups**. (A) A fully equipped probstation for optoelectronic and RF measurements shown in Chapter 3-5 and (B) A strain driver for bending flexible substrates to various degrees. This driver fits into an Asylum MFP3D atomic force microscope (used in Chapter 4).

2.4 Summary

In this chapter, the fabrication methodologies and characterization tools used throughout the thesis in the development of two-dimensional and phase change materials based nanoscale devices are reviewed. The electrical circuitry and measurement setups used for experiments are also discussed.

2.5 Contribution Statement

All steps of device fabrication and characterization were carried-out by the author. Dr Nathan Youngblood assisted with the assembly of the probstation. Codes for electroburning were written by Dr Jan Mol, although changes were made to suit the experiments.

CHAPTER 3: Graphene Nano-gap Electrodes

(A part of this chapter has been published: Syed Ghazi Sarwat, Pascal Gehring, Gerardo Rodriguez Hernandez, Jamie H. Warner, G. Andrew D. Briggs, Jan A. Mol, and Harish Bhaskaran. 2017, 17(6), Nanoletters)

Graphene Nano-gap electrodes

3.1 Device concept

A crucial aspect of scaling down charge based silicon devices is that conventionally such scaling increased the computational and data storage performance in terms of speed (operations per second). However, the race to increase operating frequency beyond a few GHz has now stopped because the dissipated electrical power[92] has increased to more than 100 W/cm^2. Further device scaling with Si technology would only contribute to increased power consumption and chip heating issues. Therefore, there is now an increased interest in unconventional device concepts, such as nano-gap devices[93,94], especially for use in molecular electronics[95] and phase change/oxide memories[76,96,97]. Nano-gap electrodes are composed of a pair of electrodes that are separated by a gap of a few nanometres[93]. Historically, metals such as gold, platinum etc. comprised these electrodes, but more recently sp^2-bonded carbon materials (graphene, carbon nanotubes) have gained traction as the electrode material of choice, due to their superior electrical, thermal and mechanical characteristics, as well as atomic thickness that enables transparency and reduced screening of the gate field. The ability to create nanometer-sized gaps in sp^2-bonded carbon materials, therefore, offers a means of contacting nanoscale objects, for example, nanocrystals and single molecules and represents the ultimate limit of device scaling. Approaching the ultimate scaling limit is crucial for enhancing device performance. For example, the energy consumption and access speed of phase change memories[76] and other data storage technologies, including oxide memory[97] have been shown to improve significantly as a result of scaling down the dimensions between the contact electrodes. Ultimately the performance of these memory devices is determined by the active volume that switches between two states of contrasting electrical resistance. In theory, this volume could be scaled to the dimension of a single unit cell volume that requires sub-2 nm spaced electrodes, which the nano-gap electrodes enable. Of the carbon materials, graphene is the most favorable choice for the simple reason that

it can be grown at a wafer scale and be integrated with conventional lithography tools, unlike carbon nanotubes. Graphene nano-gap devices have been used to demonstrate a variety of applications, such as rectifiers[98], switches[99], transistors[100] and sensors[101], and are being actively explored for new applications such as DNA sequencing[101,102]. These devices are also used for fundamental research, such as in quantum interference studies, spintronics, charge transport, and plasmonics[103].

3.2 Device Fabrication

Because of the high interest in this field, there is an imminent need for fabricating such devices reliably and at a large scale. Present-day lithography tools cannot reliably manufacture such sub-5 nm devices, so more unconventional techniques must be used. These include mechanical breakdown, helium-ion-beam lithography, atomic-force microscopy driven etching, tailored chemical etching and cracking of the electrodes. While these techniques have been demonstrated in the fabrication of metal nano-gaps, their translation to carbon electrodes can be a challenging task. For instance, the mechanical breakdown approach requires controlled bond-rupture under an external tensile strength, whose magnitude could be strikingly high for carbon nanotube and graphene due to their exceedingly high tensile strength (~130 GPa). The use of sp^2 carbon materials for creating nano-gaps has resulted from the more reliable method of feedback controlled electroburning[104,105], which benefits from its simplicity, high yield (~ 95%) and scalability. This approach uses controlled Joule heating and has been previously used in creating sub-5 nm gaps in mechanically exfoliated[104], chemical vapor deposition (CVD) grown[106] and epitaxial graphene[107]. Despite the interest, the formation of nano-gaps in graphene using this technique remains less understood. For this technique to become a technology, some aspects will require deeper research, such as (a) the gap formation mechanism and uniformity, (b) the effect of substrates, and atmospheric conditions on the gap formation, and (c) the ability to visualize the nano-gaps. This is the context of the work reported in this chapter.

To fabricate the graphene nano-gaps devices, 2-3 layered chemical vapor deposition (CVD) grown graphene was used. First, the CVD grown graphene was transferred using standard wet-transfer method onto a Si wafer, with 300 nm SiO_2 insulation and Au/Cr (80/10 nm) pads patterned by optical lithography (see Figure 16). Following this, graphene was patterned in a bow-tie geometry with a constriction 100 nm wide using electron beam lithography. Electroburning under a feedback control scheme was then performed on these devices under ambient conditions to open a nano-gap in the graphene ribbons. In this scheme, a voltage (V) ramp at a rate of 0.75V/s was applied across the graphene ribbon, while the current (I) was continuously recorded with a fast (200 μs) sampling rate. This was all done using a custom-programmed ADWIN microcontroller (see Figure 13D). The variations in the conductance (G= I/V) were continuously monitored, and for different drops in G (depending upon the ramp cycle number), a feedback response was set. This was done, as I will discuss later in detail, to prevent any abrupt degradation of graphene, which could cause uncontrolled burning and hence larger gap size. Upon the occurrence of such drops, the voltage was swept back to zero in 10 ms, and the the next cycle would begin. After each ramp cycle, the device resistance was measured. Electroburning was stopped when a threshold resistance was reached, which was set to >500 MΩ (an indicator that a gap is produced). Figure 17C shows a typical evolution of feedback-controlled electroburning. During the first few voltage ramp cycles, nonlinear IV traces and high device resistance can be noticed, which become increasingly linear and less resistive over newer cycles. These effects can be attributed to the removal of contaminants (resists) from current annealing. Thus, not only does this approach of electroburning allows for the formation of a nano-gap, but also cleans graphene, which is critical and generally a challenging problem. Since the electric field strength, thus current density is greatest at the neck of our graphene electrodes, gap formation occurs here. This method of electroburning is analogous to electromigration. However, unlike in electromigration, the gap is produced due to Joule heating and not electric field drove wind force.

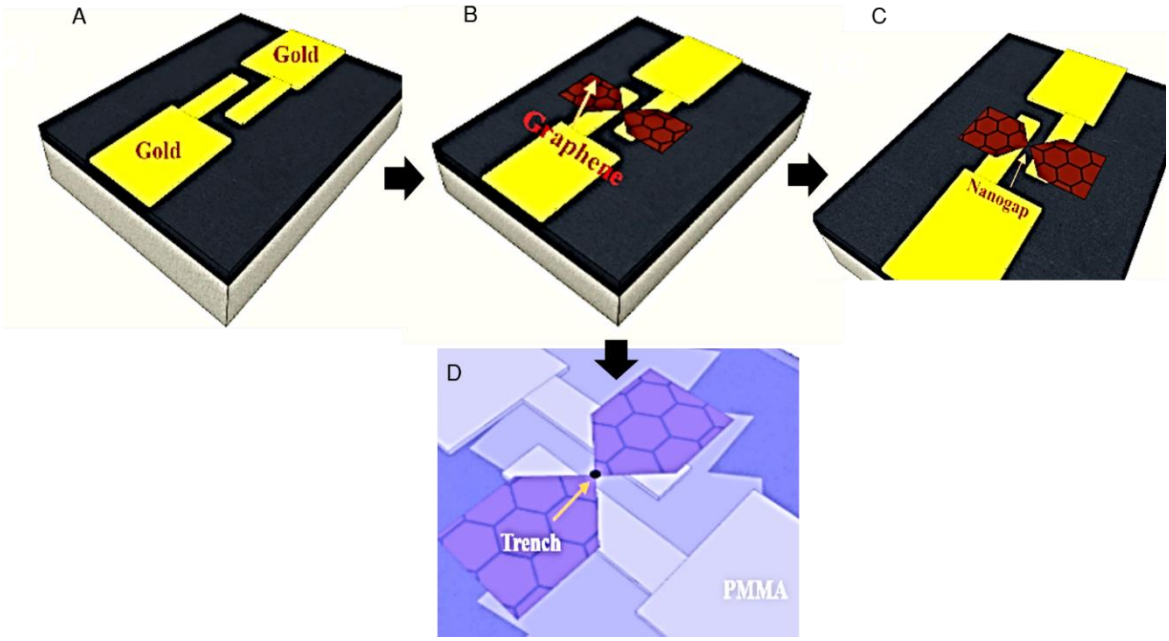

Figure 16. **Device fabrication steps:** Four-inch silicon wafers were sliced into 1 cm x 1cm sized chips. (A) Using optical lithography, and thermal evaporation, 20/80 nm thick Cr/Au bond pads were patterned. (B) 2-3 layered graphene grown using CVD was transferred on to the chip using the wet-transfer method. Graphene was then patterned in a bow-tie shaped (~160 nm wide constriction). (B to C) Feedback controlled electroburning was carried-out on the graphene electrodes on a CASCADE probstation to produce nano-gaps. (B to D) The chips were spin-coated with PMMA and baked at 160 °C for 5 mins. Feedback controlled electroburning was performed in laboratory conditions. Joule heating resulted in localized evaporation of PMMA, producing a nano-scaled sized trench. For devices on h BN, CVD grown hBN was first wet-transferred on the chip, followed by steps (A), (B) and (C).

Since it is difficult to reliably resolve the width of sub-5 nm gaps using scanning electron microscopy (SEM) and atomic force microscopy (AFM) due the very high-resolution required, the width of these gaps is estimated by fitting the measured current-voltage curve to the Simmons model. The Simmons model approximates a rectangular tunneling barrier between the two graphene electrodes[104] and takes the following expression for the tunneling current density.

$$J_{sd} = e/4\pi^2 hd[(\Phi - eV_{sd}/2)e^{-2d/\hbar\sqrt{2m(\Phi - eV_{sd}/2)}} - (\Phi + eV_{sd}/2)e^{-2d/\hbar\sqrt{2m(\Phi + eV_{sd}/2)}}]$$

J_{sd} is the current density, e the electron charge, m is electron mass, Φ is barrier height, d is gap size, and V_{sd} is the applied voltage. Parameters fitted to the Simmons model are the pre-factor A (which contains the cross-section (nm^2) of the junction), the barrier height Φ and the gap size d. The gap size d is quite a robust fitting parameter, whereas Φ and the prefactor A strongly

depend on the initial parameter set. In the devices studied here, the gap size ranged between 1 to 4 nm. Figure 17D illustrates a typical fit of the experimental IV trace with the Simmons model. The estimated gap size is 0.99 nm and barrier height is 0.18 eV. It is interesting to note that the electroburning cycles (see Figure 17C) show a kink, which is suggestive of the bipolar transport characteristics of graphene. This feature is similar to the pinch-off effect known in field-effect transistors and occurs due to the change in the majority carrier type from holes to electrons at the drain end of the device due increasing source to drain voltage. This pinch-off[105] behavior is present until the very last cycle, indicative of graphene sustaining its transport behavior even at very small dimensions. A schematic of the nano-gap is illustrated in Figure 17A, and an atomic force micrograph of a real device is shown in Figure 17B.

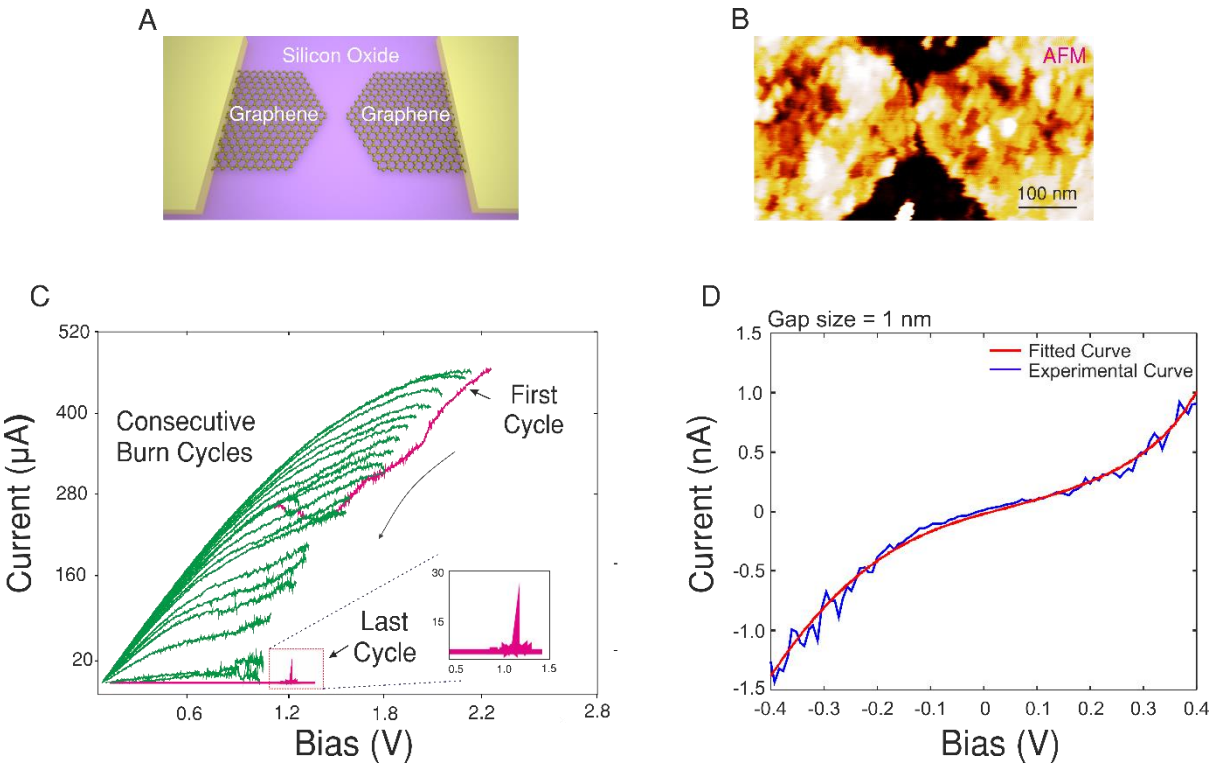

Figure 17**. A graphene nano-gap device.** (A) Schematic representation of a graphene nano-gap device; gap size is exaggerated for visualization (B) AFM image of a graphene nano-gap device; the gap (~ 1 nm) is not resolvable near the center of the constriction. (C) Current-voltage (I-V) characteristics during feedback-controlled electroburning of graphene in ambient conditions. The inset represents the last cycle of the burning process, which shows a spike in conductance just before the gap forms. This current spike is attributed to single carbon filament formation. (D) Typical current-voltage behavior in a graphene nano-gap device. The red line is the fitted curve with the Simmons model.

3.2.1 Mechanism of Gap Evolution

In order to understand the process of gap evolution, the electroburning process was simulated using finite element analysis (COMSOL Multiphysics software). In the simulation, an electrical model is used to predict the voltage and current distribution in the device by solving the Poisson and continuity equations ($\nabla.(\sigma_{(x,y,z,t)}.\nabla V)=0$, where σ is electrical conductivity and V is the potential) and a thermal model is employed to predict the temperature distribution by solving the heat diffusion equation ($\rho C_p(\partial T/\partial t)-k.\nabla^2 T=Q$, where k is the thermal conductivity, T is the temperature, $Q=I^2R(\sigma|E|^2)$ is the Joule heat generation and C_P is the heat capacity). Various boundary conditions, including thermal resistance at the interfaces, were modelled. The greatest current density, hence temperature rise due to Joule heating occurs at the notches, and hence at the constriction of the graphene ribbon (see Figure 18). These steady-state solution results suggest that during electroburning, local temperatures greater than the graphene's oxidation temperature[106] (470 K) are attained at the constriction, which suggests that the gap formation initiates from the notches. Given the results of the model above, it is most likely that the gap evolution mechanism is as one illustrated in Figure 20A. During electroburning, the edge carbon atoms at the notches are oxidized due to their instability, a result of double coordination and dangling bonds. The graphene ribbon, therefore, narrows down across its width through the column by column removal of the edge carbon atoms. This understanding is also backed by the current-voltage behaviour evolved during electroburning. The last burning cycle has a spike in conductance (see the left inset in Figure 17C) just before the device is burnt to produce a gap (last ramp cycle). This current enlargement has been attributed to the formation of the carbon chain (s)[96,108]. Therefore, the constriction thins down in steps before the gap forms. A similar thinning process of graphene ribbons has been observed in transmission electron microscopy (TEM) studies, where the removal of the edge carbon atoms is driven by sputtering (a knock-on mechanism, where fast-moving electrons knock-out the carbon atoms through momentum

transfer)[109]. The temperature rise due to Joule heating for different neck widths (10 to 100 nm, is steps of 10 nm) is also simulated in order to approximate the thinning process (see Figure 18B). Graphene's oxidation temperature is attained at lower biases as the constriction thins down. The simulation results match well with the experimental current-voltage behaviour, and also implicitly suggest that multiple columns of edge carbon atoms are oxidized during each cycle of feedback controlled electroburning.

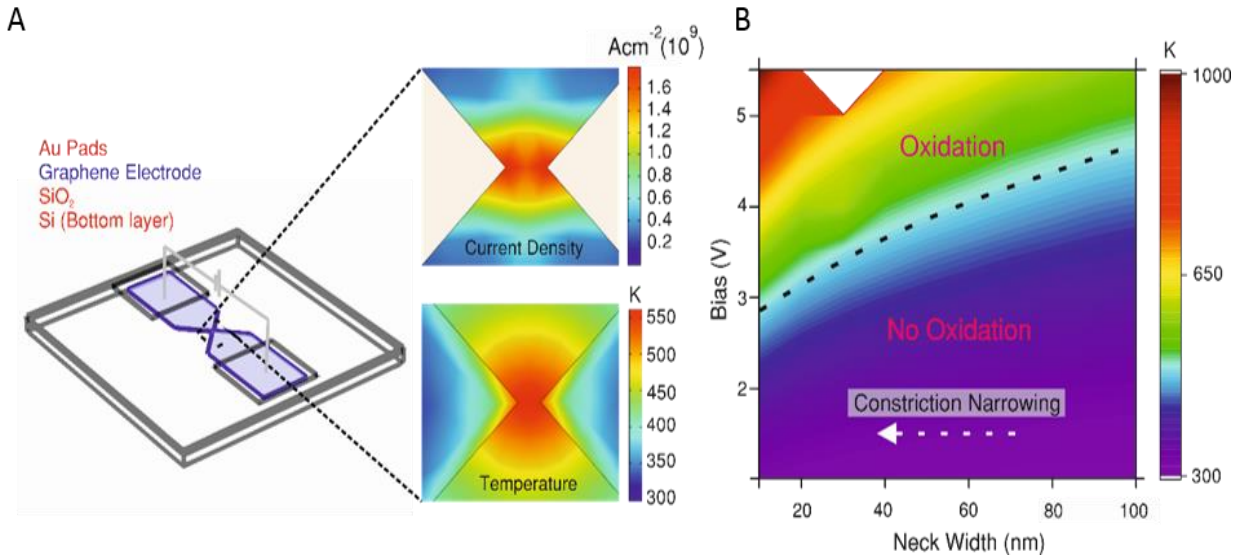

Figure 18. **Simulating Electroburning Process**. (A) Simulated (Finite elemental analysis) current density and temperature profiles during electroburning for a 100 nm wide constriction. Highest current density and hence the highest temperature is at the notches, which exceeds Graphene's oxidation temperature. (B) Heat map illustrating Joule heating for different neck widths (10 to 100 nm, in steps of 10 nm). The bias required to oxidize graphene decreases with a decrease in the constriction width.

The oxidation driven carbon etching must be an anisotropic process: the oxidation fronts have been indicated by the black arrows (see Figure 20A). Since the current density is the greatest at the apex of the notches at the constriction, the oxidation front must be highest in the lateral direction. If this were the case, the gap size will greatest at the edges, and smallest at the center. However, this is an ideal scenario; almost every study, including this one, observes rather an asymmetry in the gap; the gap on one side is bigger than on the other side. This is likely a result of defects such as pre-existing cracks placed away from the constriction which translates into a gap formed much faster during electroburning. Pre-existing cracks in graphene can be formed

during chemical vapor deposition, wet-transfer, during oxygen plasma etching and/or due to stress corrosion from chemical reactions with water vapour[110,111]. To prove if this indeed is the case, I investigated the cracks that were laid away from the constrictions. Because the measurements were difficult using SEM and AFM -given the size of the nano-gaps- an approach based on the burning of a sacrificial polymer was developed. In this approach, a 200 nm poly (methyl methacrylate) (PMMA) photoresist was spin-coated on the wafer with hundreds of unburnt graphene constrictions. The devices were then individually accessed using electrical probes and electroburnt in laboratory conditions. Figure 20B ((i) and (ii)) illustrates AFM images of two electroburnt nano-gap devices. Nanoscale trenches appear in the PMMA thin film after electroburning. The trench formation is a result of localized degradation of PMMA film due to intense Joule heating[77,96] in the underlying graphene constriction when the process of electroburning is carried-out. In order to deduce the temperatures evolved during the process of electroburning, and quantify the trench sizes, the electroburning process was simulated; this time with an overlaying PMMA thin film (discussed later). It is found that temperatures greater than the degradation temperature of PMMA (573 K) are locally reached at the graphene's constriction. Such high temperatures locally evaporate the PMMA layer, resulting in a nanoscale sized trench. Moreover, it is observed that the size of the trench is a strong function of the spin-coated PMMA thickness (see Figure 19). With thinner PMMA layer, the trenches are smaller, likely because the convective cooling due to air becomes more significant. However, I find that lift-off, which is a crucial device fabrication step, becomes more difficult with smaller trenches and thinner films. This is likely because of more uniformity of the deposited film along its thickness and hence, greater cohesion; typically the resist thickness should be 3-4 times the thickness of the deposited film. Therefore for devices, which will be shown in the following sections, striking a trade-off between the gap size and PMMA thickness was necessary.

Figure Number	PMMA Type	PMMA Thickness (nm)	Trench Size (nm)
1	A2-495K	100	170
2	A4-495k	150	283
3	A2-950K	125	145
4	A4-950k	192	247

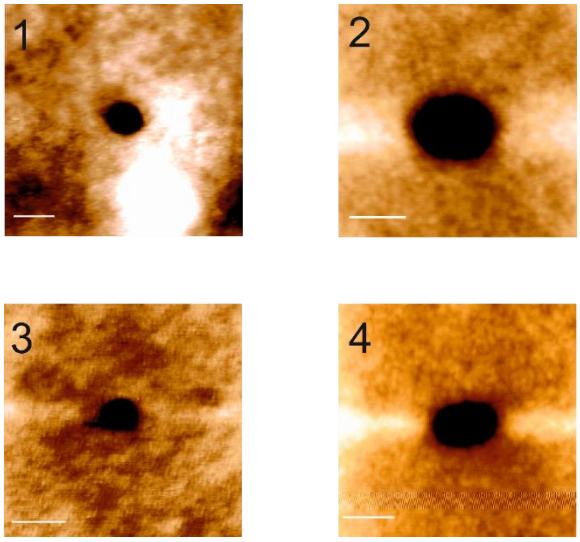

Figure 19. **Trench Size as a function PMMA thickness**. Atomic Force Micrographs of trenches in the PMMA layer of varying thickness (described in the table above). Film thickness was measured using an atomic force microscope. PMMA (poly methyl methacrylate) was spin coated at 3450 rpm. Scale bar is 200 nm.

Nano-gaps at the center of the constriction always produced trenches of the kind shown in Figure 20B (i) or were dumbbell-shaped (see Figure 26). Nano-gaps displaced from the constriction center gave irregular shapes. Figure 20B (ii) shows one such trench. This observation implies that the shape and propagation of the nano-gap can be controlled by introducing defects, similar to what has been demonstrated using controlled cracking to create defined patterns[112].

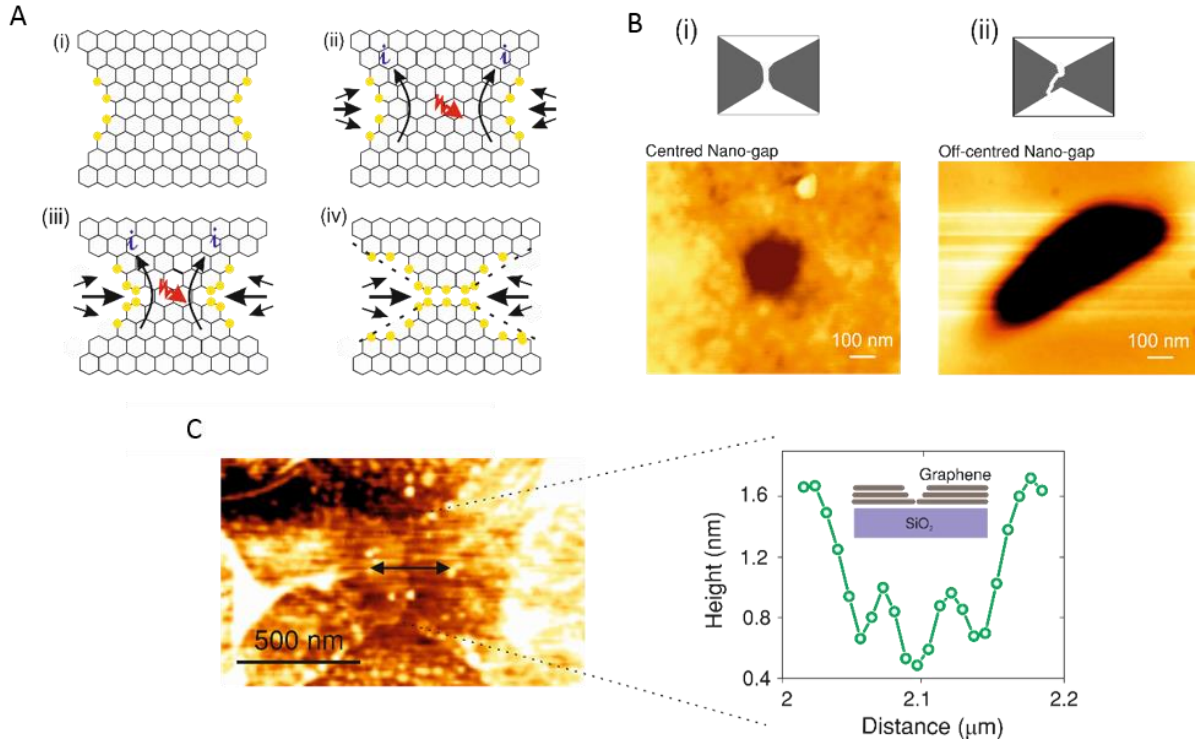

Figure 20. **Gap Formation**. (A) A proposed scheme for the formation of a nano-gap. The edge carbon atoms (yellow) are removed via oxidation, where the arrows indicate the directional oxidation rate. (B) AFM images of PMMA coated graphene nano-gap devices: (i) A centered trench and (ii) an off-centered trench in the PMMA layer. The sketches above the AFM micrographs are likely the shapes of nano-gaps in the underlying graphene ribbon. (C) AFM image of a 20.2 nm nano-gap device. The graph is a line scan along the gap, illustrating the non-uniformity in the distribution of gap size. The smallest gap (indicated by the central 0.4 nm dip in the line scan) forms at the bottom-most graphene layer. Inset is a schematic that illustrates the gap distribution.

So far, I have shown that the gap size is not uniform along the neck. I carried-out experiments to further investigate if the gap is uniform along the depth, which is asking are all graphene layers burnt equally? Figure 20C illustrates an AFM image of a gap with the smallest gap size ~20 nm. Bigger nano-gaps were produced by adjusting the feedback parameters (see Appendix 4). It is imperative to have bigger gaps for this experiment (bigger than the AFM probe's tip diameter) in order to resolve the variations. The graph (see Figure 20C) is a line scan along the gap. Two drops in the heights can be noted. The second drop corresponds to a width of 20.2 nm, and a depth of 0.4 nm, which equals the thickness of monolayer graphene. This indicates that the smallest gap that yields the tunneling current forms only on the bottom-most graphene layer that is in direct contact with the underlying substrate (SiO_2), while the top layers are burnt

into bigger gaps (see inset of Figure 20C). Such a variation can be understood from the fact that top layers carry adsorbed vapor and oxygen molecules that eases the oxidation process, and also from the gradients in the heat transfer rates. Heat is dissipated fastest from the bottom-most layer through phonons coupling with the substrate (remote phonons at the graphene/SiO_2 interface)[106,113]. This makes the oxidation of the bottom-most layer relatively slower, thereby favoring the smallest gap to be formed on it.

A further investigation was carried-out to understand if the choice of the substrate affects the electroburning process (see Figure 21). In particular, can carbon -chains and -quantum dots, which show quantum interference (QI) and Coulomb blockade effects respectively, be formed during and after burning on all substrates? This area[100,103] is currently researched extensively as QI can be exploited for highly efficient logic devices and Coulomb blockade in thermoelectricity and transistors. Electroburning was carried-out on three different substrates: SiO_2 (Si/300 nm SiO_2) strained Si_3N_4 on insulator (330 nm Si_3N_4 on 550 μm SiO_2) and hBN (hexagonal boron nitride) under laboratory conditions. No noticeable differences in the electroburning process (current-voltage behavior) and on the gap sizes and junction resistance were observed. For example, the average gap size, irrespective of the substrate lies in the range 1 to 2 nm, while the resistance is between 500-1000 MΩThis is rather striking, given the thermal conductivity of these materials differ (k_{oxide}=1.4 W/mK, $k_{nitride}$=2.5 W/mK and k_{hBN}=250 W/mK (in-plane)). While the difference between silicon oxide and nitride is less significant, the high in-plane conductivity in hBN should in principle increase the electrical power required to cause sufficient Joule heating due to increased heat dissipation[114]. The fact that the aforementioned results do not imply otherwise is suggestive of the quality of the hBN films. It is likely that the films are not uniform in both size (broken into micron-sized domains) and composition. Indeed, I show later that the hBN film fail to act as passivating layers on flexible substrates. Regardless, features in the current-voltage behavior that are suggestive of carbon chains and quantum dots can be noted for all the

three substrates (see Appendix 5). These results strongly suggest that under ambient conditions probably all insulating materials can serve as substrates and that QI and Coulomb blockade are intrinsic to graphene and not significantly influenced by the substrates. This is particularly encouraging for emerging applications with graphene nano-gaps that focuses on beyond SiO_2 substrates, such as in DNA sequencing[101].

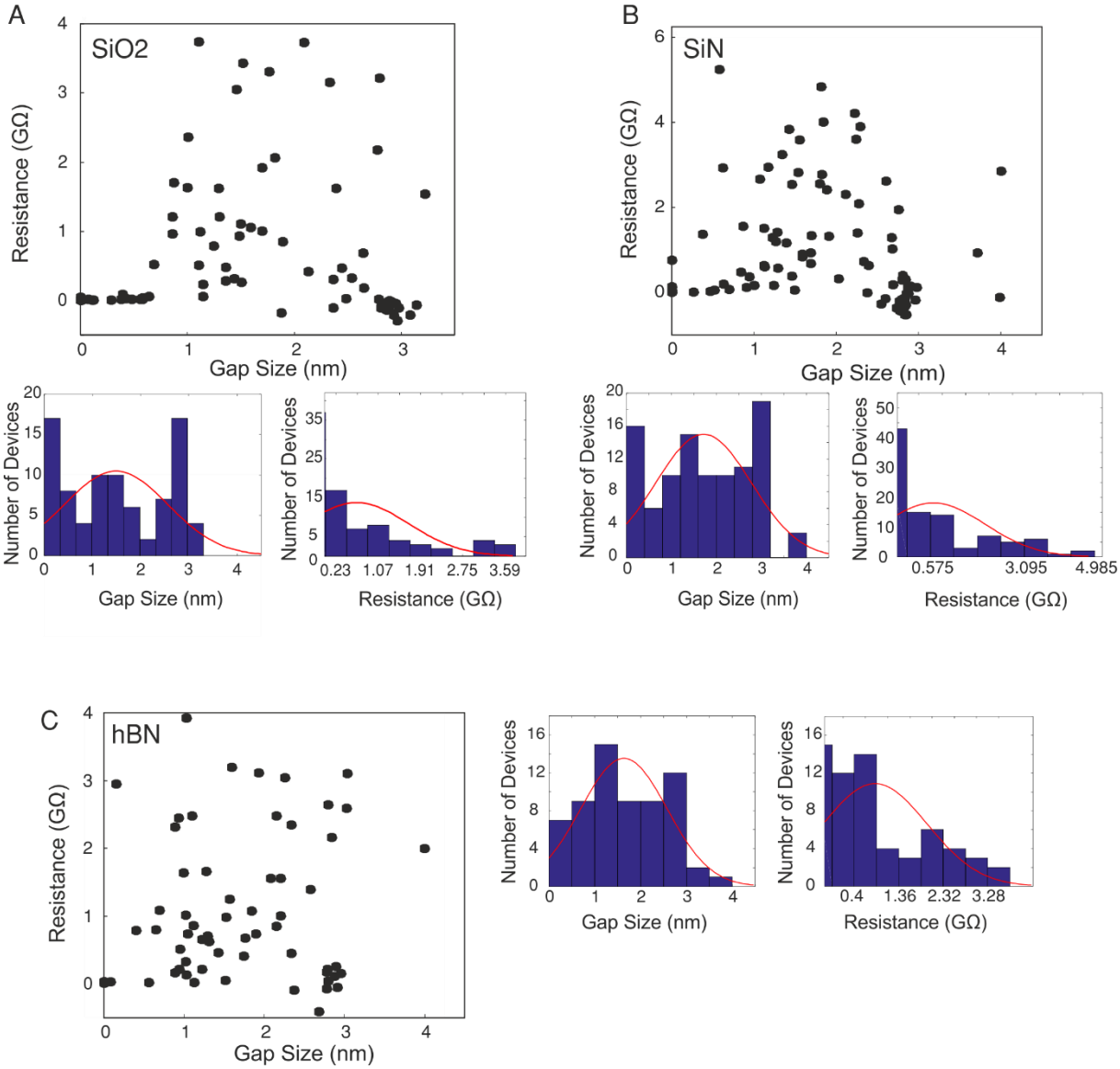

Figure 21. **Electroburning on different substrates:** Scatter plots illustrating the gap size and the gap resistance on a (A) SiO_2 substrate (mean gap size and resistance are 1.52 nm and 670 MΩ respectively), (B) Si_3N_4 substrate (mean gap size and resistance are 1.74 nm and 1012 MΩ and (C) SiO_2 substrate (mean gap size and resistance are 1.66 nm and 1123 MΩ respectively). All three substrates were coated with a 150 nm thick PMMA layer. Note that the distribution of the size and resistance of the nano-gaps follow a similar distribution irrespective of the choice of substrates. Most nano-gaps lie in range 1.5 to 2.0 nm and beyond ~3.2 nm, the device ceases to produce tunneling current for a small applied bias.

3.2.2 Imaging Nano-gaps Using Kelvin Probe Microscopy

A technique to image the nano-gaps is now demonstrated. Sub-5 nm nano-gaps produced using feedback controlled electroburning are difficult to image using AFM and SEM. I present a technique based on Kelvin Probe Microscopy (KPM) to image nano-gaps. This technique captures a three-dimensional image of the device while locating, and characterizing local potential drops[115,116]. Typically, KPM measures the contact potential difference (CPD) between the sample (here graphene and SiO_2), and the AFM tip (n-doped Si), from which the work functions can be deduced. If an external DC biased is applied, the AFM tip sees a different surface potential which is a sum of the applied voltage and the pre-existing electrostatic potential. From these, the local voltage drops in the device can be determined simply by subtracting the biased surface potential ($V_{CPD} + V_{BIAS}$) from the unbiased surface potential (V_{CPD}). Two different configurations of KPM are illustrated in demonstrating this technique.

In the first configuration (see Figure 22A (i)), the AFM cantilever was pressed against one side of the graphene electrode, and a bias (150 mV) was applied between the tip and ground. The applied bias resulted in charging of the device; adding an extra component to the electrostatic potential between the sample and AFM tip. The tip was then retrieved, and a non-contact KPM scan was carried-out. A sharp potential drop (graph in Figure 22A (i)) can be noted from the KPM micrograph, which defines the nano-gap. However, this approach despite being exciting in terms of its simplicity is limited by the need for fast scan rates as the electrodes become discharged quickly. This limitation is mitigated in the second configuration.

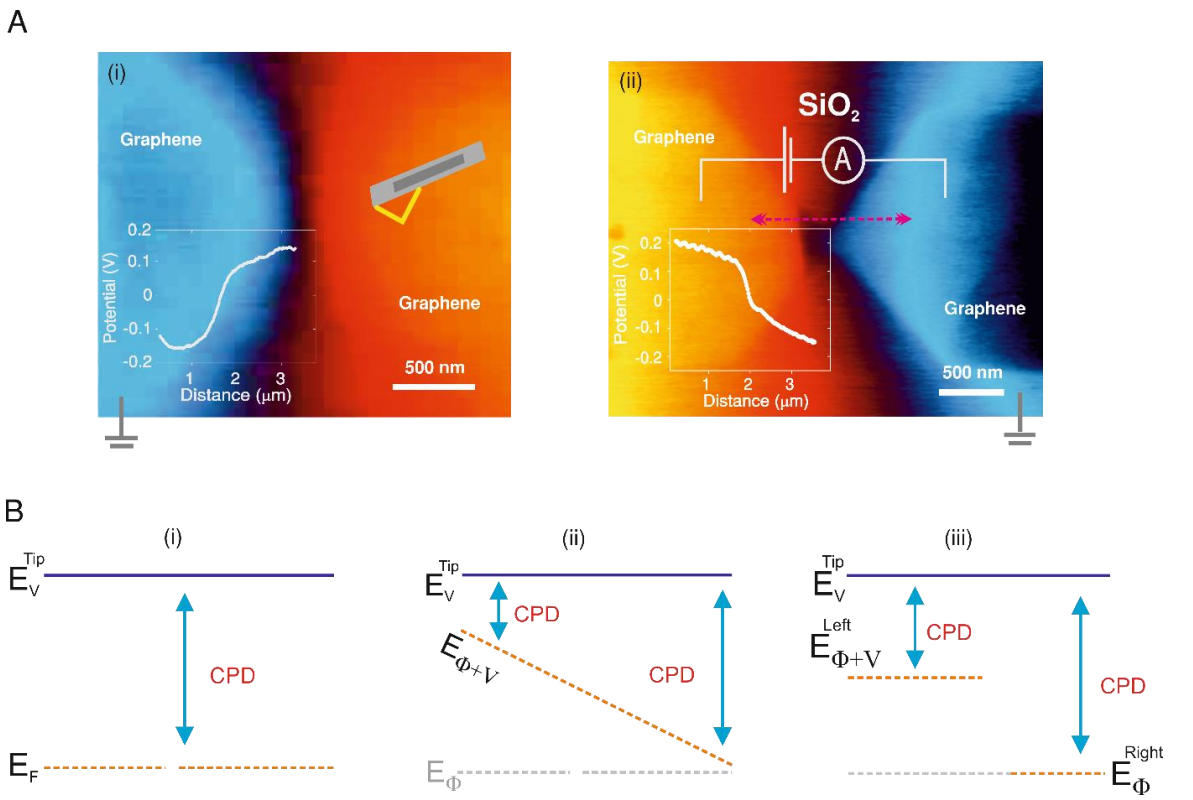

Figure 22. **Metrology of graphene nano-gaps.** (i) A Kelvin Probe Micrograph of a graphene nano-gap device biased momentarily at 150 mV by an AFM probe, (ii) KPM of a second graphene nano-gap device DC biased at 500 mV. A clear junction is evident in the potentials, indicative of a physical gap. The gap in (ii) is off-centered. (B) Energy band diagrams of graphene ribbon under the (i) unbiased state, (ii) biased state (without nano-gap), and (iii) biased state (with nano-gap), respectively. Biasing results in a shift of the Fermi level of the graphene leads, the nature of which depends on the presence or absence of a nano-gap. E_F is the Fermi level and $E_\Phi$is the work function of graphene.

In the second configuration, the device was connected to an external sourcemeter (Keithley 2614B) using wire bonds. A DC bias was applied and held during the entire KPM scan time. This negated any discharging effects (the sharpness of images) as is apparent in the micrographs (see Figure 22A (ii)). Note that the potential drop in Figure 22A ((ii) is not at the constriction. This is indicative of the nano-gap being off-centred (not at the constriction), which is likely a result of pre-existing defects as previously discussed. Thus, this KPM based technique enables visualizing and locating the nano-gaps at a nano-metric resolution. The electrostatic potential profiles of the device under different conditions are illustrated in Figure 22B. In the absence of an external bias (Figure 22B (i)), KPM records the electrostatic potential of graphene and SiO_2 (see Appendix 6), with similar CPD on the right and left graphene leads of a nano-gap device. This is suggestive of

graphene's uniformity. When an external bias is applied on an unburnt (no nano-gap) graphene ribbon, the Fermi level of the entire graphene channel changes (see Figure 22B (ii)). When an external bias is applied on a burnt (with nano-gap) graphene ribbon however, the situation approximates to a parallel plate capacitor as is illustrated in Figure 22B (iii)). This is the case experimentally observed in Figure 22A. This technique with sub-nm sized probes can also enable the study of molecules (their geometrical arrangements and charge transport characteristics) bridging the nano-gaps for molecular electronics.

3.3 Scaling Limit of Graphene Nano-gap Electrodes

In approximately half of the graphene nano-gap devices, a sharp increase in the conductance prior to the formation of a nano-gap was observed (see inset of Figure 17C). Similar conductance enhancement behavior has been reported before and is attributed to the formation of carbon filaments[108,117,118]. Density functional theory and tight-binding simulations have shown that the transition from a multi-path configuration to a single-path configuration may lead to an enhancement of quantum transport[108]. In the following section, the observation of reversible resistance-switching in the nano-gap devices is described, which is attributed to the controlled formation of carbon filaments.

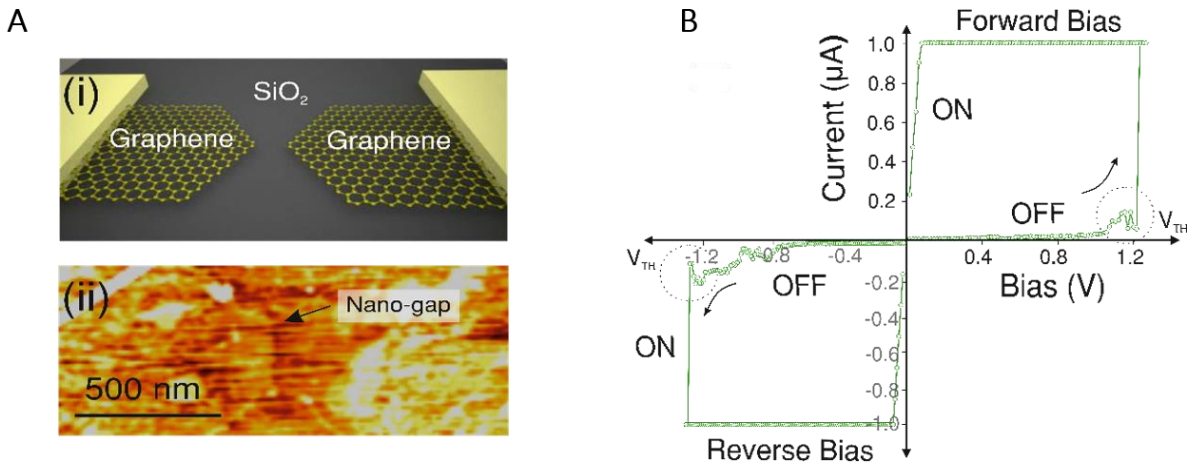

Figure 23. **Intrinsic conductance switching.** (A) Schematic representation (i) of a graphene nano-gap device (ii) AFM image of a graphene nano-gap device; the gap (< 4 nm) is not resolvable near the center of the constriction. Both (i) and (ii) imply that a graphene nano-gap is representative of an open-circuit. (B) Low bias switching of a graphene nano-gap device (3 nm gap size) in ambient conditions. The first quadrant represents switching with a forward (positive) bias. The device switched from a high resistive state to a low resistive state in ambient conditions at a switching voltage of 1.22 V, and a current of 60 nA. The third quadrant shows the current-voltage characteristics of the same device under reverse (negative) polarity. The device switched at a voltage of 1.28 V and a current of 100 nA. For all reversible switching experiments, current compliance of 1000 nA was used.

After a nano-gap using feedback-controlled electroburning is formed, the device can be set to its low resistance state by sweeping the bias voltage past a threshold voltage in ambient conditions (see Figure 23B). This switching behavior is observed to be independent of the bias polarity, after having switched the device from the high resistive 'OFF' to the low resistive 'ON' state by applying a forward bias, the device can be switched OFF by repeating the electroburning and then switched ON again by applying a negative bias. As shown in Figure 24A and 24B, the conductance switching is fully reversible; the device can be switched from the ON to the OFF state by performing the feedback-controlled electroburning process; and switched back from the OFF to the ON state by sweeping the bias voltage beyond the threshold voltage. The SET (from OFF to ON) and RESET (from ON to OFF) can be repeated multiple times.

Reversible conductance switching of graphene nano-gaps has previously been reported for graphene on SiO_2 and suspended graphene in vacuum[99,119,120]. The temperature dependence

observed in these studies, as well as in this chapter (see Appendix 7) provides a strong indication that the switching process involves the rearrangement of atoms and/or chemical bonds that requires overcoming a barrier[120]. A possible mechanism for this rearrangement is the formation of carbon filaments[121], which in the case of carbon nanotubes was identified as the process through which they unravel by the action of an electric field. Figure 24A shows a schematic depiction of the filamentation process; the force exerted by the electric field breaks the C-C bond of an edge atom with incomplete sp^2 bonding. The filamentation process then proceeds as a rupture of C-C bonds parallel to the graphene edge. The fact that a reversible switching is observed in ambient conditions is potentially because of the feedback-control when switching the device OFF. The gap size resulting from electroburning without feedback-control strongly depends on the oxygen concentration of the atmosphere and ranges between ~100 nm in ambient condition to ~5 nm under a vacuum of ~10^{-5} mbar[122]. I also found that the devices which were made by electroburning without feedback-control did not undergo the SET operation.

The SET requires a field strength F_{crit} = 400 mV/nm by assuming to a first approximation that the applied bias voltage drops linearly across the 0.75 nm gap. This field strength is similar to that observed previously for a gap size of ~ 10 nm, which switched at ~4 V, suggesting that there is a critical field strength required to unzip the carbon filament(s) from graphene[99]. The likely switching mechanism is as follows: during SET (OFF to ON), formation of a carbon filament initiates from the edge of the graphene; when the local electric field at atomically sharp edges gets sufficiently high, it breaks a bond parallel to the axial electric field (between red and yellow atoms in the schematic). Filamentation then proceeds in a row-by-row fashion as indicated by the dashed arrows. For RESET (ON to OFF), Joule heating provides sufficient thermal energy for the rupture of bonds through oxidation of carbon atoms (oxygen represented by blue circles). Interestingly, this electric field strength is two orders of magnitude lower than the field strength

that has been theoretically estimated (≥20 V/nm)[123,124] for unraveling a carbon filament from a graphene edge. This discrepancy can be attributed to the weakening of the C-C bond strength resulting from incomplete sp^2 hybridization and enhancement of the local electric field at atomically sharp graphene edges.

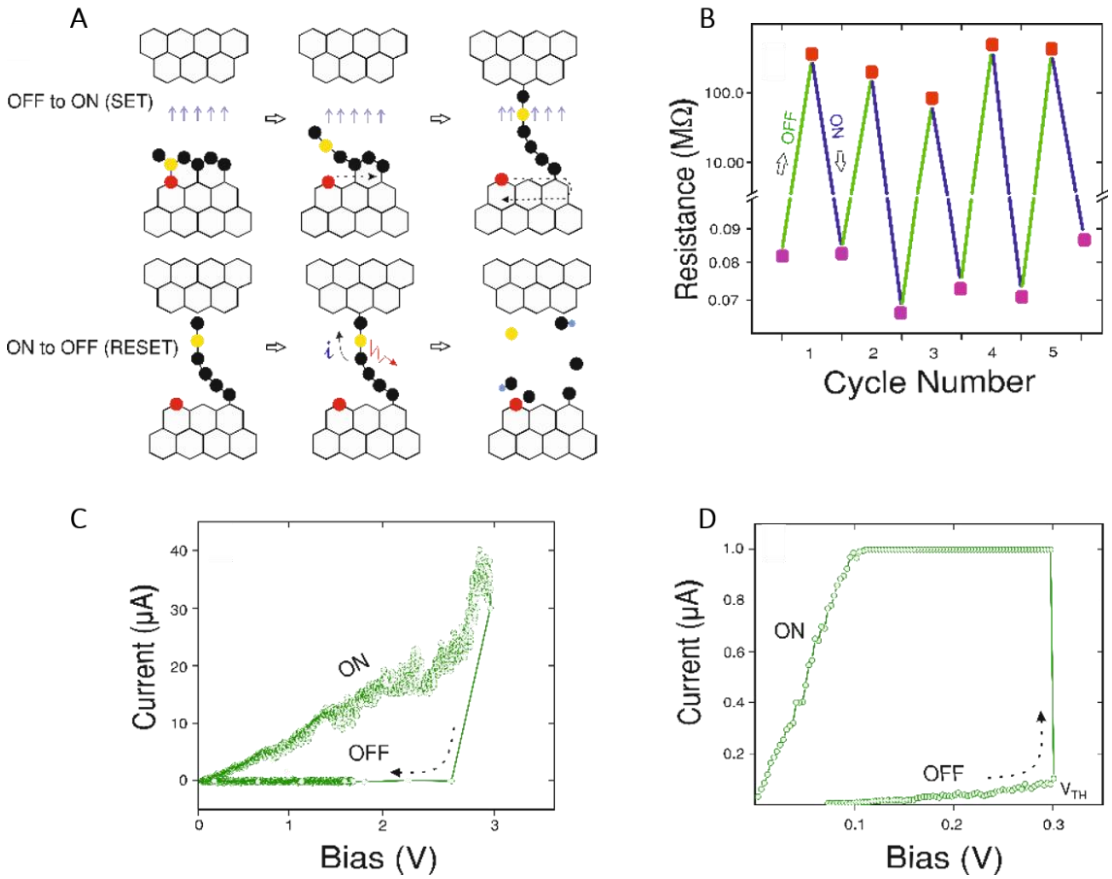

Figure 24. **Cyclic switching via filamentation in a graphene nano-gap device.** (A) Proposed scheme for the formation and breaking of carbon filaments. (B) The device is switched between the high resistance and low resistance state multiple times in ambient conditions. (C) Current-voltage behavior during RESET operation in ambient conditions. (D) Illustrates a typical SET I-V characteristic in ambient conditions. The device switched at a switching voltage of 300 mV and current of 80 nA.

3.4 Phase Change Memory and Self-Alignment Approach

Based on measurements of the critical field required for switching graphene, it can be estimated that to switch a $Ge_2Sb_2Te_5$ (GST) volume with a voltage less than 4 V, a gap size of no more than 10 nm is required. To demonstrate this, GST contacted in both 1 nm and 20 nm wide graphene nano-gaps is compared. In order to place the GST volume over the graphene nano-gap, a self-alignment method is developed. This method relies on the local removal of PMMA in the

vicinity of the graphene constriction during the electroburning process. The process was described earlier in the mechanism section. Similar self-alignment techniques have been previously demonstrated for fabrication of CNT nano-gaps based PCM devices[77], however not in combination with feedback-controlled electroburning. Here the applicability of this technique on CVD grown graphene is demonstrated, which allows for scalability as graphene can be grown on wafers and subsequently patterned using lithography. The simplified one-step process requires no high-resolution lithography or vacuum. After several cycles of electroburning, photoresists such as PMMA were spin-coated onto the devices. Continuing the feedback-controlled electroburning process, the graphene constriction locally heats-up, which leads to the formation of trenches resulting from the local evaporation of PMMA. These trenches serve as self-aligned windows for subsequent deposition of the phase change material, which in this study is GST. The size of the trenches depends on the number of electroburning cycles, i.e. the resistance of the graphene device prior to spinning the resist. The effect of PMMA thickness on the resulting trench sizes was shown earlier.

It is observed that graphene is susceptible to sputter deposition. Crucially, for standard low-RF power deposition, I found graphene to be severely damaged. An experiment to more accurately elucidate the effect of sputter deposition of a PCM on graphene was carried-out by transferring a graphene film on a transparent quartz substrate (see Figure 25) for Raman spectroscopy measurements. No detectable Raman signals of graphene could be collected from regions where PCM was deposited, while the region that was masked during deposited remained intact. This suggested a knock-on induced back sputtering of carbon atoms from graphene[78]. To circumvent this I sputtered PCM at high working pressure ($\sim 10^{-2}$ Torr as opposed to $\sim 10^{-3}$ Torr at room temperature) and used multilayer graphene as the electrode.

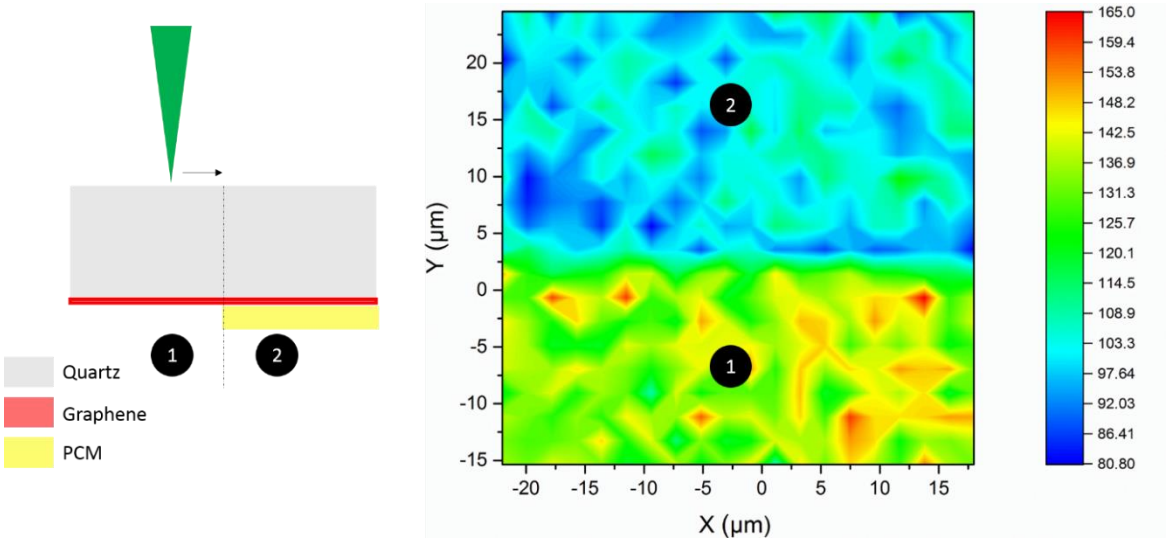

Figure 25. **Sputter-deposition induced damage in graphene**. (A) A cartoon of the experimental setup, wherein Raman spectroscopy was carried-out across a region on graphene with (region 2) and without (region 2) overlaying PCM. (B) A Raman map illustrating 2D peak intensity of graphene in region 1 and 2. Clearly, PCM deposition resulted in degradation of graphene, likely due to knock-on induced back-sputtering

The electroburning process driven trench formation in the PMMA layer (see Figure 26) was simulated using finite element analysis. Joule heating combined with a heat transfer module was used. Figure 26 illustrates the geometry and simulation results of my model. Various boundary conditions, including thermal boundary resistances (0.5 to 1e-8 m^2K/W) between different layers was included[76,77,125]. The trench size on PMMA is deduced from the thermal contours. PMMA layer evaporates at 523 K. For a 150 nm thick PMMA, at a burning current of 500 µA, the size of the trench (shown by the dotted circle) is 0.3 µm (longest dimension). The resulting trench sizes agree well with my experimental observations. Figure 27 (A and B) show an AFM image of a self-aligned trench in PMMA, and an SEM image of the device after sputter-deposition of GST (~ 12 nm at room temperature), respectively. Use of capping layers was avoided in order to eliminate any probable interfacial interactions between the capping layer and GST, which are known to influence the switching behaviour[126].

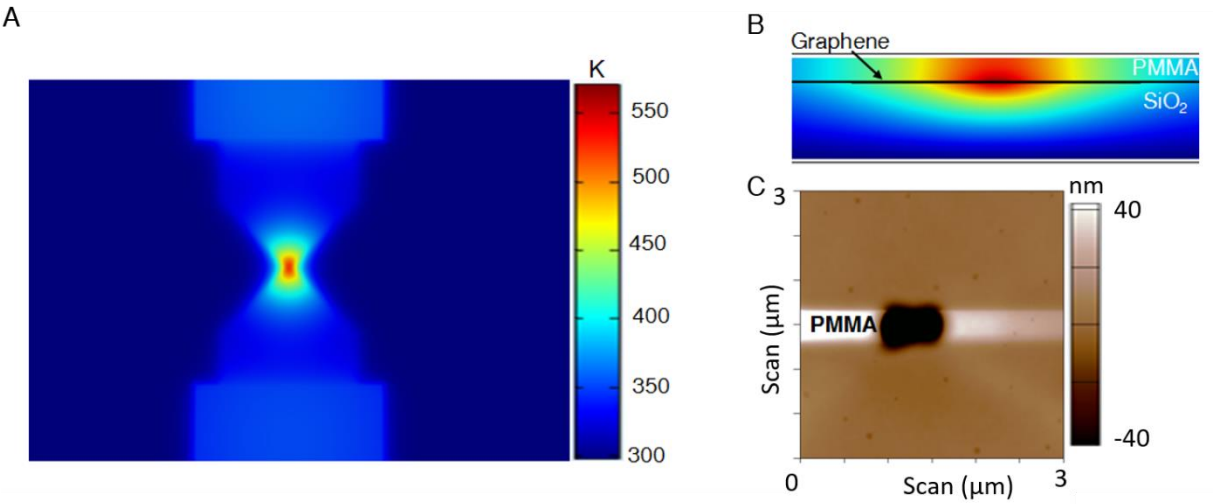

Figure 26. **Temperature distribution in PMMA coated device:** (A and B) Cross-sectional view of simulated thermal contour resultant of Joule Heating (500 µA) in a graphene ribbon of a 100 nm wide constriction. The temperature at the constriction exceeds the degradation temperature of PMMA (523 K), producing a trench, (C) Atomic Force Micrograph of a trench on PMMA. The shape and size of the trench match well with the simulation

The process of crystallization in GST is nucleation driven. Therefore, the limit to scaling GST will be switching it at its single-nucleus scale, of size approaching the critical radius (r_c). The critical radius can be calculated from the classical nucleation theory using the interfacial free energy σ and the Gibbs free energy difference between the liquid and the crystalline phase per unit volume ($\Delta G_{lc,V}$) as $r_c = 2\sigma/\Delta G_{lc,V}$. Note that strain effects are ignored in these calculations, which in practice exist in real devices and contribute differently to the critical radius depending on their sign (compression/tensile). Using σ = 40 mJ/m^2 and ΔG_c = 1.15 eV in the relationship $\Delta G_c = (16\pi/3)\sigma^3/(\Delta G_{lc,V})$, the critical radius[76] is calculated to be ~ 1.05 nm. This is the smallest GST size that can be switched.

Figure 27C shows the current-voltage characteristics of a self-aligned PCM device in a 1 nm wide nano-gap. The device switches from a highly resistive state to a low resistive state at 0.37 V, showing switching characteristics that are similar to the that observed in bare graphene nano-gaps in Figure 24D. Figure 27C highlights the switching characteristics of a self-aligned PCM device in a 20 nm wide nano-gap, where the device undergoes a non-volatile switching from a high to a

low resistive state at 2.5 V. GST is a semiconductor in both its amorphous and crystalline states, and therefore a linear I-V character in either the ON and the OFF state is not expected. However, the I-V characteristics of the ON state of the GST in a 1 nm gap is linear, similar to the bare nano-gap. From this, it can be inferred that switching in the 1 nm nano-gap is dominated by the formation of carbon filaments. By contrast, for GST deposited in a 20 nm gap the I-V characteristics shows an exponential dependence in both the ON and the OFF state, in agreement with previous measurements of GST. Switching in GST devices occurs at relatively high power and the resistance ratio between the highly resistive and less resistive state is ~1000, indicative of switching in GST. Finally, a device with a ~20 nm nano-gap without GST was tested, which exhibits open circuit characteristics, displaying no switching behavior even at very large bias values. At very large voltages of ~120-150 V, dielectric breakdown of the underlying SiO_2 substrate is seen to occur (see Appendix 8). The absence of filamentation in wider gaps can be attributed to the instabilities of longer carbon filaments[109,127].

Reversible conductance switching has also been observed in SiO_2-based devices[128,129]. To exclude effects of SiO_2 mediated conductance switching, two experiments were carried-out. In the first experiment, a 15 nm thick SiO_2 was placed in the sub-4 nm gaps using the self-alignment technique. No switching behavior was observed, other than dielectric breakdown at ~ 10 V (see Appendix 8). In the second, graphene nano-gaps were fabricated on a Si_3N_4 substrate (see Fig see Appendix 8), a material that shows no intrinsic switching[128,129]. Similar switching behavior on this substrate was observed as on the SiO_2 substrate. Furthermore, the formation of Si nanoclusters through reduction of SiO_2 is recognized as the mechanism behind resistance switching in SiO_2 switching. Therefore an oxygen deficient atmosphere is a prerequisite[97,128,129] for switching in unpassivated SiO_2.

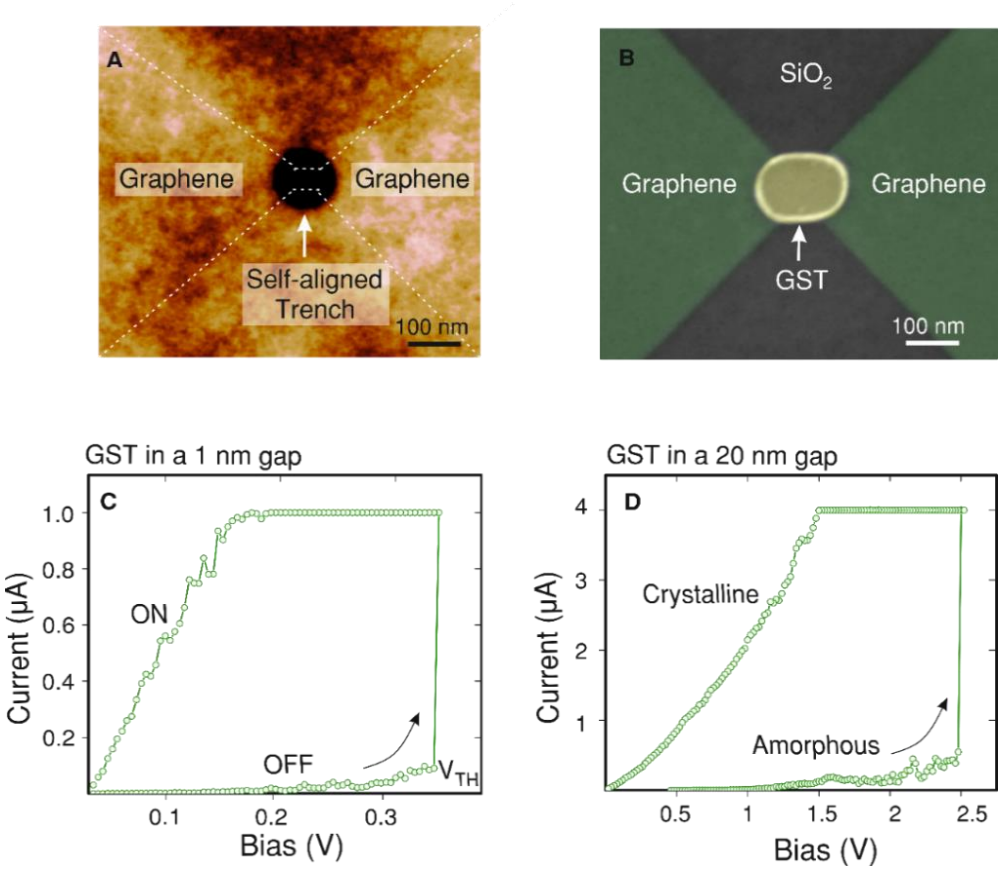

Figure 27. **Self-alignment approach and Phase Change Memory device.** (A) An AFM micrograph showing a trench of size 148 nm (largest lateral dimension) in PMMA. Dotted line outlines the graphene ribbon underneath PMMA. (B) Coloured SEM image of a self-aligned PCM device showing the GST in the nano-gap. (C and D) Current-voltage trace of a GST nano-gap device of spacing 1 nm and 20 nm, respectively. The device switches from a high resistive state to a low resistive state in laboratory conditions at a switching voltage of 370 mV and current 100 nA in Figure (C), and at 2.5 V and 500 nA in Figure (D).

Devices shown in this chapter can be switched both ways readily in ambient conditions. It is therefore highly unlikely that SiO_2 switches in my devices since the switching site, which is the surface, is exposed to an oxygen-rich atmosphere. In addition, the ratio of resistance between the OFF and the ON state is typically > 10^4 in SiO_2, which is an order magnitude more than observed in my devices. Readers are directed to Appendix 8 for more experimental data. Low-temperature (4 K-liquid helium) measurements were carried-out (see Figure 28), where SET was performed and the source-drain conductance was measured as a function of back-gate voltage. In 12 devices that were studied, 4 devices showed interference effects while the rest Coulomb blockade. It was found that increasing the current density in the filament switched Coulomb blockade to

interference effects, which possibly arises from the increase in the transmission coefficient in the Landauer transport scheme[130].

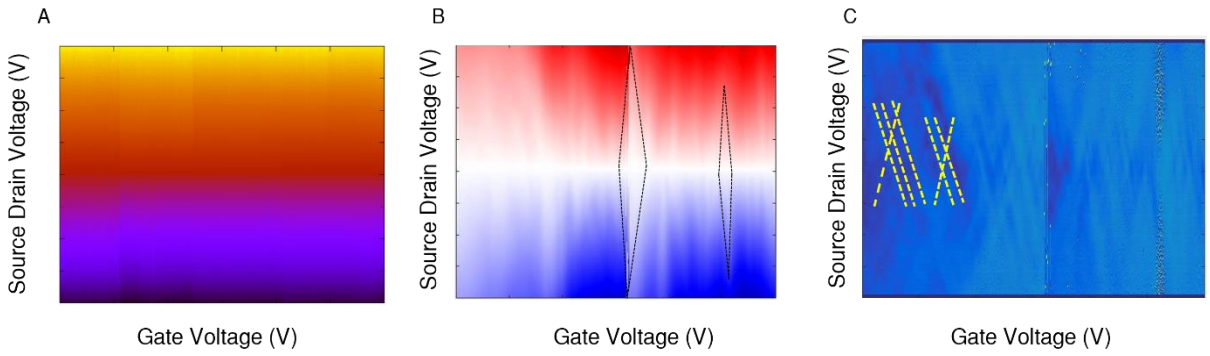

Figure 28. Low-Temperature Transport Measurements (4K) of nano-gap devices. The devices are fabricated in field-effect transistor configuration, where underlying Si is used as a global backgate. The gate voltage is swept from -30 to 30 V (X-axis) for each source-drain voltage that is swept from -200 to 200 mV (Y-axis). (A) An OFF state device, showing no gate voltage dependence of the source-drain current. The current colour bar range from -0.15 to 0.15 μA. (B) An ON state device showing distinct diamond peaks in the source-drain current which are indicative of Coulomb blockade (two Coulomb diamonds are shown by dotted black lines). (C) An ON state device showing chessboard like interference pattern in the source-drain current (dotted yellow lines highlight this).

Observation of such quantum effects indicates the presence of a well-confined finite system (the carbon filament). Although further work is needed to confirm the origins of these effects, they highlight the prospect of quantum transistors. Having thus established sufficient evidence for switching from carbon filament(s) formation in nano-gaps, an important question is how filamentation is possible when the phase change materials I use ($Ge_2Sb_2Te_5$ or GST) fills the 0.75 nm gap. The answer lies in the structuring of the GST film during sputter deposition. Chalcogenide atoms show strong bonding preference for each other over SiO_2 for reasons relating to minimization of strain and surface energies, and in the case of GST on SiO_2, this results in poor adhesion with the SiO_2 substrate[131]. Thus, it is expected that the island growth mode or the Volmer-Weber mode is preferred over the layer by layer growth mode during deposition[132]. Furthermore, graphene shows a catalytic property towards the growth of chalcogenides[133]. This would result in the GST islands on graphene growing in all directions; bridging but not filling

the gap. This is supported by the absence of switching in the graphene nano-gaps with SiO_2 in the gap. Furthermore, it can be deduced from experiments (see Figure 29) that for a 1 nm gap, GST should switch at ~ 2.15 V. However, switching in GST-bridged sub-5 nm devices occurs mostly at V_T ~ 0.6 V (with a standard deviation of 0.5 V), which is similar to observed in empty graphene nano-gaps. This strongly supports the argument that the presence of sputtered GST does not influence the switching behavior. Thus, there is a clear indication that regardless of the switching mechanism, there is a fundamental limit to scaling graphene nano-gaps for such relevant material systems. This perhaps also applies for carbon nanotube nano-gaps, which share similar bonding configuration (sp^2) as graphene, and could be a subject of future work. Importantly, molecular electronics where the actual gap is not filled entirely by the molecule but has several areas where such chains can grow might also have a similar scaling limit. Additionally, crystalline GST behaves as an intrinsic degenerate semiconductor. The work-function mismatch between graphene and GST should create a Schottky barrier that should result in non-linear IV traces. Indeed, a non-linearity can be observed in both in the crystalline and amorphous GST in < 20 nm gaps. However, the non-linear behavior is absent in the sub-5 nm switched GST graphene nano-gap devices. Furthermore, a conductance quantum (77 μS) is observed in the ON state of devices with and without GST (derived from the slope of the I-V characteristics), suggesting the presence of a filament that confines the charge transport to a single channel (mode).

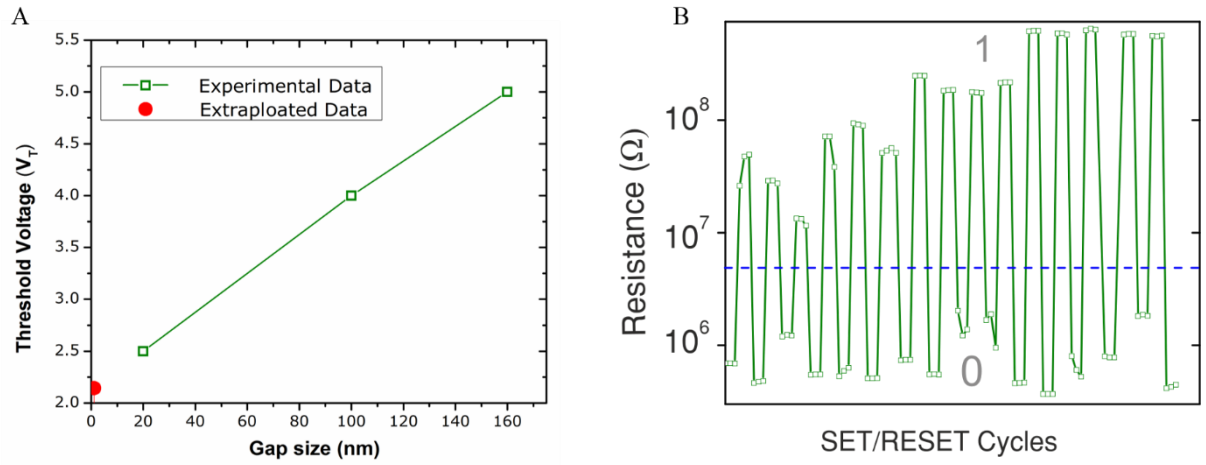

Figure 29. **Scaling Threshold Voltage and Multiple Switching**: Threshold Voltage (V_T) vs gap-size plot. Threshold voltage increases with an increase in the gap size. For a 1 nm gap, extrapolated V_T is ~ 2.15 V which is significantly higher than the voltage required for carbon filamentation. (B) Example of multi-cyclic switching in memory devices. Standard IV was carried-out for crystallization and 3.5-4 V pulses 25 ns wide, 5 ns in fall and rise edge were applied for amorphization. The device conditions after a few cycles. 1 corresponds to amorphous state and 0 to crystalline.

Therefore, these observations indicate resistance switching in graphene nano-gaps, which can be attributed to the controlled formation and breakdown of carbon filaments. Analyzing the switching behavior, it is found that the formation of carbon filaments is electric field dependent and only occurs in sub-5 nm gaps. These experiments demonstrate for the first time, reversible resistance switching in graphene nano-gaps in ambient conditions. For PCM devices with electrode separations less than 5 nm, I find the resistance switching to be fully dominated by the formation of carbon filaments. While the actual mechanism that is proposed (carbon filamentation) need further unambiguous proof, nonetheless these results point towards a key scaling limit to using such electrodes. Thus, electric-field-driven resistance switching in graphene nano-gaps constrains the operational voltages possible in such devices. It is found that at room temperature switching can occur at $V_{th} < 0.4$ V, which is, for example, the typical operating voltage for single-molecule devices. The noise typically observed in graphene-based single-molecule transistors at room temperature is likely to be the result of a rearrangement of atoms and bonds

at the edges of the electrodes. These results highlight the importance of gaining a better knowledge of the edge chemistry in graphene nano-gaps.

3.5 Summary

This chapter has laid the grounds to the better understanding of graphene nano-gap electrodes which have been of recent interest in a variety of fields ranging from molecular electronics to phase change memories. In particular, the manufacture and metrology of graphene nano-gaps manufactured using the feedback electroburning approach are detailed. Various modeling tools and experimental testbeds have been used to reveal the nano-gap formation mechanism in 1-2 layered graphene. In particular, the nano-gap formation is studied on different substrates and the gaps are found to be non-uniform along both the lateral and vertical directions. An approach to produce gaps of varying sizes is also proposed. Two different techniques to image nano-gaps are developed: (a) sacrificial polymer and (b) Kelvin probe microscopy. The latter approach is used to image the nano-gaps in-situ with a nanometric resolution. The fundamental limit to scaling carbon nano-gap electrodes is demonstrated using ultra-scaled phase change memory devices that show state-of-art resistive switching performance. A lithography free self-alignment technique is developed to fabricate such demonstrator devices. Graphene nano-gaps are observed to undergo switching from a highly electrically resistive state to low resistive state at very-low programming powers and in ambient conditions, which is associated with the formation and rupture of carbon chains. The results present in this chapter enable a better understanding of graphene nano-gaps, particularly gap -size and -location control and carry many implications from the scaling limit perspective, both for discovery science and potential applications.

3.6 Contribution Statement and Peek into Chapter 4

All steps of device fabrication and characterization were carried-out by the author. Dr Benjamin Porter assisted with some aspects of Kelvin Probe Microscopy. Members of the Nanostructured Materials group assisted with graphene synthesis.

The next chapter studies the effects of mechanical strain on graphene and WS_2 based heterostructures using Kelvin Probe Microscopy, which I developed in this chapter. This chapter's motivation is the need to translate the graphene nano-gaps electrodes onto flexible substrates, where strain will always exist, and to develop strain-effect transistors by overlaying two-dimensional materials and phase change materials.

CHAPTER 4: Strain Effects: Characterization and Applications

(A part of this chapter has been published: Syed Ghazi Sarwat, Martin Tweedie, Benjamin F. Porter, Yingqiu Zhou, Yuewen Sheng, Jan Mol, Jamie Warner, and Harish Bhaskaran. 2018, 18(4), Nanoletters)

Strain Effects: Characterization and Applications

4.1 Motivation for the Study

Two-dimensional materials are being increasingly studied, particularly for flexible and wearable technologies because of their inherent thinness and flexibility. A variety of applications from flexible photodetectors[134], transistors[135], and photovoltaics[136] to data storage[137], gas sensors[138], and artificial skin[139], have thus far been demonstrated, mostly through combinations of various two-dimensional materials. As a reminder from chapter 1, devices are commonly grown by chemical vapor deposition (CVD), where graphene is used as the electrode[140,141] and TMDCs as the active units[140]. Crucially, I wanted to translate graphene nano-gaps on a flexible substrate for they can enable not only highly efficient data-storage devices but also sensitive strain and bio-sensors. Nevertheless, before realizing a real device it became important to understand the effect of strain on two-dimensional materials. This is because a unique characteristic of most two-dimensional materials is the property of tuneability, i.e., their physical and chemical properties can be altered through varying the number of stacking layers[142], and/or by application of external stimuli, such as mechanical strain[143–145] and electric fields[135]. The role of strain is particularly relevant in flexible and wearable technologies, where materials would always bear a certain degree of variable strain. The strain is capable of causing semiconductor-metallic[146] and direct-indirect bandgap transitions[147], bandgap changes[148], Schottky barrier height shifts and/or physical debonding[144]. Whilst they can be detrimental to the device performance, they can also be harnessed for use in making field effect transistors[144,149], strain sensors[139] and in catalysis[150]. Thus there has been significant progress in understanding the underlying effect of strain on isolated two-dimensional materials. However, presently there are shortcomings to existing strain characterization techniques. Limitations of techniques such as optical (photo-luminescence) spectroscopy include poor resolution (diffraction limited) and only the applicability to direct

band gap materials. Indeed, in the heterostructure presented in this chapter, based on graphene and WS_2, only monolayer WS_2 would be measurable using such techniques.

4.2 Kelvin Probe Microscopy on Atomic Thick Heterostructures

We were introduced to KPM in the previous chapter. In essence, KPM is a form of scanning probe microscopy that measures the electrostatic potential distribution over a conductive substrate[116]. This is done through measurements of the contact potential difference (CPD) between the sample (here two-dimensional materials) and the AFM tip. The work function of the two-dimensional materials can be derived from the CPD, using the relation $\Phi_{sample}(x,y) = \Phi_{tip} - e \times CPD(x,y)$, where Φ is the work function and e is the elementary charge (see Appendix 9). Unlike photoluminescence spectroscopy, a commonly used strain characterization tool for two-dimensional materials[151–153], KPM measures the changes in the work function of the materials and not their bandgaps (see Figure 30). Therefore, as has been demonstrated in this chapter, KPM enables measurement of the influence of strain in zero-bandgap and indirect bandgap materials such as graphene and WS_2 multilayers, respectively, and at the nanoscale. Use of KPM also overcomes any substrate effects (such as suppression and masking of the material dependent signature vibrational modes), which may limit characterization of strain effects. Furthermore, it is found that KPM also aids in the understanding of charge transport through the visualization of junction potentials.

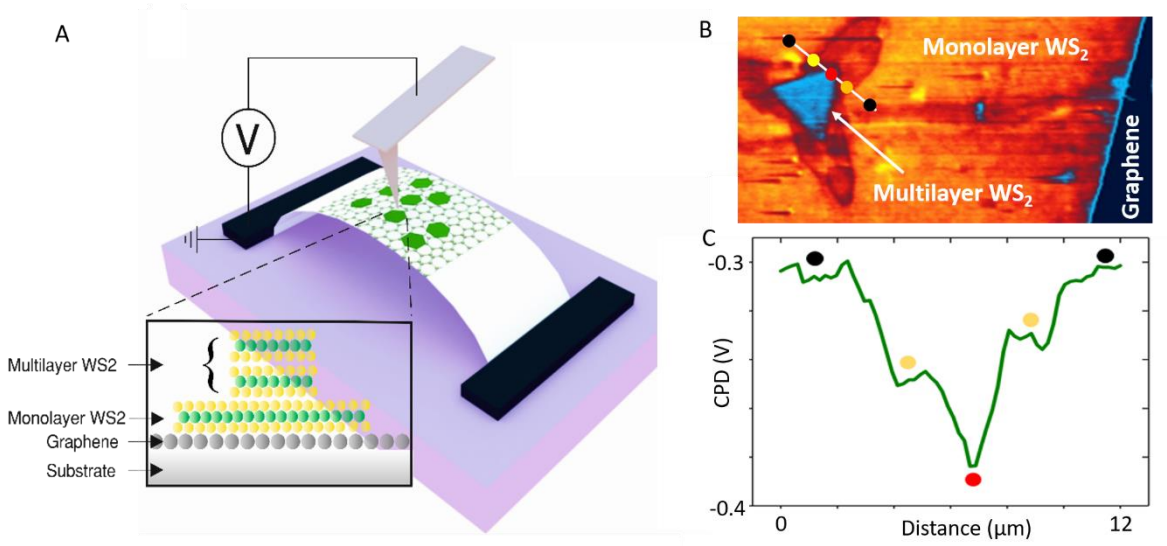

Figure 30. **The Setup.** (A) A schematic illustration of the strain characterization setup. Bottom left inset illustrates the heterostructure stack. (B) Kelvin probe micrograph of a monolayer WS_2 domain with a flower-shaped multilayer WS_2 domain in the center. Such a structure evolves during CVD growth: first the triangular heterostructure nucleates, on the boundaries of which a monolayer of WS_2 grows. (C) The graph illustrates the variation in the contact potential difference, hence the work function as a function of the number of layers of WS_2.

CVD grown multilayer (1-2 layers) graphene and monolayer/multilayer WS_2 are used for the study. A 2 by 2 cm PEN substrate was diced from a continuous 200 μm thick PEN role using laser cutting. The two-dimensional materials were transferred onto the PEN substrate using a non-aqueous sliding transfer method. Briefly, a PMMA film was spun coated on the copper substrate containing a graphene film. The copper foil was then placed on an $(NH_4)_2S_2O_8$ (0.1 M) solution in order to etch away the copper. The remaining intact PMMA/graphene film was then transferred into deionized water three times (in three different beakers) to get rid-off residual $(NH_4)_2S_2O_8$. A clean cover slide was dipped into the third beaker and the graphene/PMMA film was scooped out from the beaker (it was ensured that the cover slide did not dry out until the next step). The cover slide was placed at a 45^0 angle with respect to the PEN substrate and using a pipette, IPA was dropped on the cover slide. The IPA pushes the stack from the cover slide onto the PEN substrate. The IPA was then let to dry (first at room temperature, and then on a hotplate at 100℃ for 3 hours), leaving behind a uniformly oriented graphene film on PEN. For WS_2, the

Si containing WS_2 domains were first spin-coated with PMMA, following which the PMMA/WS_2 film was placed on a KOH solution (0.1 M) in order to etch away the SiO_2. Once etched, the floating PMMA/WS_2 film was scooped-out using a cover slide in a similar fashion as described earlier, and transferred using IPA droplets from a pipette onto the graphene covered PEN substrate. After transfer, the devices were annealed at 100 ^{0}C for 40 minutes in room conditions in order to improve the adhesion of graphene and WS_2 with each other and with the substrate. Optical characterization reveals the graphene and WS_2 to be of good quality (see Figure 31 and Figure 32).

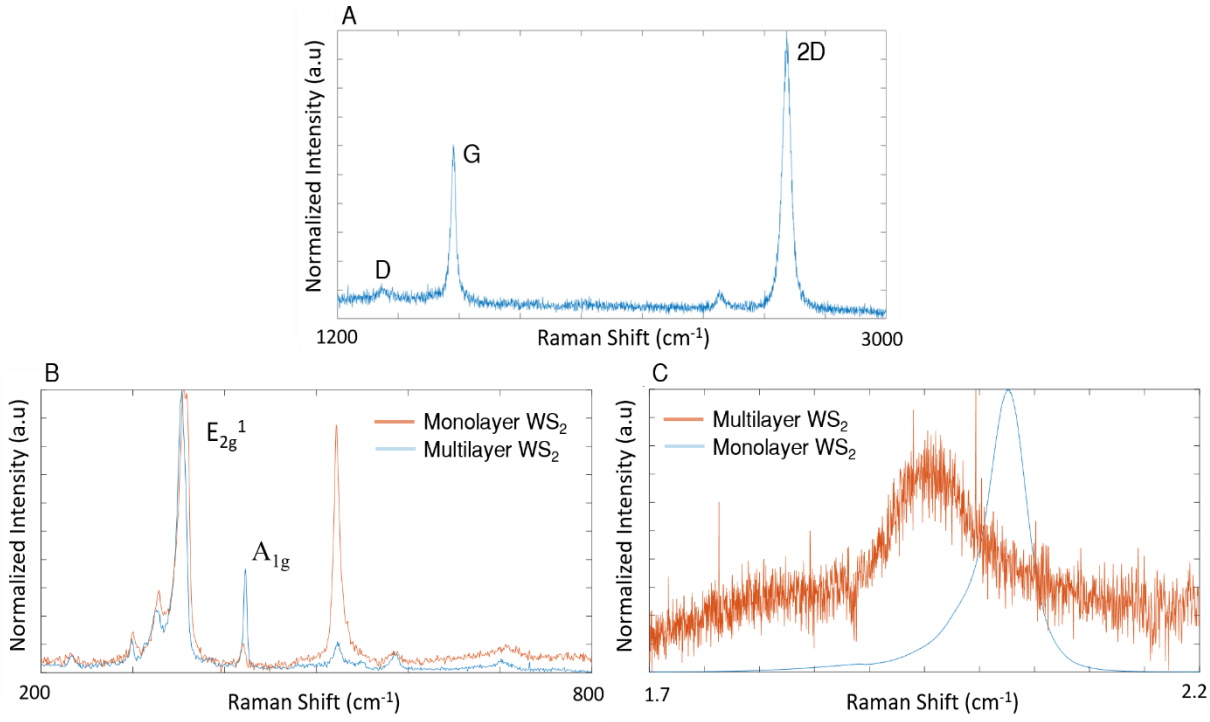

Figure 31. **Optical Characterization on a Silicon Substrate**. (A) The signature Raman peaks of graphene 2D and G are clearly evident, with their ratio > 2.0 ratio suggestive of graphene to be monolayered. The D peak is indicative of defect/disorder in the lattice. (B) Normalized Raman spectra of mono and multilayered WS_2 after transfer to a silicon chip. The signature peaks of WS_2 E_{2g}^1 (354.64 cm^{-1}) and A_{1g} (422.6 cm^{-1}) are evident. (C) Normalized photoluminescence spectra (PL) of mono and multilayered WS_2 from the same spot as for the Raman. Note the red-shift for multilayered WS_2, which is likely from the tensile strain induced during transfer.

The ability to anneal the devices was one major reason why PEN was chosen as the flexible substrate since on a comparison scale against commonly used PET (Polyethylene terephthalate)

substrates, it has a higher glass transition temperature (121 ^{0}C). The experimental set-up utilizes a custom-built sample holder and strain driver for two-point bending measurements and KPM (see Figure 15B and Figure 30). Figure 30A illustrates the schematic of the set-up. The atomic force microscopy (AFM) cantilevers (n-doped Si) were calibrated for their work function against highly oriented pyrolytic graphite (HOPG). Strain imparted to two-dimensional materials from bending a flexible substrate on which they reside has been approximated using a continuum mechanics model for elastic beams. Based on this model, shear and normal stresses can be considered negligible because the dominant deformation is along the longitudinal direction. If strong coupling is assumed between PEN and the two-dimensional materials, which is often the case due to strong van der Waals interaction at the interface, the strain on the two-dimensional materials can be represented by the equation[36,147] $\varepsilon = \tau \times sin\theta/d$, where τ is the PEN substrate thickness (200 μm), θ is the angle between the tangent to the curved substrate and the normal to the clamp, and d is the distance between the substrate edges. In the AFM set-up used here, the sample is grounded, and DC/AC bias is applied to the AFM cantilever.

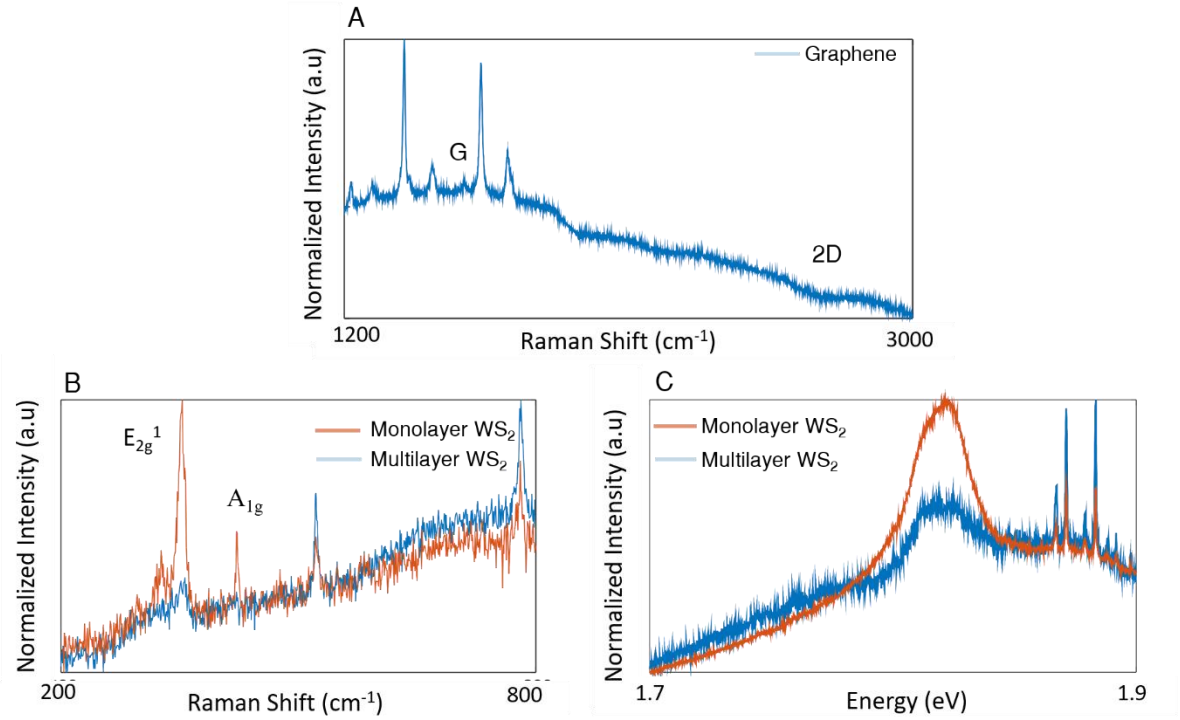

Figure 32**. Optical Characterization on a PEN Substrate.** (A) Raman spectra of transferred graphene on a PEN substrate. The signature peaks of graphene 2D and G are not evident, which is likely due to overlapping peaks (such as the peak G) and their suppression from hybridization and background noise. (B) Normalized Raman spectra of mono and multilayered WS_2 after transfer on PEN. The signature peaks of monolayer WS_2 E_{2g}^1 (353 cm^{-1}) and A_{1g} (420 cm^{-1}) are clearly evident. (C) Normalized photoluminescence spectra (PL) of mono and multilayered WS_2 from the same spot as for the Raman. PL signals of multilayered WS_2 are suppressed due to its indirect bandgap as opposed to monolayer WS_2 which has a direct bandgap (2.0 eV).

4.2.1 Effect of Uniaxial Tensile Strain

Figure 33A is an optical micrograph of a typical sample. Individual WS_2 domains are visible, while the graphene film on which these domains sit is indiscernible with an optical microscope (due to the high optical transparency and uniform coverage of graphene). An example of a KPM scan of the outlined region in Figure 33A is illustrated in Figure 33B. Due to their atomic thickness, graphene and WS_2 (including other two-dimensional materials) are difficult to resolve under normal topographic AFM measurements on flexible substrates, as their thickness is less than of the same order as the substrate‘s roughness. KPM, however, resolves them quite distinctly, thus enabling identification. Figure 33B reveals three regions of distinct electrostatic potentials. These regions correspond to graphene (S1), monolayer WS_2 (S2) and multilayer WS_2 (S3),

respectively. The smaller potential of monolayer WS_2 over multilayer WS_2 is indicative of the thickness (number of layers) induced lowering of the work-function[154]. At zero strain, the work functions of S1, S2, and S3 are 4.75 eV, 4.54 eV, and 4.72 eV, respectively. These values agree well with literature[155–157] and are suggestive of graphene being in a *p*-doped state, and WS_2 in an *n*-doped state.

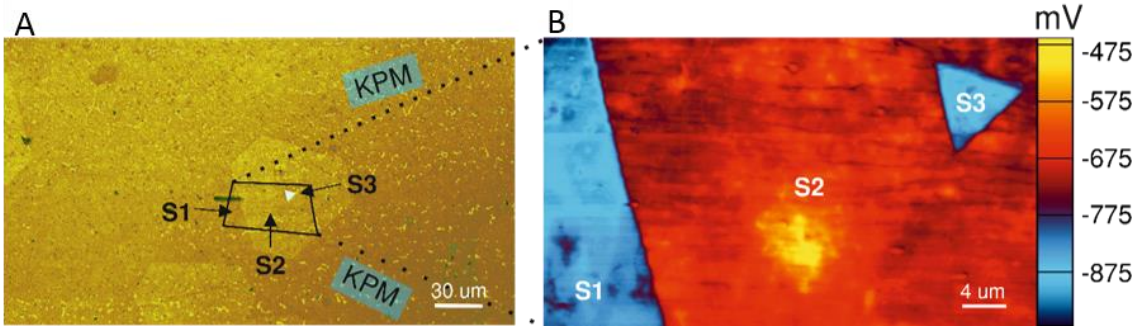

Figure 33. **Two-dimensional heterostructures**. (A) A false-colored optical micrograph of a typical sample revealing graphene/WS_2 heterostructure placed on a PEN substrate. S1, S2, and S3 correspond to graphene, monolayer WS_2, and multilayer WS_2 respectively and (B) The Kelvin Probe Micrograph of the highlighted region in (B).

However, it can be noted that these values can be influenced significantly by the environment and vary between samples. For example, I observed that commonly used organic solvents can influence the work-functions of graphene and WS_2 and this occurs at very different rates (graphene is more readily affected than WS_2); in particular acetone results in an increased *p*-doping (see Figure 34), which is likely a result of the electron withdrawing nature of the carbonyl group in acetone. Similar variations in the work functions in response to variations in the environment (humidity) have been demonstrated using KPM in both CVD and exfoliated forms of MoS_2[158,159] and graphene[160] suggesting this to be a tunable intrinsic property of two-dimensional materials.

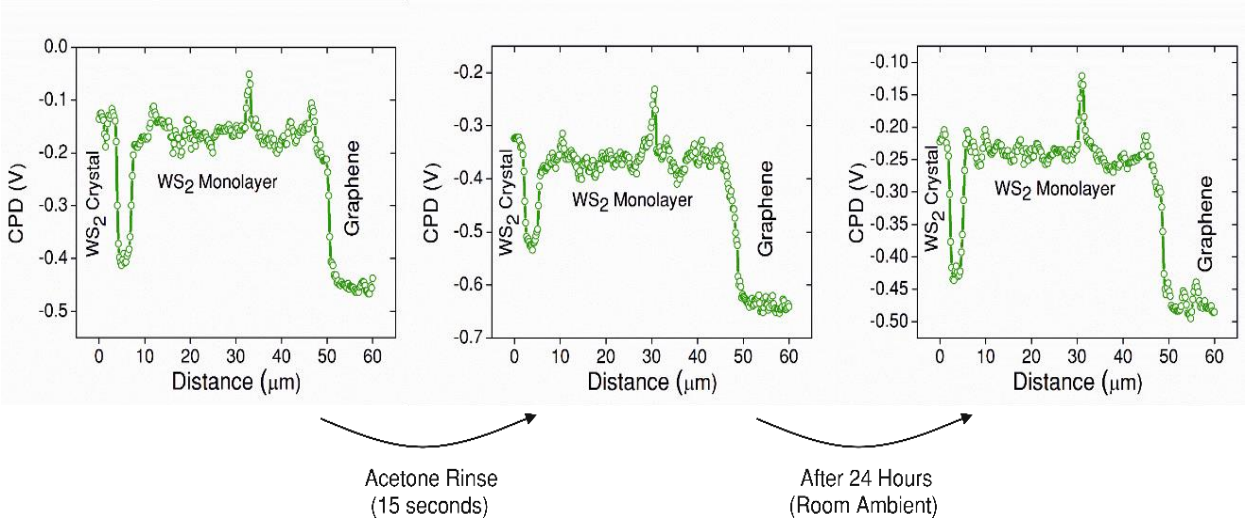

Figure 34. **Effect of Contaminants on the Work-functions**. Kelvin probe line spectra of the sample before, after and much after rinsing with acetone. Exposure to acetone results to an increase in the work function of WS_2 and graphene indicative of *p*-doping, likely a result of the electron withdrawing nature of ketone. The device almost recovers after 24 hours in room ambient. Note that graphene and WS_2 react differently to acetone, resulting in changes in the junctions. Such a behavior can be used in sensing applications (gas, temperature, and solvents).

The work functions differ between samples (shown later in Figure 37), which can be linked to the fabrication process induced (from solvents and sacrificial polymers) and the humidity[159] differences during experimentations. It can be noted that for multilayered WS_2, this difference is most pronounced. This is attributed to the differences in the thickness (81 layers in sample 1 and 91 layers in sample 2) and to the W:S ratio (see Figure 35 and 36), both, within (different domains) and across the samples.

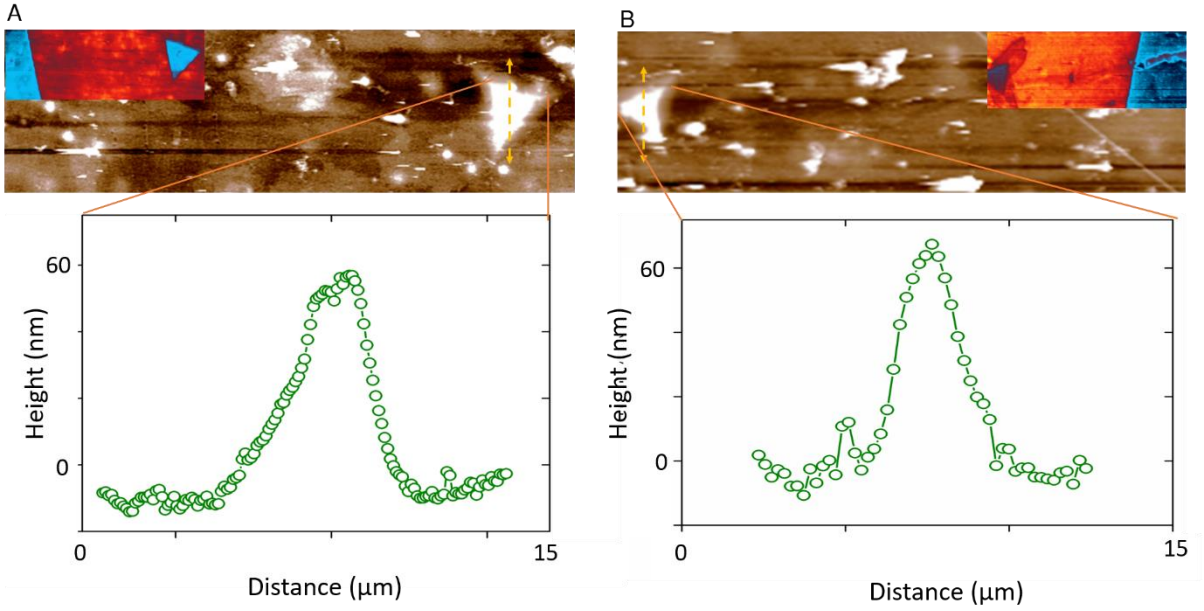

Figure 35. **Atomic Force and Kelvin Probe Micrographs**. (A and B) Atomic force micrographs of two different samples, respectively. Monolayer WS_2 is indiscernible due to its atomic thickness and the high substrate roughness. Multilayer WS_2 is discernible, and a line scan across it is shown in the graphs. The thicknesses of multilayer WS_2 areas in sample 1 and 2 are 64.4 nm and 72.2 nm, respectively. Insets are Kelvin Probe Micrographs. The root mean square value of the substrate roughness is found to be 6.2 nm, which is significantly higher than the thickness of graphene (0.35-0.70 nm) and monolayer WS_2 (0.80 nm).

It is also found that the WS_2 domains are mostly hexagonal (irregular) rather than triangular as has been commonly reported. This follows from the understanding that the shapes of individual WS_2 domains can be a strong function of their location while growth on the silicon substrate (local variations in temperature and pressure in the CVD chamber) and to the variations in the W:S ratio, as has been previously studied in MoS_2[34,38]

An independent set of standard field effect measurements (see Figure 37D) using a 300 nm SiO_2 back gate were performed to further confirm the nature of doping predicted by KPM in graphene and WS_2, Previous reports have confirmed that adsorbates (H_2O, O_2) and charge traps such as oxygen dangling bonds on the SiO_2 surface induce *p*-doping in two-dimensional materials[154,161,162]; this behavior, as will be explained next, approximates the PEN substrate. It is found that graphene and WS_2 are indeed *p*-doped and *n*-doped, respectively. The carrier mobility of the two-dimensional materials are estimated using $\mu = (L/WC_iV_{DS})(dI_{DS}/dV_G)$, where L and

W are channel length and width, respectively, V_{DS} is the source-drain bias and C_i is the gate capacitance (11.505e-9 F/cm^2). For graphene and WS_2 these are 996 cm^2 V^{-1}s^{-1} and 0.22 cm^2 V^{-1}s^{-1}, respectively; values typical of CVD grown materials due to larger defect densities resulting from contamination (during growth, transfer, and handling)[29,30]. The most significant source for contamination were observed to be the PMMA residues and the dirt on the cover slides that were used for the wet-transfer of the materials. The transfer of graphene was found to not contribute significantly to contamination, while the subsequent transfer of WS_2 did. This is likely a result of strong WS_2-PMMA interactions.

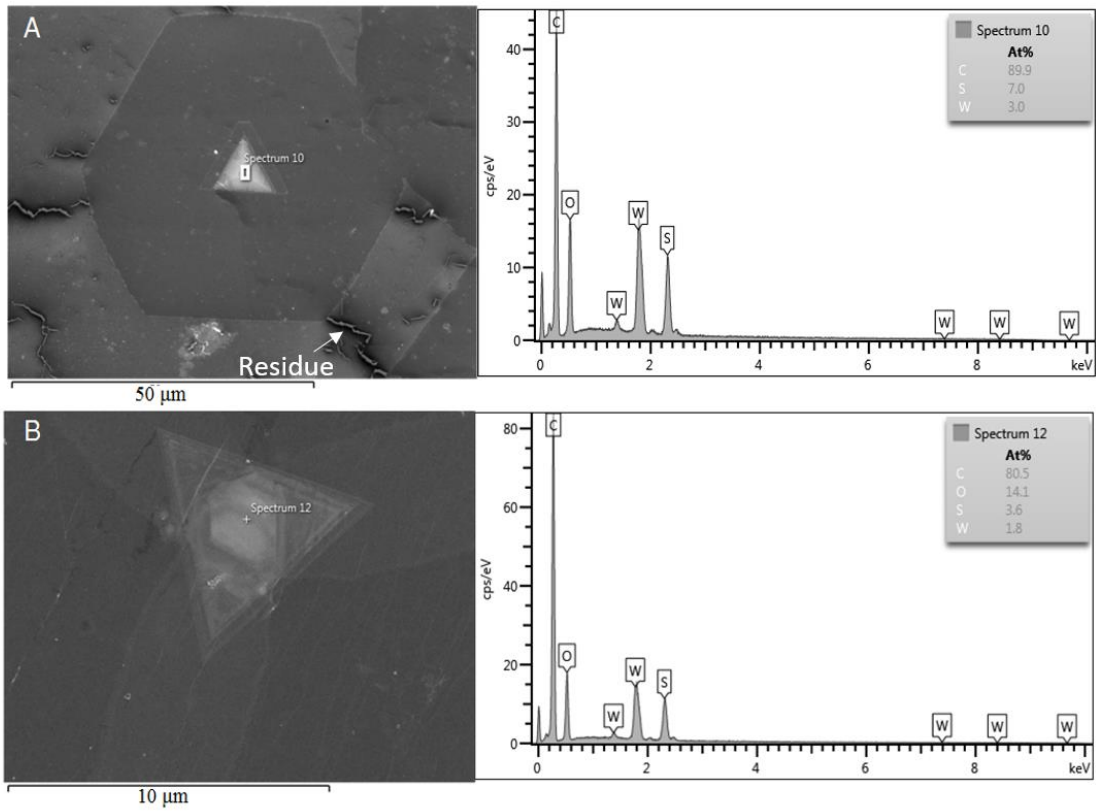

Figure 36. **Scanning electron micrographs of WS_2 domains on graphene**. (A) A region from sample 1 and (B) from sample 2; and their corresponding energy dispersive X-ray point spectra. The difference observed in the work function of multilayer WS_2 under KPM is likely a result of the differences in the W:S ratio and the thickness. Contamination in the form of residues can be observed in Figure A.

In order to study the effect of strain on the work functions in these regions, a varying uniaxial tensile stress was applied on the substrate through the strain driver, and the work functions were recorded (see Figure 37A). The devices were strained below 1 % strain multiple

times to remove any residual stresses that may have resulted from the annealing step before performing KPM measurements. On the KPM measurements, the work function in all the three regions can be observed to increase with strain (see Figure 37A and 37B). Furthermore, the fact that the change in the work function of WS_2 responds proportionally with graphene implies an effective strain transfer between graphene and WS_2. This is suggestive of strong van der Waals interaction/coupling between graphene and WS_2, which is crucial in determining their charge transfer efficiency and mechanical stability. It is found that the degree of modulation in the work function per unit strain is different for graphene and multi/mono layered WS_2. These can be calculated to a first approximation using the slope of a linear fit and reach values as high as 0.117 eV (1 eV = 1.6e-19 J) for graphene, 0.098eV for multilayered WS_2 and 0.089 eV for monolayered WS_2. It is emphasized that these are significant modulation in the work functions. The work functions on the reverse cycles are found to not follow a clear trend and match the values on the forward cycles, which can be attributed to the viscoelastic nature of PEN and to the fact that slipped graphene and WS_2 adhere differently to the substrate (I discuss this later in this chapter). It is however noted that the work functions of graphene and WS_2 return to their original state each time after the cyclic measurements.

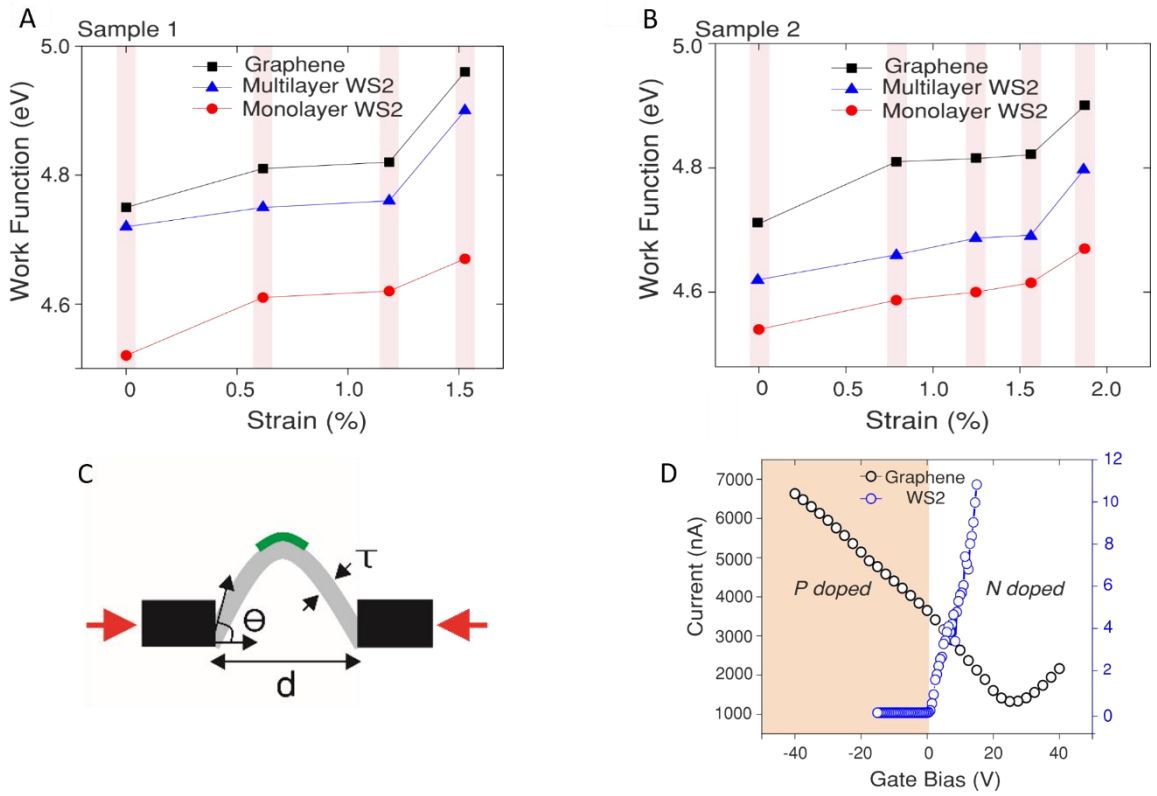

Figure 37. **Strain characterization**. (A and B) Plots illustrating work function of graphene, monolayer WS_2 and multilayer WS_2 on PEN in two different samples; the work function increases with strain. (C) A schematic of the two-point bending apparatus. (D) Field effect (gate) measurements of graphene and monolayer WS_2 channels on a SiO_2 substrate indicating WS_2 is n-doped, while graphene is p-doped. This measurement is difficult to perform on the PEN because of its high roughness, high defect density, and large thickness.

In cases where graphene and WS_2 slipped, an annealing step on the hotplate at 100 ^{0}C for 10 mins could restore the original work function values for subsequent measurements. Given the response of the materials to strain is non-linear, it is believed an imperfect strain transfer occurs between the substrate and the two-dimensional materials; meaning the geometrical strains do not equal the actual strain felt by graphene and WS_2, which stands contrary to assumptions made in the literature[163].

4.2.2 Optical Measurements and Mechanism

These observations on the strain induced increase in the work function can be attributed to the modulation of the electronic energy landscapes (energy band diagrams) of graphene and WS_2. Such a modulation must originate from the interplay of uniaxial tensile strain and charge

transfer with the PEN substrate since the changes in the work function are significant. The effect of uniaxial strain on the work function would depend on how the Fermi level and the vacuum level are modulated ($\Phi = E_{Fermi} - E_{vacuum}$). While for bulk materials, these effects are well understood, for two-dimensional materials, particularly TMDCs, the theoretical and experimental results do not consistently support each other[143,145,164].

It is understood that in the case of M-X systems (like WS_2) strain can modulate the in-plane W-S bond length while distorting the out-of-plane S-W-S in terms of both length and angle. Theoretical calculations[145,165] suggest that in WS_2 (unlike $MoTe_2$) this results in the work function to decrease at a slower rate as the vacuum level is also modulated with strain. However, this is contradictory to the observations discussed before (the work function is noted to increase from strain), and also to a previous experimental study on WS_2[164]. This discrepancy can be attributed to the nature of theoretical calculations, which consider WS_2 in its isolated form, ignoring the effects of substrates and environment. Charge transfer with the substrate, which depends on the degree of adhesion[166,167] and strain-enhanced chemical reactivity[34,38], can also play a significant role in modulating the work function. The chemistry of PEN, which is composed of the electron-withdrawing aromatic rings and ester groups should induce *p*-doping (or decreased *n*-doping) in the two-dimensional materials[168]. *P* doping implies Fermi level lowering or work function increase as correctly observed in my experiments. Using this line of reasoning, the last data point in Figure 37 A and 37B can be attributed to the improved conformation of the two-dimensional materials onto the substrate roughness, and their enhanced chemical reactivity from the strain that results in improved charge transfer.

On the other hand, since graphene is formed by a single sheet of carbon atoms, all the carbon-carbon bonds get elongated under the uniaxial tensile strain. Strain-induced lowering of graphene's work function has been linked to changes in its density of states (DOS)[169]. An increase in the lattice parameter is understood to cause an increase in the DOS of graphene due to

decreased average anisotropic Fermi group velocities. Increased DOS results in the lowering of the Fermi level as higher energy electrons can fill the lower energy states. Overall, this results in an increase in the work function, as has been correctly observed in this study and in another study, where the substrate was polydimethylsiloxane (PDMS)[170]. In comparison, however, a relatively larger change in work function is observed. Here, this can be attributed to the choice of substrate, which unlike PDMS has a smaller Poisson's ratio, because of which graphene does not undergo significant lateral compression with uniaxial tension[151], and to enhanced *p*-doping from PEN due to charge transfer. Therefore graphene's Fermi level is more effectively modulated, resulting in a larger change in the work function.

In situ optical spectroscopic measurements (see Figure 38) were performed to back my KPM based observations. It is found that in the case of monolayer WS_2, the E_{2g}^1 Raman peak that defines the in-plane vibrations (anti-parallel W and S vibrations) red-shifts by 2.2 cm^{-1} from the strain (2%). In essence, this is indicative of lattice expansion as would be expected from a tensile strain. The A_{1g} Raman peak that defines the out-of-plane vibrations of S atoms, however, is suppressed due to the large background noise (signal). In multilayered WS_2 a similar strain (2%) response is observed as in monolayer; the E_{2g}^1 red-shifts by 1.77 cm^{-1} upon strain, and the A_{1g} peaks which gets evident in multilayered WS_2 due to its greater thickness also red-shifts by 1.06 cm^{-1} with strain (2%). This anomalous A_{1g} mode softening can be although not entirely associated with doping and/or to strain and thickness induced changes in intra/inter-layer bonding[35,37]. For doping to govern this peak shift, the change has to be more significant than observed in the current study[43], and because the work function is observed to increase with strain, it is more likely that changes in the intra/inter-layer bonding are dominant in the peak shift. In fact, these observations of red-shifts in the E_{2g}^1 and A_{1g} (with $E_{2g}^1 > A_{1g}$) modes are in a good agreement with a recent study on the effect of uniaxial strain on the Raman spectrum of WS_2[171]. In addition, it is noted from these measurements that monolayer WS_2 is modulated more strongly than the

multilayers counterpart. This greater sensitivity of monolayer WS_2 to strain over the multilayers has also been observed in multilayered -MoS_2 and -graphene, and -exfoliated WS_2, and is associated with the variations in the intra-layer bonding as more layers get stacked in these materials[171–173]. In graphene it is found that the signature Raman peaks become weaker on the PEN substrate, partly due to overlapping (G) peaks and partly because of the suppression from hybridization and larger background noise; these factors limit understanding the strain induced effects in graphene[174]. Using photoluminescence spectroscopy, clear red-shifts in the peak position (that define direct valence to conduction band transitions) of both monolayered and multilayered WS_2 are found. This is indicative of bandgap reduction and is in agreement with strain-induced effects in isolated WS_2. The peak intensity on the other is observed to either increase or decrease across the sample. A decrease is indicative of either bandgap transition (direct to indirect) or increased photoluminescence quenching from improved charge transfer to the substrate (due to enhanced contact). An increase on the other hand suggests the contrary. The fact that I see a mixed behaviour in my samples is suggestive of the heterostructure making inhomogeneous contact with the substrate. Indeed, this has recently been observed in another independent study that I co-authored[175].

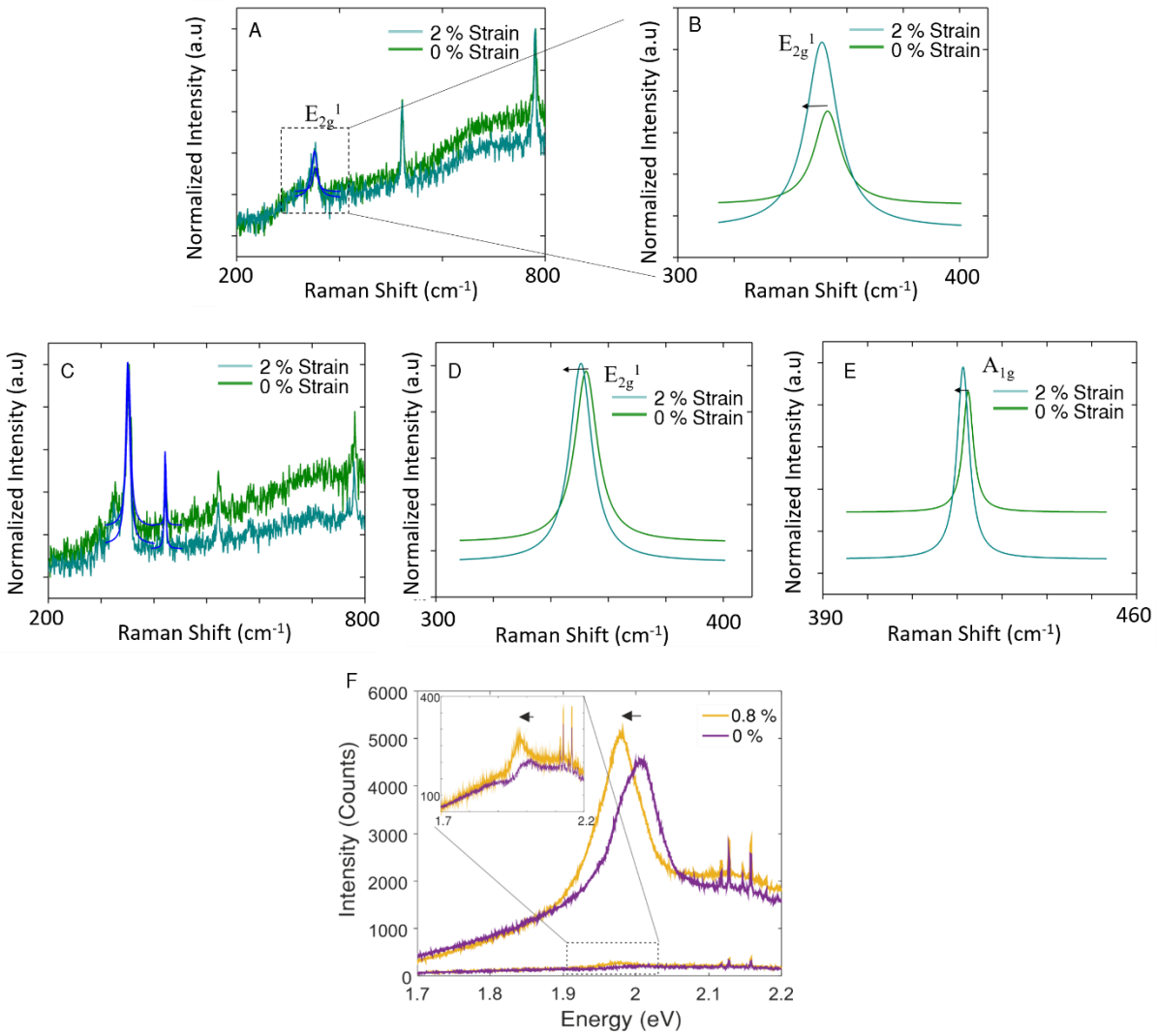

Figure 38. **Optical Characterisation of Strain Effects (532 nm excitation) in WS_2.** (A) Normalized Raman spectra of monolayered WS_2 under zero and 2 % strain. The E_{2g}^1 peak redshifts by 2.2 cm^{-1} upon strain, indicative of lattice expansion. (B) Normalized PL spectra of monolayered WS_2 under zero and 2 % strain. The PL peak (related to the direct band gap transition) is red-shifted by 100 meV upon strain. (C) Normalized Raman spectra of multilayered WS_2 under zero and 2 % strain. The E_{2g}^1 peak redshifts by 1.77 cm^{-1} upon strain. The A_{1g} peak that defines the out-of-plane vibration is also red-shifted by 1.06 cm^{-1} upon strain. (F) Strain-induced red-shifts in the direct gap transition peak in both mono-and multilayered WS_2, indicative of a reduction in the bandgap.

Since graphene, WS_2 monolayers and WS_2 multilayers have different doping levels and band gaps, their Fermi levels in a non-contacted state will be different. When in contact, charge transfer occurs in order to equalize the Fermi levels, which would result in the formation of junctions. One can estimate the nature of these junctions from the KPM measurements. It is found that a Schottky barrier forms at the lateral graphene/WS_2 interface, while a type-I

heterojunction forms at the lateral WS_2 monolayer/WS_2 multilayer interface. In a non-strained state, the conduction band offsets can be estimated using the following equation

$$\Phi_{WS2multilayer} - \Phi_{WS2monolayer} = \Delta E_C - (3/2 \times kT \times \ln(_{monolayer}/_{multilayer})) \quad (1)$$

Equation 1 makes a Boltzmann approximation and considers identical doping levels per unit volume in monolayered and multilayered WS_2[142]. ΔE_C is the conduction band offset at the junction between mono and multilayered WS_2, k is the Boltzmann constant, T is the temperature, and m_{mono} ($0.349m_0$) and m_{multi} ($0.569m_0$) are the effective masses of electrons[176]. Equation 1 is derived using the following expressions

$$n_{WS_2 multilayer} = N_C \exp^{(E_C - E_F/kT)}$$
$$n_{WS_2 monolayer} = N_C \exp^{(E_C - E_F/kT)}$$
$$where, N_C = 2(m_C kT / 2\pi\hbar^2)$$
$$E_{F(WS_2 multilayer)} = E_C - kT \ln(n / N_C)$$
$$E_{F(WS_2 monolayer)} = E_C - kT \ln(n / N_C)$$

Where, N_C is the density of states. Subtracting the last 2 equations and making an approximation for $\Delta CPD_{(WS2monolayer-WS2multilayer)} = \Phi_{WS2multilayer} - \Phi_{WS2monolayer} = \Delta E_{Fermi}$, gives the expression 1. At zero strain, the conduction band offset between monolayered and multilayered WS_2 in sample 1 is computed as 181 meV. Given the band gaps of monolayered and multilayered WS_2 are 2.14 eV and 1.4 eV, repectively[177], this indicates a type-I heterojunction. Similarly, the Schottky barrier height can be approximated using the following expression

$$\Phi_{shocktty} = \Phi_{Graphene} - E_{affinity\ (WS2)} \quad (2)$$

Using equation 2, at the graphene/monolayer WS_2 junction and for the given electron affinity ($E_{affinity}$)[178] of 4.0 eV for WS_2, the Schottky barrier height ($\Phi_{shocktty}$) is 0.6 eV. This value match with experimental field-effect measurements on SiO_2 substrate[140]. This, while backing the accuracy of results, also supports my reasoning of approximating the *p*-doping nature of SiO_2.

It is however emphasized that these band offsets and the barrier height at the junctions also possess an offset due to interactions with the underlying graphene (this interaction is in the vertical direction and is expected to originate from the formation of dipoles rather than from Schottky barriers, owing to the atomic thicknesses of WS_2). For this discussion of my results, it is sufficient that we focus on the Fermi levels of graphene and WS_2 since both the nature and magnitude of the junctions is dependent on differences in the Fermi levels between graphene, monolayered and multilayered WS_2. The difference between Fermi levels of graphene/WS_2 monolayer and WS_2 monolayer/WS_2 multilayer can be obtained by computing the difference in their CPDs[179] ($\Delta CPD_{WS2monolayer\text{-}Graphene}$ and $\Delta CPD_{WS2monolayer\text{-}WS2multilayer}$)

$$\Delta CPD_{(WS2monolayer\text{-}Graphene/WS2multilayer)} = \Phi_{WS2multilayer} - \Phi_{Graphene/WS2monolayer} = \Delta E_{Fermi}$$

Figure 39A represents a typical KPM line scan at 0.6 % strain. The highlighted region marks the WS_2 monolayer/WS_2 multilayer interface. A value ΔE_{Fermi} = 0.145eV, and a depletion width of 2 μm can be extracted from the WS_2 monolayer/WS_2 multilayer junction (see Figure 39A). This indicates that the Fermi level of WS_2 monolayer is higher than WS_2 multilayer by 0.145eV, suggesting a *p-n* junction at the interface. The built-in potential is further estimated and the field is calculated by fitting the junction with a sigmoidal function (see Figure 39B). The built-in potential is 0.14eV. If WS_2 multilayer is considered to be similar to a MoS_2 monolayer (a reasonable approximation on the basis of similar bandgaps), this value matches with the experimentally observed open circuit voltage of WS_2/MoS_2 junctions[42]. The derivative of the sigmoidal fitting is illustrated in the inset of Figure 39B and represents the electric field profile at the interface. The maximum field is at the center of the depletion region (162 mV/μm).

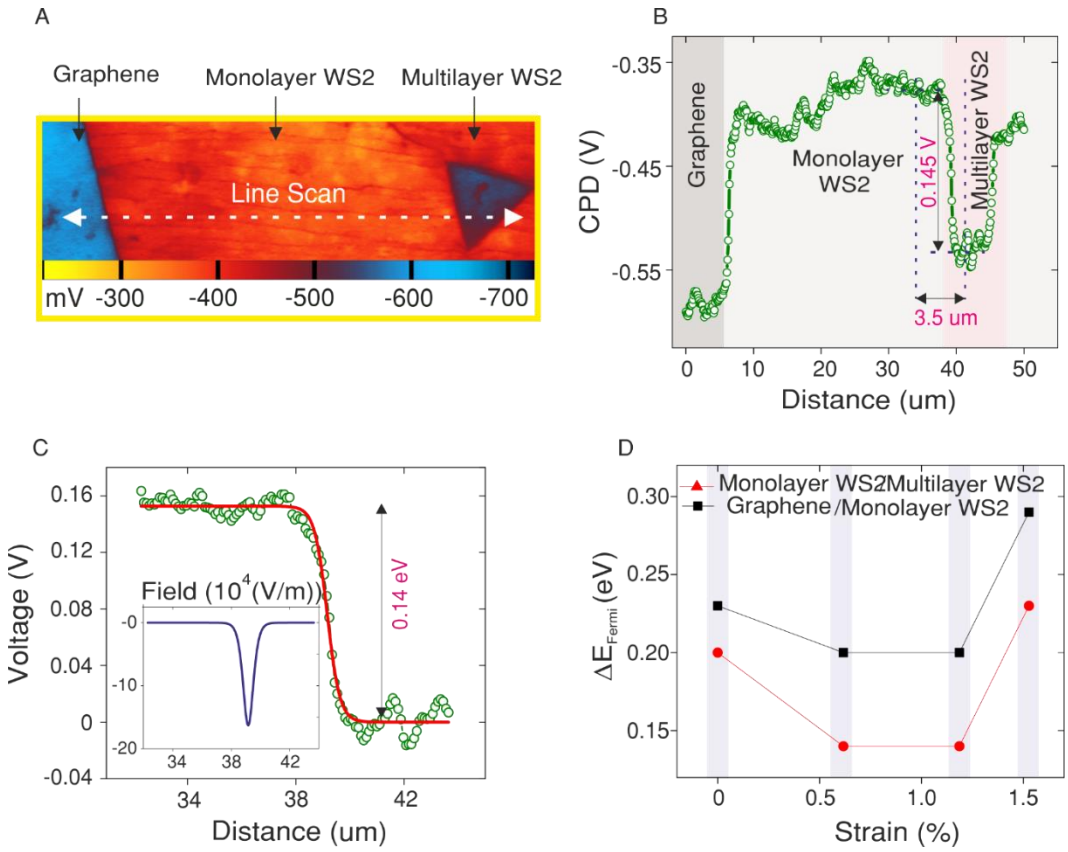

Figure 39**. Heterojunction characterization**. (A) A KPM map of a heterostructure. (B) A line scan on the map at 0.6 % strain. The region with arrows is the interface (*pn* junction) between monolayer WS_2 and multilayer WS_2. (C) The junction is fitted with a sigmoidal function, and its derivative is plotted in the inset which represents the electric field profile; the direction of the field is from multilayer WS_2 to monolayer WS_2. (D) Plot illustrating strain modulated junctions. Strain can either increase or decrease the Schottky barrier height and the built-in potentials due to anisotropic modulation of the work functions.

The effect of strain on the built-in potential, hence electric field, is illustrated in Figure 39C. The built-in potential is observed to show a non-linear behavior with strain: a decrease is akin to applying a forward electrical bias and an increase akin to applying a reverse electrical bias. Regardless of the direction, this has significant implications as junctions govern the electrical (charge flow) and optoelectronic (photovoltaic and -conductive) functioning of two-dimensional heterostructure based devices[180].

The energy band diagrams of graphene and mono/multilayer WS_2 under relaxed and strained conditions are now analyzed. In their isolated states, the Fermi levels of the graphene, mono and multilayer WS_2 are different and distinct with respect to each other and the AFM tip.

From the KPM and gate sweep measurements, it is deduced that the AFM tip and WS_2 are *n*-doped, while graphene is *p*-doped (see Figure 40A (red dashed lines)). When the two-dimensional materials are in contact with each other, an equilibrium is achieved such that a new Fermi level is established under zero strain conditions (represented by the green dashed lines in Figure 40B and 40C). The uniaxial tensile strain disturbs the equilibrium (giving rise to quasi-Fermi levels). In graphene, it is observed that the DOS increases as a function of strain[169]. Increased DOS would imply that the Fermi level gets decreased. Further lowering of Fermi level can come from enhanced electron transfer to the PEN substrate and to the adsorbed molecules owing to strain mediated increase in graphene's adhesion and chemical reactivity. No significant shift in the vacuum level occurs during straining as has been theoretically predicted[181]. Overall, these effects result in an increase in the work function of graphene. The new Fermi level of graphene synergistically affects WS_2. In WS_2, with strain, the electrons diffuse into graphene due to graphene's lower Fermi level. Consequently, this lowers the Fermi level of WS_2.

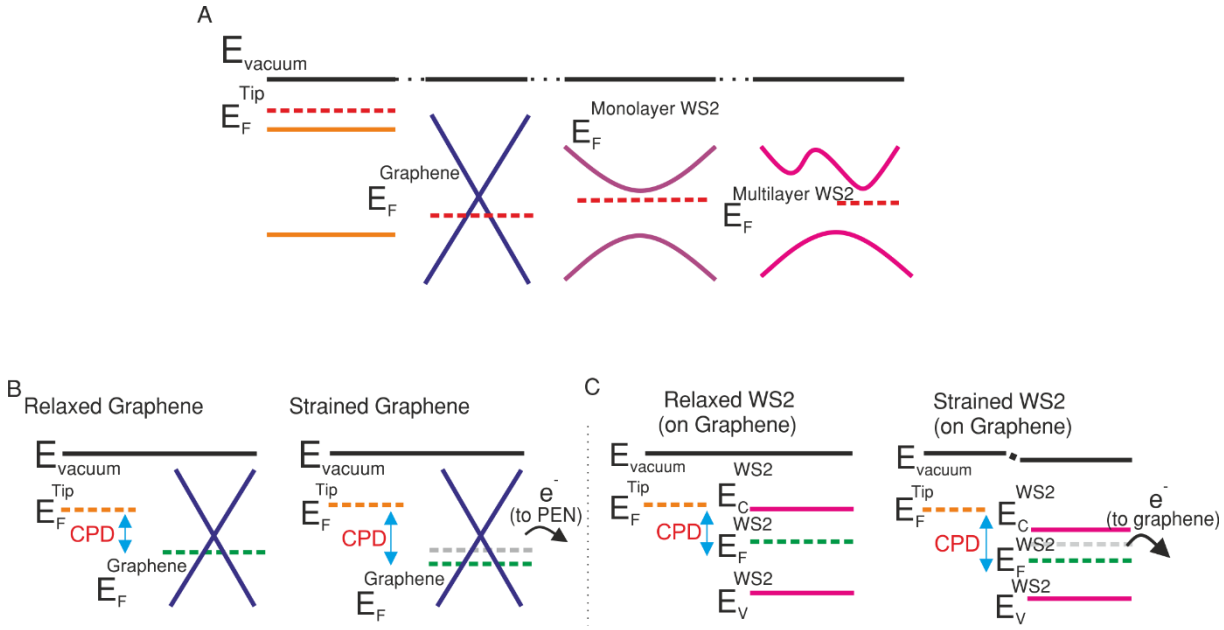

Figure 40. **Charge transfer mechanism**. (A) Electronic energy landscapes of AFM tip, graphene, monolayer WS_2, and multilayer WS_2 under equilibrium and isolated conditions. Graphene is p-type doped, while WS_2 is n-type doped (red dashed lines are the Fermi levels). (B and C) Uniaxial tensile strain influenced energy band diagrams of the heterostructure. The green dashed line represents the equilibrium Fermi level. (B) Uniaxial tensile strain downshifts the Fermi level of graphene (E_F), illustrated by the increase in the contact potential difference (CPD). (C) Uniaxial tensile strain downshifts the Fermi level (E_F) of WS_2 (mono and multilayer), as well as decreases the vacuum level (E_{Vacuum}) and the bandgap.

Thus decreased *n*-doping of the WS_2 depends on how well the graphene becomes *p*-doped. In addition, strain enhanced chemical reactivity can further *p*-dope WS_2. This is in agreement with the experimental observations described earlier: changes in the work function of WS_2 closely follows that in graphene. However, for the work function to increase in WS_2, its vacuum level, which is theorized on first principle calculations to decrease with strain[145], has to decrease at a slower rate than the decrease in its Fermi level from charge transfer. Furthermore, a monotonous bandgap shortening in WS_2 from the application of uniaxial tensile strain using photoluminescence spectroscopy (see Figure 41A) is noted, which complements the literature[152]. Drops in the work function at certain strains (see Figure 41B) were also observed in the Kelvin Probe Microscopy results, which were followed by an increase.

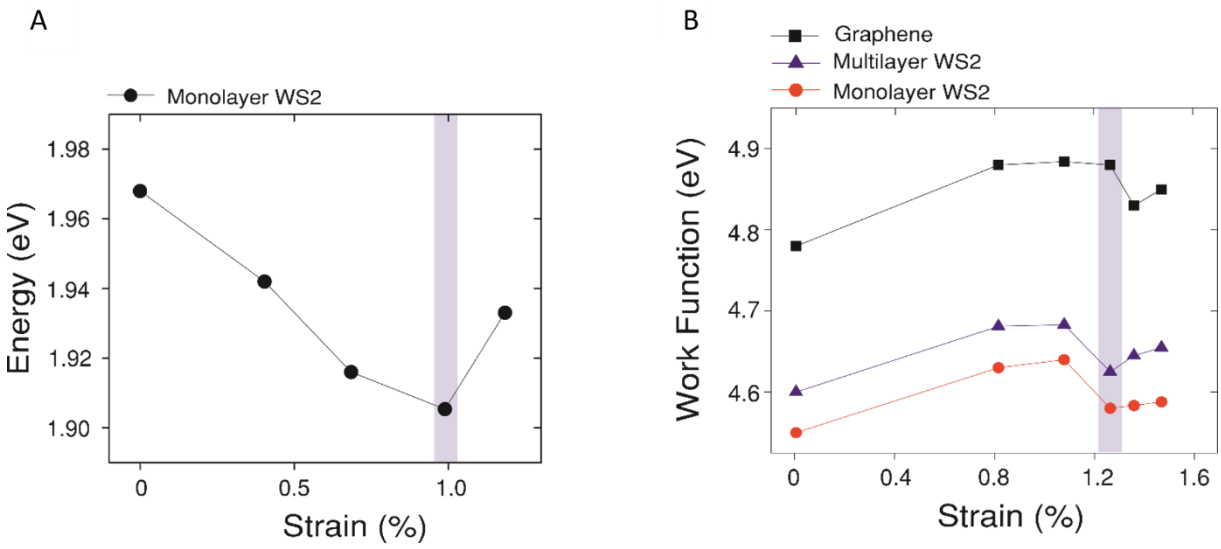

Figure 41. **Photoluminescence spectroscopy studies of the heterostructure**. (A) A spectrum of the graphene/WS_2 heterostructure as a function of uniaxial tensile strain. The exciton peak position redshifts with increasing strain. This is indicative of band gap narrowing. At 1% strain the bandgap is observed to increase due to slippage. (B) Slippage induced relaxation is also observed in the KPM measurements. The work function drops at 1.26% strain and then continues to increase as a function of strain.

These drops can be attributed to slippage or slip-driven relaxation. Slippage is a phenomenon commonly observed in two-dimensional materials under unanchored conditions[144] (as in this study), and deteriorates the adhesion between graphene and WS_2 with the substrate resulting in an ineffective strain and charge transfer. It is emphasize that several WS_2 domains sit on graphene, each of which is expected to strain differently due to different –crystal orientations, -edge geometries and -local substrate roughness. Overall, clear signatures of strain-induced changes in the electronic landscape of the heterostructures can be recorded using KPM. These results highlight the importance of gaining a better knowledge of strain induced effects in such applications oriented heterostructures.

4.3 Nano-gap Electrodes on Flexible Substrates

Having studied the effect of strain on two-dimensional materials, graphene nano-gap electrodes were fabricated on flexible substrates (PEN and PET) for wearable nano-gap phase change memories of similar architecture, as discussed in Chapter 2. The devices on PEN substrates were studied in greater detail because of its high thermal stability, given high

temperatures are attained during the electroburning process. It was consistently found that the nano-gap formation resulted in localized burning of the underlying polymer substrate (see Figure 42). This local degradation of the substrate indicates the electroburning approach for making nano-gaps is ill-suited for flexible substrates.

In a further experiment, the substrate was passivated with CVD grown multilayer (2-3) hexagonal boron-nitride (hBN) film (see Figure 42C), which is a two-dimensional electrical insulator. Unlike oxides and carbides, which are commonly used refractory materials (thermal shields), hBN has optical transparency and flexibility due to its two-dimensional nature. hBN is therefore well suited as a thermal coating in flexible and wearable technologies. hBN layers can be effective heat spreaders[182,183] due to their anisotropic thermal conductivity: very high in-plane ($\sim$ 390 $Wm^{-1}K^{-1}$, which is 280 times that of SiO_2) and low out-of-plane thermal conductivity (0.25 $Wm^{-1}K^{-1}$). Crucially, hBN layers can reduce the formation of local temperature hot spots. An example of hBN passivated nano-gap device is illustrated in Figure 42. A similar wet-transfer approach was used to transfer CVD grown hBN as for graphene.

I found that despite the hBN layers isolating the devices from the underlying polymer substrate, the substrate underwent local degradation (melting), as is shown in Figure 42B. PEN melts at 270^0 C and local temperatures greater than 277 ^{0}C are typically reached at the graphene's constriction during the electroburning process, which was shown in Chapter 3. A likely explanation for the failure of hBN layers to effectively dissipate heat to prevent substrate melting could be twofold: (a) poor quality of the hBN film and (b) few stacking hBN layers. An experiment which could elucidate this, and a subject of future study is the use of the technique in-situ scanning thermometry[184] in probing the temperature gradients produced during the electroburning process.

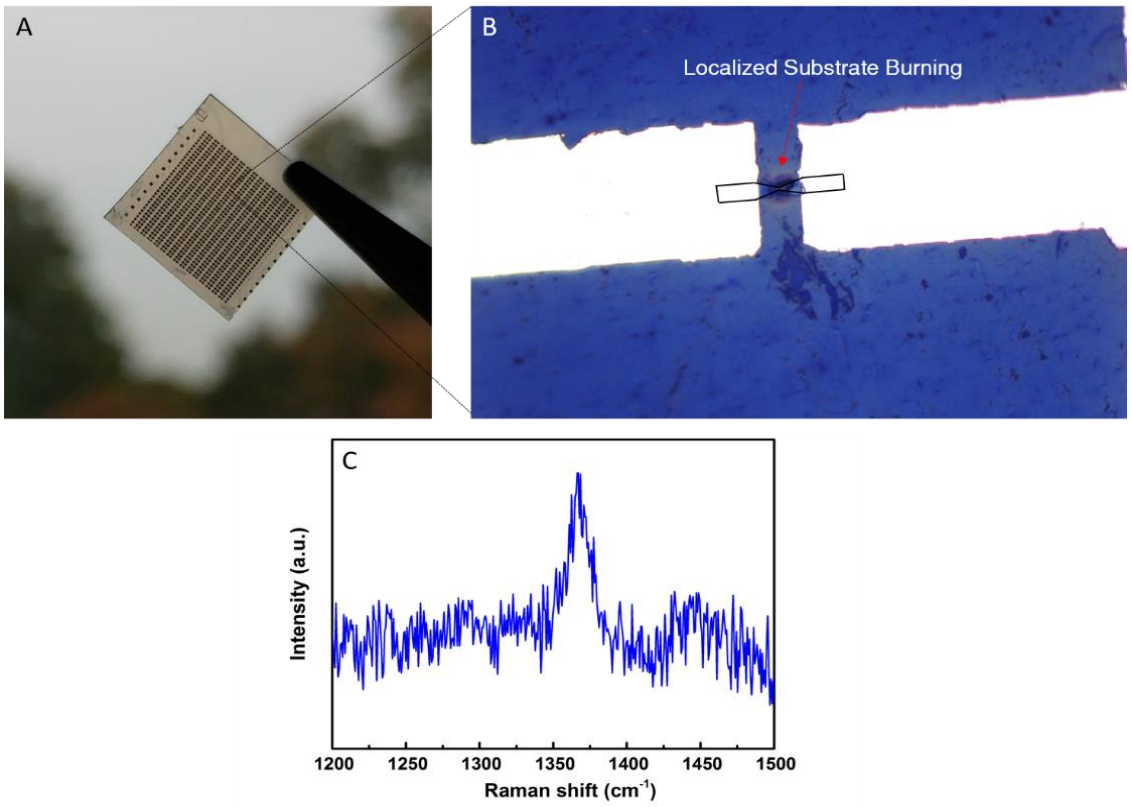

Figure 42. **Flexible graphene nano-gaps**. (A) Graphene nano-gaps electrodes fabricated on a flexible PEN substrate. The devices could be readily fabricated by the schemes described in Chapter 2. (B) Electroburning results in high localized heating (see Figure 18) that degrades the underlying the substrate even in the presence of passivating refractory hBN layers. The graphene ribbon is highlighted in black lines. (C) Raman Spectrum of a CVD grown hBN film. The peak is centered at 1366 cm^{-1} which is indicative of the signature in-plane vibrational mode of multilayer hBN.

4.4 Utilizing Strain in Chalcogenide Glasses

An idea that evolved from these strain experiments was to develop an on-chip platform to reversibly impart strain to two-dimensional materials. Such a platform could enable strain-effect transistors, where strain can regulate the on/off ratio of the transistors either by causing reversible phase transitions in systems such as monolayer $MoTe_2$ or through reversibly tuning the size of the bandgap in other two-dimensional materials (discussed in Chapter 1). The former effect can even result in the development of graphene-based transistors that could facilitate very high bandwidth data computation speed due to graphene's high carrier mobilities. To realize this an approach would be to overlay two-dimensional materials on chalcogenide glasses. Most phase change materials are known to undergo a reversible volume change during the amorphous-

crystalline transition. For example $Ge_{22}Sb_{22}Te_{55}$ thin films contract by ~9 % on crystallization[185]. Such volume changes are understood to occur from cyclic changes in the long-range (crystalline state) and short-range (amorphous) ordering and are considered a nuisance for memory devices, as they add to device's failure (interfacial stress-induced void formation); limiting the endurance limit for data storage[44,48]. However, in the proposed case, such volume changes can be harnessed in the form of strain driver for two-dimensional materials. While a 9 % volume change is sufficient to cause a phase transition in $MoTe_2$, it falls short for other TMDCs[186] and graphene (for example, ~23 % uniaxial or ~16 % shear strain is required to open a bandgap in monolayer graphene). In the exploratory research for materials which can undergo high volume changes, I narrowed down to the composition $GeSe_3$ (a comparison is described in the following section).

In this thesis, I do not show a working strain-effect device (a prototype device design is shown in Appendix 10), due to premature device failures. In these devices, two-dimensional materials were placed on a photo-lithographically patterned patch of phase change material. The phase change material, itself was deposited on a stack that consisted of a NiCr heater. A heater was used to thermally induce a phase change in the phase change material as opposed to what we saw in Chapter 3, where the current was directly sent through the phase change material. This was done to electrically isolate the two-dimensional materials in the scope of preventing crosstalk, as it is the variation in the electrical conductance of the two-dimensional material that is measured as a function of strain induced by the phase change material. In the first set of devices made, the most common cause of device failures was: (a) delamination of PCM due to its poor adhesion with the underlying heater stack, (b) cracking of the heater electrodes due to intense Joule heating and (c) inability to reversibly switch the $GeSe_3$ thin films. Future experiments are planned, where the device stacks are better optimized using thermal modeling, as well as other thin films are explored for better adhesion. In experiments being carried-out currently, a 1 μm thick GST thin film is explored as the strain driver. Regardless, the very large volume change in the $GeSe_3$ films

is rather unusual and I demonstrate optical and photonic devices which utilize such volume changes for light modulation. These are described in the following section.

4.4.1 Non-lossy colour changing thin films

Constructive and destructive interference of light waves is the reason why thin films, such as oil on water and soap bubbles, show colourful patterns. In fact, this optical phenomenon contributes to the colouration in many animals, including many species of butterflies, fish, beetles, and chameleons, and is essential to their behavioral characteristics. Indeed, for its straightforward realization through standard fabrication techniques and robustness against degradation, unlike chemical pigments, thin-film interference has been well-harnessed and drives almost every optics and photonics technology today. Some common examples include anti-reflection coatings such as those on prescription glasses and imaging lenses, optical -filters and -absorbers in photodetectors and solar cells, thermal emitters in radiative heating, coatings for artistic effects and more. Such an interference effect, which is a Fabry–Perot-type, requires dielectric thin films, typically at least a quarter wavelength thick ($h=\lambda/4n$, h is the thin film thickness, λ is the wavelength of light and n is the refractive index), sandwiched between partial or full reflectors that could be some combination of thin metal films and/or other dielectrics[187]. In this framework, the incident light trapped within the thin film (optical cavity) undergoes multi-pass light circulation, such that it accumulates a phase through propagation and interfaces reflections, eventually interfering either constructively or destructively with the wave reflected on the upper boundary to produce colours. However such engineered interference effects are static in nature, meaning they are fixed for a given thin films stack, thus failing to emulate the variable colourations observed in most naturally perceived examples. One approach for achieving dynamic interferences could be the use of phase change materials that undergo either a reversible yet non-volatile change in the refractive index or physical thickness change on phase transition. However existing phase change materials are optically opaque in the visible spectrum and require

secondary effects (such as interfacial) for functioning. Indeed here it is shown how the volume change in $GeSe_3$ thin films assisted by the change in the refractive index can be used for this very purpose. See Appendix 11 for material characterization results.

$GeSe_3$ thin films of varying thicknesses were deposited on a variety of substrates: silicon, platinum, gold, quartz and aluminum foil (see Figure 43) using RF-sputter-deposition. The resulting samples display a range of colours, which I find to be dependent on both the thickness of the $GeSe_3$ thin films and the underlying substrate. More importantly, it can be noted that thermal annealing of the as-deposited thin films on a hot plate under ambient conditions brings forth a significant colour shift. Similar colour changes are notably observed in phase change materials, which are also chalcogenide glasses. In phase change materials, this occurs due to a reversible amorphous-crystalline phase transformation of the thin film. From in-situ reflectometry measurements, (see Figure 43A) of a $GeSe_3$ thin film on a heated stage, the onset for a change (optical reflection) is observed to occur at 257 ^{0}C. The change is gradual and does not seemingly saturate with temperature, unlike in phase change materials, where it is instantaneous and bi-state (see Appendix 12). Figure 43B is a photograph of a few $GeSe_3$ coated p-doped Si wafers, which depending on the thickness of the film exhibit a range of colours. More importantly, thermal annealing of the samples beyond the onset temperature induces a significant change in the sample colours, visible when incident 'white' light is reflected back. The colour variations show the potential for such films for tunable optical and photonics applications (discussed later).

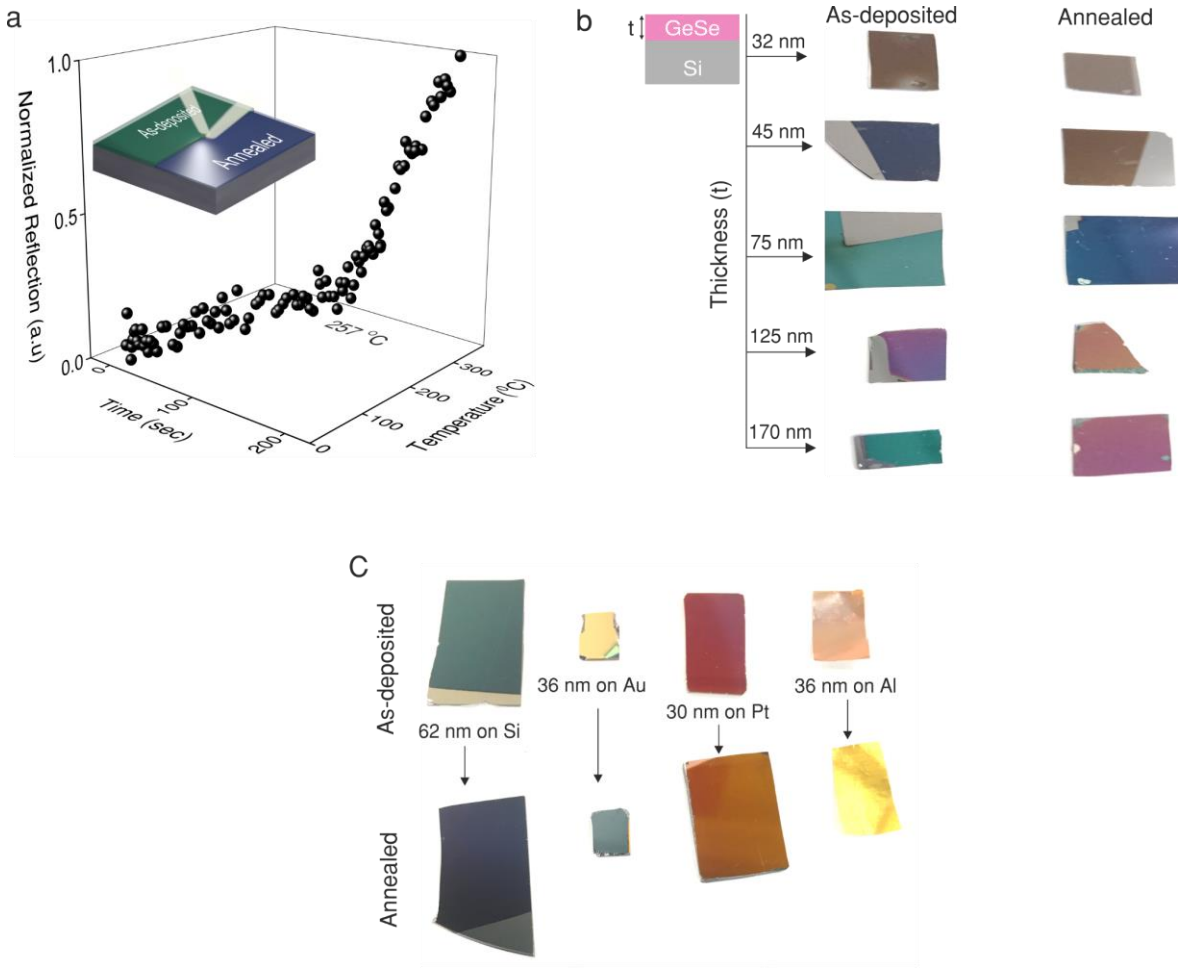

Figure 43. **Lossless colour changing thin films**. (A) Reflection change of a 60 nm $GeSe_3$ thin film on p-doped silicon substrate, as a function of temperature and time. The reflection change is translated as a colour change of the film. (B) Photographs of five different films $GeSe_3$ films of varying thickness on p-doped Si substrate before and after thermal annealing at 370 °C for 6 minutes. (C) Photographs of $GeSe_3$ thin films on different substrates before and after annealing at 350 ^{0}C for 5 minutes in room conditions. Note the substrate-dependent colouring and change in colour from annealing.

Figure 44A and 44B illustrates the reflectivity measurements on some of the sputtered films before and after thermal annealing, respectively. Distinct optical resonances, indicated by the peaks, which redshift proportionally with the film thickness are evident on both figures. However, the resonances get effectively blueshifted by as much as 27 % (also see Appendix 13) from thermal annealing. It is emphasized that the magnitude of these peak shifts are significant (Figure 44C) particularly for an optical cavity that is only a single thin film.

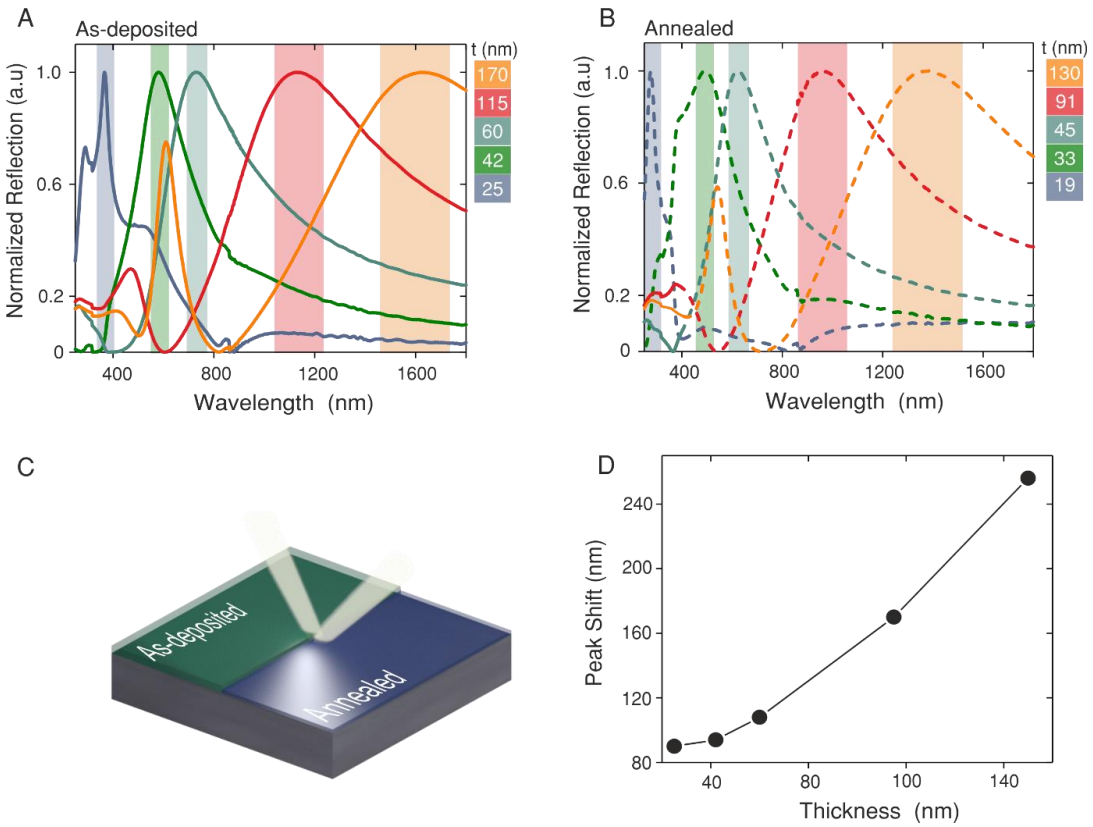

Figure 44. **Optical Resonances in the thin film**. (A and B) The reflection spectra of as-deposited and thermal annealed $GeSe_3$ thin films of varying thickness on a p-doped silicon substrate. The reflection peaks blueshift significantly from thermal treatment. (C) A sketch illustrating the colour change in the thin film that results from the blueshift in a reflection peak. (D) A graph illustrating the magnitude of the peak shifts for in every as-deposited thin films after thermal annealing at 370 ^{0}C for 6 minutes in laboratory conditions. All shifts are non-volatile, meaning they stay last indefinitely after the thermal exposure is removed.

The optical transmission in a $GeSe_3$ thin film on a quartz substrate before and after annealing is highlighted in Figure 45A. Notably, the film is highly transmissive and the transmission is observed to increase from annealing. The finding that the film is absorptive in the ultraviolet (UV) and transmissive in the visible and infra-red has important technological relevance. Figure 45B illustrates the refractive indexes of a $GeSe_3$ thin film in its as-deposited and annealed states. The refractive index ($n = n + ik$) is generally complex-valued with an imaginary part (k) and a real part (n). The real part of the refractive index defines the factor by which the velocity of light in the thin film reduces (can also be thought of as the factor by which the wavelength shortens in the film), while the imaginary part of the refractive index defines the

absorption or losses of light within the film. It is the real part that governs interference in loss less films (like $GeSe_3$). In the visible region of the spectra (400-800 nm), the *n* of the film peaks at 2.94, while *k* at 0.5. The high *n* enables ultra-thin film thickness for resonances, down to $\lambda/12$ while low *k* enables phase accumulation in the film without notable optical losses, thereby yielding high Q factors. Annealing causes a blueshift in the refractive indices (both the *n* and *k* decrease). Furthermore, a correlative change in the physical volume of the material from annealing can also be noted. The thickness of the film shrinks by 22 % (see Figure 45C) from thermal annealing beyond the onset temperature. This is a significant change and it is found that the amount of shrinkage is rather independent of the film thickness (see Figure 46A), which suggests that it is linked to the material and not deposition inconsistencies.

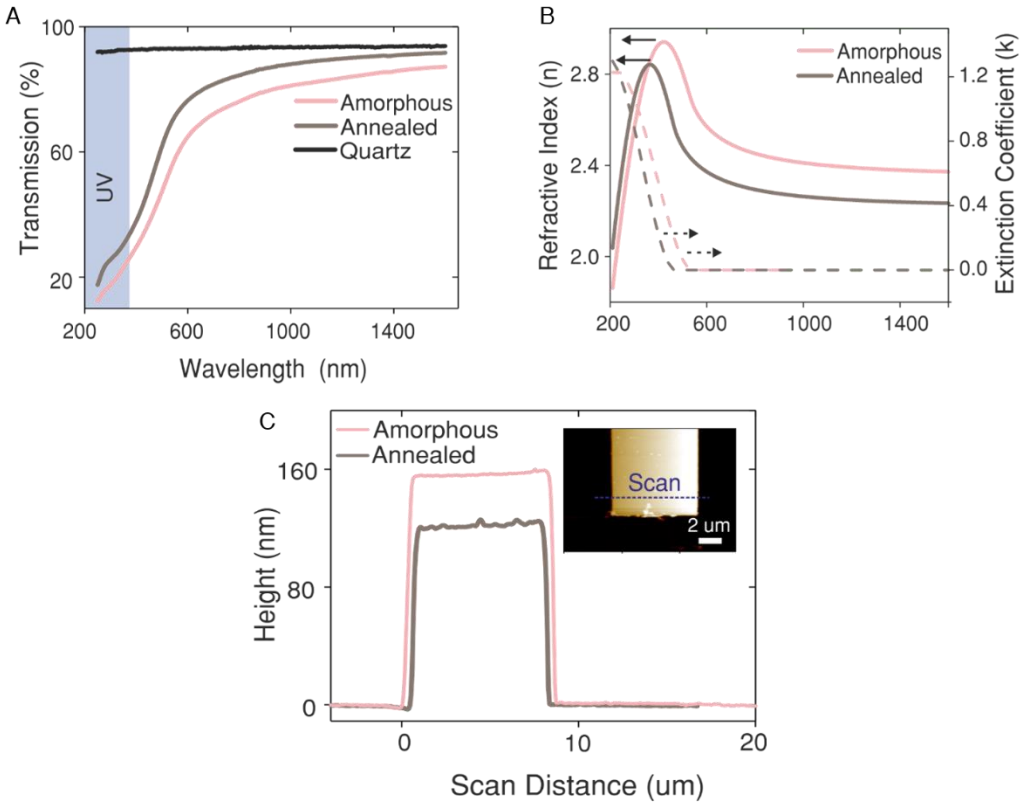

Figure 45. **Optical and Structural Properties**. (A) Optical transmission spectra of a 72 nm $GeSe_3$ thin film on a quartz substrate. Annealing at 370 ^{0}C in ambient conditions drives a non-volatile change, making the film more transmissive across all wavelengths. (B) Complex refractive index profile of a 25 nm $GeSe_3$ thin-film in its as-deposited and annealed states. The refractive indexes blue shift from annealing, resulting in low optical absorption. (C) A typical atomic force micrograph of a $GeSe_3$ thin-film before and after thermal annealing at 370 ^{0}C on a hot-plate, in ambient conditions. The film shrinks by 22 %.

The inset in Figure 46A compares the thickness shrinkage in $GeSe_3$ films against prototypical chalcogenide glasses[94,188]: $Ge_2Sb_2Te_5$,$Ge_{40}Te_{60,}$ and AgInSbTe deposited and annealed under similar conditions: the shrinkage in $GeSe_3$ is significantly higher than in these systems. On contrary, annealing driven changes in the optical properties of the thin films are observed to be thickness dependent (see Figure 46B). Compared against prototypical chalcogenide glasses, the *k* that determines optical absorption is very low in the $GeSe_3$ films (see inset in Figure 46B). Based on these observations, the mechanism determining the high magnitude of the peak shifts (highlighted in Figure 46C) can be explained simply by approximating the samples as Fabry–Perot type cavity[189]. The resonance condition is then a function of film's thickness and refractive index and at first, approximation follows the relation $\lambda = h*4n$. Thermal annealing results in a decrease, in both the film thickness and its refractive index. Concomitantly, the summation of these effects should drive profound blue shifts in the resonance conditions (see Figure 46C), as has been correctly observed in my experiments. To back this argument, I made similar samples with lossy $Ge_2Sb_2Te_5$ (also a chalcogenide glass) thin films and observed the absence of optical resonances, as well as thermal driven shifts in the spectra (see Appendix 14).

However, it can be observed from Figure 44D that a linear relationship between the degree of shift and materials property change for $GeSe_3$ films does not exist, implying that non-linear optical effects likely play a role. Such discrepancy could also be associated with the spurious compounds that form at the interface between the film and the substrate due to interfacial reactions, as observed on the TEM micrographs (see Figure 47B). Regardless, the fact that the films can be tuned significantly in a lossless fashion, can be applied inexpensively due to simple stack design directly for a range of optical and photonic applications[190].

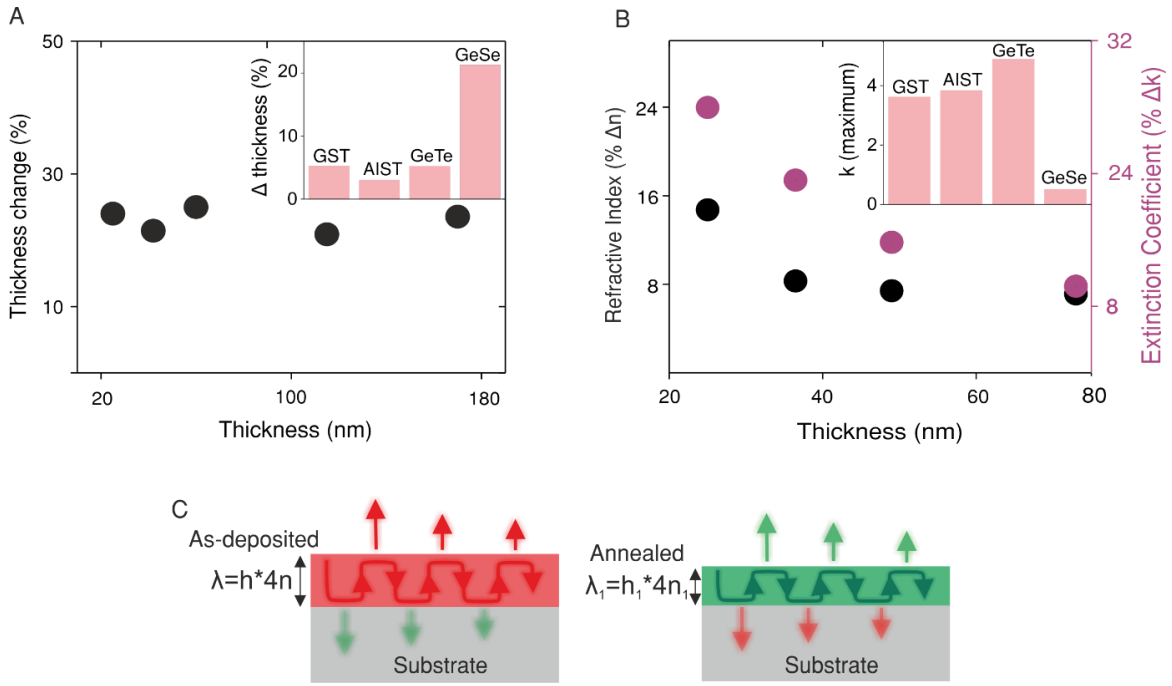

Figure 46. **Thermal annealing-induced changes**. (A) A scatter plot of the percentage shrink of $GeSe_3$ thin-films as a function of its thickness. The inset illustrates and compares the percentage of shrink in prototypical chalcogenide glasses. (B) A scatter plot highlighting the changes in optical properties of the $GeSe_3$ films from annealing, as a function of film thickness. The inset illustrates a comparison of maximum extinction coefficient in prototypical chalcogenide glasses in the visible spectra. (C) A schematic illustrating the incident light from air being reflected from a structure comprising $GeSe_3$ films with thickness h and refractive n. Thermal annealing results in a decrease in both h and n of the film, which concomitantly changes the resonances supported by the film, based on the simple relation $\lambda = h*4n$.

In order to understand the observed changes in the optical and physical properties, I studied the materials behavior at the atomic and molecular scale. I find that unlike phase change materials, the aforementioned changes in the optical and structural properties in the $GeSe_3$ thin films are not from simple amorphous to crystalline phase transition[94]. Indeed, for the temperature the samples are annealed to, no crystallization event is observed on the X-ray diffraction (see Figure 47A) and Raman Spectroscopy studies (see Figure 48), even at the nanoscale (on TEM measurements (see insets of Figure 47)). It is therefore hypothesized that the thin films undergo structural relaxation or reordering at the atomic scale, towards a more stable amorphous phase configuration upon annealing. The phase diagram of the binary Ge-Se system, and accompanying

literature[191] suggests that ideally, the $GeSe_3$ thin films should undergo crystallization at ~300 ^{0}C through phase segregation of the film into $GeSe_2$ and Se grains, while melting should occur at ~742 ^{0}C.

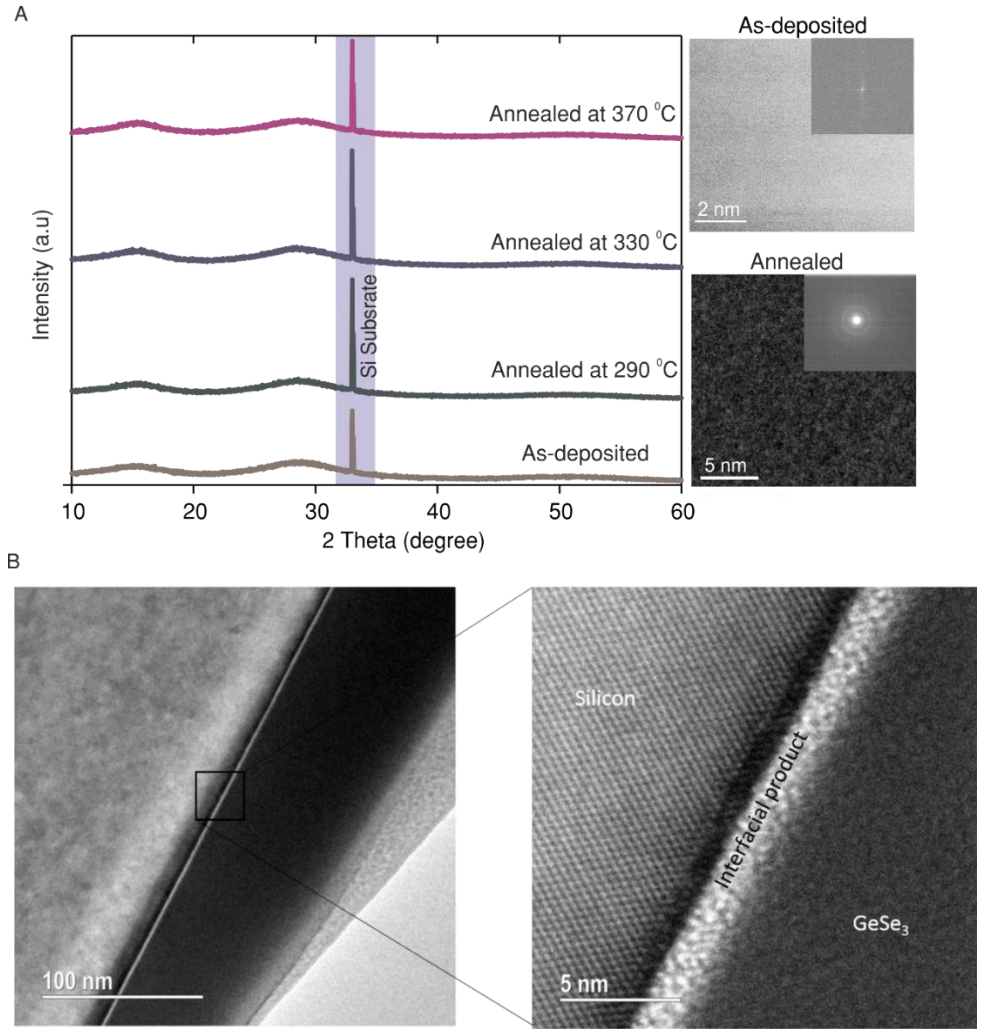

Figure 47. **Structural Changes**. (A) X-ray diffraction scans of a 1 μm thick $GeSe_3$ film on silicon substrates, in as-deposited and after different annealing temperature at 290, 330, and 370 ^{0}C conditions, using Cu Kα radiation. No signature peaks indicating crystallization is evident. Insets are the TEM diffraction patterns of a 160 nm thick film in as-deposited and annealed conditions. Halo diffraction pattern confirms the amorphous nature of the film. (B) TEM micrographs highlighting the interface between the film and the silicon substrate. The $GeSe_3$ film is homogenous.

The fact that the optical properties, which are a function of nearest neighbor stoichiometry, changes from annealing indicate that the atomic rearrangements also involves the formation of new bonds. Indeed, this is substantiated on the Raman spectroscopy measurements. Figure 48 highlights Raman spectra of a thin film (90 nm) recorded at low laser power to negate photo-

annealing. Signature Raman peaks[192,193] of GeSe alloy are evident and represent various vibrational modes of the alloy (see Figure 48A and 48B). Structural blocks of GeSe alloys are understood to be Ge centered tetrahedrons and chains and rings of Se. The 194 cm^{-1} corresponds to ETH vibration modes of the corner sharing $GeSe_{4/2}$ tetrahedrons and the companion peak at 211 cm^{-1} represents the ES breathing vibrations of the edge-shared $Ge_2Se_{8/2}$ bi-tetrahedrons. The peak at 262 cm^{-1} corresponds to the Se–Se bonds, and suggest that predominant configuration of Se in the form of Se-8 rings. The thermal annealing is observed to induce a decrease in the Se–Se peak intensity. This, however, occurs with an increase in the ES peak intensity (also see Figure 48B).

Collectively, these indicate the intrinsic structural changes on annealing includes an increased formation of Ge-Se heteropolar bonds at the expense of homopolar Se-Se bonds[194]. On the contrary, an intense optical exposure is observed to induce segregation effects in such low dimensional films, instead of structural ordering. Figure 48B also illustrates that an intense laser exposure does not favor reconfiguration of Se-Se bonds, instead it gives rise to a new peak at 302 cm^{-1}. This peak corresponds to a vibration mode of strained Ge-Ge bonds[195]. Similar changes, but of smaller magnitudes are also observed in UV illuminated films (see Appendix 15). Optical exposure to pulsed UV laser is found to ablate the thin films (see Appendix 15). The optical and thermal exposure of thicker films (1 μm), however, causes preferential conversion of the heteropolar bonds to homopolar bonds, in line with literature: although there is a discernible hump at 302 cm^{-1}, thicker films are found to be more resilient to segregation effects (see Figure 48C). The contrast in the material's behavior to the optical and thermal response probably arise from beyond thermal effects, such as electronic excitations. The segregation effects are intensified in thinner films, likely due to increased disorder[196] and interfacial stress effects[197] from the substrate.

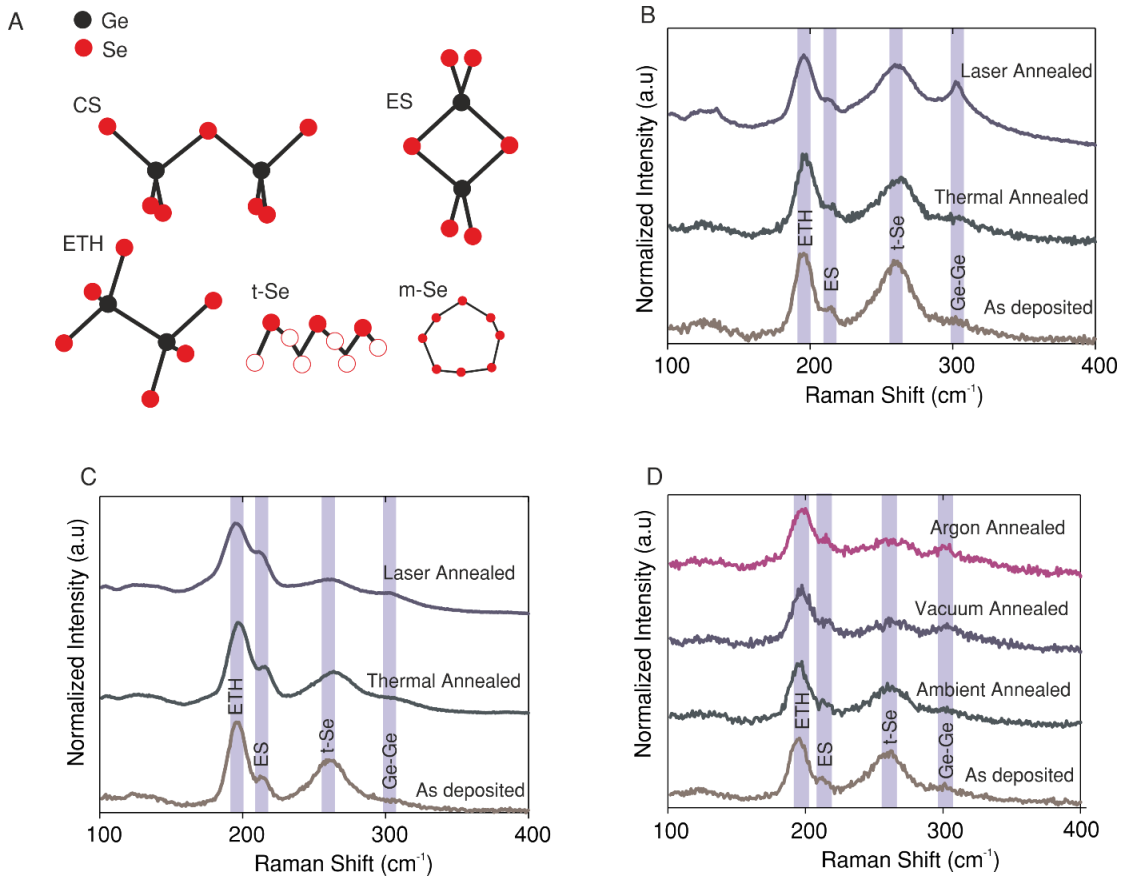

Figure 48. **Atomic Bond Reconfigurations**. (A) A ball-stick model of active Raman modes in GeSe alloy. (B) Raman spectra of a 90 nm thick $GeSe_3$ film in as-deposited, thermal annealed (370 ^{0}C) and laser annealed conditions (12.5 mW/532 nm/Spot Size 1um). (C) Raman spectra of a 1 μm thick $GeSe_3$ thin film before and after thermal and optical exposure. Similar results as in (C) can be noted, however, the film is more resilient to Ge-Ge bonds formation under optical exposure. (D) Raman spectra of a 75 nm thin film annealed to 370 ^{0}C, in room, vacuum, and argon environment. Similar structural changes as observed in (B and C) can be noted.

The effect of the annealing environment on the microstructure of a thin film is illustrated on the Raman spectra in Figure 48D. Similar observations as in Figure 48B stand, however, for samples annealed in the vacuum (10^{-6} torr) and in an argon atmosphere (100 sccm constant flow) the 302 cm^{-1} peak becomes apparent. However, it should be noted that this peak emerges not from thermal annealing, but from the laser exposure during Raman measurements. The samples annealed in vacuum and argon are found to be more susceptible to photo-annealing than the samples annealed in ambient conditions likely due to longer thermal exposure (the thermal time constant of the furnaces are several minutes). From X-ray photoelectron spectroscopy measurements the chemical changes in the thin film can be deduced, which are induced in the

films from thermal treatment. The Ge-3d core-level peak (see Figure 49A) of the as-deposited thin film is centered at 31.1 eV, which is in line with the literature. There is an accompanying shoulder peak at 33.2 eV, which is suggestive of GeO_x. Annealing is observed to induce slight peak shifts, but more notably an increase in the GeO_x intensity, which is indicative of surface oxidation[198]. Figure 49B highlights the changes in the Se-3d peak from annealing. There is a blue shift in the peak, which is suggestive of spin-orbit splitting. No signatures of Se-O oxides are observed on the spectra. Along these lines, the intensity of the Oxygen-1s peak is observed to increase from annealing (see Figure 49C). The fact that the oxygen concentration in the film increases even when annealing in high vacuum and under argon indicates that the surface of the film is likely enriched with oxygen that diffuses from the bulk of the material during thermal treatment, and that oxygen plays a role in the structural changes of the film. The formation of GeO_x and re-ordering of the amorphous lattice to a more stable disordered state from a decreased concentration of Se-Se bonds, perhaps explain the change in the optical properties of the film after annealing. These results are further complemented by a decrease in the GeSe peak intensity of annealed samples on the Raman spectra, suggestive of Ge being oxidized. Based on the results, it can be hypothesized that the $GeSe_3$ films undergo thermal bleaching and oxidation upon annealing, independent of environment (room/vacuum/argon)) that results in the dynamic changes discussed above[199]. The optical exposure of thin films is also found to result in similar changes. Contrary to my observations, photo-darkening effects have been reported in similar alloy systems[200], which were synthesized using other techniques. Alongside, conversion of photo-darkening effects into photo-bleaching has also been reported in GeSe films[201,202]. Therefore, changes the material undergoes likely depend on the starting as-deposited state of the amorphous structure, which varies with the method of deposition.

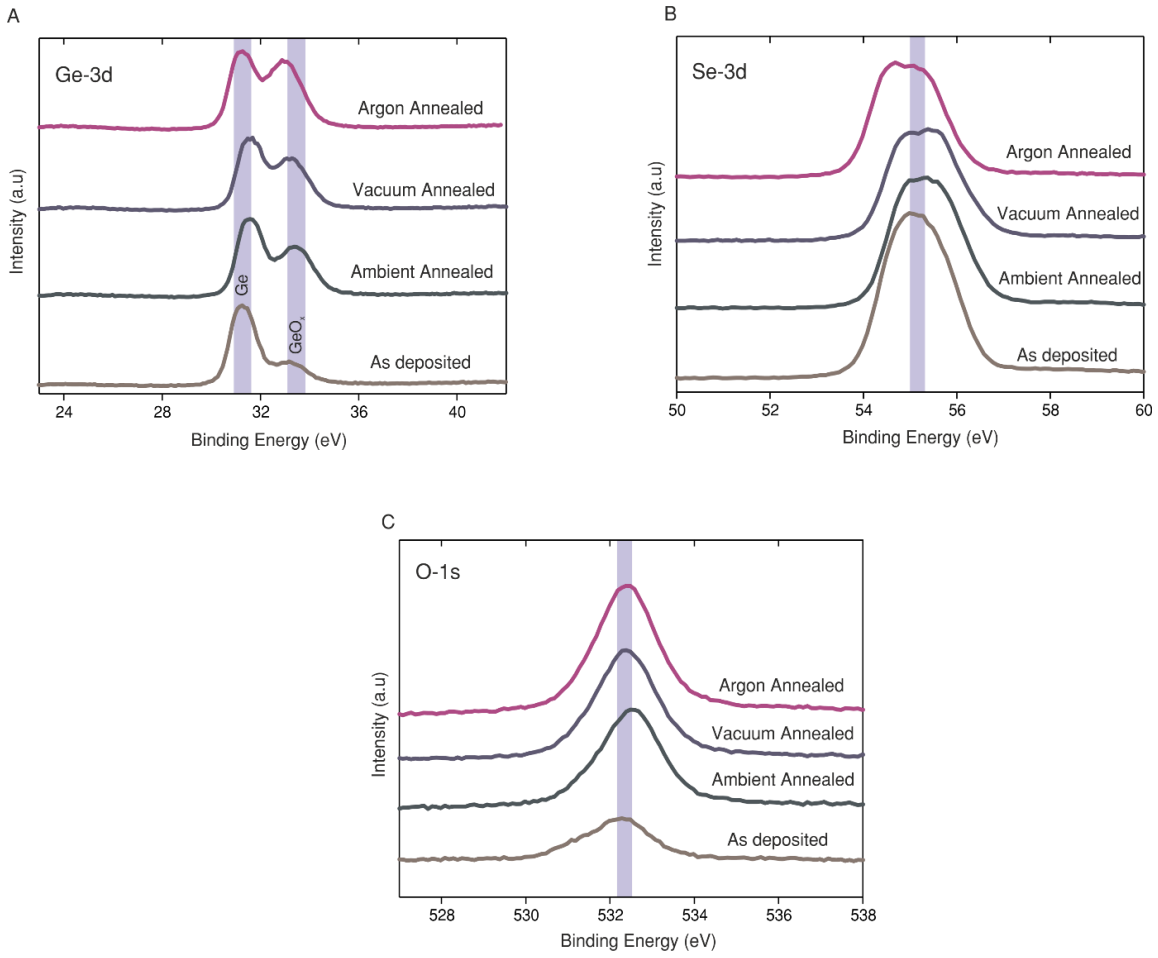

Figure 49. **Chemical changes in thin films**. (F) XPS spectra of the prominent Ge 3d and GeO_x peak in the film, in the as-deposited and annealed conditions. Annealing results to peak shift in 3D peaks and an increase in the intensity of the GeO_X peak; both indicative of a change in Ge oxidation state. (G) Blueshift in the binding energy of Se is also observed, which is indicative of spin orbit splitting. (H) Signature O-1s peak. Increase in its intensity is indicative of surface oxidation of the film.

On the basis of the above observations, it is suggested that the thermal treatment relaxes the amorphous film towards a more entropy driven disordered (equilibrium) state[194,203,204] while also oxidizing it. The bandgap of GeSe is known to increase, while the refractive index decrease with increased Ge concentration. In the amorphous thin films, this essentially translates into more Ge-Se and Ge-O heteropolar bonds at the expense of Ge-Ge and Se-Se bonds. Amorphous chalcogenide glasses are characterized by severe atomic disorder[205], where disorder implies wrong bonds (mainly homopolar), structural defects, and dangling bonds. Concomitantly, these defects result in several localized states at the edge of the conduction band, which minimizes the optical bandgap. Annealing (both thermal and photo) likely provides sufficient activation energy for

breakage of wrong bonds (and formation of heteropolar bonds), as well as induce atomic re-ordering in the short and medium range. These effects result in the annihilation of the localized states, enlarging the optical band-gap and decrease the material volume due to smaller lattice constants of the heteropolar bonds (Ge-Se and Ge-O) over homopolar bonds (Ge-Ge and Se-Se chains). The shrinkage in film thickness is also a consequence of the free-volume reduction. Indeed, on the Raman spectra a drastic decrease in the Se-Se density from annealing, while an increase in the Ge-Se bonds[206,207] is observed.. While volume changes in S based glasses are well studied, changes in Se glasses are scarce. Some literature associates the densification to void annihilation that originates from porous deposition[199]. However, the fact that similar volume contraction is observed in sputtered thin films (in the current study) suggest that the material change is intrinsic and likely associated with both bond re-ordering and mass transport. Indeed, thin films of other chalcogenide glasses of similar thickness deposited under exact conditions do not undergo similar volume change on annealing (see inset in Figure 46A). Furthermore, on multiple TEM cross-sections, I found good homogeneity and uniformity in the films under both as-deposited and annealed states (see inset of Figure 47B).

I now demonstrate three tuneable applications, which make use of the coupled opto and physical changes in the lossless $GeSe_3$ thin films. First is a demonstration of a tunable optical coating. Figure 50A illustrates the blue shift in the peak position of a thin film on p-doped Si substrate from annealing on a hotplate. It is observed that in contrast to phase change materials, which are bi-state, there exists a considerable dynamic range for tuning the peak position in $GeSe_3$ films. Essentially, this dictates modulation in the reflected colour, by simply heating the film to different temperatures (the inset in Figure 50A highlights the 126 nm blue shift in the reflection spectra of a 60 nm thick $GeSe_3$ thin film on Si substrate). Each shift is non-volatile and is found to be stable for over 5 months. This tunability can be used for artistic effects and temperature sensors for example, where colours are modulated on thermal treatment[187]. Figure 50B and 50C

demonstrate the device level integration of $GeSe_3$ films. In the first example, the local structural modification in the $GeSe_3$ films is done using laser scanning. Optical absorption in $GeSe_3$ films becomes notable for wavelengths < 540 nm: therefore an optical exposure at these wavelengths induces photo-thermal annealing, causing a localized colour change of the film. The second device is a solid-state colour pixel, highlighting the colour change between the amorphous and annealed states of $GeSe_3$ films done electronically using a micro-heater[72]. The device, which has a resistance 850 Ω is a stack comprising 100 nm NiCr (heater)/200 nm SiN_x/20 nm SiO_2/100 nm Ag/45 nm $GeSe_3$. Herein, Joule heating is induced from microsecond current pulses which anneal the films. For application where transparency is crucial such as filters, graphene can be used as the microheater. Another direct application of $GeSe_3$ films could be in optical filters, in particular towards filtering high energy electromagnetic radiation. Figure 50D illustrates photographs of sub-100 nm $GeSe_3$ films on a quartz substrate, under both as-deposited and annealed states. Figure 50D (i) highlights good transparency in the films, which increases significantly in the annealed (370 ^{0}C) samples. The degree of transparency can again be accumulated as a function of temperature, with Figure 50D (ii) illustrating relatively reduced transparency when the film is annealed to a lesser temperature (330 ^{0}C).

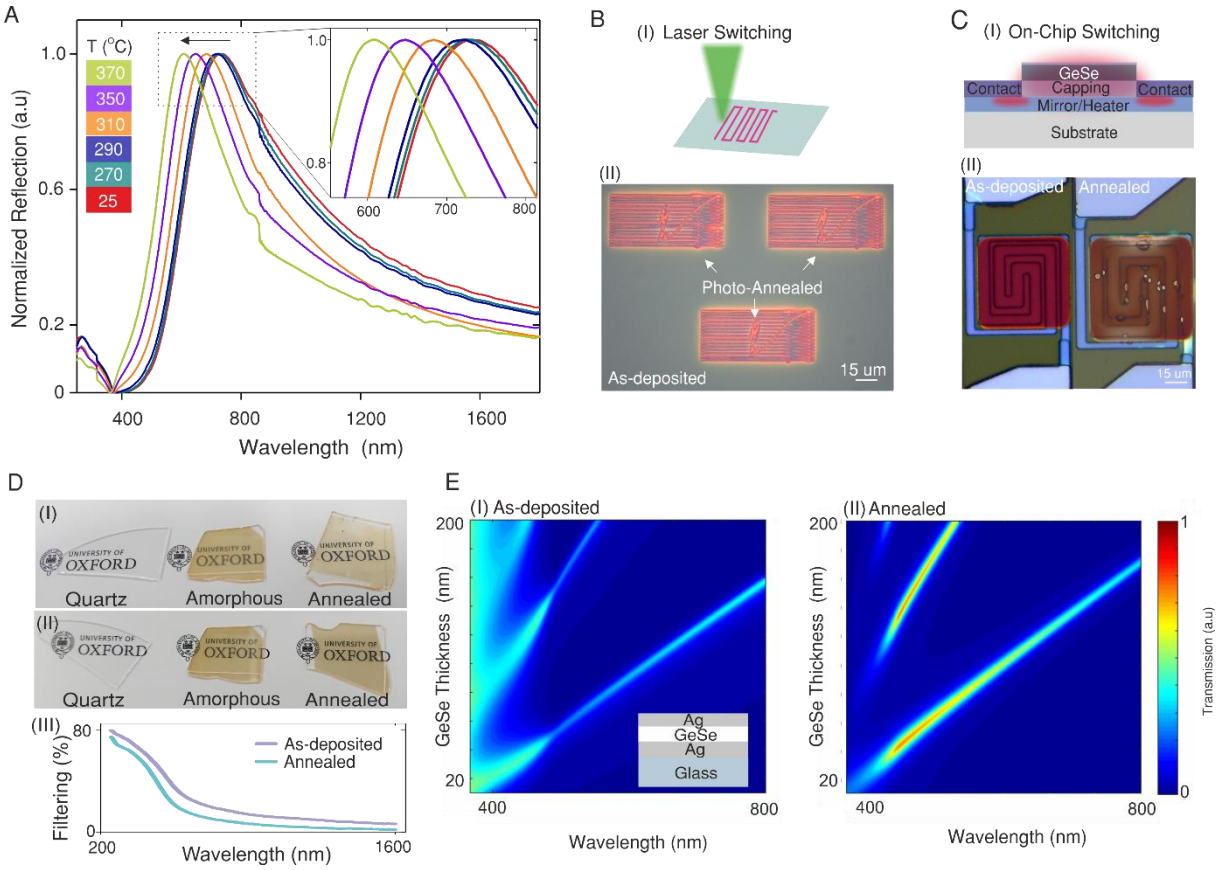

Figure 50. **Optical Devices utilizing $GeSe_3$ thin films.** (A) Peaks shifts are achieved in a 60 nm thin film in a non-volatile manner with select annealing temperature. (B) Laser Patterning of a 170 nm thick $GeSe_3$ thin film. The pattern is written using an 8 kW/cm^2 532 nm laser. (C) Optical micrographs of solid-state reflective display pixels. A colour contrast before and after passing 2.5 V, 100 µs square pulses to the device can be noted. (D) Photographs of transmissive filters utilizing 72 nm thick $GeSe_3$ coating on quartz substrates in as-deposited and annealed states in laboratory conditions. Transmission increases in annealed samples. (E) Simulated reflectivity spectra of planar thin-film Ag (30 nm)/$GeSe_3$/Ag (30 nm) cavity with near-perfect transmission. The illumination source is normal incident to the planar surface with arbitrary polarization.

UV radiation, in particular, type UV B and UV C can be hazardous to not only biological systems, such as tissues but also to many electronic and optical components, namely photodetectors, organic solar cells and lenses[208–210]. Figure 50D (iii) illustrates the wavelength dependent filtration of electromagnetic radiation. Wherein UV can be blocked as much as by 80 %, while visible and infra-red can be appreciably transmitted. Another interesting prospect is to utilize the broadband transparency of $GeSe_3$ thin films in spectrally selective optical (color and absorber) filters[211]. Figure 50E(I) and (II)) are simulated spectra of Fabry-Perot-type resonant cavity comprising a thin metallic layer coupled through the $GeSe_3$ spacer and the bottom metallic layer.

The transmission of the stack is plotted as a function of wavelength and spacer thickness in Figure 50E. The thickness dependent sharp optical resonances approach near unity transmission owing to the loss less characteristic of the film. Moreover, the resonances can be shifted through tuning the state of the film by annealing (see Figure 50E (II)).

The very low optical absorption in the infrared spectra, yet tunability in the real part of the refractive index can be further exploited for a wide range of photonic devices including optical switches, photonic memories, and all-optical computers[190,212–214]. Chalcogenide glasses currently used for these applications induce high optical losses due to their intrinsic absorptive optical property[214] and photonic materials that can effectively modulate light for the above applications over broadband are elusive. Figure 51A illustrates a photonic racetrack resonator made on a SiN_x wafer (330 nm Si_3N_4 on 3 μm SiO_2). By placing a strip of $GeSe_3$ thin film on the resonator and annealing it step-wise, the resonance frequency of the resonator can be efficiently tuned. Figure 51B and 51C illustrates the peaks shift that can be achieved in the resonance frequency as much as 6 nm without compromising the Q factor, and in a non-volatile manner. The shifts are resultant of the change in the effective refractive index of the propagation modes that are confined in the resonator. Crucially, these demonstration exemplifies the use of loss less $GeSe_3$ films for corrective optics, where post-fabrication modifications through $GeSe_3$ thin films deposition and thermal treatment can tune the photonic component.

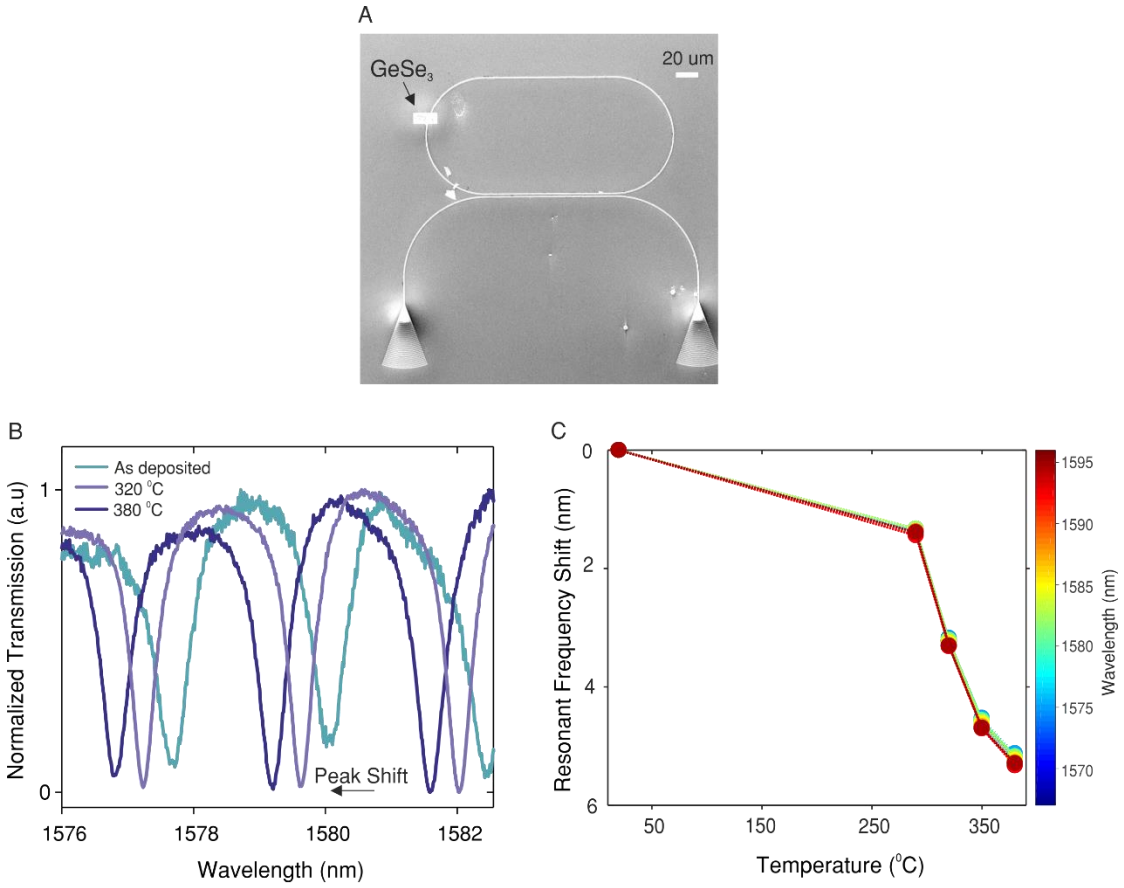

Figure 51. **Photonic Devices utilizing $GeSe_3$ thin films.** (F) Scanning electron micrograph of a photonic race track resonator. A strip of 150 nm thick thin film of $GeSe_3$ is highlighted. The resonant frequency of the resonator can be tuned step-wise by thermal annealing the thin film (shown in Figure B and C) without affecting the Q-factor. This occurs due to changes in the effective refractive index of the waveguide. Such a device concept can be used for corrective-optics, where a desired resonant frequency can be attained by suitable thermal treatment.

Several reports have highlighted reversible crystallization of GeSe alloys, across wide composition range[191,215–219]. The structural changes driven properties modulation discussed in this chapter can, therefore, augment the otherwise conventional phase change characteristic of this chalcogenide glass. This can potentially usher a wide array of applications, due to the broadband lossless characteristic of the $GeSe_3$ thin films; including solid-state displays[220], smart windows[190,220], transmissive optical filters[185], multi-level optical data storage, and tuneable holograms[221].

4.5 Summary

In this chapter, I have demonstrated the use of Kelvin probe microscopy in capturing the influence of uniaxial tensile strain on the band-structures of graphene and WS_2 (mono and multilayered) based heterostructures at high resolution. This technique enabled a single-shot capture of strain defined changes in a heterogeneous system at the nanoscale, overcoming the limitations (materials, resolution, and substrate effects) of existing techniques such as optical spectroscopy. Crucially, strain enhanced charge transfer with the substrate plays is found to play a dominant role, causing the heterostructures to behave differently from two-dimensional materials in their isolated forms. The nature of the interfacial heterojunctions in the heterostructure is also extracted and found to get strongly modulated from applied mechanical strains. Following these experiments, fabrication of graphene nano-gaps on flexible substrates is discussed. The approach of underlying insulting hBN layers as thermal layers is discussed to prevent local degradation of the substrate. A new device concept termed strain-effect transistor is presented that uses the strain effects explored earlier in two-dimensional material. Herein, two-dimensional materials overlaid on phase change materials can undergo cyclic straining from the volume change during amorphous-crystalline phase transitions. A new phase change material ($GeSe_3$) with very large volume changes is explored for this purpose. Although a working strain-effect transistor device is not demonstrated in this thesis, due to premature device failures, future experiments are proposed. Furthermore, using $GeSe_3$ films a new optoelectronic framework for smart devices (for example solid-state displays) is presented.

4.6 Contribution Statement and Peek into Chapter 5

All steps of device fabrication and characterization were carried-out by the author. Members of the Nanostructured Materials group assisted with graphene and WS_2 synthesis and transfer. hBN was synthesized by Renjie Chen from the Nanostructured Materials group. XRD and XPS were carried-out by Dr Philip Holdway from Oxford Materials Characterization Services. Data

were interpreted by the author. Dr Zengguang Cheng assisted with the on-chip photonics experiment.

The next chapter studies the light-matter interaction in prototypical phase change materials, such as GeSbTe and GeTe alloys, as well as in $GeSe_3$ thin films. There is a lack of such experiments at the nanoscale. With the nanoscale device concepts discussed in the previous chapters, the next chapter details the mechanisms of the phase change material's response to optical exposure and illustrates concepts of new optoelectronic platforms such as tuneable photodetectors.

CHAPTER 5: Light Matter Interaction in Phase Change Materials

(A part of this chapter has been published: Syed Ghazi Sarwat, Nathan Youngblood, Yat-Yin Au, Jan A. Mol, C David Wright, and Harish Bhaskaran. 2018, ACS Applied Materials and Interfaces)

Light Matter Interaction in Phase Change Materials

5.1 Motivation for the Study

Optical or image sensors are at the heart of a wide range of applications, ranging from medical instrumentation to consumer electronics. Commercially available optical sensors that operate at room temperature in the visible to the near-infrared spectral range are typically based on semiconductor materials such as silicon (Si) or indium gallium arsenide (InGaAs). Such sensors offer high photo-sensitivity but are expensive to manufacture, have a limited dynamic range and are not easily scaled down in size. As such, for a given incident optical power the photo-response is largely determined by material specific properties that govern photocarrier generation and drift such as optical absorption and charge carrier mobility. These properties are fixed. The dynamic range, i.e. the useful range of optical power over which the device can operate, is also limited by material specific properties, meaning that typical optical devices saturate at fixed and relatively low light levels. By contrast, the human eye has a wide dynamic range because it can adapt to varying levels of light intensity via the contractual structure around the pupil. Alternative optoelectronic devices and methods of photodetection are therefore desirable, preferably with increased adaptability to light levels. In this chapter, I explore the candidacy of phase change materials using nano-gaps and crossbar devices, for light detection applications. In the first part of this chapter, I underlie the light-matter interaction mechanisms in phase change materials, which in the second part I use for the development of spiking detectors, such as artificial retinas.

5.2 Light-matter interaction in phase change materials

In recent years, prototypical phase change materials such as GeSbTe and GeTe alloys have gathered interest for beyond data storage technologies, mostly directed towards photonic platforms. These include phase change displays[220,222], holograms[221], smart windows[190,220], photonic memories[67], neuromorphic computing[223], metadevices[190,224] and more. Many of these applications depend on the so-called “mixed-mode” or optoelectronic operation of PCMs, relying on the

change in their electrical resistivity to modulate their optical properties or vice versa[225–227]. Crucially, however, the understanding of light-matter interaction in these materials, which is the crux for the aforementioned applications, is limited.

PCMs are low-bandgap semiconductors and their amorphous state, in particular, is disordered[228,229] with high trap densities that favor short lifetime of free carriers[17]. Photothermal (bolometric) effects that aid crystallization through light-induced heating are therefore considered to dominate photoexcitation effects (photoconductivity) in prototypical PCMs, such as $Ge_2Sb_2Te_5$ (GST)[1,230,231]. This is rather unusual, given that other chalcogenide systems such as Cd-Te and amorphous selenium have been leading candidates for solar cells[232] and image sensors[233], where photoexcitation effects dominate. In this chapter, using nanoscale devices, the observation of strong photoconductive behavior in PCM-based devices (under both continuous and pulsed illumination conditions) is reported that is tuneable in magnitude by tuning the solid-phase of the PCM. Furthermore, it is found that the contribution of the photoconductive and photothermal effects to the overall photoresponse can be tuned, leading to potential new PCM based applications, for example in self-powered PCM based photonic devices, particularly photodetectors, displays and smart windows. Because such devices are expected to undergo continual optical exposure, the susceptibility of PCMs to light-induced material degradation (photo-induced oxidation for example)[234,235] that can be detrimental to the device performance is also studied in this chapter. Non-linear optical-characteristics[236,237] (non-linear dependency of photocurrent to incident luminescence) are observed to be an intrinsic property of both the amorphous and crystalline states of PCMs, and tuneable photodetection –bandwidth and –responsivity capability is found through amorphous-crystalline phase transformation. The following results discussed in this chapter further our understanding of the photophysics of PCMs and offer exciting opportunities to develop more potential technologies based around these remarkable materials.

5.2.1 Device Fabrication

The devices (see Figure 52 A and B) used in this chapter are optical cavities consisting of sputter-deposited thin films of ITO (indium tin oxide, 80nm)/ GST (21 nm)/ ITO (40nm)/ Pt (50nm) that make-up a cross-bar geometry (see Figure 52 A). The fabrication process for such devices is sketched in Figure 52. Briefly, the process is as follows: (i) a four-inch silicon wafer with 300 nm thermally grown SiO_2 passivating layer was diced into 1 cm by 1 cm chips. (ii) Using photolithography (S1813 positive resist) top ITO electrodes were patterned on the wafer, which were subsequently used as a mask for reactive ion etching (CHF_3+Ar+O_2) to selectively etch SiO_2 into trenches (the black feature in Figure 52). (iii) Using a sputtering tool Ta (10nm)/Pt(50nm)/ITO(40nm) deposition was carried-out to fill the trenches. Ta is used as an adhesive layer, Pt as the mirror, and ITO is the bottom electrode and (iv) another photolithography step (S1813 positive resist) is performed to pattern the top electrode, such that only the finger electrodes overlap with the bottom electrode, after which deposition of PCM (GST/GT) and ITO stack using the same sputtering under similar conditions is carried-out. ITO serves as electrodes across which the voltage is applied, while GST acts as the active photosensitive layer. ITO is chosen as the electrode material for its transparency and technological relevance in PCM based displays and smart windows. Although graphene can also be used, its incorporation jeopardizes the phase change material quality due to potential surface-oxidation of the phase change material from wet-transfer. A scanning electron micrograph of a typical device is illustrated in Figure 53B, where the photo-active region is the cross-section where the two electrodes overlay. The stack is designed (see Figure 52 C) for broadband absorption using transfer matrix calculations[222], peaking at 98.96 % absorption for the amorphous and 93.46 % for the crystalline state of GST at 637 nm. The transfer matrix is analogous to a scattering matrix that relates the initial state and the final state of a physical system (electric fields) undergoing a scattering process. The transfer matrix takes the following expressions

$$\begin{bmatrix} E_0^+ \\ E_0^- \end{bmatrix} = S \begin{bmatrix} E_{m+1}^+ \\ E_{m-1}^- \end{bmatrix}$$

Where E_0^+ is the forward propagating and E_0^- is the backward propagating wave and the subscript m is the layers between a semi-infinite transparent ambient and a semi-infinite substrate

$$S = \begin{bmatrix} S_{11} & S_{12} \\ S_{21} & S_{22} \end{bmatrix} = \prod_{v=1}^{m} I_{(v-1)v} L_v * I_{m(m+1)}$$

Where,

$$I_{jk} = 1/t_{jk} \begin{bmatrix} 1 & r_{jk} \\ r_{jk} & 1 \end{bmatrix}$$

I_{jk} is the interface matrix between j and k layers of the multi-layered stack and t_{jk} and r_{jk} are the Fresnel transmission and reflection coefficients, respectively

$$L_{jk} = \begin{bmatrix} e^{-id_j\xi_j} & 0 \\ 0 & e^{-id_j\xi_j} \end{bmatrix}$$

$$\xi_j = (2\pi / \lambda) * [n_j^2 - n_0^2 \sin(\Phi_0]^{1/2}$$

L_{jk} is the layer matrix phase matrix describing the propagation (phase accumulation) through layer j of thickness d and complex refractive index n and Φ_0 is the angle of incidence.

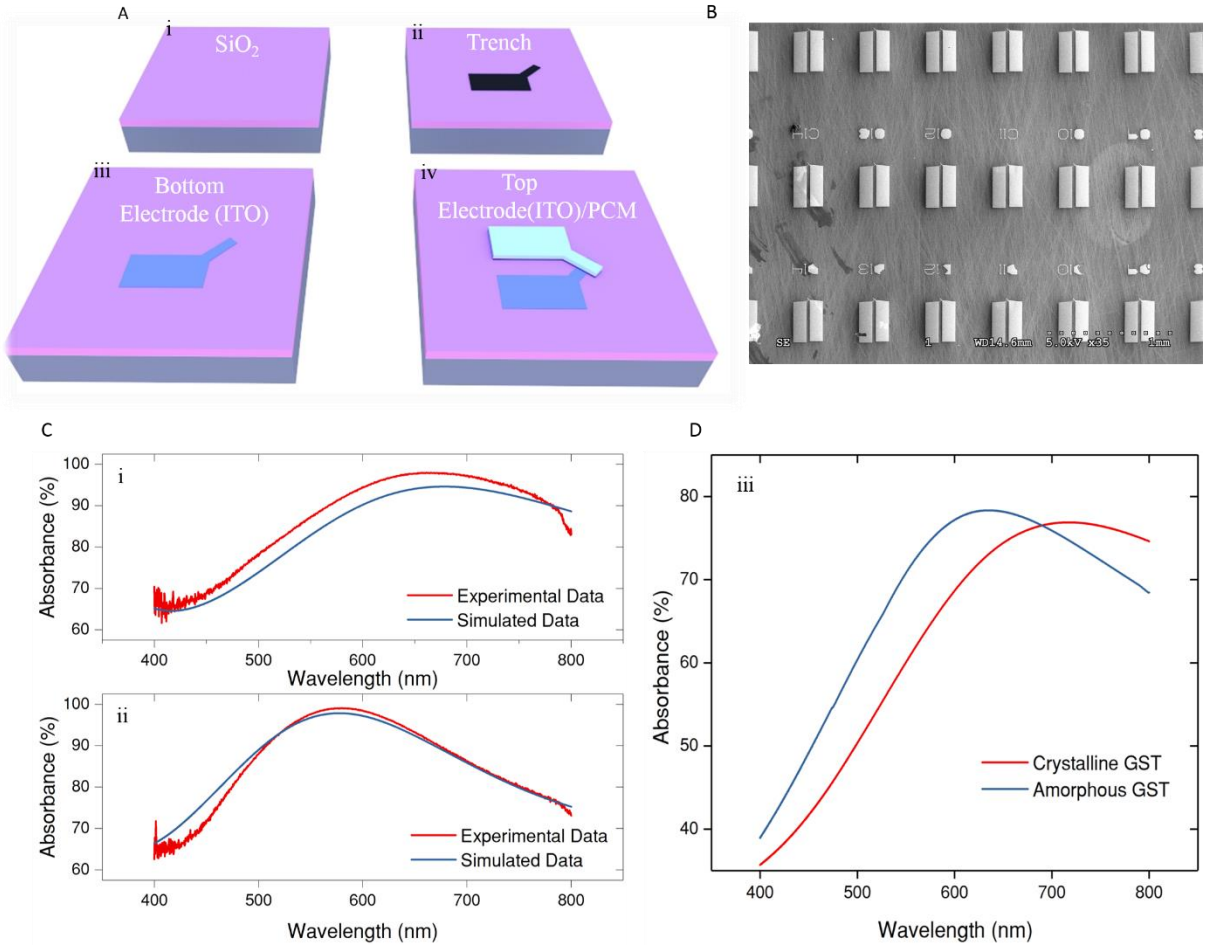

Figure 52. **Fabrication of Crossbar devices**. (A) A cartoon illustrating the device fabrication process. (B) A scanning electron micrograph of one of the chips. A 1 cm by 1 cm carries 155 crossbar devices. (C) (i and ii) Experimental (using reflectance measurements on a customized set-up, with assumption that transmission is zero) and simulated measurements (using transfer matrix calculations) for the stack (Ta/Pt(50nm)/ITO (40nm)/GST(21nm)/ITO (80nm)) in the crystalline (i) and amorphous (ii) state of GST. The stack shows high absorption in the visible region of the spectra in both the states of GST and (iii) from fitting using transfer matrix calculations the percentage absorption only in the GST layer is computed. The amorphous state absorbs more than crystalline state up to ~700 nm beyond which the crystalline state becomes more absorptive.

Wavelength-selective and sub-micron devices can also be made through optimization of thin-film thicknesses (particularly the bottom ITO) and the fabrication processes. Typical current-voltage (I-V) characteristics of a device after optical exposure are illustrated in Figure 53C. The device shows threshold switching which is indicative of an amorphous to crystalline phase transformation in GST. The device is switched from the amorphous to crystalline state at sub-3

V and at significantly higher currents (mA), likely due to diminished Joule heating from increased thermal losses and partial crystallization of the amorphous phase from photo-induced heating.

Under illumination conditions, a significant photoresponse in devices with all three states of GST is observed i.e. in the (i) amorphous, (ii) electrically-switched and (iii) thermally crystallized states. This is illustrated in Figure 53 for a 20 × 20 μm device. For amorphous GST (see Figure 53D, black trace), the device exhibits low dark-current (~ 10^{-8}-10^{-7} A) due to trap-limited charge transport[228,238]. On illumination, two orders of magnitude increase in current are observed, along with a significant zero-bias photocurrent (red trace), which is indicative of a photovoltaic effect. Photoresponse I-V characteristics (with forward and reverse sweeps) reveal no signature of hysteresis, which is suggestive of the absence of any crystallization event and/or long-term trapping of the photo-excited carriers. The GST is then partially crystallized electrically by ramping-up the voltage above the threshold voltage. This state is referred to as the electrically-switched crystalline. The dark current of the device (see Figure 53E, black trace) in this state of GST is significantly enhanced as would be expected due to the ordering of the lattice and annihilation of the trap states within the volume of the crystalline filament. On illumination, a substantial rise in current (red trace) is observed, with a persistent zero-bias current of nearly similar magnitude as observed in devices with amorphous GST. The device is further heated on a hot-plate to 235 ^{0}C for 10 minutes, which is above the crystallization temperature[222] (150 ^{0}C) of GST in order to completely crystallize the layer; this state is referred as thermally-annealed crystalline GST. The dark current (Figure 53F, black trace) of the device further increases due to increased crystalline volume fraction in the GST layer. On illumination, the device still exhibits photocurrent under zero-bias biasing conditions (red trace).

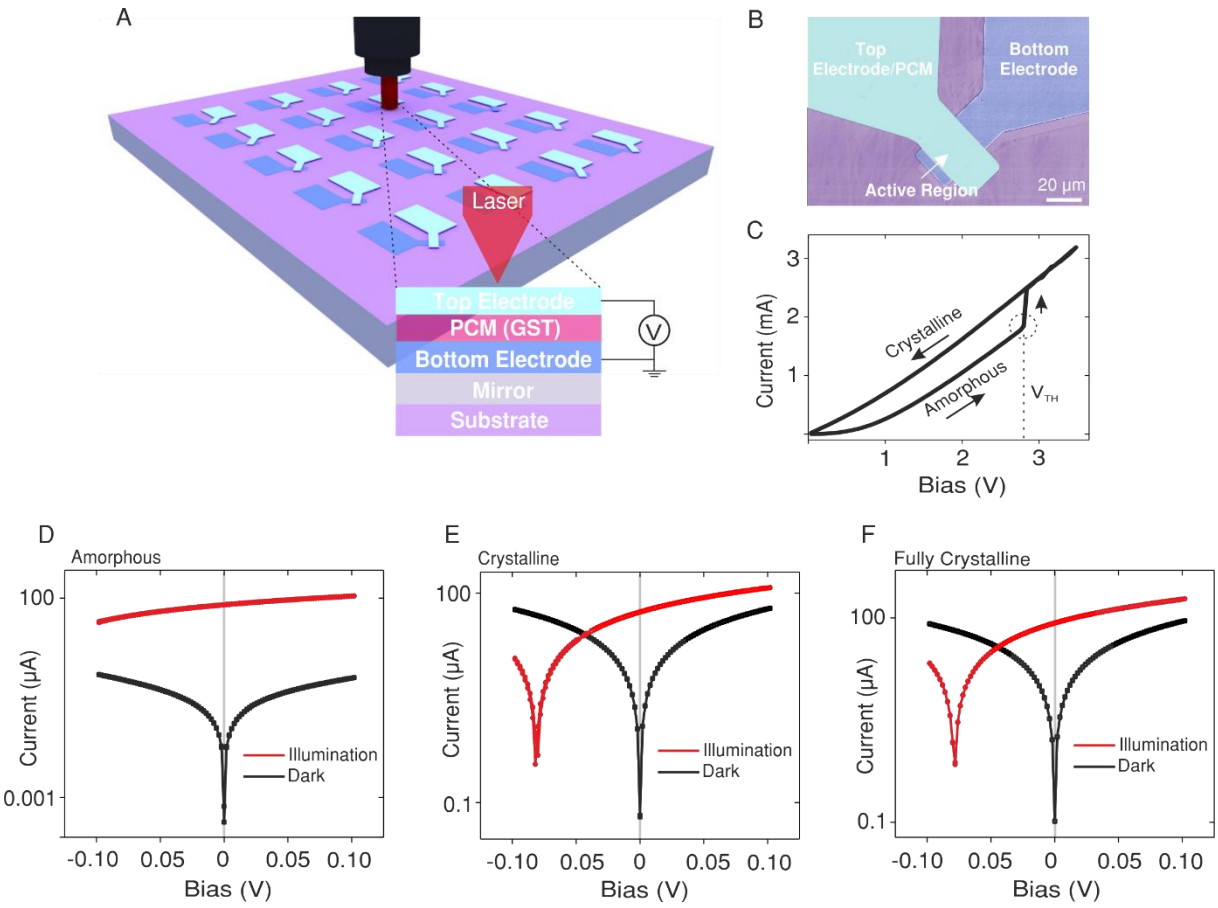

Figure 53**. A crossbar device**. (A) A schematic illustration of the device and the measurement setup. (B) A false-colored scanning electron micrograph of a crossbar device. (C) Typical current-voltage characteristics. (D) Current-voltage of the device in the amorphous state of GST under dark and illumination conditions. The device shows significant photo-response (red trace) with the signature of pronounced zero-bias current. (E) Current-voltage of the same device in its crystalline state (induced electrically) of GST. (F) Current-voltage of the same device in the fully crystalline (induced thermally) state of GST under dark and illumination conditions. Plots are in the semi-log scale and illumination conditions were 637nm/3158 Wcm^{-2}.

The X-intercepts of the above I-V characteristics, under illumination conditions are the open-circuit voltages of the devices. For devices with amorphous GST, the open circuit voltage scales to 160 mV (deduced from extrapolation of Figure 53D), while for the crystalline GST based devices, the open circuit is halved to 80 mV. This is in line with the bandgaps of GST (amorphous state has a higher bandgap than the crystalline state). Figure 54 illustrates the scaling behavior of the photoresponse as a function of the device cross-sectional area. The photoresponse increases with a power law dependence on the device area (fitting factor > 0.50). The fact that the photocurrent does not scale linearly with the device area as should be expected to is likely due to

experimental inconsistencies. The focal point of the laser is manually adjusted for every measurement and the devices undergo mechanical drift due to residual stresses in the duct tapes that were used to hold the printed circuit board, as well as from the electrical probes that are pressed on the contact pads. Either can result in varying illumination conditions. Future experiments with wire bonded devices and using solar stimulators for broadband illumination source (for example, by utilizing xenon arc and tungsten halogen lamps as a light source) are planned.

Regardless, the solar irradiance can be captured through standard and simulated spectrums. The AM1.5 global spectrum is the most commonly used standard and has an integrated power of 1000 W/m^2 (100 mW/cm^2). If an approximation is made for AM1.5 solar radiation to instead be fully composed of the 637 nm light, the devices I show in this chapter will produce a peak short-circuit current density of ~ 17 mA/cm^2. This figure is on par with commercial silicon solar cells and is significant for a notionally symmetric device. Obviously, such narrow-band devices do not tell the whole story and require unambiguous measurements over broad-band illumination.

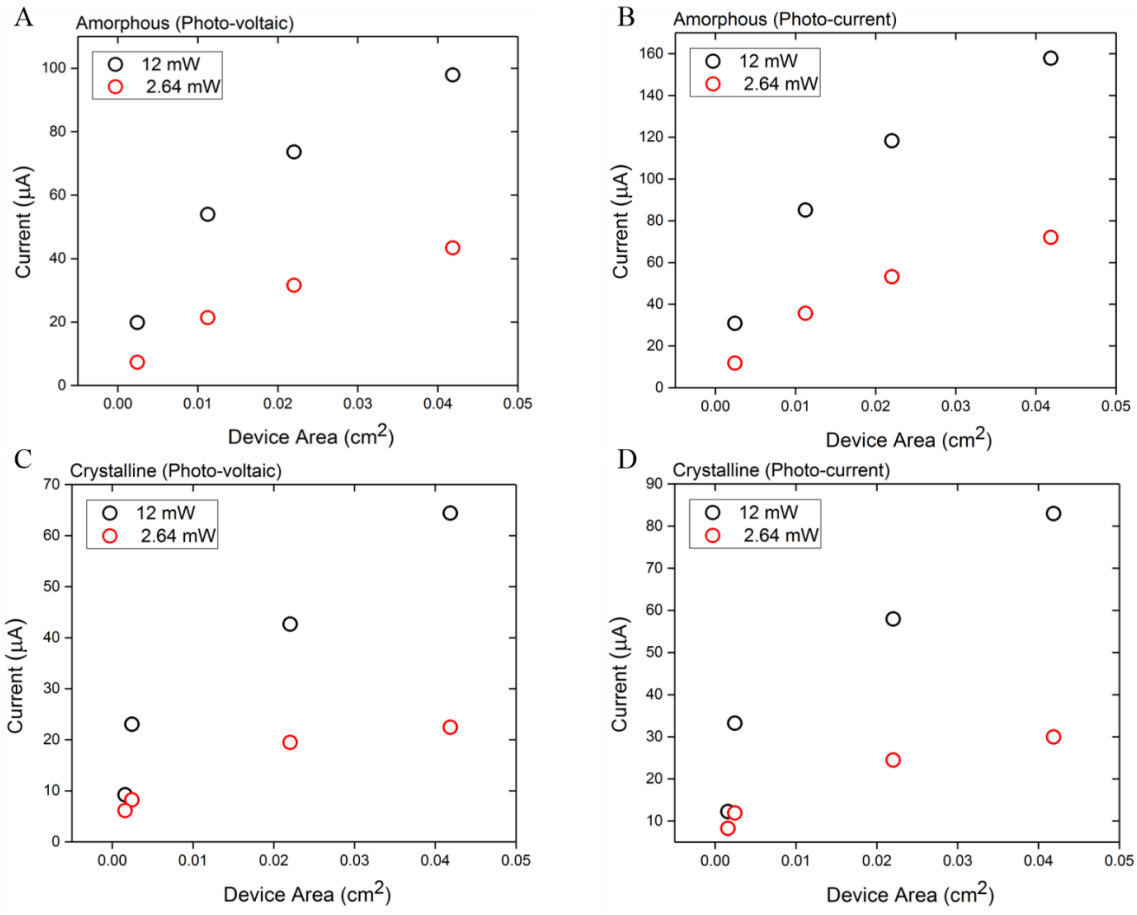

Figure 54**. Scaling behavior**. (A) Photo-voltaic short-circuit current scaling as a function of the active device area in the amorphous state of GST at 12 mW and 2.64 mW exposure (637 nm). (B) Photo-current ($I_{Illumination}$-I_{Dark}) measured at 100 mV as a function of the active device area in the amorphous state of GST under similar illumination conditions. (C) Photo-voltaic short-circuit current scaling as a function of the active device area in the crystalline state of GST 12 mW and 2.64 mW exposure (637 nm). (D) Photocurrent ($i_{Illumination}$-I_{Dark}) measured at 100 mV as a function of the active device area in the crystalline state of GST under similar illumination conditions.

Based on the above observations and those that follow, it can be hypothesized that the photo-excitation effects in the devices at these wavelengths (greater than the bandgap of the materials) are not strongly influenced by the nature of the chemical bonding in GST in its amorphous and crystalline states[190]. Furthermore, the existence of a photovoltaic effect confirms that the photocurrent in these devices originates from photoconductive effects; not solely from photothermal and photothermal conductive (thermally generated carriers) as has been traditionally believed[230]. Temperature dependent *I-V* characteristics (see Figure 55) were carried-out to verify the charge transport characteristics of GST in the crossbar devices. Strong

temperature dependence on the charge transport is found in the amorphous state while the effect is negligible in crystalline state GST. From fitting my experimental results with a modified Poole-Frenkel model ($I = K'e^{(-\Phi b/KT)} \sinh((q/KT).(Vdz/2t))$, where K' is a fitting parameter, k is the Boltzmann constant in eV, Φ_b is the activation energy (energy barrier) in eV, V is the applied voltage in volts, dz is the inter-trap distance and t is the GST thickness)[228], an inter-trap distance of 8 nm and 16 nm, and activation energies of 0.20 eV and 0.40 eV is calculated for the positive and negative polarity of the applied bias, respectively. Although these values are typical for sputter-deposited GST, the strong dependence of the fitting on the bias polarity is indicative of asymmetry in the devices. This abnormality is indicative of the IV characteristics to be modulated by the contacts (Schottky barriers). I also find that the IVs cannot be fitted to a thermionic charge model that is generally used in describing the charge transport characteristics in metal-semiconductor-metal devices. In essence, this suggests that charge transport in the above crossbar devices is convoluted: it results from the Poole-Frenkel transport, the thermionic emission as well as from direct tunneling. On the contrary, the current in the crystalline state of GST is found to not linearly increase with temperature, but instead decrease. This is indicative of the metallic behavior in crystalline GST. Crystalline GST is known to be a degenerate p-type semiconductor due to the existence of structural vacancies, resulting in the Fermi level to reside within the valence band[239]. Metal like behaviour in crystalline GST has also been observed in field-effect experiments[76,77].

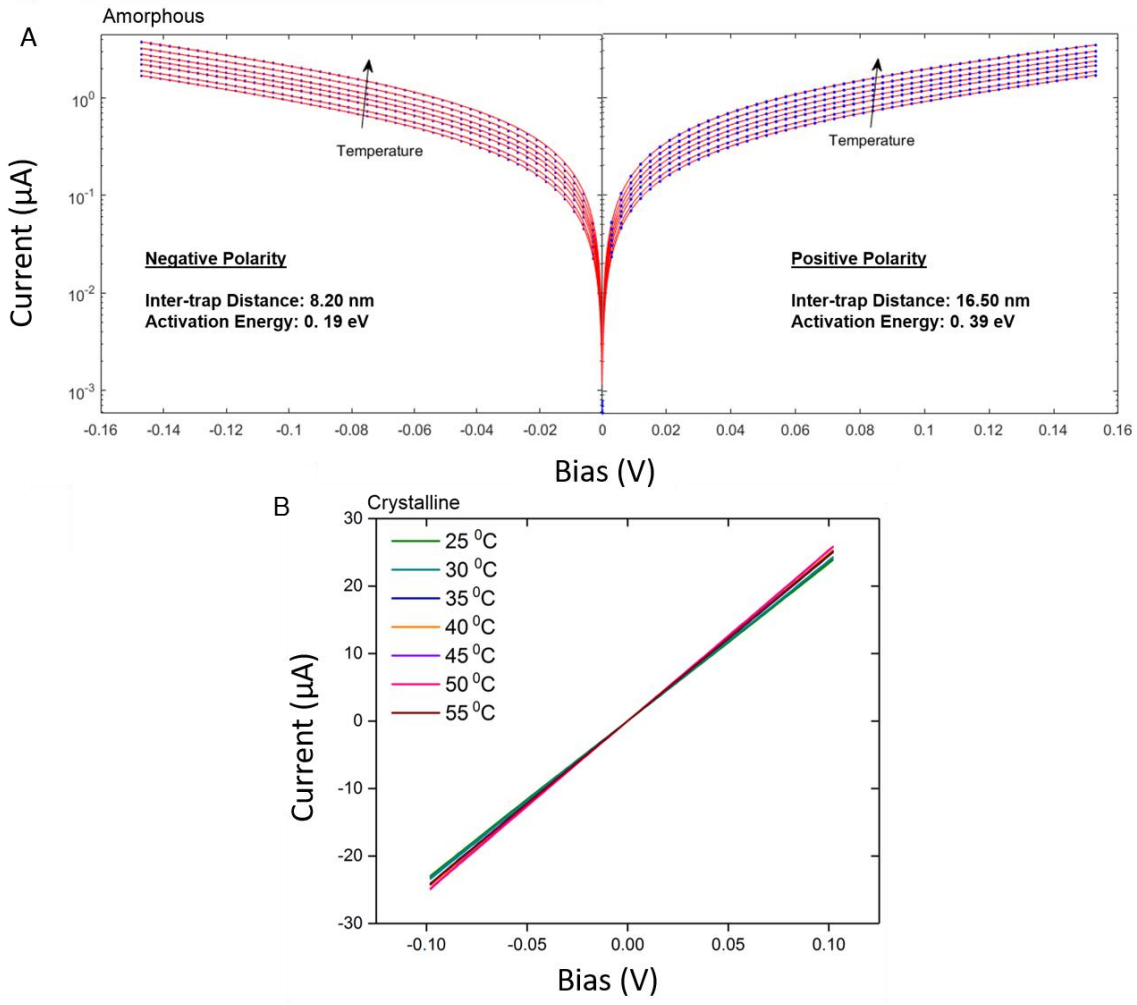

Figure 55. **I-V fitting of the amorphous state**. (A) The IV data of the device in the amorphous state of GST at temperatures spanning from 30 ^{0}C to 60 ^{0}C in increments of 5 ^{0}C and corresponding fits the modified Poole-Frenkel model. The model only fits nicely when the IV data is considered separately for the negative and positive polarities. For the negative polarity, the inter trap distance is calculated to be 8.20 nm as opposed to 16.50 nm in the positive polarity, and similarly, the activation energy is found to be 0.2 eV as opposed to 0.4 eV in the positive polarity. (B) The IV data in the crystalline state of GST. The current is found to not linearly increase with temperature, but instead decrease. This is indicative of the metallic behavior in crystalline GST due to its degenerate nature (heavy p-doping).

Both Poole-Frenkel and Schottky emission transport schemes invoke a field dependence of the conductivity. However, if a Schottky barrier were to dominate the conduction in the crossbar cells, a rectifying diode-like I–V characteristic would be expected, which is not necessarily the case. The rectification ratio of the crossbar devices range between 1.21-1.50. It is therefore reasonable to assume that the Poole–Frenkel effect is more appropriate to describe the electrical transport. However, because of the convolution between the mechanisms, it is not

straightforward to deduce the built-in Schottky potentials. It is also noted that the photoresponse of the devices is a strong function of the incident wavelength (see Figure 56). This is likely due to thin film interference from the device layers. I model this effect with standard optical transfer matrix calculations, which were shown earlier and using refractive indices, which are determined experimentally for the thin films using ellipsometry (see Appendix 14C).

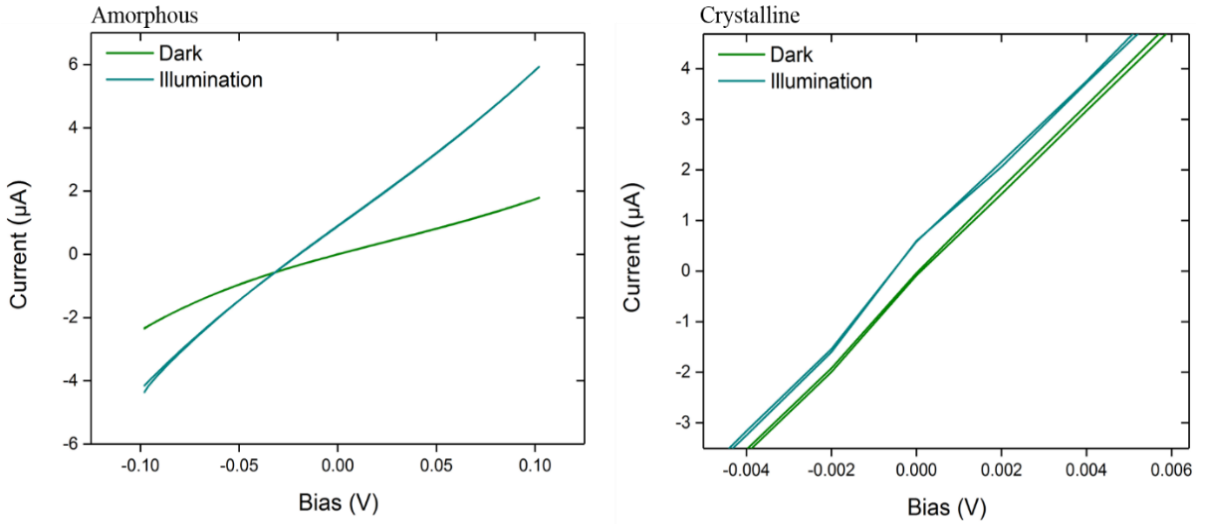

Figure 56. Current-Voltage Characteristics under 1550 nm illumination. (A) IV characteristics of a 25 um by 25 um device (Ta/Pt(50nm)/ITO (40nm)/GST(21nm)/ITO(80nm)) illuminated at 2mW of 1550 nm in the amorphous state of GST, and (B) similar measurements in the crystalline state of GST.

5.2.2 Photo-behaviour of phase change materials

The photo-generation behavior of the crossbar devices was studied in the amorphous and crystalline state of GST (see Figure 57) for differing intensities of light (0 to 3158 W/cm^2). To clarify the nomenclature used below, by crystalline I mean the electrically-switched GST, which is the technologically more relevant crystalline form of GST. It is found that the photocurrent ($I_{Photocurrent}=I_{Illumination}-I_{Dark}$) in such devices under both zero-bias and biased conditions increases linearly with the light intensity before saturating at higher powers in both the amorphous (see Figure 57 A and 57B) and the crystalline states of GST (see Figure 57C and 57D). It is also found that partial crystallization of amorphous GST occurs with increased irradiance, as illustrated by the linear drop in the device resistance seen as a function of irradiance (see inset in Figure 57B). From the resistance change, approximately 40 % crystallization of the device may be inferred.

This is indicative of photothermal effects that are reported[230,234] to dominate in PCMs and indicates that the GST heats-up under illumination, such that it partially crystallizes.

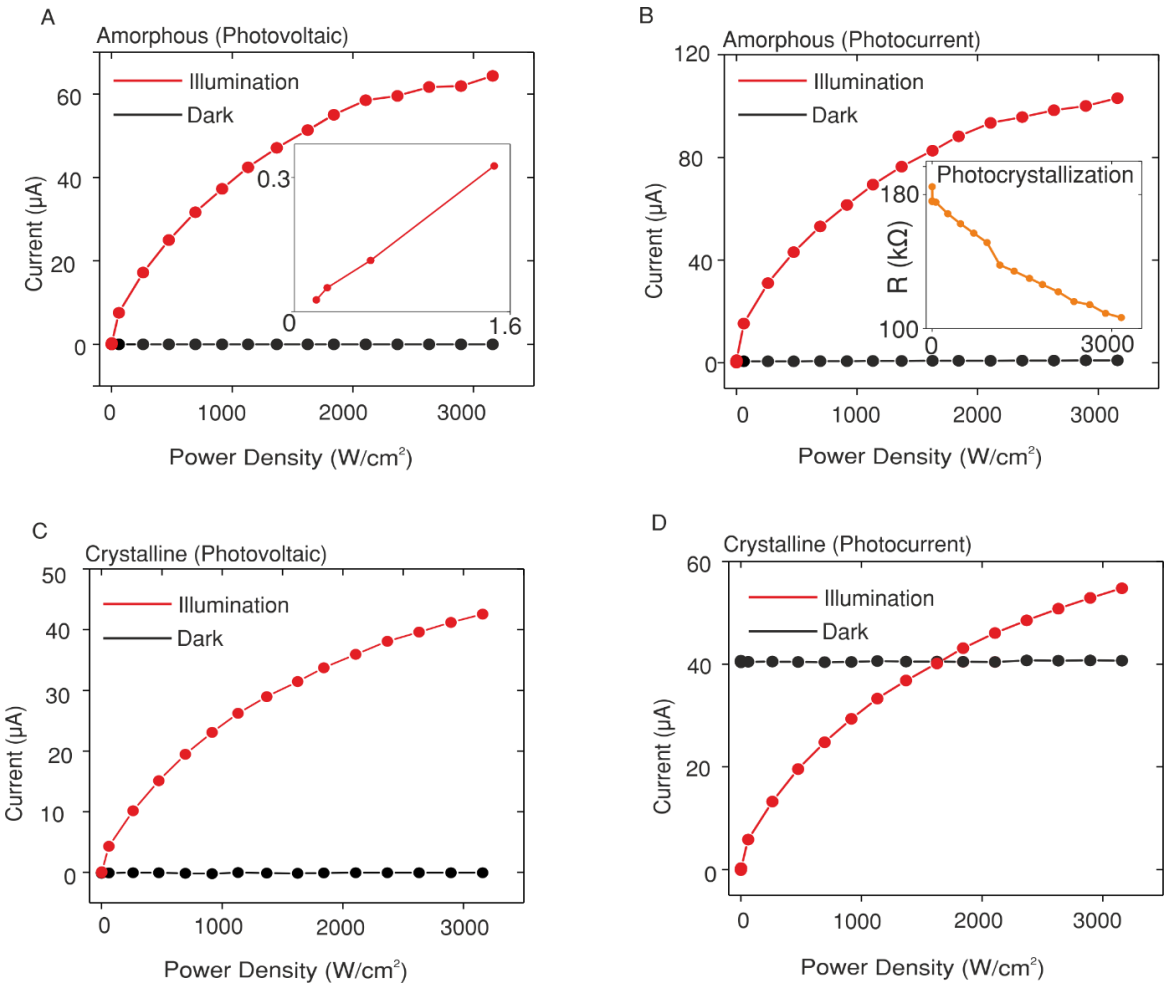

Figure 57. **Photobehavior of the devices.** (A) Current-irradiance characteristics of a device in the amorphous state of GST at zero bias conditions. The photocurrent (red trace) increases linearly with irradiance. The inset illustrates the photoresponse at low irradiance values. (B) Current-irradiance characteristics of the same device at 100 mV bias conditions. The inset shows the device resistance as a function of laser irradiance. (C) Current-irradiance characteristics of the same device at zero bias conditions in the crystalline state of GST. (D) Characteristics of the same device at 100 mV bias conditions. The black traces in Figure (A to D) is the dark current after every measurement made under illumination (637 nm).

However, it is found from the experiments that the photothermal effects are non-linear in nature; i.e., the drop in the device resistance which is a cue for crystallization energetics begins to occur only beyond some threshold irradiance (1.5 W/cm^2 for a 20 × 20 μm device). The threshold irradiance demarcates the photoconductive and photothermal effects; that is below the threshold

irradiance photoexcitation effects predominate, beyond it both the effects co-exist. Based on the magnitude of these effects it is observed that the irreversible photo-crystallization contributes only ~0.4 % to the increased current ($I_{Photocurrent}/(I_{Dark(after\ exposure)}-I_{Dark(before\ exposure)})$) under illumination for the given range of irradiance and when the GST is in the amorphous state. On the contrary, it is found that the device with the crystalline GST exhibits only photoconductivity, showing no signatures of variation in the device resistance under irradiance. Crucially, it is observed that the percentage contribution of photoconductivity and photothermal effects to the photoresponse of amorphous GST based devices can be tuned through device engineering. For example, it is observed that in smaller devices (micron and sub-micron) large irradiance can readily induce crystallization of the amorphous state (see Figure 58). These effects are indicative of increased contribution from photothermal effects and are a result of decreased heat transfer (greater heating of GST) to the contact pads due to smaller device active area and thinner electrodes in such devices. That said, these effects can be optimized through device engineering (e.g. choice of the electrode material and their volume). It is also noted that for devices with Pt bottom-electrodes (see Figure 58) diminished photothermal effects (both amorphization/crystallization) are observed, which is likely from increased thermal dissipation due to the greater thermal conductivity[225,227] of Pt (69.1 WmK^{-1}) over ITO (11 WmK^{-1}). The above reasons, i.e. device dependent photoresponse, may well explain why photoconductive effects in GST (and similar chalcogenides) have not previously been reported. The fact that at high irradiance the device photocurrent in both the amorphous and crystalline states of GST saturates limits the dynamic range for photo-detection. Time-resolved optical pump-probe measurements have observed similar behavior in crystalline GST which was attributed to saturation absorption (Pauli blocking from conduction band filling)[236]. However, given that both the amorphous and crystalline states of GST have a parabolic dispersion in their density of states and that the incident wavelength corresponds to excitation energy much higher than the bandgap of both the states, it is less likely

that saturation absorption alone dominates the photocurrent saturation in these devices. The optical properties of GST are known to be temperature sensitive[240,241] and therefore changes in refractive index and/or drop in the absorption coefficient can result in decreased photogeneration in the device.

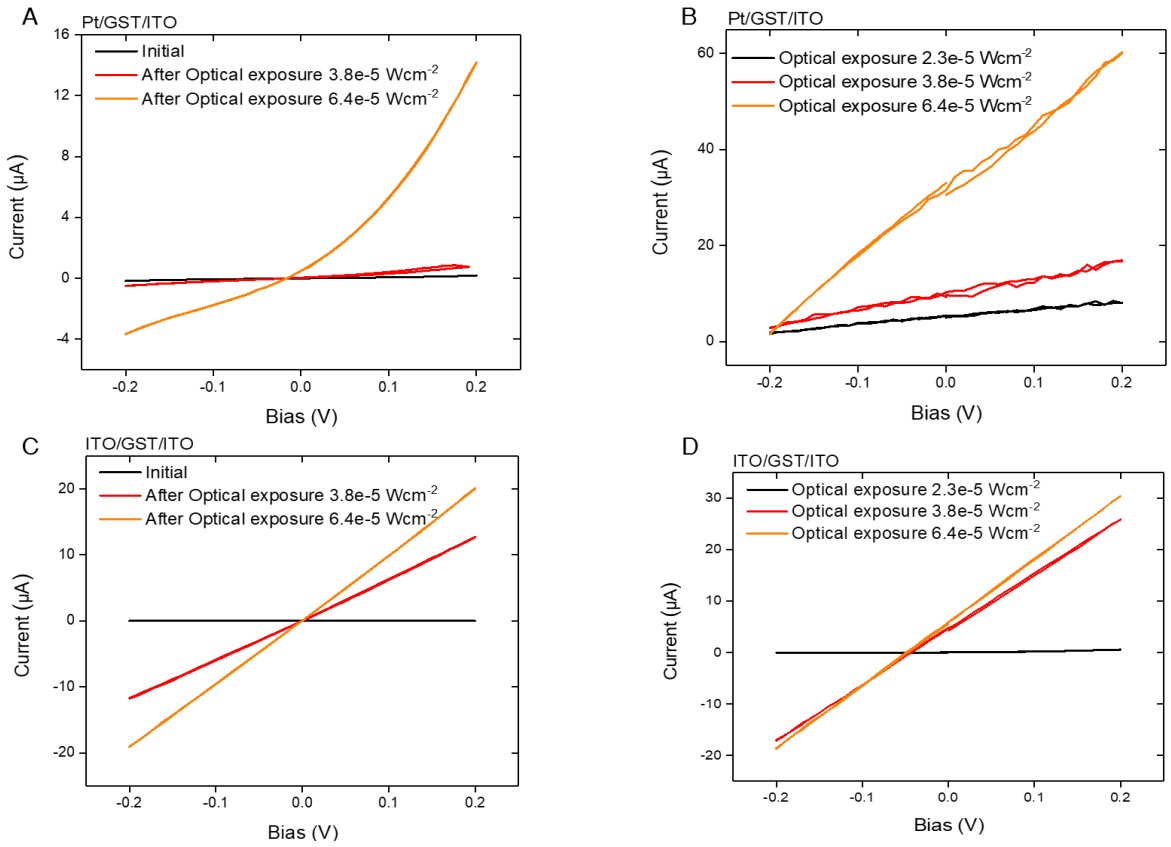

Figure 58. **Photobehaviour in micron-sized devices**. (A) IV characteristics of a 1 μm by 1 μm device ITO (30nm)/GST (15nm)/Pt (7nm) under dark condition. (B) The same devices illuminated under 405 nm exposure. The device's photovoltaic and photoresponse increases with increasing laser power. (C) IV characteristics of a device ITO (30nm)/GST (15nm)/ITO (20 nm) illuminated under dark conditions. (D) IV characteristics of the same device under illumination (405 nm). Comparison of Figure A and C show that the device crystallizes more readily with ITO electrodes than with Pt electrodes.

In addition, barriers at the GST/ITO interfaces (discussed later) can strongly influence saturation. Regardless of the mechanism, the fact that saturation exists in these crossbar devices for both states of GST can enable non-linear optical effects such as self-focusing, which could potentially be harnessed in super-resolution bit writing for optical data storage. The photo-responsivity ($R = I_{Photocurrent} / P_{Laser}$, where P_{Laser} is the laser power density (W/cm^2)) and the

internal quantum efficiency $IQE = (I_{Photocurrent} / e) / ((P_{Laser} / h\upsilon) \times \alpha)$), where e is the electronic charge (1.6×10^{-19} C), P_{Laser} is the laser power (W), $h\nu$ is photo energy (eV) and α is the absorption coefficient (%)) for the devices are estimated since these are the typical figures-of-merit for photon to electron conversion in optoelectronic devices. The absorption coefficient (α) of the stack is experimentally computed and the percentage absorption for both crystalline and amorphous GST (see Figure 52 C and 52D) is deduced by fitting the data. It is found that the amorphous state of GST absorbs 78.5 % of the incident light as opposed to the crystalline counterpart that absorbs 73 % of the light (see Figure 52D). It is also found that the photo-responsivity of the device with amorphous GST is an order of magnitude higher than that of the crystalline state and that in both the states the device exhibits an inverse relationship to the irradiance (see Figure 59A). It is also interesting to note that the near-unity photo-responsivity of amorphous GST based devices is comparable to that of commercial silicon photodetectors and better than that of emerging 2D transition metal dichalcogenide (TMDC) photodetectors[242]. The internal quantum efficiency follows a similar trend, with amorphous GST devices exhibiting higher photoexcited carrier collection at contacts than devices with the crystalline state (see Figure 59B). More importantly, at low irradiance, the internal quantum efficiency of the device with the amorphous state exceeds 100 %, a case which is usually also observed in TMDC based photodetectors[243]. This is indicative of photoconductive gain, which is likely due to an imbalance between the trap lifetimes of holes and electrons -due to trap states-, such that one carrier type circulates several times in the circuit contributing to the photocurrent before eventually undergoing recombination[243]. This difference in carrier lifetimes is also implicated on the transient measurements (discussed later), where the decay of the device photo-response with amorphous GST is extended in time. A likely explanation for the diminished photoresponse of devices with crystalline GST compared with the amorphous counterpart (as shown in Figure 59A and 59B) is

the lower absorption of light (by 5.5 %) by the stack when GST is crystalline, and a weaker built-in electric field (that governs the recombination rate of the carriers and is discussed later).

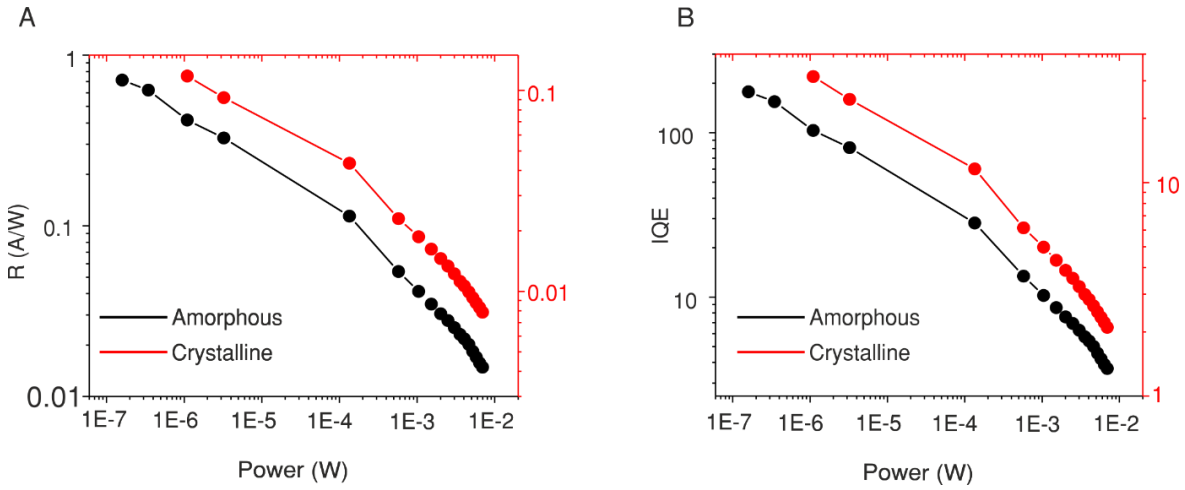

Figure 59. **Figures-of-merit of the devices.** (A) Photo-responsivity of the device as a function of laser power incident on the device. When in the amorphous state of GST (black trace), the device shows one magnitude higher photo-responsivity compared to the crystalline state. (B) The internal quantum efficiency of the device as a function of the laser power incident on the device. When in the amorphous state of GST (black trace), the device shows a magnitude higher internal quantum efficiency compared to the crystalline state.

Regardless of the cause, the fact that PCMs can be tuned for their photo-responsivity and IQE by an order of magnitude in a non-volatile manner is rather an unusual trait, which can potentially be exploited for many applications, such as for artificial retinas. It is also emphasized that a further contrast enhancement in the photo-responsivity and internal quantum efficiency can be achieved by utilizing the shifts in the absorption resonance from amorphous to crystalline phase transformations. This can be done using stack engineering, as has been done in phase change displays[222,220]. These data are suggestive of strong potential of phase change materials for optoelectronic applications. Such narrow-band devices require future work using solar stimulators to understand the quantum efficiency spread over a broad-band illumination source.

5.2.3 Stability and transient response under optical exposure

Time-resolved measurements were performed to study the stability of devices under illumination conditions, with the GST in both its amorphous and crystalline states (see Figure

60 (A,B) and (C,D)). Light-induced structural changes (photostructural effects) are commonly observed in amorphous semiconductors, due to their lattice flexibility that favors multiple atomic configurations. Such changes can have photothermal and/or photoexcitation origins, with the former understood to commonly aid crystallization while the latter understood to cause material degradation. For the latter a case in point is the Staebler Wronski effect[234] that deteriorates the photoconductive behavior, such as in amorphous silicon (used in solar cells). However, it is found that both the amorphous and crystalline states of GST are stable under continuous exposure to light, despite producing an increasing concentration of photoexcited carriers that generally favor photostructural effects (besides photocrystallization). This is hinted at by the stability of the baseline (see Figure 60 A and B, dark current) and the consistencies of different levels (see Figure 60 C and D, photocurrent) under differing light intensities. These findings, therefore, indicate that the photostructural effects in technologically relevant PCMs are likely limited to photocrystallization only, which was discussed earlier. This favors the use of PCMs for displays and smart windows where they are expected to experience continuous exposure to ambient light. The absence of the photostructural effects in GST as was revealed on the electrical measurements shown in this chapter can be attributed to the presence of highly coordinated atoms, such as Ge, in the lattice which enhances the activation energy for structural changes[235] of the otherwise weak framework of Te[205]. I also studied the stability of Ge_4Te_6 (GT) thin films (see Appendix 16) under optical exposure to implicitly support the role of Ge in rigidization of the lattice. The GT films exhibit similar stability to that of GST under continuous light illumination.

In order to study the dynamic process of photogeneration and –recombination, transient response measurements were carried-out for devices in all three states of GST: amorphous, electrically-switched crystalline and thermally crystallized (see Figure 60E), at zero-bias. The device was illuminated with 25 μs wide optical pulses with rising and falling edges of 5 ns and the corresponding electrical response was recorded on a high bandwidth (1 GHz) oscilloscope. The

speed of photo-detection is estimated by computing the rise time (τ_{rise} = 10 to 90%) and fall time (τ_{fall} = 90 to 10%) of the transient response. It is found that both the rise and fall time of the device decreases with increasing crystalline volume fraction of GST (τ_{rise}: thermally-annealed (0.62 μs) < electrically-switched (0.95 μs) < amorphous (1.98 μs), and τ_{fall}: thermally-annealed (0.50 μs) < electrically-switched (0.80 μs) < amorphous (20.60 μs)). The decay transient of the device with amorphous GST fits a single-exponential decay equation, which is indicative of the photo-excited trapping process being dominated by non-radiative Shockley-Read-Hall recombination due to the presence of mid-gap defect states[243].

The photodetection bandwidths of the devices (1 MHz for the crystalline and 50 kHz for the amorphous state) are lower than conventional silicon photodiodes; however, they are higher than emerging transitional metal chalcogenides that are being actively studied for photodetection applications[242]. Moreover, unlike conventional detectors, the photoresponse of the devices can be tuned, by changing the state of PCM, which in turn determines the rise/fall times and detection bandwidth.

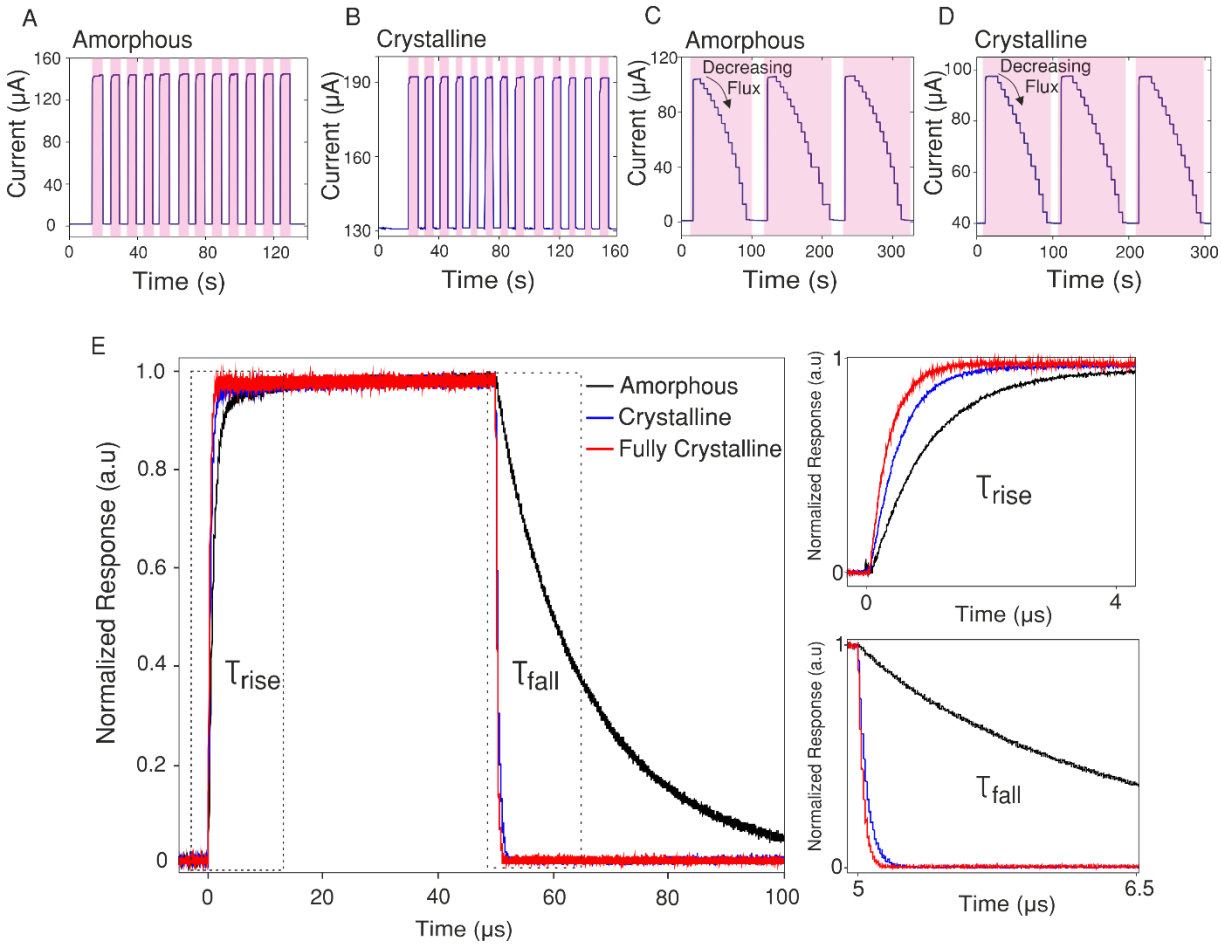

Figure 60. **Photo-stability and transient response**. (A) The current-time response of a device at 100 mV bias conditions in the amorphous state of GST under pulsed illumination (highlighted in pink). (B) The current-time response of the same device at 100 mV bias conditions in the crystalline state of GST under pulsed illumination (highlighted in pink). (C and D) The current-time response of a different device at 100 mV bias conditions in the amorphous and crystalline state of GST under continuous but varied irradiance (3158 to 0 Wcm^{-2}). (E) Transient response of the photocurrent in three different states of GST at zero-bias and under illumination of a 25 μs (5 ns edges) light pulse. Illumination conditions were 637nm/3158 Wcm^{-2}.

It is also intriguing to note the two orders of magnitude difference between the decay times of the device between the crystalline and amorphous states of GST, which is indicative of the photo-conductive gain discussed earlier. It is well known the speed of photo-detection is a function of the photo-excited carrier's transit time to the contacts and the RC-time delay of the circuit. Given that the mobilities of the carriers -which determine the transit time- are smaller in the amorphous GST[238], it is expected that the device with amorphous state exhibits slower transient response than that of the crystalline state.

The origin of the photocurrent in the crossbar devices is now discussed. The photoresponse could arise from either photo-voltaic effects and/or photo-induced thermoelectric effects[232,244,245]. The former requires an asymmetric distribution of the built-in electric field at zero bias such that the photo-excited carriers (holes and electrons) are separated from each other and a net photocurrent is generated at the contacts. The latter (thermoelectric) effect requires a temperature difference between the top and bottom contacts that lead to a charge flow by diffusion. Based on the transient measurements which are described in Figure 60E, I find that the photo-induced thermoelectric effect is not the dominant mechanism that governs the zero-bias photocurrent. This follows from the assumption that the decay time of the device would not considerably different between the amorphous and the crystalline state of GST if this process were to be thermally dominated. For a photocurrent that is mostly thermal in nature, the response would be limited by the thermal properties of the device and substrate which do not significantly differ between the two states of GST. For example, the thermal conductivity difference[76] between the amorphous and the crystalline state (FCC) of GST is typically less than 0.2 W/mK. The decay time observed in the transient measurements shown above, however, show a difference of an order of magnitude between amorphous and crystalline states. In addition, the photocurrent should scale linearly with irradiance[246], if thermoelectric effects are dominant, which is not the case here. As further verification, the top ITO electrode was preferentially heated to intentionally create a temperature difference in order to emulate the photothermoelectric effects[247]. In photothermoelectric effects, the top ITO electrode should get heated-up preferentially over the bottom ITO electrode from laser illumination. In these measurements, for amorphous GST based devices, I observed positive zero-bias current (see Figure 61 and 62(A and B)) that scaled linearly with the temperature difference (1.34 nA/^{0}C) similar to the zero-bias photocurrent that scaled linearly with the irradiance. These findings, therefore, suggest that the photoresponse of PCMs is, in fact, unusual- governed by the interplay of three independent mechanisms:

photocrystallization, photoconductivity, and photothermoelectricity. However, it is noted that the contribution of the photothermoelectric effects is expected to be small, given that the photocurrent recorded in these mixed-mode experiments is ~1000 times higher than for purely thermoelectric effects.

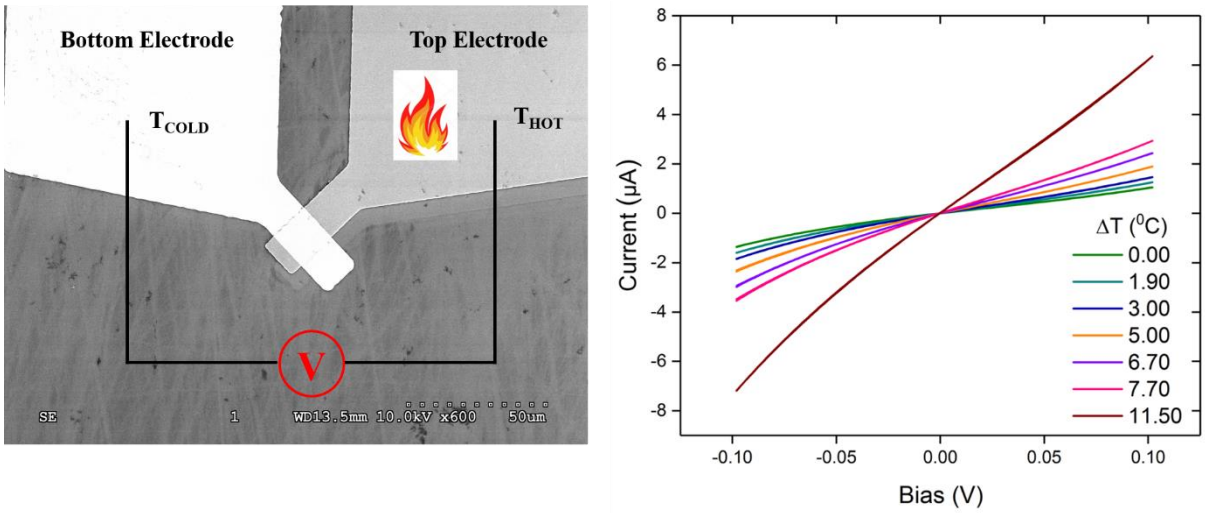

Figure 61. **Thermoelectric effects in amorphous GST**. (a) Scanning electron micrograph of the device illustrating thermoelectric measurements. The top ITO electrode is preferentially heated to create a temperature difference in order to emulate photo-thermoelectric effects. IV characteristics of the device at various temperature differences.

5.2.4 Mechanism of photocurrent and -voltaic effects

On the basis of the above observations, it is therefore concluded that the photoresponse observed in GST is due to a photovoltaic effect in my devices. It is likely driven by the existence of an asymmetric built-in electric field from Schottky barriers at the GST/ITO interfaces. The asymmetricity arises from the differences in the work function (Φ) of GST and ITO[248,249] at both top and bottom interfaces. The fabrication process and the differing thickness of the top and bottom ITO layers likely results in a larger work-function difference between top the ITO layer and GST compared with the bottom ITO layer and GST ($\Delta\Phi_{\text{top-ITO/GST}} > \Delta\Phi_{\text{bottom-ITO/GST}}$). Such an asymmetricity at the interfaces have been recorded before in several notionally symmetric devices (i.e. photoactive material sandwiched between electrodes made from the same material)[250,251]. In the amorphous state GST is a *p*-type semiconductor due to Fermi pinning by

the localized defect states, which result from lone pairs, structural defects, and dangling bonds, while the crystalline state is known to be a degenerate *p*-type semiconductor with its Fermi level placed within its valance band due to large hole concentration that comes from its intrinsic structural vacancies[229,238,252]. Charge transport in the devices across the GST/ITO interface thereby switches from thermionic to direct tunneling due to the amorphous to crystalline phase transformation. This is evident on the I-V traces: the charge transport characteristics that are non-linear in the amorphous state become linear in the crystalline state. It is also observed that under illumination the I-V traces become increasingly linear with irradiance, particularly for the amorphous state. This is indicative of the Schottky barrier lowering which likely stems from photo-gating effects. For instance, trapping of photo-excited (hot) holes at interfacial defect sites and increased hole concentration; effects that lower the Schottky barrier height and width, respectively[253,254]. Such effects are also expected to contribute to the tailing-off of the photocurrent at higher irradiance. Based on these results, the photocurrent mechanism is illustrated in Figure 62C for both the amorphous and crystalline states of GST. For devices with amorphous GST at thermal equilibrium, the energy band profile is illustrated in (i). The slant in the energy band profile highlights the asymmetricity in the Schottky barriers that result in an in-built field pointing from the top to bottom electrode. (ii) On illumination, the photo-excited carriers are swept in either direction contributing to the photocurrent. Some carriers recombine at the trap sites during their transit. The accumulation of holes at the interface with the bottom electrode reduces the width of the barrier, causing holes to transit to the contacts by direct tunneling instead of thermionic emission. (iii) At 100 mV applied bias and under illumination, the in-built field and the applied electric field point in the same direction, resulting in faster transit time of the carriers and their decreased recombination rate; either resulting in greater photocurrent.

In devices with crystalline GST, at thermal equilibrium, the energy band profile is illustrated in (i). The trap states are significantly annihilated by crystallization. Because the work-function difference between the crystalline GST and ITO is smaller than the amorphous GST and ITO, the Schottky barriers and therefore the in-built field is expected to be weaker in the crystalline GST based devices. This implies decreased photoresponse in the crystalline GST devices, which is indeed evident on the photocurrent vs irradiance measurements discussed earlier. In those measurements, the photo-responsivity and the internal quantum efficiency of the amorphous state were found to be an order of magnitude higher than the crystalline state. The difference is also evident in the I-V characteristics of the devices (see Figure 53) as they show reduced bias dependence of photocurrent for crystalline, as opposed to amorphous GST. Since the crystalline material is much more conductive, the electric field is dropped across the entire device rather than predominately at the Schottky barriers where most efficient charge collection occurs. Furthermore, a higher open-circuit voltage (zero-current), which is indicative of a larger Schottky barrier (height and depletion width) is observed in the electrically resistive amorphous GST based devices. The slant in the energy band profile that highlight the asymmetricity in the Schottky barriers, hence the built-in electric field is reduced compared to amorphous GST. Charge transport across the barrier occurs by direct tunneling at thermal equilibrium due to $p+$ doping of crystalline GST. (ii) On illumination, the photo-excited carriers are swept in either direction contributing to the photocurrent. Some carriers recombine at the trap sites during their transit, and the accumulation of holes at the interface with the bottom electrode reduces further the barrier width, causing holes to transit to the contacts more easily by direct tunneling. (iii) Like before, at 100 mV applied bias and under illumination, the in-built field and the applied electric field point in the same direction, resulting in faster transit time for carriers that results in greater photocurrent.

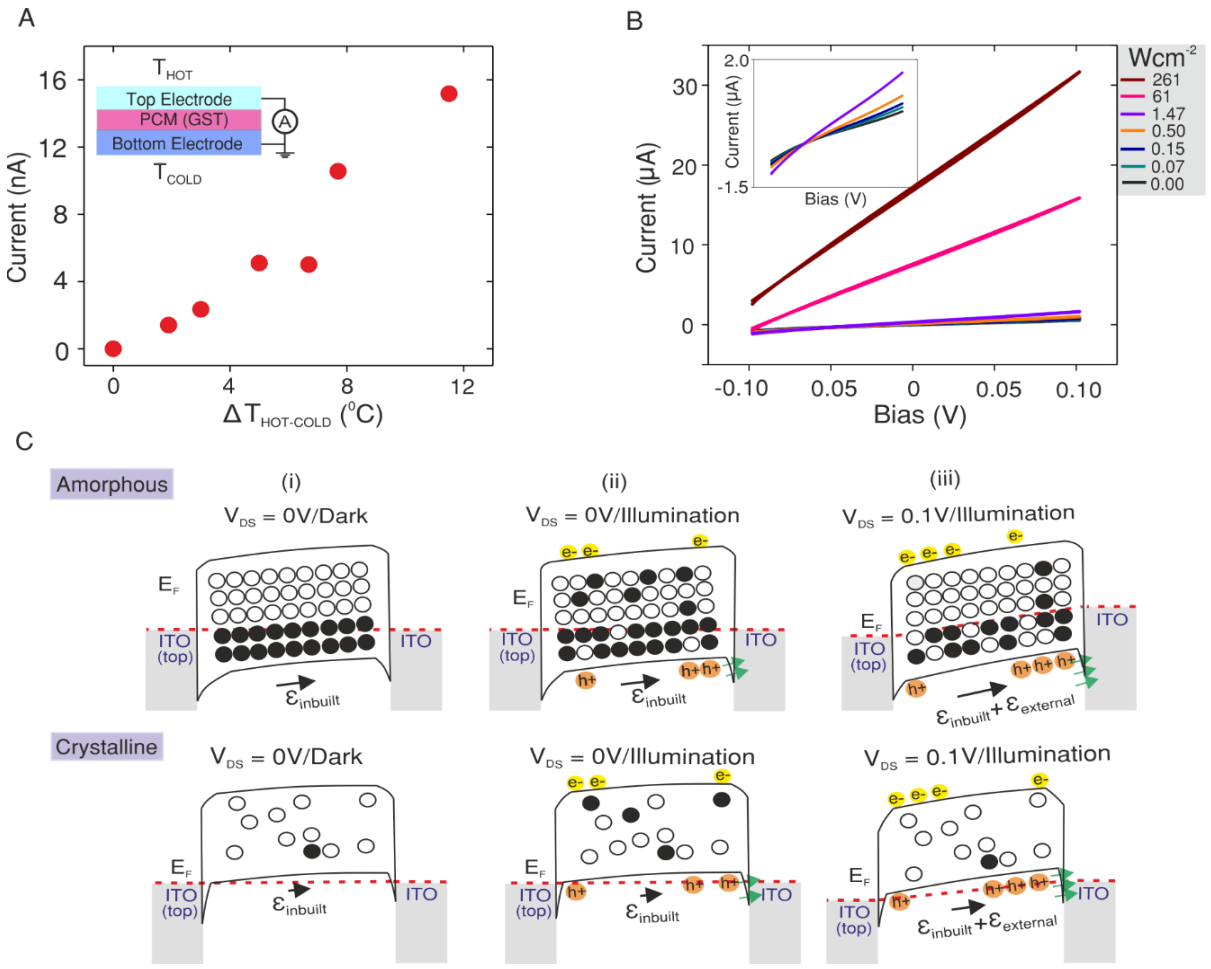

Figure 62. **Photo-response mechanism.** (A) Thermoelectric measurements at zero-bias. The top electrode of the device is preferentially heated to produce a temperature difference that results in a photovoltaic effect**.** (B) The current-voltage characteristics of the device in the amorphous state of GST under increasing illumination conditions. The traces become linear as a function of irradiance. Inset is an enlarged view of the current-voltage characteristics. (C) Energy band diagrams of the devices based in both the amorphous and crystalline states of GST at (i) thermal equilibrium, (ii) under illumination, and (iii) under applied electrical bias**.** The empty circles represent unfilled trap states, while the solid circles represent filled trap states.

In order to ascertain that the built-in electric field originates from the asymmetric Schottky barriers only, two set of experiments were carried-out. In the first experiment, the photo-response was studied in asymmetric devices (ITO/GST/Pt) devices, where asymmetricity in the Schottky barriers, hence built-in electric field intrinsically exists. Very similar characteristics in the photo-response (see Figure 58) were observed, as were noted for the symmetric devices (ITO/GST/ITO). In the second experiment devices (see Figure 63) were tested for polarisation effects using piezoresponse force microscopy (PFM)[244]. No signatures of ferroelectric switching were observed

that could suggest the existence of a remnant field in the hysteresis loop measurements. These results, therefore, confirm that the photocurrent in the devices is in fact governed dominantly by the asymmetric Schottky barriers at the GST/ITO interfaces.

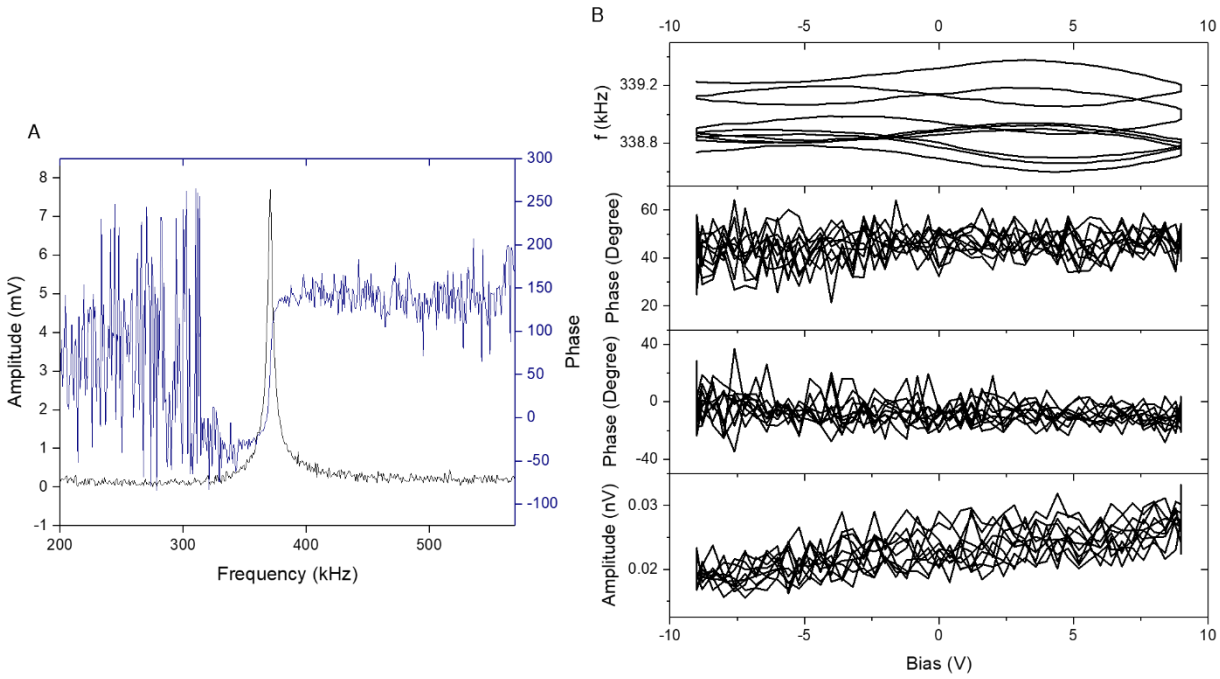

Figure 63. **Ferroelectricity measurements**. (a) Contact Resonance Measurements. An n-doped silicon atomic force microscopy probe is scanned over a range of frequencies on the device (amorphous GST) in the contact-mode operation to determine the resonance frequency (indicative of tip-sample stiffness). (b) Hysteresis loop measurements carried-out at the contact resonance frequency to maximize the signal to noise ratio. (i) Five cycles of frequency sweep (forward and reverse), (ii) and (iii) corresponding phase of the probe from deflections. Hysteresis is not observed which is indicative of the absence of ferroelectric switching. (iv) The amplitude of the probe deflection. Hysteresis is not observed which is indicative of the absence of ferroelectric switching[255].

5.3 Spiking Detectors

The devices discussed so far function on a mixed mode configuration in which the electrical conductance of the device is modulated by the optical flux. This scheme truly utilizes the electrical and optical energies and essentially replicates functioning of a human eye. A human eye is a spiking detector where incident photons trigger pulsed action potentials and consists of a cleverly engineered feedback system, which regulates the optical intensity striking the retina. For example, under bright conditions, the diameter of the pupil, which serves as an aperture, decreases, while

under dark conditions, it increases, in controlling the optical flux striking the retina, which hosts the photodetectors. This gives a human a very high dynamic range for photo-detection and is a feature that lacks in the hardware of current charge-coupled devices (CCD) and complementary metal oxide semiconductor (CMOS) CCD image sensors. Phase change materials can be used as spiking detectors: by electrically biasing the phase change material to various degrees, and allowing the optical flux to cause an amorphous crystalline phase transformation. Each time a phase transformation occurs it indicates photon(s) capture. For example, Figure 64 shows a current-voltage sweep for a graphene nano-gap device bridged by GST under dark and under a constant optical excitation at 532 nm with a power density of 1592 mW/cm^2. The PCM is in the amorphous state and the voltage is swept from 0 V to 4 V and back to 0V. Under dark conditions the crystallization event is absent. However, the device exhibits a clear threshold switching driven phase transformation from the amorphous state to the crystalline state, evidenced by the hysteretic behavior. Neither optical excitation at 1592 mW/cm^2 nor a voltage bias up to 4V, are sufficient alone to induce a phase change and it is the combined action of the light and the electrical current required in switching the PCM. Providing a bias voltage of near to 4V would mean that a relatively small incident light flux will result in the phase change of the PCM. Each time a switching event occurs, it is indicative of photo-detection. The dynamic range or the amount of light required to induce the switching event of the device can be regulated by adjusting the applied electrical bias. The further away the bias voltage is from (below) the threshold voltage, the more optical flux is required to switch the detector. Hence, for more sensitive optical detection (in a dark room), an electrical bias close to threshold voltage would enable photo-detection, while under bright conditions, an electrical bias further away from the threshold voltage (depending upon the degree of brightness away) would enable photo-detection. A RESET pulse following each switching event amorphizes the device, enabling it for cyclic photo-detection. The response time of such a detector is governed by the speed of threshold-switching, which is

known to exponentially decrease with increasing applied voltage. Phase change materials, such as GeTe and $Ge_2Sb_2Te_5$ undergo threshold switching[239] in the order of 1–4 ns, which is on par with the detection speeds of commercial (Si, Ge and InGaAs *pn* and *pin* diodes) high-speed photodetectors[256]. However, unlike commercial detectors, the proposed detector requires a RESET operation, which takes 20-100 ns. This limits the photodetection bandwidth of the detector to hundreds of MHz. The RESET operation can of course be avoided by selecting compositions, such as GeSe and $GeTe_6$ which undergo threshold switching but not crystallization.

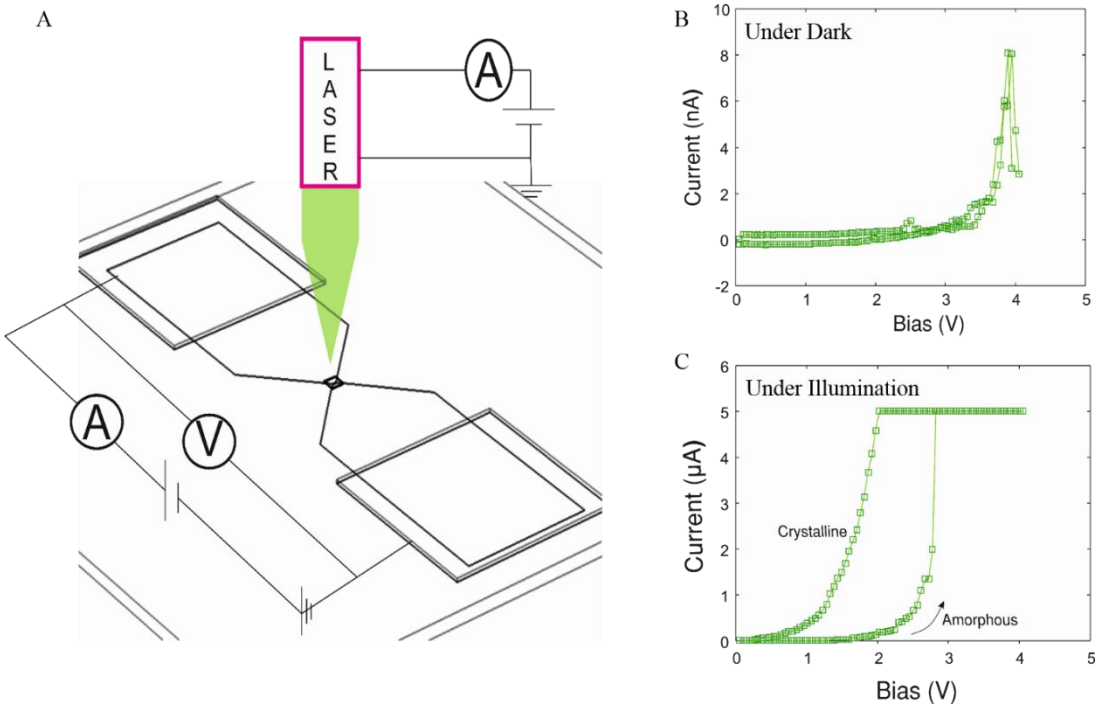

Figure 64. **Graphene Nano-gap spiking detector**. (A) A schematic of a graphene nano-gap device and apparatus for measurement. (B) Current-Voltage characteristics of the detector measured in the dark conditions. (C) The current-voltage characteristics of the detector measured under illuminated conditions. Note the device switches from amorphous to crystalline in a non-volatile manner highlighted by the hysteresis in the current. The truncation at 5 μA is the compliance that the measurement unit is set to.

Many transition metal oxides coated with metallic thin films, normally insulating, can be made conductive through external electric fields. Conduction occurs through a filamentation process, which occurs from metal ion migration. The original resistive state can be retrieved by breaking the filaments from through Joule heating and/or applying electric field in the opposite direction. Such devices are called filament forming metal oxides; and can also enable spiking

photodetectors. I find that $GeSe_3$, a material which we discussed in good detail in the previous chapter can be an ideal material for this application. Appendix 18a shows cross-bar devices that use $GeSe_3$ as the insulating matrix and Ag (silver) as the filamenting material. Cross-bar devices with different electrode materials where studied and the switching behavior were found to be of two distinct types. In the first (see Appendix 18b), the switching was non-volatile just like in $Ge_2Sb_2Te_5$ and in the second volatile (see Appendix 18c). I studied various electrode materials (see Appendix 18d) to differentiate the nature of such switching and made essentially two important observations: (a) the electrode material dictates the switching behavior, for example Ag and W enable non-volatile switching, while Pt and ITO favor volatile switching, and (b) filamentation is driven not by migration of Ag^+ ions from an host electrode, instead through rearrangement of the Ag^+ ions, which are already dissolved within the $GeSe_3$ matrix. The former occurs due to differences in the interfacial energies[257] between Ag and the electrode, which dictate the degree Ag^+ ions attachment at the electrode surface. The latter is an effect observed in most chalcogenide glasses[258], which is a result of the high solubility for Ag^+ ions in the amorphous matrix (see Appendix 18e).

Figure 65A and 65B illustrate that under illumination the threshold voltage at which switching occurs can be decreased. The magnitude of the shift (decrease) scales with the intensity of light (see Figure 65 C and D) and I find this to be a result of a photovoltaic effect that generates an in-built electric field. Crucially, when the applied electric field is aligned with the in-built field, a decrease in the switching voltage occur. The dynamic response of the device is illustrated in Figure 65C. The device undergoes switching when some threshold irradiance is illuminated on it. The device switching can be cycled multiple times by resetting the device to its original state, which is done as in this example through ramping down the applied voltage to 0 V.

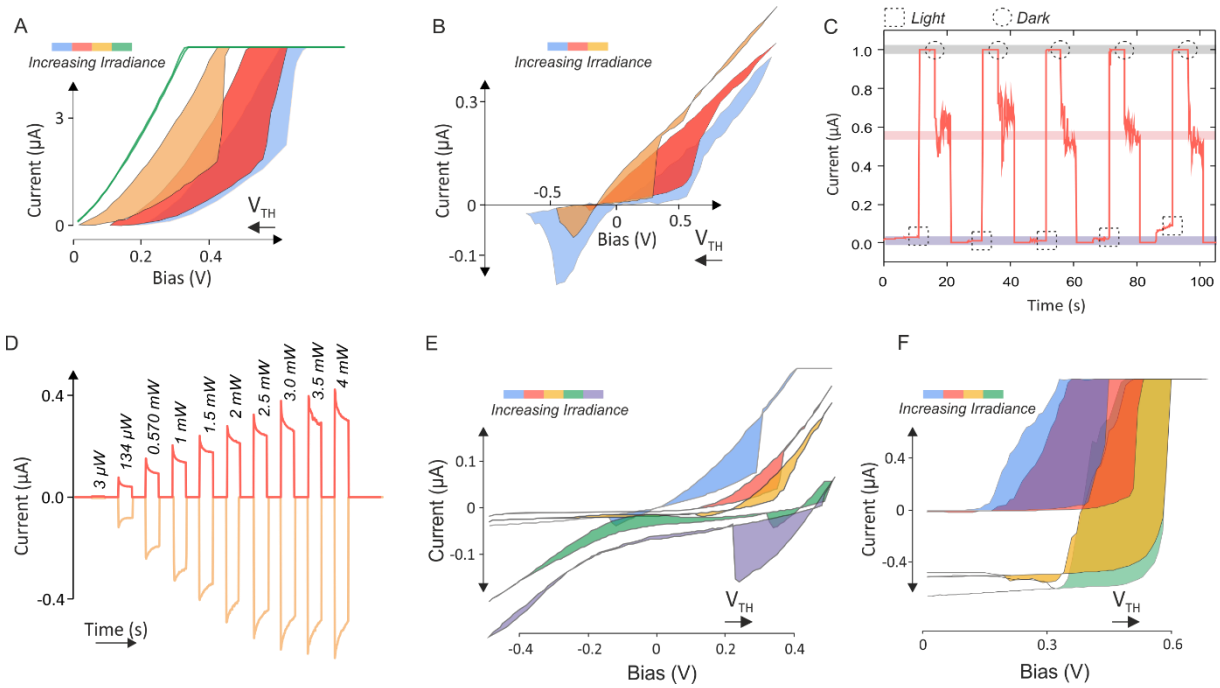

Figure 65. **Conductive bridge memory based spiking detector**. (A and B) Current-Voltage characteristics of a Pt/$GeSe_3$/Ag and an Ag/$GeSe_3$/Ag stack, respectively measured under increasing illumination. Note that in both A and B the switching voltage (V_{TH}) decreases with increasing illumination. (C) Cyclic threshold switching in a Pt/$GeSe_3$/Ag stack. The pink vertical box highlights the switched state. (D) Photocurrent in a Pt/$GeSe_3$/Ag device at 0 V. Positive current is when Pt pad is grounded, and negative current is when the Ag pad is grounded. (E and F) Current-Voltage characteristics of an Ag/$GeSe_3$/Ag and Pt/$GeSe_3$/Ag stack, respectively under increasing illumination and when biased in the opposite polarity to A and B. Note that V_{TH} increases with increasing illumination.

There are both advantages and disadvantages to using $GeSe_3$ based devices as spiking detectors over phase change materials. Advantages include the ability to not only decrease but also increase the threshold voltage under illumination. This can be done by reversing the sign of the applied voltage (see Figure 65 D and F). This has direct application for emulating neural behavior, such as mimicking both the inhibitory and excitatory behavior of neurons. Furthermore, the device switches at extremely low electrical powers (~0.5 nW) as opposed to phase change materials where Joule heating is involved. The downside includes, limited dynamic range (dictated by the magnitude of the in-built field), large inter- and intra- device variability, since only a countable number of ions are involved in the filamentation process and higher noise

floor (due to low switching voltages). Regardless, these effects can be potentially reduced with better material systems, i.e. materials with larger open-circuit voltage and photostability.

5.4 Summary

To summarise, in this part of the chapter I report complex light-matter interaction in chalcogenide phase change materials based on nanoscale crossbar devices. These results show that the photoresponse of phase change materials is not limited to only photothermal effects. Although illumination induces photocrystallization, this effect contributes minimally to the extracted device photocurrent (~0.4 %). Indeed, in this chapter, I have reported strong photoconductive effects in both the amorphous and crystalline states of a phase change material. I also find that the contribution of photothermal and photoconductive effects to the net photoresponse can be tuned through device engineering. Photovoltaic effects are also observed in such devices, effects that mean that phase change devices for photonic applications could potentially be self-powered. Moreover, a transient response study reveals that the photodetection bandwidth and photo-responsivity are tunable based on the state of the phase change material, enabling the development of tunable photodetectors. This chapter also reveals the stability of phase change materials to strong irradiance (i.e. absence of photostructural effects that may degrade the material. Recall, photostructural effects were observed in $GeSe_3$ thin films in the previous chapter). Thus, not only the results shown in this chapter help in advancing the understanding of photo behavior of phase change materials but also offers exciting opportunities to build new device architectures and develop new applications for these remarkable materials. Two examples of new devices concepts are demonstrated: a tuneable photodetector and a spiking detector.

5.5 Contribution Statement

All steps of device fabrication and characterization were carried-out by the author. 1 μm by 1 μm bottom electrode Pt devices were fabricated by Dr Yat-Yin Au (University of Exeter).

Chapter 6: Conclusions and Outlook

Conclusions and Outlook

6.1 Overall Summary

Device scaling is a challenging problem to tackle for future silicon-based electronic and optoelectronic technologies due to irresolvable quantum effects and increased power dissipation at very small length scale. In this context, two-dimensional and phase change materials have attracted wide interest owing to their unique set of material properties and fabrication compatibility. The work described in thesis details unconventional nanoscale device architectures utilizing two-dimensional and phase change materials, and studies their fundamental behavior to an external stimulus, such as strain, heat, and light, utilizing both modeling and experimental tools.

The first results chapter (chapter 3) illustrates the concept of graphene nano-gap electrodes. Such electrodes enable contacting nanoscale objects, for example, nanocrystals and single molecules that cannot be achieved efficiently with conventional metallic electrodes. This makes them one of the few approaches towards the development of molecular electronics and test-beds for fundamental studies. Devices studied here are graphene ribbons that are spaced sub-5 nm apart using the feedback controlled electroburning technique. This technique is unconventional, therefore the first part of the chapter discusses the rudiments of this technique for nano-gap fabrication. Crucially, studies were carried-out on the following themes: (a) the gap formation mechanism and uniformity and (b) the effect of substrates, and atmospheric conditions on the gap formation. Two new techniques are then proposed to visualize the nano-gaps as the use of conventional tools for characterization become increasingly difficult at such length scales. In the second part of this chapter, using phase change material in the nano-gap as the demonstrator device, the scaling limit of phase change memories is explored. Such devices are fabricated using a lithography-free self-alignment approach that uses sacrificial burning of a top polymer layer for

direct placement of the phase change material in the nano-gap. While such memory devices show energy-efficient performance, it is noted that for gap sizes approaching 1 nm the switching is dominated by carbon chain formation and not phase change in the bridging phase change material, creating a fundamental scaling limit for potential devices.

The following chapter (chapter 4) describes the effect of external perturbations on the electronic properties of two-dimensional materials, such as strain. Two-dimensional materials are uniquely-suited for flexible and wearable technologies due to their two-dimensional geometry, where they will also bear a certain degree of variable strain. A new technique based on Kelvin Probe Microscopy is demonstrated to capture, in a single-shot the effects of strain on the band-structure of two-dimensional materials. This technique could be a major advance in strain characterization tools because it overcomes the limitations (materials, resolution and substrate effects) of commonly used optical spectroscopy tools. For example, the effect of strain in both graphene and multilayered WS_2 have been studied, which are otherwise difficult with optical spectroscopy because of their zero and indirect bandgaps, respectively. Furthermore, the nanoscale resolution enabled by this technique provides a study of the nature and magnitude of junctions in atomic thick heterostructures, which is missing with conventional tools. The strain sensitivity of two-dimensional materials is then explored in a proposed device concept of a strain-effect transistor. Such a device uses reversible volume changes from reversible amorphous-crystalline phase transition. By overlaying a two-dimensional material on a phase change material, cyclic strains can be reversibly induced to tune the electronic properties, such as bandgap which governs a transistors operation. A new chalcogenide glass $GeSe_3$ is explored for the underlying phase change material. It is found that $GeSe_3$ thin films can undergo ~23% volume change from thermal exposure, which is significant for the proposed application. Additionally, the optical properties of $GeSe_3$ thin films are studied, and its volume change combined with the changes in

its optical properties is used to demonstrate reflective solid-state displays, down to a single pixel level. A lossless and tunable photonic resonator is also demonstrated.

Finally, the last results chapter (chapter 5) reveals the complex light-matter interaction in chalcogenide phase change materials, using nanoscale crossbar devices. The results discussed here use a custom-built probe station for high-bandwidth measurements. The measurements highlight that the photoresponse of phase change materials is not limited to only photothermal effects. Although illumination induces photocrystallization, this effect contributes to minimally (~0.4 %) to the extracted device photocurrent. Indeed, strong photoconductive effects are reported in this chapter in both the amorphous and crystalline state of phase change materials. It is observed that the contribution of photothermal and photoconductive effects to the net photoresponse can be tuned through device engineering; Pt electrodes reduce photothermal effects over ITO due to their greater thermal conductivity (more efficient heat sink). For the given device design, the amorphous state of the phase change material is found to be more photo-active than the crystalline state. Photovoltaic effects in such devices are also reported, effects that mean that the phase change devices for photonic applications could potentially be self-powered. Moreover, a transient response study reveals that the photodetection bandwidth and photo-responsivity are tunable based on the state of the phase change material, enabling the development of tunable photodetectors. The gain of the device in the amorphous states exceeds unity highlighting the role of trap states in this material. The photodetection capability of phase change materials in terms of responsivity is on par with commercial silicon detectors. Phase change materials are found to be stable to strong irradiance (i.e. absence of photostructural effects), favoring their use for photonics technologies. Finally, a spiking detector device concept is illustarted that utilizes the light driven threshold switching in chalocgenide glasses, such as phase change materials. Such devices can be used in the development of artificial retinas.

6.2 Future Work

The following is a chapter wise break-down of the research planned in near the future and other potential ideas for others to try.

Chapter 3 (Graphene Nano-electrodes):

The initial findings on carbon filamentation reported in this chapter need further investigation by techniques such as atomic-scale imaging to verify the nature of these atomic chains, as well as the influence of the actual material in the gap on the formation of these chains. Although the potential formation of graphene filaments poses challenges to the development of graphene-based nanoelectrodes, it also offers exciting opportunities to study charge transport in atomic carbon chains. The formation of carbon chains (cumulene and polyyne chains) have been observed using transmission electron microscopy. If these structures could be controllably formed between graphene nanoelectrodes, they could serve as a test bed for the observation of a plethora of transport phenomena predicted in atomic chains and could further also be extended for various applications such as all carbon-based transistors[109,127,259].

The self-alignment technique can be used to place other functional materials in the nano-gaps, such as chromophores, which can be used as nanoscale light sources. In particular, the device based on single molecules for molecular electronics could benefit as the yield of the devices with molecules bridging the gap can be improved from trenches directing the flow of molecules (contained in a solvent) into the gap. Furthermore, graphene nano-gaps can be used in their very form for gas sensing applications, due to graphene's large surface area and optimal absorption energy of gas molecules on its surfaces/edges. The analyte of interest, when absorbed on graphene, would change the doping levels of the electrodes, magnitudes of which could translate into changes in the tunneling current.

The feedback controlled electroburning can be used to produce nano-gap in ribbons of other materials including phase change materials. Nano-gap in ribbons of crystalline phase change

material is particularly appealing as it can be harnessed for an enhanced photo-voltage response (likely much greater than metal-based detectors) due to higher intrinsic plasmonic and thermoelectric behavior in such materials. Such devices can be used as self-powered detectors, for photodecomposition of chemicals and for bio-sensing.

Chapter 4 (Strain Effects: Characterization and Applications):

The initial findings of strain effects in two-dimensional materials discussed in this chapter need further investigation using atomic-scale simulations, as well as finite elemental modeling to verify the nature of bands-alignment and strain transfer. Nevertheless, the use of Kelvin Probe Microscopy can be used for strain characterization for beyond two-dimensional materials systems. For example, in studies that require the realization of strain modulation in individual components in a multicomponent system with a nanoscale resolution. A case in point could be an alloy with grains of multiple stoichiometries. Furthermore, it could be used in the study of spatial strain distribution in a homogeneous system, namely strain response of dislocations and grain boundaries. The observation of greater sensitivity of the junctions in the two-dimensional heterostructures to solvents can be used in the construction of nanoscale gas and bio-sensors.

The use of insulating two-dimensional material, such as hBN as a heat sink can enable the development of integrated circuits on flexible substrates: hBN layers as thermal layers can prevent local degradation of the substrate, which is a concern in current flexible technologies.

The sensitivity of the electronic properties of two-dimensional materials to strain can be utilized for developing strain-effect transistors. Strain can be induced reversibly through volume changes that occur in phase change materials from amorphous-crystalline phase transition. The lossless phase change material discussed for this application also shows a strong coupling between its structural and optical properties. This can be exploited for the development of tunable optical coatings such as for reflective displays, holograms, optical filters, and smart windows. Such devices

would function from the reversible and non-volatile interferences created in sub-wavelength thin films of the phase change material.

Chapter 5 (Light-Matter Interaction in Phase Change Materials):

The optoelectronic measurements on GeSbTe and GeTe alloy discussed in this Chapter need to be extended to other prototypical phase change materials, such as GeSb, AgInSbTe in order to catalog the composition dependent photoresponse, which is speculated to be different due to the different potential energy landscape of charges between the systems. These mixed-mode measurements and the set-up can however, be extended towards understanding the elusive threshold switching behavior that exists in phase change materials. If the mechanism is truly based on band-profile instability, caused by filling of traps, the use of a third stimulus, which is light should complement the effects of voltage, which is does (discussed in the spiking detector example). A more thorough experimental study is however required to unambiguously understand the physics.

The photoconductive behavior in the phase change materials, particularly photovoltaic can be enhanced using device engineering (choice of contacts); an effect that could mean the photonics applications, in which the material is always exposed to illumination can be made self-powered. The application that can particularly benefit from this could be smart windows.

The tunability in the photo-behavior of the phase change material and other chalcogenide systems can be exploited in developing photodetectors. Particularly of a kind suitable for artificial retinas, in which the photo-sensitivity needs to be adjusted as a function of illumination intensity. In similar lines, alternative optoelectronic devices and methods of photodetection can be realized by utilizing the threshold switching or the amorphous-crystalline phase change transition in chalcogenide glasses and phase change materials, respectively. Given such devices do not function purely on charges as current platforms, they could enable very high dynamic range for photo-detection.

List of Figures

Chapter 1

Chapter 2

Chapter 3

Chapter 4

Chapter 5

Appendix

Appendix

A1. Chemical Vapour Deposition Synthesis (referred from Chapter 1)

WS_2:

WS_2 was synthesized using S (300 mg) and WO_3 (200 mg) precursors (≥99.5%, Sigma-Aldrich) on a 2 by 2 cm silicon chip (300 nm SiO_2) with a two furnaces system. Before insertion into the CVD quartz tube, the chip was thoroughly cleaned through sonication in acetone (15 min), in 2-propanal (15 min), followed by O_2 plasma cleaning (5 min). The tube with precursors and substrate inside was then put into the two furnaces, with S in first furnace and WO_3 in second. The system was flushed with 500 sccm Ar for at least 30 min (inorder to remove air), following which the first and second furnaces were set to ramp to 180 ℃ and 1170 ℃. The reaction process then lasted for 3 mins (at Ar flow at 250 sccm and with the two furnaces stable at their set temperatures). After 3 mins, the reaction was force stopped by decreasing Ar flow to 10 sccm, meanwhile, the first furnace was heated to 450 ℃ inorder to evaporate remaining S, and the second furnace was cooled to room temperature. When the temperature of the second furnace reached 950 ℃, Ar flow rate was ramped up of 500 sccm in order to blow away the S. Once the second furnace reached room temperature, the silicon chip was taken out of the chamber and processed for characterization.

Graphene:

Large area uniform graphene was synthesized in a single furnace system on a polished copper foil. Methane was introduced as the gaseous carbon source for graphene nucleation and growth. The copper foil besides serving as the substrate also served as the catalyst. The whole system was first flushed with argon (1000 sccm), hydrogen (500 sccm) and methane (50 sccm) for 30 mins inorder to get rid-off any air in the quartz tube. The flow was then modulated (methane flow completely stopped, while Ar at 600 sccm and H2 at 300 sccm) and the temperature was ramped-up at 50℃/min to 1060 ℃ (see Ref[260] for temperature profiles) inorder to anneal Copper. Graphene growth was then carried-out at 1060 ℃ by introducing 20 sccm of methane into the tube. The growth lasted for 1 Hr, after which the furnace was moved away and the sample was allowed to gradually cool to room temperature using table fans.

A2. Sputter-deposition- best optimized recipes (referred from Chapter 2)

Target	Working Pressure (mtorr)	RF Power (W)	Rate (nm/minute)
$Ge_{22}Sb_{22}Te_{55}$	3.6e-3	30	7.6
$Ge_{40}Te_{60}$	3.6e-3	30	2.4
$Ge_{96}T_4$	3.6e-3	30	8.0
$Ag_{5.4}In_{4.4}Sb_{63.5}Te_{25.6}$	3.6e-3	30	2.8
$GeSe_3$	3.6e-3	30	4.9
ITO	3.6e-3	30	3.8
SiO_2	3.6e-3	130	0.8
Ta	9.8e-3	120	4.6
Pt	9.8e-3	40	4.2
Ag	3.6e-3	30	4.5

A3. LabView Scripts and Matlab Codes (referred from Chapter 2)

For clarity, the scripts are enclosed in the following link.

https://bit.ly/2S0LVl2

For LabView scripts, LabView software is a prerequisite, while the Matlab scripts are readily accessible using software such as notepad. Declaration: All Codes except in the folder Transfer matrix and Mixed Mode Measurements were fully written by the author

A4. Nanoscale control on the gap size (referred from Chapter 3)

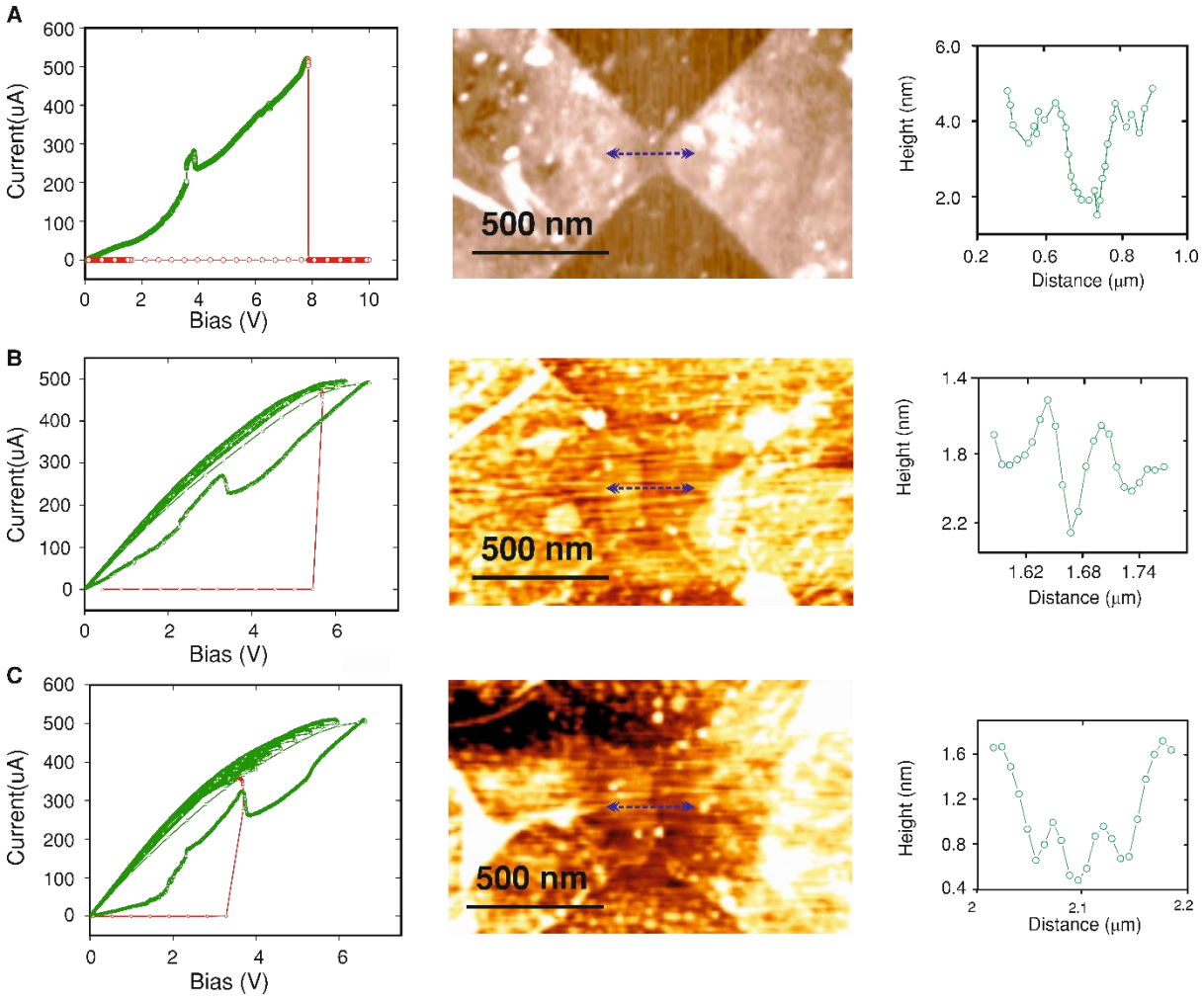

Controlled Feedback Electroburning Cycles: (A) Gap evolution without feedback. Graphene was electroburnt with a single cycle producing a 163 nm gap. (B) Gap evolution with controlled feedback. Graphene was electroburnt first by using feedback, which was triggered off at a threshold voltage of 5.5 V. The gap size is 62.4 nm, and (C) Gap evolution with controlled feedback. Graphene was electroburnt first by using feedback, which was triggered off at a certain cycle threshold voltage of 3.75 V. The gap size is 20 nm. Although we are able to demonstrate control on the gap size by optimizing the feedback parameters, the results need further investigation and is a subject of my current study

A5. Features suggesting Q.I and Columb Blockade Effect (referred from Chapter 3)

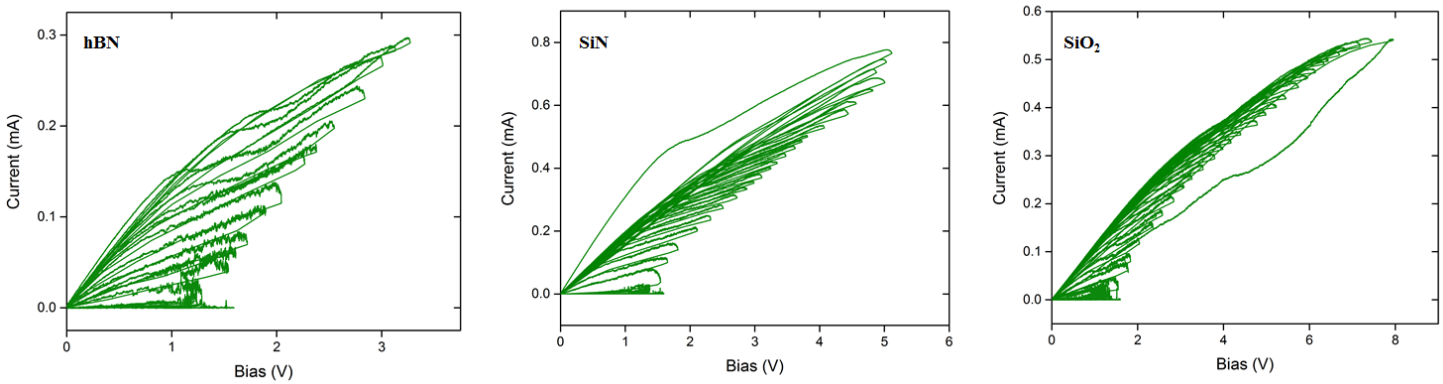

Example electroburning cycles of graphene on h BN, Si_3N_4, and SiO_2 substrates: Current spikes which are indicative of carbon chains (s) can be observed on all the three substrates. Also note the pinch-off behavior is preserved on all three substrates, indicative of graphene's electronic properties remaining uninfluenced by substrate choice

A6. Kelvin Probe Micrographs (referred from Chapter 3)

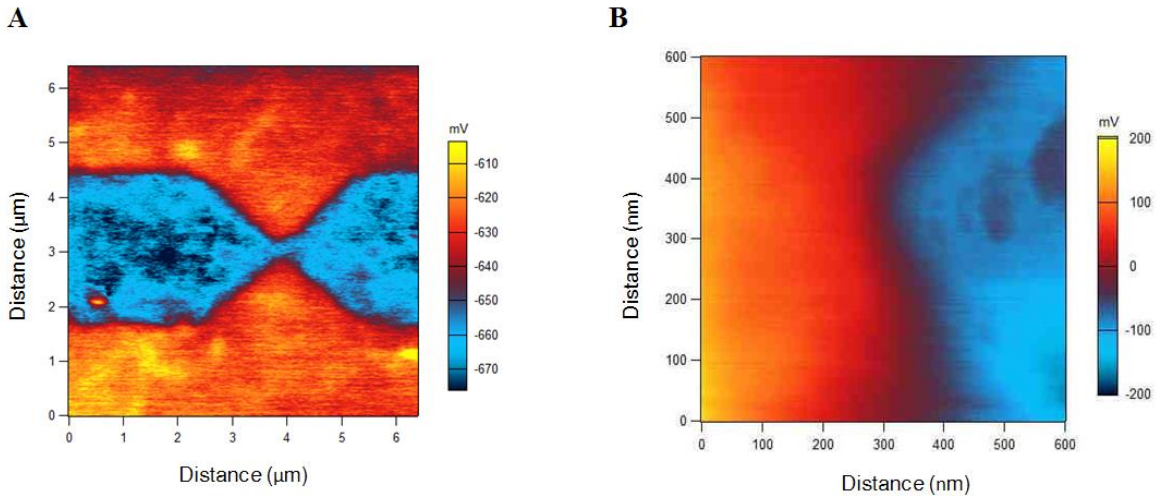

Kelvin Probe Micrographs: (A) Kelvin Probe Micrograph of a graphene nano-gap device under the absence of an external bias. A uniform contrast is suggestive of the graphene's homogeneity, and (B) Kelvin Probe Micrograph of a graphene nano-gap device biased on the left graphene lead using an AFM probe. A sharp drop in the potential drop is observed at the gap

A7. Switching Characteristics (referred from Chapter 3)

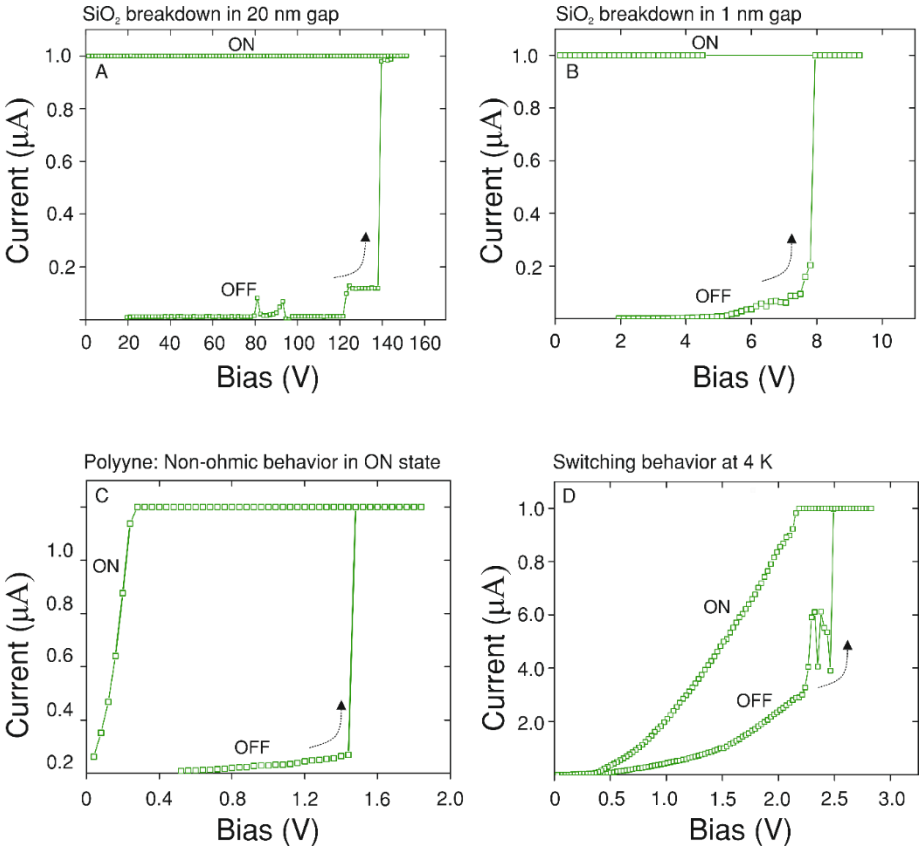

(a) Dielectric breakdown of SiO_2 in a ~20 nm graphene nano-gap, (b) dielectric breakdown of SiO_2 volume placed in a 1 nm sized graphene nano-gap, (d) a typical SET I-V characteristic of a graphene nano-gap in ambient conditions; the ON state is non-linear, and (d) switching characteristics at 4 K temperature.

A8. Switching Characteristics in more devices

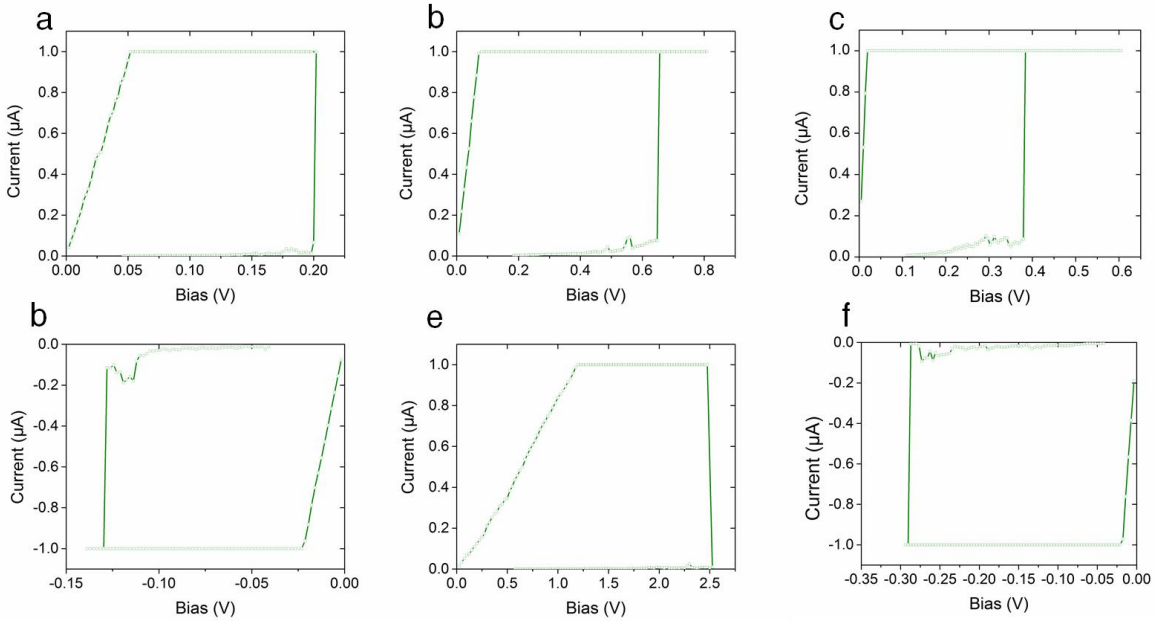

8.1: (a to f) SET I-V characteristics of six different graphene nano-gap devices in ambient conditions

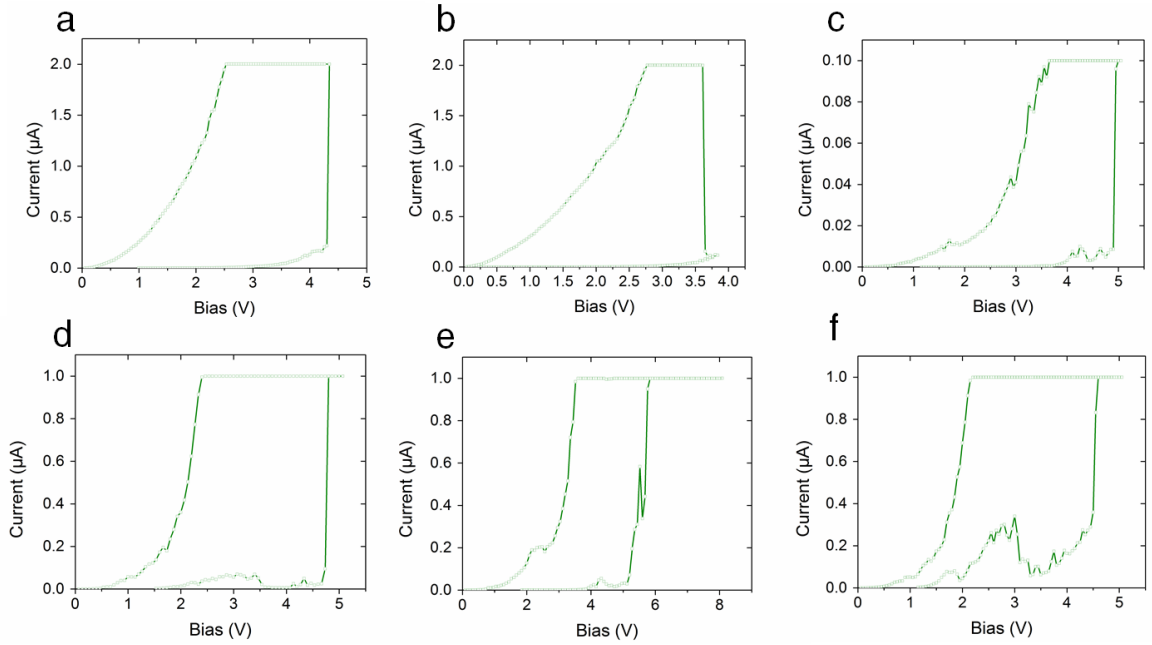

8.2: (a to f) SET I-V characteristics of six different GST-graphene nano-gap devices of gap size > 20 nm, measured in ambient conditions

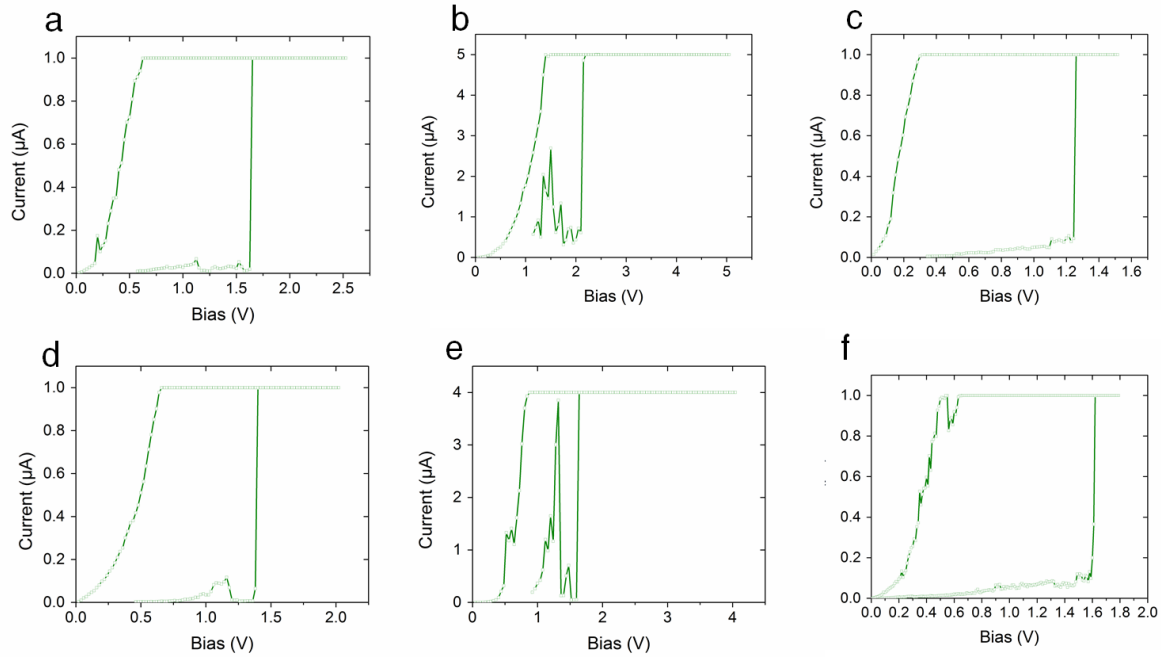

8.3: (a to f) SET I-V characteristics of six different graphene nano-gap devices in high vacuum (10^{-7} bar)

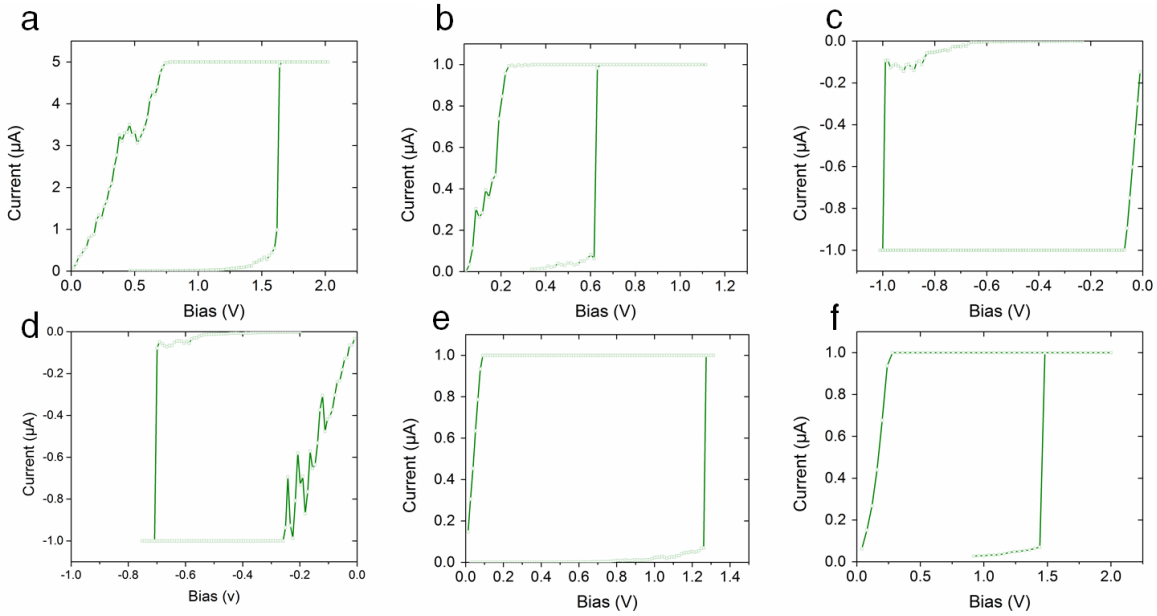

8.4: (a to f) SET I-V characteristics of six different graphene nano-gap devices on SiN substrate, measured in ambient conditions

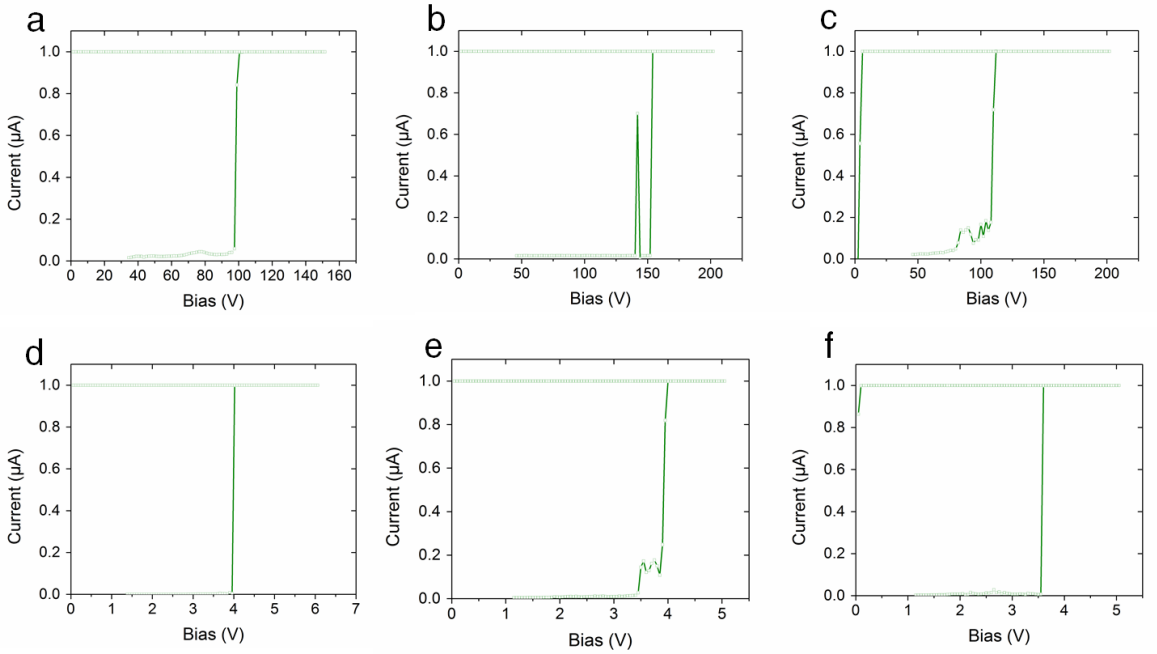

8.5: a to c) Dielectric breakdown of SiO_2 in > 20 nm graphene nano-gap devices, and (d to f) dielectric breakdown of SiO_2 volume placed in sub-5 nm sized graphene nano-gap devices in ambient conditions

A9. Work Function Extraction (referred from Chapter 4)

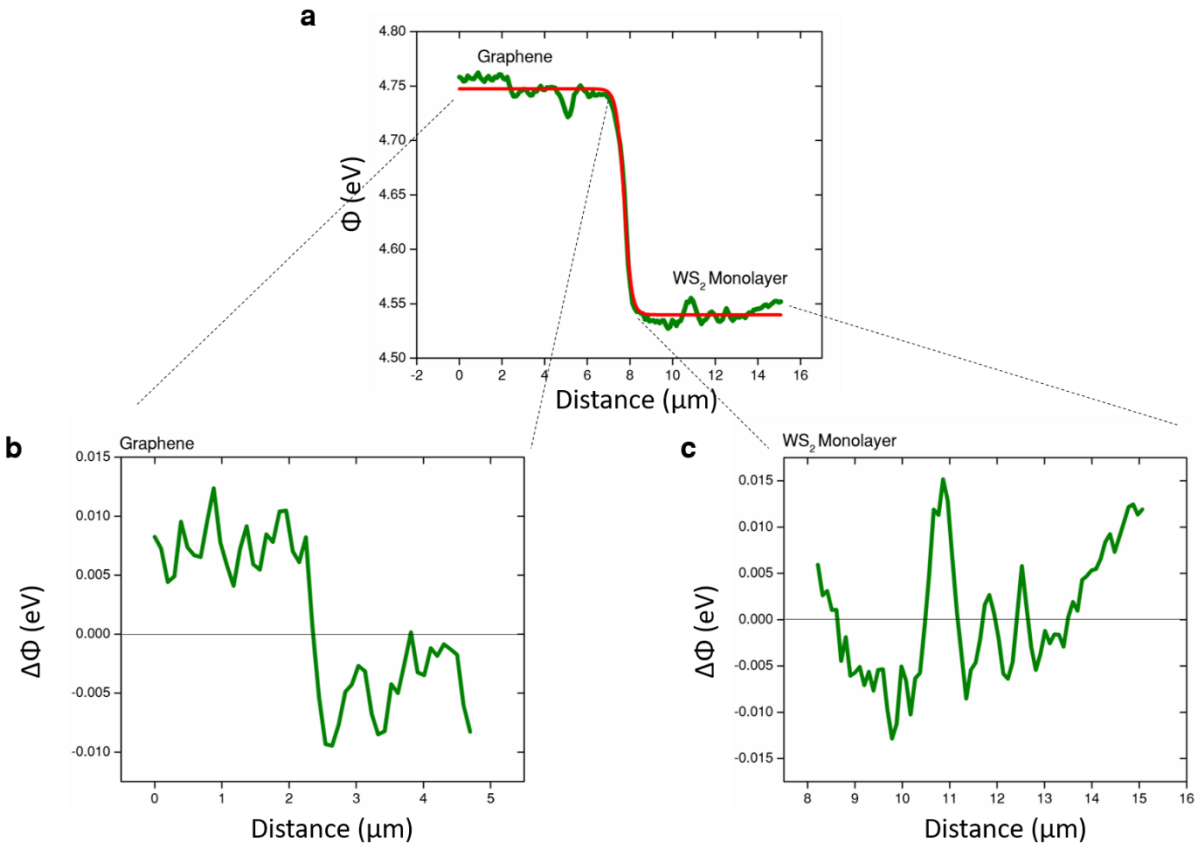

Work Function Extraction. (a) First the work function from the raw data (CPD) is computed using the equation $\Phi_{sample}(x,y) = \Phi_{tip} - e \times CPD(x,y)$, where Φ is the work function and then the work function line (green trace) scan is fitted using a sigmoidal function (red trace). Best fitting parameters for the Y-Axis are used as the work functions of the two-dimensional materials. (b and c) Residual plots illustrating the error bars. Here work function derived from the fitting is subtracted from the measured work function at each point of the scan.

A10. Strain Effect Transistor: Device Concept (referred from Chapter 4)

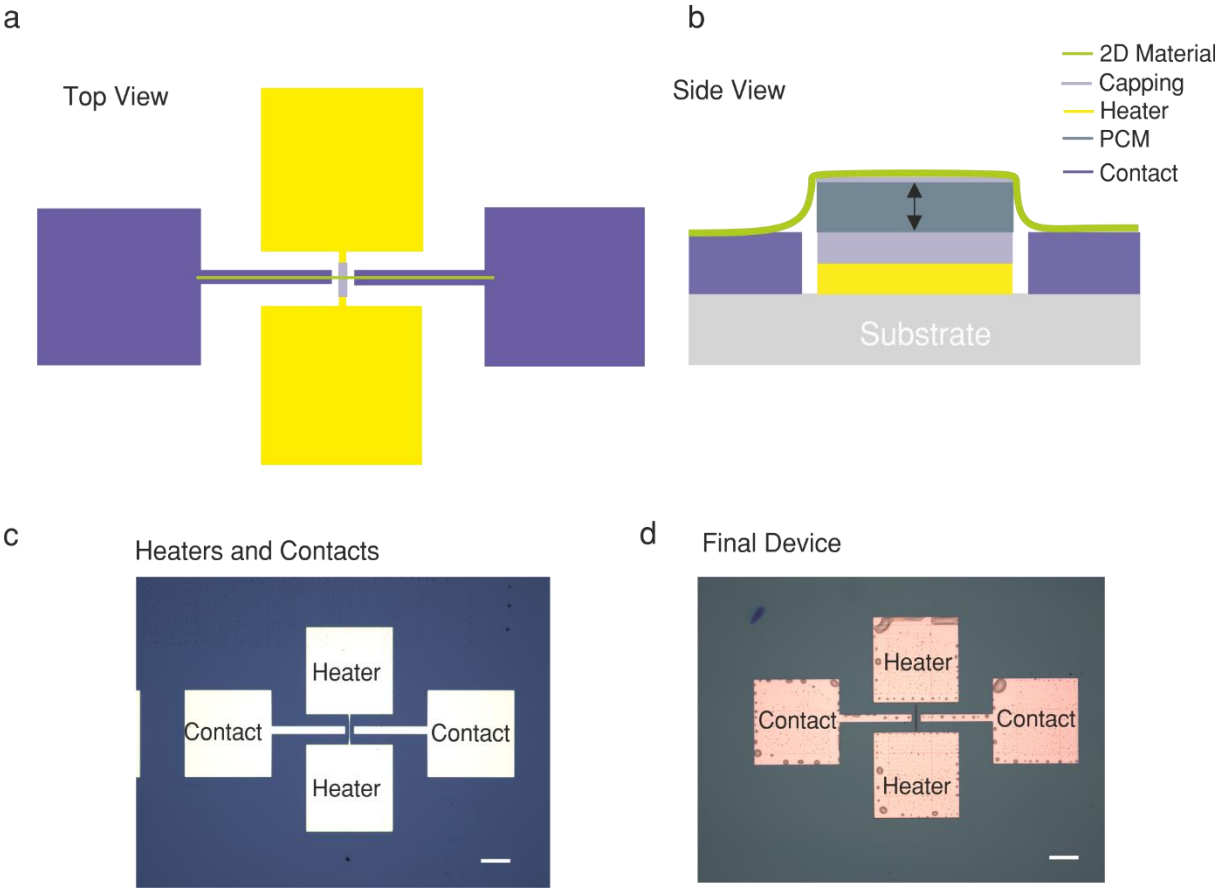

Strain-effect transistor proposed design: (a) Top view of a 4 terminal device. (b) Side view of the active region of the device. A two-dimensional material is overlaid on the phase change material (PCM). The PCM is switched between the amorphous and crystalline states using the underlying heaters. The change in the thickness of PCM results in strain on the two-dimensional material. Changes in the electronic properties from strain are recorded on a source-meter using the contacts. (c) An optical micrograph of the sample after deposition of the heaters. For this, a 100 nm trench was etched for heaters in the 300 nm thick thermally grown SiO_2 that exists on a Si wafer. The heater 75 nm NiCr was then sputter deposited. Plasma-enhanced chemical vapor deposition was carried-out at 250 ^{0}C for the growth of 100 nm SiO_2 layer from silane and NO_2 precursors. The SiO_2 covering the contact and heater pads was etched using reactive ion etching in order to access the pads for electrical connections. (D) An optical micrograph of the final device. A micron thick PCM was sputter-deposited on the finger heater. A 10 nm ZnS-SiO_2 was then sputter deposited to cap the PCM from oxidation. This layer is chosen for minimal stress effects Electrical connection to the heater and the contacts pads are then made by wire-bonding. Besides electrical conductance measurement, Raman measurement was also carried-out to ascertain the strain effects in the two-dimensional material. In the first set of devices made, the common most cause of device failure was delamination of PCM from poor adhesion and heater (fingers) cracking due to increased heating. The scale bar is 50 um.

A11. $GeSe_3$ Compositional Characterization (referred from Chapter 4)

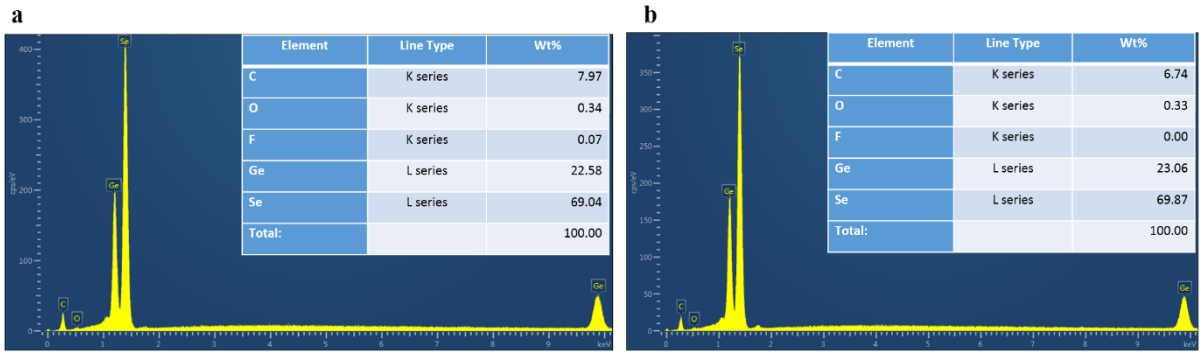

Material Analysis. (a and b) Energy dispersive X-ray spectra of a 90 nm thick film before and after thermal annealing at 375 ^{0}C, respectively. The stoichiometry between Ge: Se is close 1:3.

A12. Reflectometry measurements of $Ge_2Sb_2Te_5$ (referred from Chapter 4)

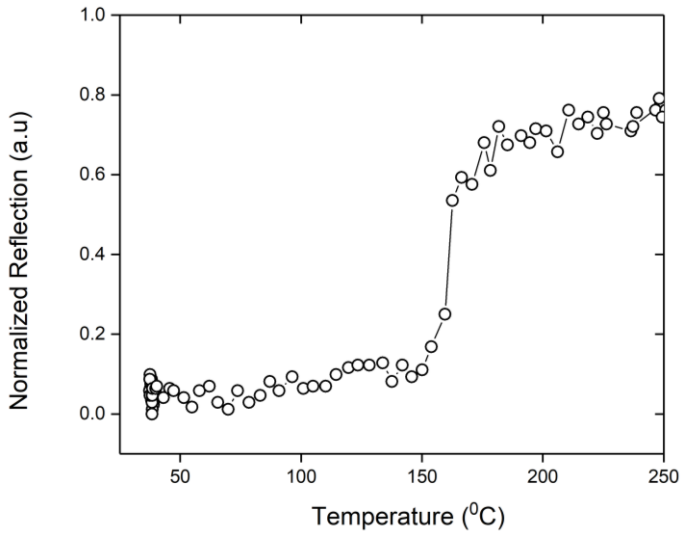

Reflectometry measurements of $Ge_2Sb_2Te_5$ thin film on p-doped Si substrate. The instantaneous change in the reflection at 150 ^{0}C indicates amorphous to crystalline phase transformation

A13. Peak Shifts in $GeSe_3$ films (referred from Chapter 4)

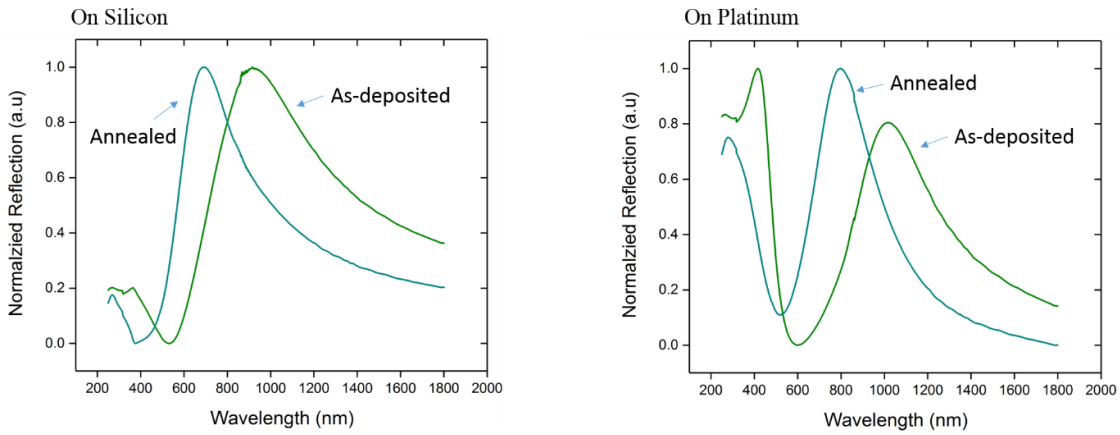

A 90 nm thick $GeSe_3$ film on silicon and platinum substrate. Annealing at 360 ^{0}C in ambient conditions for 6 mins results in the blue-shift of the peak by ~27 %

A14. Optical Spectra of Phase Change Materials (referred from Chapter 4)

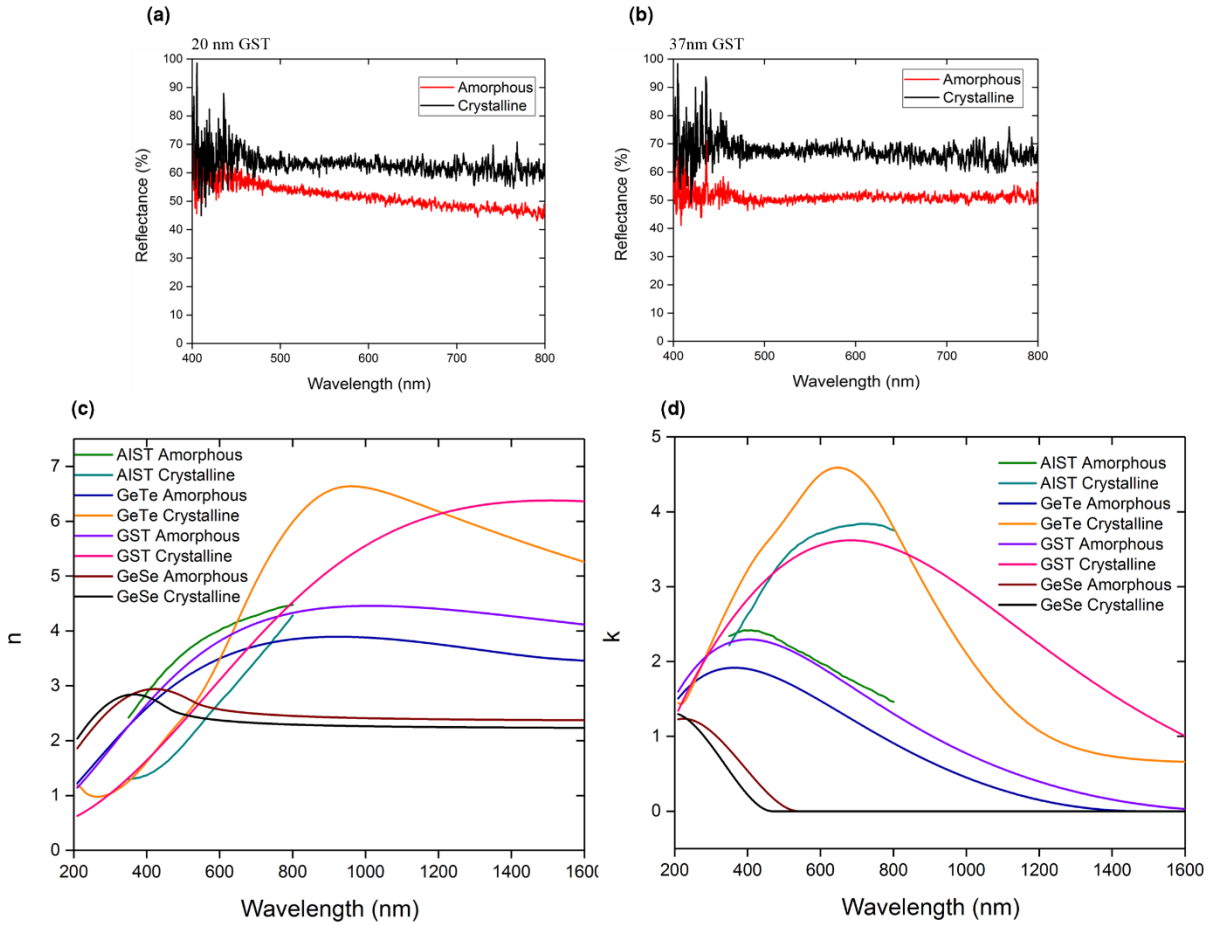

(a and b) Normalized reflection spectra of 20 nm and 37nm GST thin film on a p-doped Si chip, respectively. No resonance peaks can be observed due to the lossy nature of GST. Annealing at 360 ^{0}C also brings no significant change in the spectra. The films were sputter-deposited under exactly similar conditions as $GeSe_3$ films. (c and d) Comparison of the real (n) and imaginary (k) components of the complex refractive index of $Ge_{15}Se_{75}$ against prototypical chalcogenide glasses: $G_{22}Sb_{22}Te_{55}$, $Ag_{5.4}In_{4.4}Sb_{63.5}Te_{25.6}$, and $Ge_{40}Te_{60}$.

A15. Structural change under UV exposure (referred from Chapter 4)

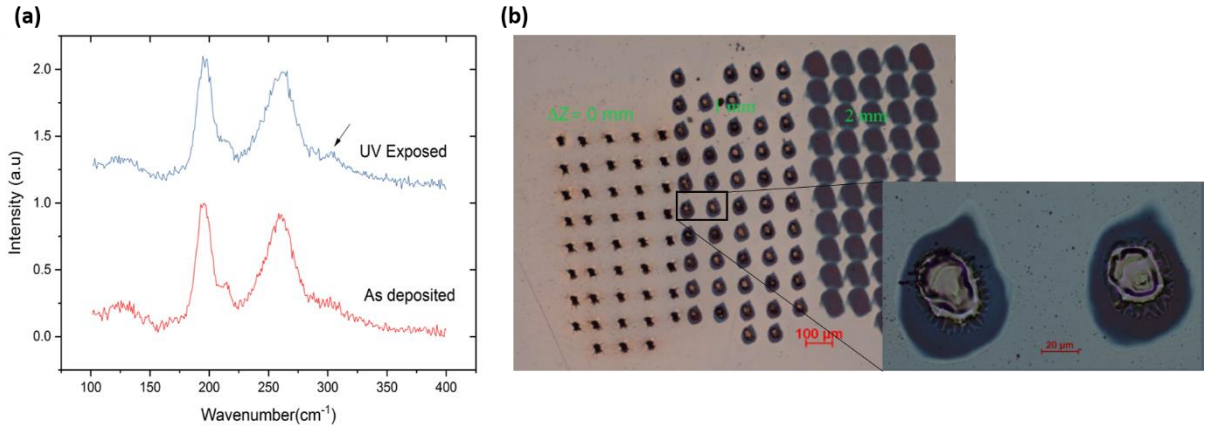

(a) Raman spectra of the film optically exposed to continuous UV Exposure. Ge-Ge segregation is evident at 302 cm^{-1} and (b) optical micrographs of a $GeSe_3$ film on exposure to pulses of the UV laser. At high power the film ablates (see inset) and even higher power the Si sample degrades.

A16. Photo-stability of GeTe alloys (referred from Chapter 5)

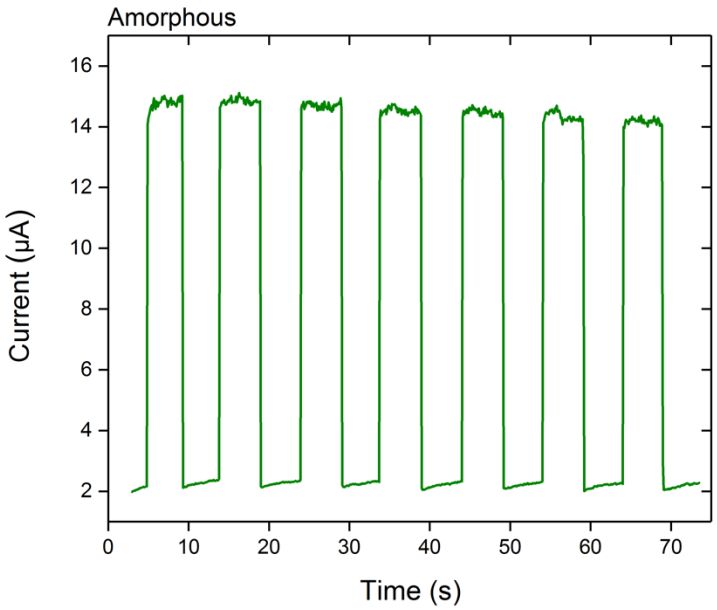

Photo-stability of $Ge_{40}Te_{60}$. Current vs time characteristics of a device: Ta (10nm)/Pt (50nm)/GeTe (19nm)/65 nm (ITO) under pulsed illumination (637 nm/1 mW) in the amorphous state of $Ge_{40}Te_{60}$. Note that the dark current is stable after every measurement, which is indicative of the absence of photostructural effects that are understood to alter the dark current. The slight deviation in the photo-current is from the drift in the laser beam away from the sample. Photoresponse in GeTe films is weaker than in the GeSbTe films, highlighting the photoresponse to be sensitive to the material composition.

A17. Multiple Switching Cycles (referred from Chapter 5)

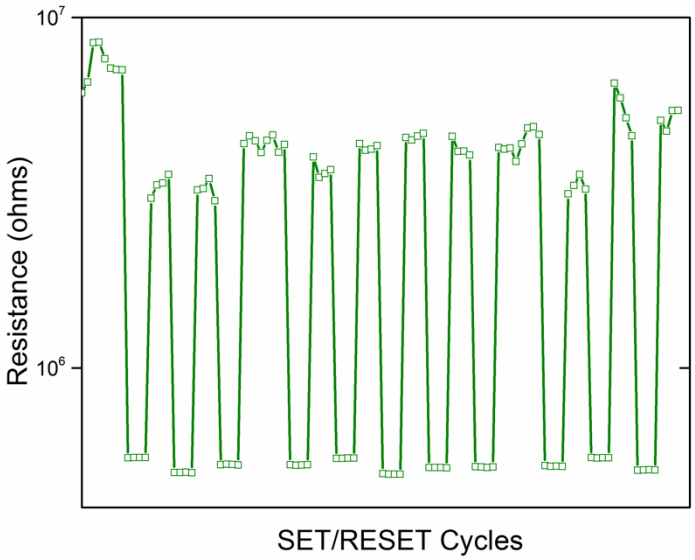

Cyclic Switching: A crossbar device (IT0 (20nm)/GST(15nm)/ITO(20nm)) with active region 1um by 1um crystallized (using standard IVs) and amorphized (4 V, 50 ns Wide, 5 ns rise and fall edge, single pules) multiple times. An order magnitude change in resistance is observed from phase transformation.

A18. $GeSe_3$ based resistive memories (referred from Chapter 5)

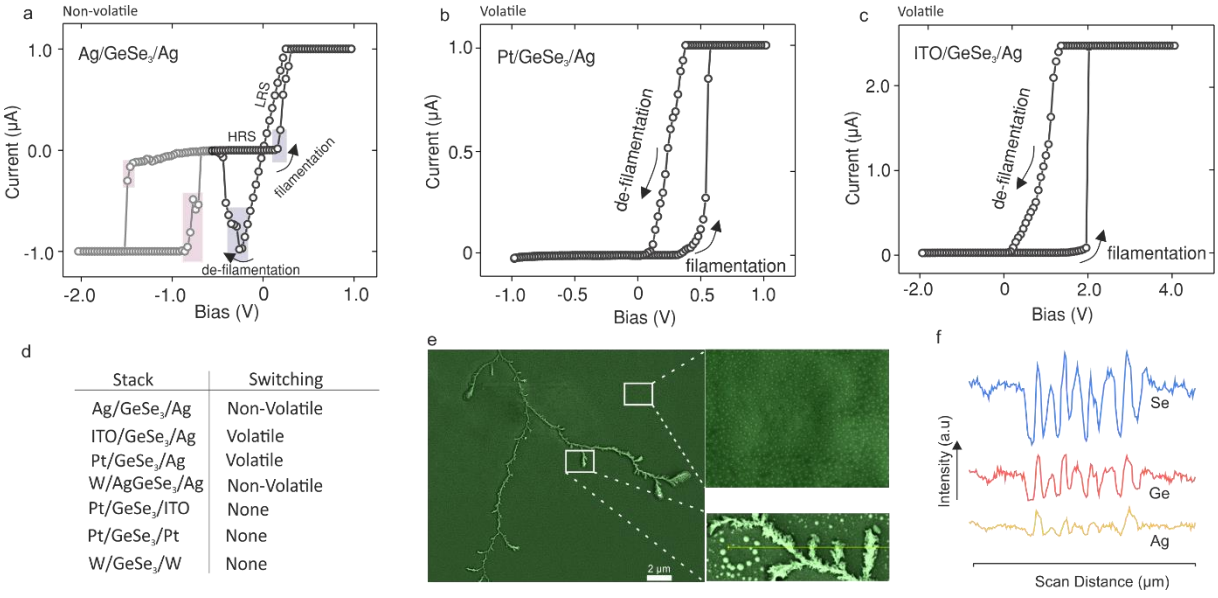

(a to d) Non-volatile and volatile switching characteristics of $GeSe_3$ sandwiched cross-bar devices. (e) Colored SEM micrograph of an Ag/$GeSe_3$ film. Note that Ag dissolves as nanoparticles in $GeSe_3$ (top inset). Under an electric field (applied using two tungsten probes) a filament forms (bottom inset), which is Ag rich and electrically conductive as shown in (f).

Publications, Patents, and Conferences

The direct contributions of this thesis are summarised in the following list of writings.

Publication in peer-reviewed journals

Syed Ghazi Sarwat, Pascal Gehring, Gerardo Rodriguez Hernandez, Jamie H. Warner, G. Andrew D. Briggs, Jan A. Mol, and Harish Bhaskaran, 'Scaling Limit of Graphene Nano-electrodes', Nanoletters, 17 (6) 2017

Syed Ghazi Sarwat, 'Materials Science and Engineering of Phase Change Random Access Memories', Materials Science and Technology, (33) 2017

Syed Ghazi Sarwat, Martin Tweedie, Benjamin F. Porter, Yingqiu Zhou, Yuewen Sheng, Jan Mol, Jamie Warner, and Harish Bhaskaran, 'Revealing Strain-Induced Effects in Ultrathin Heterostructures at the Nanoscale', Nanoletters, 18 (4) 2018

Syed Ghazi Sarwat, Nathan Youngblood, Yat-Yin Au, Jan A. Mol, C David Wright, and Harish Bhaskaran, 'Engineering Interface-Dependent Photoconductivity in $Ge_2Sb_2Te_5$ Nanoscale Devices', ACS Applied Materials and Interfaces, 10 (51) 2018

Publication with co-authorship

Yingqiu Zhou, **Syed Ghazi Sarwat**, Harish Bhaskaran, Jamie Warner. 2018, 'Grain Boundaries Mediated Charge Transport in Monolayer WS_2, ACS Applied Materials and Interfaces, 11 (10) 2018

Martin Tweedie, Yuewen Sheng, **Syed Ghazi Sarwat**, Wenshuo Xu, Harish Bhaskaran; Jamie Warner. 2018, 'Inhomogeneous Strain Release during Bending of WS_2 on Flexible Substrates', ACS Applied Materials and Interfaces, 10 (45) 2018

Wenshuo Xu, Sha Li, Si Zhou, Jakyung Lee, Shanshan Wang, **Syed Ghazi Sarwat**, Xiaochen Wang, Harish Bhaskaran, Mauro Pasta, and Jamie H. Warner., 'Large dendritic monolayer MoS_2 grown by atmospheric pressure chemical vapor deposition for electrocatalysis', ACS Applied Materials and Interfaces, 10 (5) 2018

Publication in preparation

Syed Ghazi Sarwat, Benjamin Porter, Yuewan Sheng, Jamie H. Warner, and Harish Bhaskaran, 'Manufacture and Metrology of Graphene Nano-gap Electrodes', 2018

Syed Ghazi Sarwat, Zenguangg Cheng, Nathan Youngblood, and Harish Bhaskaran, 'Strong Optostructural Coupling in GeSe Thin Films', 2018 (Under review)

Eugene Soh*, **Syed Ghazi Sarwat*** and Harish Bhaskaran, **'**High-Resolution Kelvin Microscopy Probes Using Filamentation in Amorphous Carbon', 2018 (* equal contribution)

Syed Ghazi Sarwat*, Yingqiu Zhou*, Jamie H. Warner, and Harish Bhaskaran, 'Optoelectrostatics Influenced Performance of Ultrathin Heterostructures', 2019 (Under Review)

Syed Ghazi Sarwat, and Harish Bhaskaran, 'Light Modulated Switching Dynamics in Ultra Low Power Resistive Memories', 2019

Patents

Syed Ghazi Sarwat, Gerardo Rodriguez Hernandez and Harish Bhaskaran, 'An Optoelectronic device Using Phase Change Materials', 2017 (PCT/GB2018/051198)

Syed Ghazi Sarwat, Zenguangg Cheng, Nathan Youngblood, and Harish Bhaskaran, 'Tuneable Optical Coating', 2019

Conferences

'Nanoelectronics Using Low Dimensional Materials' in IBM Zurich, Switzerland, 2019 (Invited talk)

'Light-Matter Interaction in Phase Change Materials' in the European Phase Change and Ovonic Symposium, Catania, Italy, 2018 (Oral Presentation)

'Phase Change Materials for optical applications' in the 2nd International Symposium on Doped Amorphous Chalcogenides and Devices, Lake District, UK, 2018 (Oral Presentation)

'Two-dimensional Materials for Nanoelectronics' in the Wearable and Flexible Technologies Symposium on Flexible Electronics, 2018

'Graphene Nano-gaps: Performance and Scaling Limits' in the International Union of Materials Research Societies, Bangalore, India 2017 (Oral Presentation)

'Ultimate Scaling Limit of nanoscale devices: graphene nanoelectrodes' in the International Symposium for Research Scholars, Chennai, India 2017 (Poster Presentation)

'Truly Flexible Technologies' in the Wearable and Flexible Technologies Symposium on Flexible Electronics, 2017

'Scaling Limit of Graphene Nano-electrodes' in the 28th Micromechanics and Microsystems Workshop, Sweden, 2017 (Poster Presentation)

'Ultimate Scaling Limit of nanoscale devices: graphene nanoelectrodes' in the 43rd International Conference on Micro and Nano-Engineering', Portugal 2017 (Poster Presentation)

Bibliography

(1) Meena, J. S.; Sze, S. M.; Chand, U.; Tseng, T.-Y. Overview of Emerging Nonvolatile Memory Technologies. *Nanoscale Res. Lett.* **2014**, *9*, 526.

(2) Chen, T. C. Challenges for Silicon Technology Scaling in the Nanoscale Era. *ESSCIRC 2009 - Proc. 35th Eur. Solid-State Circuits Conf.* **2009**, 1–7.

(3) Moore, B. G. E. Cramming More Components onto Integrated Circuits. *Electronics* **1975**, *38*.

(4) https://En.Wikipedia.Org/Wiki/Von_Neumann_architecture (Retrieved on 05.09.2018).

(5) Geim, A. K.; Novoselov, K. S. The Rise of Graphene. *Nat. Mater.* **2007**, *6*, 183.

(6) Gupta, A.; Sakthivel, T.; Seal, S. Recent Development in 2D Materials beyond Graphene. *Prog. Mater. Sci.* **2015**, *73*, 44–126.

(7) Das, S.; Robinson, J. A.; Dubey, M.; Terrones, H.; Terrones, M. Beyond Graphene: Progress in Novel Two-Dimensional Materials and van Der Waals Solids. *Annu. Rev. Mater. Res.* **2015**, *45*, 1–27.

(8) Cheon, G.; Duerloo, K.-A. N.; Sendek, A. D.; Porter, C.; Chen, Y.; Reed, E. J. Data Mining for New Two- and One-Dimensional Weakly Bonded Solids and Lattice-Commensurate Heterostructures. *Nano Lett.* **2017**, *17*, 1915–1923.

(9) Https://www.Graphenea.Com/Pages/Graphene-Properties#.W5EY2M5KjIU (Retrieved on 06.09.2018).

(10) Dvorak, M.; Oswald, W.; Wu, Z. Bandgap Opening by Patterning Graphene. *Sci. Rep.* **2013**, *3*, 2289.

(11) https://www.megapixl.com/graphene-sheet-illustration-24493615 (Retrieved on 05.12.2018).

(12) Graphene's Cousin Silicene Makes Transistor Debut. *Nature* **2015**, *518*, 17–18.

(13) Zhao, H., Guo, Q., Xia, F., et al. Two-Dimensional Materials for Nanophotonics Application. Nanophotonics. *Nanophotonics* **2015**, *4*, 128–142.

(14) He, Z.; Que, W. Molybdenum Disulfide Nanomaterials: Structures, Properties, Synthesis and Recent Progress on Hydrogen Evolution Reaction. *Appl. Mater. Today* **2016**, *3*, 23–56.

(15) Geim, A. K.; Grigorieva, I. V. Van Der Waals Heterostructures. *Nature* **2013**, *499*, 419.

(16) Allen, M. J.; Tung, V. C.; Kaner, R. B. Honeycomb Carbon: A Review of Graphene. *Chem. Rev.* **2010**, *110*, 132–145.

(17) Novoselov, K. S.; Mishchenko, A.; Carvalho, A.; Castro Neto, A. H. 2D Materials and van Der Waals Heterostructures. *Science (80-.).* **2016**, *353*.

(18) Zhang, Y.; Zhang, L.; Zhou, C. Review of Chemical Vapor Deposition of Graphene and Related Applications. *Acc. Chem. Res.* **2013**, *46*, 2329–2339.

(19) Niu, T.; Li, A. From Two-Dimensional Materials to Heterostructures. *Prog. Surf. Sci.* **2015**,

90, 21–45.

(20) Radisavljevic, B.; Radenovic, A.; Brivio, J.; Giacometti, V.; Kis, A. Single-Layer MoS2 Transistors. *Nat. Nanotechnol.* **2011**, *6*, 147.

(21) Krasnozhon, D.; Lembke, D.; Nyffeler, C.; Leblebici, Y.; Kis, A. MoS2 Transistors Operating at Gigahertz Frequencies. *Nano Lett.* **2014**, *14*, 5905–5911.

(22) Britnell, L.; Ribeiro, R. M.; Eckmann, A.; Jalil, R.; Belle, B. D.; Mishchenko, A.; Kim, Y.-J.; Gorbachev, R. V; Georgiou, T.; Morozov, S. V; *et al.* Strong Light-Matter Interactions in Heterostructures of Atomically Thin Films. *Science (80-.).* **2013**, *340*, 1311–1314.

(23) Wang, Y.; Xiao, J.; Zhu, H.; Li, Y.; Alsaid, Y.; Fong, K. Y.; Zhou, Y.; Wang, S.; Shi, W.; Wang, Y.; *et al.* Structural Phase Transition in Monolayer MoTe2 Driven by Electrostatic Doping. *Nature* **2017**, *550*, 487.

(24) Song, S.; Keum, D. H.; Cho, S.; Perello, D.; Kim, Y.; Lee, Y. H. Room Temperature Semiconductor–Metal Transition of MoTe2 Thin Films Engineered by Strain. *Nano Lett.* **2016**, *16*, 188–193.

(25) Li, Y.; Duerloo, K.-A. N.; Wauson, K.; Reed, E. J. Structural Semiconductor-to-Semimetal Phase Transition in Two-Dimensional Materials Induced by Electrostatic Gating. *Nat. Commun.* **2016**, *7*, 10671.

(26) Zöpfl, A.; Lemberger, M.-M.; König, M.; Ruhl, G.; Matysik, F.-M.; Hirsch, T. Reduced Graphene Oxide and Graphene Composite Materials for Improved Gas Sensing at Low Temperature. *Faraday Discuss.* **2014**, *173*, 403–414.

(27) Kobayashi, T.; Bando, M.; Kimura, N.; Shimizu, K.; Kadono, K.; Umezu, N.; Miyahara, K.; Hayazaki, S.; Nagai, S.; Mizuguchi, Y.; *et al.* Production of a 100-m-Long High-Quality Graphene Transparent Conductive Film by Roll-to-Roll Chemical Vapor Deposition and Transfer Process. *Appl. Phys. Lett.* **2013**, *102*, 23112.

(28) https://Www.Graphenesq.Com/Whatis/Mass.Asp (Retrieved 06.09.2018).

(29) Ahn, J.-H.; Parkin, W. M.; Naylor, C. H.; Johnson, A. T. C.; Drndić, M. Ambient Effects on Electrical Characteristics of CVD-Grown Monolayer MoS2 Field-Effect Transistors. *Sci. Rep.* **2017**, *7*, 4075.

(30) Song, H. S.; Li, S. L.; Miyazaki, H.; Sato, S.; Hayashi, K.; Yamada, A.; Yokoyama, N.; Tsukagoshi, K. Origin of the Relatively Low Transport Mobility of Graphene Grown through Chemical Vapor Deposition. *Sci. Rep.* **2012**, *2*, 1–6.

(31) https://www.graphenesq.com/whatis/how.asp (retrieved on 06.09.2018).

(32) Chyan, Y.; Ye, R.; Li, Y.; Singh, S. P.; Arnusch, C. J.; Tour, J. M. Laser-Induced Graphene by Multiple Lasing: Toward Electronics on Cloth, Paper, and Food. *ACS Nano* **2018**, *12*, 2176–2183.

(33) Naghdi, S.; Rhee, K. Y.; Park, S. J. A Catalytic, Catalyst-Free, and Roll-to-Roll Production of Graphene via Chemical Vapor Deposition: Low Temperature Growth. *Carbon N. Y.* **2018**, *127*, 1–12.

(34) Kou, L.; Du, A.; Chen, C.; Frauenheim, T. Strain Engineering of Selective Chemical Adsorption on Monolayer MoS2. *Nanoscale* **2014**, *6*, 5156–5161.

(35) Castellanos-Gomez, A.; Roldán, R.; Cappelluti, E.; Buscema, M.; Guinea, F.; Van Der Zant, H. S. J.; Steele, G. A. Local Strain Engineering in Atomically Thin MoS2. *Nano Lett.* **2013**, *13*, 5361–5366.

(36) Roldán, R.; Castellanos-Gomez, A.; Cappelluti, E.; Guinea, F. Strain Engineering in Semiconducting Two-Dimensional Crystals. *J. Phys. Condens. Matter* **2015**, *27*, 313201.

(37) Cho, B.; Hahm, M. G.; Choi, M.; Yoon, J.; Kim, A. R.; Lee, Y. J.; Park, S. G.; Kwon, J. D.; Kim, C. S.; Song, M.; *et al.* Charge-Transfer-Based Gas Sensing Using Atomic-Layer MoS2. *Sci. Rep.* **2015**, *5*, 8052.

(38) Bissett, M. A.; Konabe, S.; Okada, S.; Tsuji, M.; Ago, H. Enhanced Chemical Reactivity of Graphene Induced by Mechanical Strain. *ACS Nano* **2013**, *7*, 10335–10343.

(39) Liu, K.; Wu, J. Mechanical Properties of Two-Dimensional Materials and Heterostructures. *J. Mater. Res.* **2016**, *31*, 832–844.

(40) Hu, L.; Shan, X.; Wu, Y.; Zhao, J.; Lu, X. Laser Thinning and Patterning of MoS2 with Layer-by-Layer Precision. *Sci. Rep.* **2017**, *7*, 15538.

(41) Nozaki, J.; Fukumura, M.; Aoki, T.; Maniwa, Y.; Yomogida, Y.; Yanagi, K. Manipulation of Local Optical Properties and Structures in Molybdenum-Disulfide Monolayers Using Electric Field-Assisted near-Field Techniques. *Sci. Rep.* **2017**, *7*, 46004.

(42) Pieterson, L. Van; Lankhorst, M. H. R.; Schijndel, M. Van; Kuiper, A. E. T.; Roosen, J. H. J. Phase-Change Recording Materials with a Growth-Dominated Crystallization Mechanism : A Materials Overview. *J. Appl. Phys.* **2014**, *083520*.

(43) Raoux, S. Phase Change Materials. **2009**, *39*, 25–48.

(44) Raoux, S.; Xiong, F.; Wuttig, M.; Pop, E. Phase Change Materials and Phase Change Memory. *MRS Bull.* **2014**, *39*, 703–710.

(45) Stanford R.Ovshinsky. Reversible Electrical Switching Phenomena in Disordered Structures. *PRL* **1968**, *21*.

(46) Huang, H.; Zuo, F.; Zhai, F.; Wang, Y. Crystallization Dynamics of As-Deposited Amorphous AgInSbTe Thin Film Induced by Picosecond Laser Pulses. *175401*.

(47) Lee, B.; Shelby, R. M.; Raoux, S.; Retter, C. T.; Burr, G. W.; Bogle, S. N.; Darmawikarta, K.; Bishop, S. G.; Abelson, J. R. Nanoscale Nuclei in Phase Change Materials : Origin of Different Crystallization Mechanisms of Ge2Sb2Te5 and AgInSbTe. **2014**, *063506*, 1–10.

(48) Burr, G. W.; Breitwisch, M. J.; Franceschini, M.; Garetto, D.; Gopalakrishnan, K.; Jackson, B.; Lam, C.; Luis, A. Phase Change Memory Technology. **2010**, *28*, 223–262.

(49) Khulbe, P. K.; Hurst, T.; Horie, M.; Mansuripur, M. Crystallization Behavior of Ge-Doped Eutectic Sb70Te30 Films in Optical Disks. *Appl. Opt.* **2002**, *41*, 6220–6229.

(50) Raoux, Simone, M. W. *Phase Change Matrials: Science and Applications*; Springer, 2009.

(51) Kolobov, A. V; Fons, P.; Frenkel, A. I.; Ankudinov, A. L.; Tominaga, J.; Uruga, T. Understanding the Phase-Change Mechanism of Rewritable Optical Media. *Nat. Mater.* **2004**, *3*, 703–708.

(52) Lai, Y.; Qiao, B.; Feng, J.; Ling, Y.; Lai, L.; Lin, Y.; Tang, T.; Cai, B.; Chen, B. Nitrogen-Doped Ge2Sb2Te5 Films for Nonvolatile Memory. *J. Electron. Mater.* **2005**, *34*, 176–181.

(53) Wuttig, M.; Wuttig, M.; Raoux, S. The Science and Technology of Phase Change Materials. **2015**.

(54) Nam, S.-W.; Chung, H.-S.; Lo, Y. C.; Qi, L.; Li, J.; Lu, Y.; Johnson, a. T. C.; Jung, Y.; Nukala, P.; Agarwal, R. Electrical Wind Force-Driven and Dislocation-Templated Amorphization in Phase-Change Nanowires. *Science (80-.).* **2012**, *336*, 1561–1566.

(55) Gaspard, J. P. Structure of Covalently Bonded Materials: From the Peierls Distortion to Phase-Change Materials. *Comptes Rendus Phys.* **2016**, *17*, 389–405.

(56) R. Venkataraghavan K.S.R.K. Rao, H.L.Bhat, S. P. and G. C. D. Low Threshold Ovoniv Switching in IN A-Si : H/I&b Heterostructures. *J. Non. Cryst. Solids* **1997**, *102*, 759–762.

(57) Seo, S.; Lee, M. J.; Seo, D. H.; Jeoung, E. J.; Suh, D. S.; Joung, Y. S.; Yoo, I. K.; Hwang, I. R.; Kim, S. H.; Byun, I. S.; *et al.* Reproducible Resistance Switching in Polycrystalline NiO Films. *Appl. Phys. Lett.* **2004**, *85*, 5655–5657.

(58) Ielmini, D.; Lacaita, A. L. Phase Change Materials in Non-Volatile Storage After Revolutionizing the Technology of Optical Data Storage , Phase. *Mater. Today* **2011**, *14*, 600–607.

(59) Ielmini, D.; Zhang, Y. Analytical Model for Subthreshold Conduction and Threshold Switching in Chalcogenide-Based Memory Devices Analytical Model for Subthreshold Conduction and Threshold Switching in Chalcogenide-Based Memory Devices. **2012**, *054517*, 0–13.

(60) Manivannan, A.; Myana, S. K.; Miriyala, K.; Sahu, S.; Ramadurai, R.; Manivannan, A.; Myana, K.; Miriyala, K.; Sahu, S. Low Power Ovonic Threshold Switching Characteristics of Thin GeTe6 Films Using Conductive Atomic Force Microscopy. **2016**, *243501*.

(61) Siegrist, T.; Merkelbach, P.; Wuttig, M. Phase Change Materials: Challenges on the Path to a Universal Storage Device. *Annu. Rev. Condens. Matter Phys.* **2012**, *3*, 215–237.

(62) Wełnic, W.; Wuttig, M. Reversible Switching in Phase-Change Materials Phase-Change Materials Are Successfully Employed in Optical Data. *Mater. Today* **2008**, *11*, 20–27.

(63) Simpson, R. E.; Fons, P.; Kolobov, A. V; Fukaya, T.; Krbal, M.; Yagi, T.; Tominaga, J. Interfacial Phase-Change Memory. **2011**, *6*, 501–505.

(64) Wong, B. H. P.; Ieee, F.; Raoux, S.; Ieee, S. M.; Kim, S.; Liang, J.; Ieee, S. M.; Reifenberg, J. P.; Rajendran, B.; Ieee, M.; *et al.* Phase Change Memory. *Proc. IEE* **2010**, *98*, 2201–2227.

(65) Tuma, T.; Pantazi, A.; Le Gallo, M.; Sebastian, A.; Eleftheriou, E. Stochastic Phase-Change Neurons. *Nat. Nanotechnol.* **2016**, *11*, 693–699.

(66) Cheng, Z.; Ríos, C.; Pernice, W. H. P.; Wright, C. D.; Bhaskaran, H. On-Chip Photonic Synapse. *Sci. Adv.* **2017**, *3*.

(67) Ríos, C.; Stegmaier, M.; Hosseini, P.; Wang, D.; Scherer, T.; Wright, C. D.; Bhaskaran, H.; Pernice, W. H. P. Integrated All-Photonic Non-Volatile Multi-Level Memory. *Nat. Photonics* **2015**, *9*, 725–732.

(68) Hosseini, P.; Wright, C. D.; Bhaskaran, H. An Optoelectronic Framework Enabled by Low-Dimensional Phase-Change Films. *Nature* **2014**, *511*, 206.

(69) Nathan Youngblood, Clément Talagrand, Benjamin Porter, Carmelo Guido Galante, Steven Kneepkens, Dmitry Yarmolich, Ruy S. Bonilla, Peiman Hosseini, Robert Taylor,

and H. B. Broadly-Tuneable Smart Glazing Using Ultrathin Phase Change Materials. *Adv. Mater. (in review).*

(70) https://bit.ly/2Sn9lBx (Retrieved on 10.09.2018).

(71) https://bit.ly/2N0dDk1 (Retrieved on 10.09.2018).

(72) Broughton, B.; Bandhu, L.; Talagrand, C.; Garcia-Castillo, S.; Yang, M.; Bhaskaran, H.; Hosseini, P. Solid-State Reflective Displays (SRD ®) Utilizing Ultrathin Phase-Change Materials. *SID Symp. Dig. Tech. Pap.* **2017**, *48*, 546–549.

(73) Koelmans, W. W.; Sebastian, A.; Jonnalagadda, V. P.; Krebs, D.; Dellmann, L.; Eleftheriou, E. Projected Phase-Change Memory Devices. *Nat. Commun.* **2015**, *6*, 1–7.

(74) Min, Z.; Zhi-tang, S.; Bo, L.; Park, Y. S.; Choi, K. J.; Yeal, N.; Xu, L.; Chen, X.; Song, Z. Failure Analysis of Ge2Sb2Te5 Based Phase Change Memory Failure Analysis of Ge 2 Sb 2 Te 5 Based Phase Change Memory. *Jpn. J. Appl. Phys.* **2008**, *47*, 3372–3375.

(75) Burr, G. W.; Brightsky, M. J.; Sebastian, A.; Cheng, H. Y.; Wu, J. Y.; Kim, S.; Sosa, N. E.; Papandreou, N.; Lung, H. L.; Pozidis, H.; *et al.* Recent Progress in Phase-Change Memory Technology. *IEEE J. Emerg. Sel. Top. Circuits Syst.* **2016**, *PP*, 1–17.

(76) Xiong, F.; Liao, A. D.; Estrada, D.; Pop, E. Lower-Power Switching of Phase-Change Materials with Carbon Nanotube Electrodes. *Science (80-.).* **2011**, *332*, 568–570.

(77) Xiong, F.; Bae, M.; Dai, Y.; Liao, A. D.; Behnam, A.; Carrion, E. a; Hong, S.; Ielmini, D.; Pop, E. Self-Aligned Nanotube − Nanowire Phase Change Memory. *Nano Lett.* **2013**, *13*, 464–469.

(78) Behnam, A.; Xiong, F.; Cappelli, A.; Wang, N. C.; Carrion, E. A.; Hong, S.; Dai, Y.; Lyons, A. S.; Chow, E. K.; Piccinini, E.; *et al.* Nanoscale Phase Change Memory with Graphene Ribbon Electrodes Nanoscale Phase Change Memory with Graphene Ribbon Electrodes. *Appl. Phys. Lett.* **2015**, *123508*.

(79) Ahn, C.; Fong, S. W.; Kim, Y.; Lee, S.; Sood, A.; Neumann, C. M.; Asheghi, M.; Goodson, K. E.; Pop, E.; Wong, H. S. P. Energy-Efficient Phase-Change Memory with Graphene as a Thermal Barrier. *Nano Lett.* **2015**, *15*, 6809–6814.

(80) Zhu, C.; Ma, J.; Ge, X.; Rao, F.; Ding, K.; Lv, S.; Wu, L.; Song, Z. Low-Energy Phase Change Memory with Graphene Confined Layer. *Appl. Phys. Lett.* **2016**, *108*, 252102.

(81) https://en.wikipedia.org/wiki/Photolithography (Retrieved on 06.09.2018).

(82) Zaouk, R.; Zaouk, R.; Park, B. Y.; Park, B. Y.; Madou, M. J.; Madou, M. J. Introduction to Microfabrication Techniques. *Methods Mol. Biol.* **2006**, *321*, 5–15.

(83) Franssila, S. *Introduction to Microfabrication*; Wiley-VCH, 2010.

(84) https://nptel.ac.in/courses/103106075/8 (Retrived on 06.09.2018).

(85) https://en.wikipedia.org/wiki/Sputter_deposition (Retrieved on 06.09.2018).

(86) https://www.jic.ac.uk/microscopy/intro_EM.html(Retrieved on 06.09.2018).

(87) https://En.Wikipedia.Org/Wiki/Focused_ion_beam (Retrieved on 06.09.2018).

(88) https://Www.Ias.Ac.in/Article/Fulltext/Reso/015/07/0622-0642 (Retrieved on 10.09.2018).

(89) Https://En.Wikipedia.Org/Wiki/Raman_spectroscopy (Retrieved on 06.09.2018).

(90) Barron, A. R. Photoluminescence Spectroscopy and Its Applications. **2011**, 1–11.

(91) https://en.wikipedia.org/wiki/Ellipsometry (Retrieved on 06.09.2018).

(92) Pop, E. Energy Dissipation and Transport in Nanoscale Devices. *Nano Res.* **2010**, *3*, 147–169.

(93) Li, T.; Hu, W.; Zhu, D. Nanogap Electrodes. *Adv. Mater.* **2010**, *22*, 286–300.

(94) Sarwat, S. G. Materials Science and Engineering of Phase Change Random Access Memory. *Mater. Sci. Technol.* **2017**, *0836*, 1–17.

(95) Sun, L.; Diaz-Fernandez, Y. A.; Gschneidtner, T. A.; Westerlund, F.; Lara-Avila, S.; Moth-Poulsen, K. Single-Molecule Electronics: From Chemical Design to Functional Devices. *Chem. Soc. Rev. Chem. Soc. Rev* **2014**, *43*, 7378–7411.

(96) Sarwat, S. G.; Gehring, P.; Rodriguez Hernandez, G.; Warner, J. H.; Briggs, G. A. D.; Mol, J. A.; Bhaskaran, H. Scaling Limits of Graphene Nanoelectrodes. *Nano Lett.* **2017**, *17*, 3688–3693.

(97) He, C.; Shi, Z.; Zhang, L.; Yang, W.; Yang, R.; Shi, D.; Zhang, G. Multilevel Resistive Switching in Planar Graphene/SiO2 Nanogap Structures. *ACS Nano* **2012**, *6*, 4214–4221.

(98) Elbing, M.; Ochs, R.; Koentopp, M.; Fischer, M.; von Hänisch, C.; Weigend, F.; Evers, F.; Weber, H. B.; Mayor, M. A Single-Molecule Diode. *Proc. Natl. Acad. Sci. U. S. A.* **2005**, *102*, 8815–8820.

(99) Standley, B.; Bao, W.; Zhang, H.; Bruck, J.; Lau, C. N.; Bockrath, M. Graphene-Based Atomic-Scale Switches. *Nano Lett.* **2008**, *8*, 3345–3349.

(100) Mol, J. A.; Lau, C. S.; Lewis, W. J. M.; Sadeghi, H.; Roche, C.; Cnossen, A.; Warner, J. H.; Lambert, C. J.; Anderson, H. L.; Briggs, G. A. D. Graphene-Porphyrin Single-Molecule Transistors. *Nanoscale* **2015**, *7*, 13181–13185.

(101) Heerema, S. J.; Dekker, C. Graphene Nanodevices for DNA Sequencing. *Nat. Nanotechnol.* **2016**, *11*, 127–136.

(102) Ch Postma, H. W. Rapid Sequencing of Individual DNA Molecules in Graphene Nanogaps. *Nano Lett.* **2010**, *10*, 420–425.

(103) Gehring, P.; Sadeghi, H.; Sangtarash, S.; Lau, C. S.; Liu, J.; Ardavan, A.; Warner, J. H.; Lambert, C. J.; Briggs, G. A. D.; Mol, J. A. Quantum Interference in Graphene Nanoconstrictions. *Nano Lett.* **2016**, *16*, 4210–4216.

(104) Prins, F.; Barreiro, A.; Ruitenberg, J. W.; Seldenthuis, J. S.; Aliaga-Alcalde, N.; Vandersypen, L. M. K.; Van Der Zant, H. S. J. Room-Temperature Gating of Molecular Junctions Using Few-Layer Graphene Nanogap Electrodes. *Nano Lett.* **2011**, *11*, 4607–4611.

(105) Lau, C. S.; Mol, J. a.; Warner, J. H.; Briggs, G. a. D. Nanoscale Control of Graphene Electrodes. *Phys. Chem. Chem. Phys.* **2014**, *16*, 20398–20401.

(106) Nef, C.; Pósa, L.; Makk, P.; Fu, W.; Halbritter, A.; Schönenberger, C.; Calame, M. High-Yield Fabrication of Nm-Size Gaps in Monolayer CVD Graphene. *Nanoscale* **2014**, *4*, 1166–1169.

(107) Ullmann, K.; Coto, P. B.; Leitherer, S.; Molina-Ontoria, A.; Martín, N.; Thoss, M.; Weber, H. B. Single-Molecule Junctions with Epitaxial Graphene Nanoelectrodes. *Nano Lett.* **2015**, *15*, 3512–3518.

(108) Sadeghi, H.; Mol, J. a; Lau, C. S.; Briggs, G. A. D.; Warner, J.; Lambert, C. J. Conductance Enlargement in Picoscale Electroburnt Graphene Nanojunctions. *Proc. Natl. Acad. Sci. U. S. A.* **2015**, *112*, 2658–2663.

(109) Jin, C.; Lan, H.; Peng, L.; Suenaga, K.; Iijima, S. Deriving Carbon Atomic Chains from Graphene. *Phys. Rev. Lett.* **2009**, *102*, 1–4.

(110) Hwangbo, Y.; Lee, C.-K.; Kim, S.-M.; Kim, J.-H.; Kim, K.-S.; Jang, B.; Lee, H.-J.; Lee, S.-K.; Kim, S.-S.; Ahn, J.-H.; *et al.* Fracture Characteristics of Monolayer CVD-Graphene. *Sci. Rep.* **2014**, *4*, 4439.

(111) Lee, J.; Kim, Y.; Shin, H. J.; Lee, C.; Lee, D.; Lee, S.; Moon, C. Y.; Lee, S. C.; Kim, S. J.; Ji, J. H.; *et al.* Crack-Release Transfer Method of Wafer-Scale Grown Graphene onto Large-Area Substrates. *ACS Appl. Mater. Interfaces* **2014**, *6*, 12588–12593.

(112) Nam, K. H.; Park, I. H.; Ko, S. H. Patterning by Controlled Cracking. *Nature* **2012**, *485*, 221–224.

(113) Burzurí, E. Characterization of Nanometer-Spaced Few-Layer Graphene Electrodes. *Graphene* **2012**, *01*, 26–29.

(114) El Abbassi, M.; Pósa, L.; Makk, P.; Nef, C.; Thodkar, K.; Halbritter, A.; Calame, M. From Electroburning to Sublimation: Substrate and Environmental Effects in the Electrical Breakdown Process of Monolayer Graphene. *Nanoscale* **2017**, *9*, 17312–17317.

(115) Willke, P.; Möhle, C.; Sinterhauf, A.; Kotzott, T.; Yu, H. K.; Wodtke, A.; Wenderoth, M. Local Transport Measurements in Graphene on SiO2 Using Kelvin Probe Force Microscopy. *Carbon N. Y.* **2016**, *102*, 470–476.

(116) Muñoz-Rojo, M.; Caballero-Calero, O.; Martín-González, M. Electrical Contact Resistances of Thermoelectric Thin Films Measured by Kelvin Probe Microscopy. *Appl. Phys. Lett.* **2013**, *103*, 183905.

(117) Barreiro, A.; Börrnert, F.; Rümmeli, M. H.; Büchner, B.; Vandersypen, L. M. K. Graphene at High Bias: Cracking, Layer by Layer Sublimation, and Fusing. *Nano Lett.* **2012**, *12*, 1873–1878.

(118) Al, Y. L. et. In Situ Electronic Characterization of Graphene Nanoconstrictions Fabricated in a Transmission Electron Microscope. *Nano Lett.* **2011**, *11*, 5184–5188.

(119) Li, Y.; Sinitskii, A.; Tour, J. M. Electronic Two-Terminal Bistable Graphitic Memories. *Nat. Mater.* **2008**, *7*, 966–971.

(120) Zhang, H.; Bao, W.; Zhao, Z.; Huang, J. W.; Standley, B.; Liu, G.; Wang, F.; Kratz, P.; Jing, L.; Bockrath, M.; *et al.* Visualizing Electrical Breakdown and ON/OFF States in Electrically Switchable Suspended Graphene Break Junctions. *Nano Lett.* **2012**, *12*, 1772–1775.

(121) Rinzler, A.; Hafner, J.; Nikolaev, P.; Lou, L.; Kim, S.; Tomanek, D.; Nordlander, P.; Colbert, D.; Smalley, R. Unraveling Nanotubes: Field Emission from an Atomic Wire. *Sci. York Then Washington-* **1995**, *269*, 1550–1550.

(122) Marquardt, C. W.; Grunder, S.; Baszczyk, A.; Dehm, S.; Hennrich, F.; von Löhneysen, H.; Mayor, M.; Krupke, R. Electroluminescence from a Single Nanotube-Molecule-Nanotube Junction. *Nat. Nanotechnol.* **2010**, *5*, 863–867.

(123) Huang, H.; Li, Z.; Wang, W.; Kreuzer, H. J. Nanoribbons. *27th Int. Vac. Nanoelectron. Conf.* **2014**, 2–3.

(124) Young Hee Lee, Seong Gon Kim, D. T. Chemical Physics Letters. *Chem. Phys. Lett.* **1997**.

(125) Xiong, F.; Deshmukh, S.; Hong, S.; Dai, Y.; Behnam, A.; Lian, F.; Pop, E. SANTA: Self-Aligned Nanotrench Ablation via Joule Heating for Probing Sub-20 Nm Devices. *Nano Res.* **2016**, 1–10.

(126) Simpson, R. E.; Krbal, M.; Fons, P.; Kolobov, A. V; Tominaga, J.; Uruga, T.; Tanida, H. Toward the Ultimate Limit of Phase Change Ge2Sb2Te5. *Nano. Lett.* **2010**, *10*, 414–419.

(127) Banhart, F. Chains of Carbon Atoms: A Vision or a New Nanomaterial? *Beilstein J. Nanotechnol.* **2015**, *6*, 559–569.

(128) Fowler, B. W.; Chang, Y.-F.; Zhou, F.; Wang, Y.; Chen, P.-Y.; Xue, F.; Chen, Y.-T.; Bringhurst, B.; Pozder, S.; Lee, J. C. Electroforming and Resistive Switching in Silicon Dioxide Resistive Memory Devices. *RSC Adv.* **2015**, *5*, 21215–21236.

(129) Yao, J.; Sun, Z.; Zhong, L.; Natelson, D.; Tour, J. M. Resistive Switches and Memories from Silicon Oxide. *Nano Lett.* **2010**, *10*, 4105–4110.

(130) https://en.wikipedia.org/wiki/Landauer_formula (Retrieved on 10.09.2018).

(131) Zhou, X.; Wu, L.; Song, Z.; Rao, F.; Ren, K.; Peng, C.; Guo, X.; Liu, B.; Feng, S. Study on Interface Adhesion between Phase Change Material Film and SiO2 Layer by Nanoscratch Test. *Jpn. J. Appl. Phys.* **2011**, *50*.

(132) Thornton, J. a. Influence of Substrate Temperature and Deposition Rate on Structure of Thick Sputtered Cu Coatings. *J. Vac. Sci. Technol.* **1975**, *12*, 830.

(133) Song, C.; Wang, Y.; Jiang, Y.; Zhang, Y.; Chang, C.; Wang, L.; He, K.; Chen, X.; Jia, J.; Wang, Y.; *et al.* Topological Insulator Bi 2 Se 3 Thin Films Grown on Double-Layer Graphene by Molecular Beam Epitaxy Topological Insulator Bi 2 Se 3 Thin Films Grown on Double-Layer Graphene by Molecular Beam Epitaxy. **2016**, *013118*, 1–4.

(134) Fazio, D. De; Goykhman, I.; Yoon, D.; Bruna, M.; Eiden, A.; Milana, S.; Sassi, U.; Barbone, M.; Dumcenco, D.; Marinov, K.; *et al.* High Responsivity, Large-Area Graphene/MoS2 Flexible Photodetectors. *ACS Nano* **2016**, *10*, 8252−8262.

(135) Georgiou, T.; Jalil, R.; Belle, B. D.; Britnell, L.; Gorbachev, R. V; Morozov, S. V; Kim, Y.; Gholinia, A.; Haigh, S. J.; Makarovsky, O.; *et al.* Vertical Field-Effect Transistor Based on Graphene – WS2 Heterostructures for Flexible and Transparent Electronics. *Nat. Nanotechnol.* **2012**, *8*, 100–103.

(136) Shanmugam, M.; Jacobs-Gedrim, R.; Song, E. S.; Yu, B. Two-Dimensional Layered Semiconductor/Graphene Heterostructures for Solar Photovoltaic Applications. *Nanoscale* **2014**, *6*, 12682–12689.

(137) Bertolazzi, S.; Krasnozhon, D.; Kis, A. Nonvolatile Memory Cells Based on MoS2/Graphene. *ACS Nano* **2013**, *7*, 3246–3252.

(138) Yang, W.; GAN, L.; Li, H.; Zhai, T. Two-Dimensional Layered Nanomaterials for Gas-Sensing Applications. *Inorg. Chem. Front.* **2016**, *3*, 433–451.

(139) Feng, W.; Zheng, W.; Gao, F.; Chen, X.; Liu, G.; Hasan, T.; Cao, W.; Hu, P. Sensitive Electronic-Skin Strain Sensor Array Based on the Patterned Two-Dimensional a-In2Se3. *Chem. Mater.* **2016**, *28*, 4278–4283.

(140) Tan, H.; Fan, Y.; Zhou, Y.; Chen, Q.; Xu, W.; Warner, J. H. Ultrathin 2D Photodetectors Utilizing Chemical Vapor Deposition Grown WS2 with Graphene Electrodes. *ACS Nano* **2016**, *10*, 7866–7873.

(141) Tan, H.; Fan, Y.; Rong, Y.; Porter, B.; Lau, C. S.; Zhou, Y.; He, Z.; Wang, S.; Bhaskaran, H.; Warner, J. H. Doping Graphene Transistors Using Vertical Stacked Monolayer WS2 Heterostructures Grown by Chemical Vapor Deposition. **2016**.

(142) Tosun, M.; Fu, D.; Desai, S. B.; Ko, C.; Kang, J. S.; Lien, D.; Najmzadeh, M.; Tongay, S.; Wu, J. MoS2 Heterojunctions by Thickness Modulation. *Sci. Rep.* **2015**, *5*, 1–8.

(143) Wurstbauer, U.; Miller, B.; Parzinger, E.; Lin, Z.; Mccreary, A.; Briggs, N.; Castellanos-gomez, A.; Vicarelli, L.; Prada, E. Strain Engineering in Semiconducting Two-Dimensional Crystals. *J. Phys. Condens. Matter* **2015**, *27*, 1–18.

(144) Shen, T.; Penumatcha, A. V; Appenzeller, J. Strain Engineering for Transition Metal. *ACS Nano* **2016**, *10*, 4712–4718.

(145) Lanzillo, N. A.; Simbeck, A. J.; Nayak, S. K. Strain Engineering the Work Function in Monolayer Metal Dichalcogenides. *J. Phys. Condens. Matter* **2015**, *27*, 175501.

(146) Garg, R.; Dutta, N. K.; Choudhury, N. R. Work Function Engineering of Graphene. *Nanomaterials* **2014**, *4*, 267–300.

(147) Desai, S. B.; Seol, G.; Kang, J. S.; Fang, H.; Battaglia, C. Strain-Induced Indirect to Direct Bandgap Transition in Multilayer. *Nano Lett.* **2014**, *14*, 4592–4597.

(148) Conley, H. J.; Wang, B.; Ziegler, J. I.; Haglund, R. F.; Pantelides, S. T.; Bolotin, K. I. Bandgap Engineering of Strained Monolayer and Bilayer MoS 2. *Nano Lett.* **2013**, *13*, 3626–3630.

(149) Das, S.; Gulotty, R.; Sumant, A. V; Roelofs, A. All 2D , Flexible , Transparent and Thinnest Thin Film Transistor. *Nano Lett.* **2014**, *2*, 4–6.

(150) Bissett, M. A.; Konabe, S.; Okada, S.; Tsuji, M.; Ago, H. Enhanced Chemical Reactivity of Graphene Induced by Mechanical Strain. *ACS Nano* **2013**, *7*, 10335–10343.

(151) Bissett, M. A.; Izumida, W.; Saito, R.; Ago, H. Effect of Domain Boundaries on the Raman Spectra of Mechanically Strained Graphene. *ACS Nano* **2012**, *6*, 10229–10238.

(152) He, X.; Li, H.; Zhu, Z.; Dai, Z.; Yang, Y.; Yang, P.; Zhang, Q.; Li, P.; Schwingenschlogl, U.; Zhang, X. Strain Engineering in Monolayer WS2, MoS2, and the WS2/MoS2 Heterostructure. *Appl. Phys. Lett.* **2016**, *109*, 173105.

(153) McCreary, A.; Ghosh, R.; Amani, M.; Wang, J.; Duerloo, K. A. N.; Sharma, A.; Jarvis, K.; Reed, E. J.; Dongare, A. M.; Banerjee, S. K.; *et al.* Effects of Uniaxial and Biaxial Strain on Few-Layered Terrace Structures of MoS2 Grown by Vapor Transport. *ACS Nano* **2016**, *10*, 3186–3197.

(154) Nistor, R. A.; Kuroda, M. A.; Maarouf, A. A.; Martyna, G. J. Doping of Adsorbed

Graphene from Defects and Impurities in SiO2 Substrates. *Phys. Rev. B* **2012**, *041409*, 1–5.

(155) Yu, Y.-J.; Zhao, Y.; Ryu, S.; Brus, L. E.; Kim, K. S.; Kim, P. Tuning the Graphene Work Function by Electric Field Effect. Supplementary Information. *Nano Lett.* **2009**, *9*, 3430–3434.

(156) Hill, H. M.; Rigosi, A. F.; Rim, K. T.; Flynn, G. W.; Heinz, T. F. Band Alignment in MoS2/WS2 Transition Metal Dichalcogenide Heterostructures Probed by Scanning Tunneling Microscopy and Spectroscopy. *Nano Lett.* **2016**, *16*, 4831–4837.

(157) Kapatel, S.; Sumesh, C. K.; Pataniya, P.; Solanki, G. K.; Patel, K. D. Layer-Engineered I-V Characteristics of p-Si/WS2 Van Der Waals Heterostructure Diode. *Eur. Phys. J. Plus* **2017**, *132*, 191.

(158) Feng, Y.; Zhang, K.; Li, H.; Wang, F.; Zhou, B.; Fang, M.; Wang, W.; Wei, J.; Wong, H. S. P. In Situ Visualization and Detection of Surface Potential Variation of Mono and Multilayer MoS2 under Different Humidities Using Kelvin Probe Force Microscopy. *Nanotechnology* **2017**, *28*.

(159) Lee, S. Y.; Kim, U. J.; Chung, J.; Nam, H.; Jeong, H. Y.; Han, G. H.; Kim, H.; Oh, H. M.; Lee, H.; Kim, H.; *et al.* Large Work Function Modulation of Monolayer MoS2 by Ambient Gases. *ACS Nano* **2016**, *10*, 6100–6107.

(160) Pinto, H.; Markevich, A. Electronic and Electrochemical Doping of Graphene by Surface Adsorbates. *Beilstein J. Nanotechnol.* **2014**, *5*, 1842–1848.

(161) Meng, J.; Song, H.-D.; Li, C.-Z.; Jin, Y.; Tang, L.; Liu, D.; Liao, Z.-M.; Xiu, F.; Yu, D. Lateral Graphene P–n Junctions Formed by the Graphene/MoS2 Hybrid Interface. *Nanoscale* **2015**, *7*, 11611–11619.

(162) Piazza, A.; Giannazzo, F.; Buscarino, G.; Fisichella, G.; Magna, A. La; Roccaforte, F.; Cannas, M.; Gelardi, F. M.; Agnello, S. Effect of Air on Oxygen P-Doped Graphene on SiO2. *Phys. Status Solidi A 213,* **2016**, *2344*, 2341–2344.

(163) Rold, R.; Castellanos-gomez, A.; Cappelluti, E. Strain Engineering in Semiconducting Two-Dimensional Crystals. **2004**, 1–23.

(164) Meng, L.; Zhang, Y.; Hu, S.; Wang, X.; Liu, C.; Guo, Y.; Wang, X. Two Dimensional WS2 Lateral Heterojunctions by Strain Modulation Two Dimensional WS2 Lateral Heterojunctions by Strain Modulation. *Appl. Phys. Lett.* **2016**, *263104*.

(165) Yu, L.; Ruzsinszky, A.; Perdew, J. P. Bending Two-Dimensional Materials to Control Charge Localization and Fermi-Level Shift. *Nano Lett.* **2016**, *16*, 2444–2449.

(166) Ashraf, A.; Wu, Y.; Wang, M. C.; Yong, K.; Sun, T.; Jing, Y.; Haasch, R. T.; Aluru, N. R.; Nam, S. Doping-Induced Tunable Wettability and Adhesion of Graphene. *Nano Lett.* **2016**, *16*, 4708–4712.

(167) Jung, D. Y.; Yang, S. Y.; Park, H.; Shin, W. C.; Oh, J. G.; Cho, B. J.; Choi, S.-Y. Interface Engineering for High Performance Graphene Electronic Devices. *Nano Converg.* **2015**, *2*, 11.

(168) Dong, X.; Fu, D.; Fang, W.; Shi, Y.; Chen, P.; Li, L. Doping Single-Layer Graphene with Aromatic Molecules **. *Small* **2009**, 1422–1426.

(169) Choi, S.; Jhi, S.; Son, Y. Effects of Strain on Electronic Properties of Graphene. *Phys. Rev. Lett. B* **2010**, *81*, 23–26.

(170) He, X.; Tang, N.; Sun, X.; Gan, L.; Ke, F.; Wang, T.; Xu, F.; Wang, X.; Yang, X.; Shen, B. Tuning the Graphene Work Function by Uniaxial Strain. *Appl. Phys. Lett.* **2015**, *043106*.

(171) Wurstbauer, U.; Miller, B.; Parzinger, E.; Lin, Z.; Carvalho, B. R.; Kahn, E.; Brien, M. O.; Mcevoy, N.; Motta, C.; Wang, F.; *et al.* Strain-Induced Phonon Shifts in Tungsten Disulfi de Nanoplatelets and Nanotubes. *2D Mater.* **2016**, *4*, 015007.

(172) Rice, C.; Young, R. J.; Zan, R.; Bangert, U.; Wolverson, D.; Georgiou, T.; Jalil, R.; Novoselov, K. S. Raman-Scattering Measurements and First-Principles Calculations of Strain-Induced Phonon Shifts in Monolayer MoS2. *Phys. Rev. B - Condens. Matter Mater. Phys.* **2013**, *87*, 1–5.

(173) Gong, L.; Young, R. J.; Kinloch, I. A.; Riaz, I.; Jalil, R.; Novoselov, K. S. Optimizing the Reinforcement of Polymer-Based Nanocomposites by Graphene. *ACS Nano* **2012**, *6*, 2086–2095.

(174) Li, Z.; Kinloch, I. A.; Young, R. J.; Novoselov, K. S.; Anagnostopoulos, G.; Parthenios, J.; Galiotis, C.; Papagelis, K.; Lu, C. Y.; Britnell, L. Deformation of Wrinkled Graphene. *ACS Nano* **2015**, *9*, 3917–3925.

(175) Tweedie, M. E. P.; Sheng, Y.; Sarwat, S. G.; Xu, W.; Bhaskaran, H.; Warner, J. H. Inhomogeneous Strain Release during Bending of WS2 on Flexible Substrates. *ACS Appl. Mater. Interfaces* **2018**, *10*, 39177–39186.

(176) Reviewed, P.; Riverside, M. E. UC Riverside Electronic Theses and Dissertations. *Thesis-Electronic, Vib. Thermoelectr. Prop. Two-Dimensional Mater.* **2009**.

(177) Jo, S.; Ubrig, N.; Berger, H.; Kuzmenko, A. B.; Morpurgo, A. F. Mono- and Bilayer WS2 Light-Emitting Transistors. *Nano Lett.* **2014**, *14*, 2019–2025.

(178) Yamaguchi, T.; Moriya, R.; Inoue, Y.; Morikawa, S. Tunneling Transport in a Few Monolayer-Thick WS2/Graphene Heterojunction. *Appl. Phys. Lett.* **2014**, *105*, 223109.

(179) Chen, K.; Wan, X.; Xie, W.; Wen, J.; Kang, Z.; Zeng, X.; Chen, H.; Xu, J. Lateral Built-In Potential of Monolayer MoS2 – WS2 In-Plane Heterostructures by a Shortcut Growth Strategy. *Adv. Mater.* **2015**, 6431–6437.

(180) Zheng, L.; Zhongzhu, L.; Guozhen, S. Photodetectors Based on Two Dimensional Materials. *J. Semicond.* **2016**, *37*, 1–11.

(181) Peng, X.; Tang, F.; Copple, A. Engineering the Work Function of Armchair Graphene Nanoribbons Using Strain and Functional Species: A First Principles Study. *J. Phys. Condens. Matter* **2012**, *24*, 075501.

(182) Liu, J. B. and M. E. and S. H. and Y. Z. and Y. F. and X. L. and Z. Y. and K. J. and J. Two-Dimensional Hexagonal Boron Nitride as Lateral Heat Spreader in Electrically Insulating Packaging. *J. Phys. D. Appl. Phys.* **2016**, *49*, 265501.

(183) Zhang, K.; Feng, Y.; Wang, F.; Yang, Z.; Wang, J. Two Dimensional Hexagonal Boron Nitride (2D-HBN): Synthesis, Properties and Applications. *J. Mater. Chem. C* **2017**, *5*, 11992–12022.

(184) Tovee, P.; Pumarol, M.; Zeze, D.; Kjoller, K.; Kolosov, O. Nanoscale Spatial Resolution

Probes for Scanning Thermal Microscopy of Solid State Materials. *J. Appl. Phys.* **2012**, *112*, 114317.

(185) Rudé, M.; Mkhitaryan, V.; Cetin, A. E.; Miller, T. A.; Carrilero, A.; Wall, S.; de Abajo, F. J. G.; Altug, H.; Pruneri, V. Ultrafast and Broadband Tuning of Resonant Optical Nanostructures Using Phase-Change Materials. *Adv. Opt. Mater.* **2016**, *4*, 1060–1066.

(186) Duerloo, K.-A. N.; Li, Y.; Reed, E. J. Structural Phase Transitions in Two-Dimensional Mo- and W-Dichalcogenide Monolayers. *Nat. Commun.* **2014**, *5*, 4214.

(187) Kats, M. A.; Blanchard, R.; Genevet, P.; Capasso, F. Nanometre Optical Coatings Based on Strong Interference Effects in Highly Absorbing Media. *Nat. Mater.* **2013**, *12*, 20–24.

(188) Zhou, X.; Dong, W.; Zhang, H.; Simpson, R. E. A Zero Density Change Phase Change Memory Material: GeTe-O Structural Characteristics upon Crystallisation. *Sci. Rep.* **2015**, *5*, 11150.

(189) Ji, H.-K.; Tong, H.; Qian, H.; Hui, Y.-J.; Liu, N.; Yan, P.; Miao, X.-S. Non-Binary Colour Modulation for Display Device Based on Phase Change Materials. *Sci. Rep.* **2016**, *6*, 39206.

(190) Wuttig, M.; Bhaskaran, H.; Taubner, T. Phase-Change Materials for Non-Volatile Photonic Applications. *Nat. Photonics* **2017**, *11*, 465–476.

(191) Cros, B.; Dubourg, M.; Martinez, J. P.; Balladore, J. L. Transmission Electron Microscopy Study of Crystallization on Plasma-Deposited Ge-Se Films. *Thin Solid Films* **1991**, *205*, 13–19.

(192) Olivier, M.; Tchahame, J. C.; N, P.; Chauvet, M.; Besse, V.; Cassagne, C.; Boudebs, G.; Renversez, G.; Boidin, R.; Baudet, E.; *et al.* Structure , Nonlinear Properties , and Photosensitivity of (GeSe 2) 100-x (Sb 2 Se 3) x Glasses. **2014**, *4*, 141–148.

(193) Porezag, D. V; Pederson, M. R. Raman-Active Modes of a-GeSe2 and a-GeS2: A First-Principles Study. *Phys. Rev. B Condens. MATTER Mater. Phys. RAPID* **1999**, *60*, 985–989.

(194) Yan, Q.; Jain, H.; Ren, J.; Zhao, D.; Chen, G. Effect of Photo-Oxidation on Photobleaching of GeSe2 and Ge2Se3 Films. *J. Phys. Chem. C* **2011**, *115*, 21390–21395.

(195) Lee, M.; Chen, P. The Investigation of Selective Pre-Pattern Free Self-Assembled Ge Nano-Dot Formed by Excimer Laser Annealing. *Nanoscale Res. Lett.* **2012**, *7*, 1.

(196) Kumar, R. T. A.; Qamhieh, N. N.; Mahmoud, S. T.; Lekha, P. C.; Jeyadheepan, K.; Sanjeeviraja, C.; Padiyan, D. P. Evolution of Structural Disorder in Amorphous GeSeS Thin Films by Thickness Variation. *J. Non. Cryst. Solids* **2016**, *450*, 135–140.

(197) Cammarata, R. C. Surface and Interface Effects in Thin Films. *Prog. Surf. Sci.* **1994**, *46*, 1–38.

(198) Mukherjee, B.; Murali, G.; Lim, S. X.; Zheng, M.; Tok, E. S.; Sow, C. H. Direct Laser Micropatterning of GeSe2 Nanostructures Film with Controlled Optoelectrical Properties. *RSC Adv.* **2014**, *4*, 10013–10021.

(199) Pan, R. K.; Tao, H. Z.; Zang, H. C.; Zhao, X. J.; Zhang, T. J. Annealing Effects on the Structure and Optical Properties of GeSe 2 and GeSe 4 Films Prepared by PLD. **2009**, *484*, 645–648.

(200) Glass, C. Photo-Darkening in GeSe Film by CW Laser Irradiation. *J. Mater. Sci. Lett. 18*

2000, *8*, 1543–1545.

(201) Kumar, R. R.; Barik, A. R.; Vinod, E. M.; Bapna, M.; Sangunni, K. S.; Adarsh, K. V. Crossover from Photodarkening to Photobleaching in A-GexSe100-x Thin Films. *Opt. Lett.* **2013**, *38*, 1682–1684.

(202) Barik, A. R.; Naik, R.; Adarsh, K. V. Unusual Observation of Fast Photodarkening and Slow Photobleaching in A-GeSe 2 Thin Fi Lm. **2013**, *377*, 179–181.

(203) Afify, N. Structural Relaxation of ${\mathrm{GeSe}}_{2}$ Chalcogenide Glass Studied with Use of the Radial Distribution Function. *Phys. Rev. B* **1993**, *48*, 16304–16309.

(204) Lucas, P.; Doraiswamy, A.; King, E. A. Photoinduced Structural Relaxation in Chalcogenide Glasses. *J. Non. Cryst. Solids* **2003**, *332*, 35–42.

(205) Kolobov, A. V.; Tominaga, J. *Chalcogenides: Metastability and Phase Change Phenomena*; Springer, 2012; Vol. 164.

(206) Zhang, S.; Chen, Y.; Wang, R.; Shen, X.; Dai, S. Observation of Photobleaching in Ge-Deficient Ge16.8Se83.2 Chalcogenide Thin Film with Prolonged Irradiation. *Sci. Rep.* **2017**, *7*, 14585.

(207) Wang, Y.; Matsuda, O.; Inoue, K.; Murase, K. Photo-Induced Crystallization in Amorphous GeSe2studied by Raman Scattering. *J. Non. Cryst. Solids* **1998**, *227–230*, 728–731.

(208) Cook, P. L.; Johnson, P. S.; Liu, X.; Chin, A.; Himpsel, F. J.; Cook, P. L.; Johnson, P. S.; Liu, X.; Chin, A.; Himpsel, F. J. Radiation Damage in Biomimetic Dye Molecules for Solar Cells Radiation Damage in Biomimetic Dye Molecules for Solar Cells. **2009**, *214702*.

(209) Lindström, G. Radiation Damage in Silicon Detectors. *Nucl. Instruments Methods Phys. Res. Sect. A Accel. Spectrometers, Detect. Assoc. Equip.* **2003**, *512*, 30–43.

(210) Andrady, A. L.; Hamid, S. H.; Hu, X.; Torikai, A. Effects of Increased Solar Ultraviolet Radiation on Materials. *J. Photochem. Photobiol. B Biol.* **1998**, *46*, 96–103.

(211) Li, Z.; Butun, S.; Aydin, K. Large-Area, Lithography-Free Super Absorbers and Color Filters at Visible Frequencies Using Ultrathin Metallic Films. *ACS Photonics* **2015**, *2*, 183–188.

(212) Cheng, Z.; Ríos, C.; Youngblood, N.; Wright, C. D.; Pernice, W. H. P.; Bhaskaran, H. Device-Level Photonic Memories and Logic Applications Using Phase-Change Materials. *Adv. Mater.* **2018**, *30*, 1802435.

(213) Zhang, Y.; Chou, J. B.; Li, J.; Li, H.; Du, Q.; Zhou, S.; Shalaginov, M. Y.; Fang, Z.; Zhong, H.; Robinson, P.; *et al.* Extreme Broadband Transparent Optical Phase Change Materials for High-Performance Nonvolatile Photonics. *arXiv Prepr.* **2018**, *7014*, 1–16.

(214) Rios, C.; Hosseini, P.; Wright, C. D.; Bhaskaran, H.; Pernice, W. H. P. On-Chip Photonic Memory Elements Employing Phase-Change Materials. *Adv. Mater.* **2014**, *26*, 1372–1377.

(215) Bosse, J. L.; Grishin, I.; Gyu Choi, Y.; Cheong, B.; Lee, S.; Kolosov, O. V; Huey, B. D. Nanosecond Switching in GeSe Phase Change Memory Films by Atomic Force Microscopy. *Appl. Phys. Lett.* **2014**, *104*, 53109.

(216) Soref, R.; Hendrickson, J.; Liang, H.; Majumdar, A.; Mu, J.; Li, X.; Huang, W.-P. Electro-

Optical Switching at 1550 Nm Using a Two-State GeSe Phase-Change Layer. *Opt. Express* **2015**, *23*, 1536–1546.

(217) Griffiths, J. E.; Espinosa, G. P.; Remeika, J. P.; Phillips, J. C. Reversible Reconstruction and Crystallization of GeSe2 Glass. *Solid State Commun.* **1981**, *40*, 1077–1080.

(218) Campbell, K. A. Forced Ion Migration for Chalcogenide Phase Change Memory Device. **2011**.

(219) Letter, P. R. Physical Review Letter. **1986**, *57*.

(220) Hosseini, P.; Wright, C. D.; Bhaskaran, H. An Optoelectronic Framework Enabled by Low-Dimensional Phase-Change Films. *Nature* **2014**, *511*, 206–211.

(221) Lee, S. Y.; Kim, Y. H.; Cho, S. M.; Kim, G. H.; Kim, T. Y.; Ryu, H.; Kim, H. N.; Kang, H. B.; Hwang, C. Y.; Hwang, C. S. Holographic Image Generation with a Thin-Film Resonance Caused by Chalcogenide Phase-Change Material. *Sci. Rep.* **2017**, *7*, 1–8.

(222) Ríos, C.; Hosseini, P.; Taylor, R. A.; Bhaskaran, H. Color Depth Modulation and Resolution in Phase-Change Material Nanodisplays. *Adv. Mater.* **2016**, 4720–4726.

(223) Cheng, Z.; Ríos, C.; Pernice, W. H. P.; David Wright, C.; Bhaskaran, H. On-Chip Photonic Synapse. *Sci. Adv.* **2017**, *3*, 1–7.

(224) Raeis-Hosseini, N.; Rho, J. Metasurfaces Based on Phase-Change Material as a Reconfigurable Platform for Multifunctional Devices. *Materials (Basel).* **2017**, *10*, 1046.

(225) Au, Y. Y.; Bhaskaran, H.; Wright, C. D. Phase-Change Devices for Simultaneous Optical-Electrical Applications. *Sci. Rep.* **2017**, *7*, 9688.

(226) Lu, Y.; Stegmaier, M.; Nukala, P.; Giambra, M. A.; Ferrari, S.; Busacca, A.; Pernice, W. H. P.; Agarwal, R. Mixed-Mode Operation of Hybrid Phase-Change Nanophotonic Circuits. *Nano Lett.* **2017**, *17*, 150–155.

(227) Rodriguez-Hernandez, G.; Hosseini, P.; Ríos, C.; Wright, C. D.; Bhaskaran, H. Mixed-Mode Electro-Optical Operation of Ge2Sb2Te5 Nanoscale Crossbar Devices. *Adv. Electron. Mater.* **2017**, *3*, 1–6.

(228) Ielmini, D.; Lacaita, A. L. Phase Change Materials in Non-Volatile Storage. *Mater. Today* **2011**, *14*, 600–607.

(229) Raoux, S.; Wuttig, M. *Phase Change Materials Science and Applications*; Springer US, 2009.

(230) Tanaka, K. Comment on "Investigation of the Optical and Electronic Properties of Ge2Sb2Te5 Phase Change Material in Its Amorphous, Cubic, and Hexagonal Phases" [J. Appl. Phys. 97, 093509 (2005)]. *J. Appl. Phys.* **2007**, *101*, 026111.

(231) Lee, B.-S.; Abelson, J. R.; Bishop, S. G.; Kang, D.-H.; Cheong, B.; Kim, K.-B. Investigation of the Optical and Electronic Properties of Ge2Sb2Te5 Phase Change Material in Its Amorphous, Cubic, and Hexagonal Phases. *J. Appl. Phys.* **2005**, *97*, 093509.

(232) Roland Scheer and Hans-Werner Schock. *Chalcogenide Photovoltaics : Physics, Technologies, and Thin Film Devices*; Wiley-VCH, 2011.

(233) Rowlands, J.; Kasap, S. Amorphous Semiconductors Usher in Digital X-Ray Imaging. *Phys. Today* **1997**, *50*, 24–30.

(234) Shimakawa, K.; Kolobov, A.; Elliott, S. R. *Photoinduced Effects and Metastability in Amorphous Semiconductors and Insulators*; 1995; Vol. 44.

(235) Lee, B.S., Xiao, Y., Bishop, S.G., Abelson, J.R., Raoux, S., Deline, V.R., Kwon, M.-H.; Kim, K.-B., Cheong, B., Li, H., Taylor, P. . Photo-Oxidation and the Absence of Photodarkening in Ge2Sb2Te5 Phase Change Material. *MRS Proc.* **2006**, *918*.

(236) Lee, H. S.; Cheong, B. K.; Lee, T. S.; Jeong, J. H.; Lee, S.; Kim, W. M.; Kim, D. Origin of Nonlinear Optical Characteristics of Crystalline Ge-Sb-Te Thin Films for Possible Superresolution Effects. *Japanese J. Appl. Physics, Part 2 Lett.* **2007**, *46*, 4–7.

(237) Liu, S.; Wei, J.; Gan, F. Optical Nonlinear Absorption Characteristics of Crystalline Ge2 Sb2Te5 Thin Films. *J. Appl. Phys.* **2011**, *110*, 033503.

(238) Pirovano, A.; Lacaita, A. L.; Benvenuti, A.; Pellizzer, F.; Bez, R. Electronic Switching in Phase-Change Memories. *IEEE Trans. Electron Devices* **2004**, *51*, 452–459.

(239) Shukla, K. D.; Saxena, N.; Durai, S.; Manivannan, A. Redefining the Speed Limit of Phase Change Memory Revealed by Time-Resolved Steep Threshold-Switching Dynamics of AgInSbTe Devices. *Sci. Rep.* **2016**, *6*, 37868.

(240) Stegmaier, M.; RÍos, C.; Bhaskaran, H.; Pernice, W. H. P. Thermo-Optical Effect in Phase-Change Nanophotonics. *ACS Photonics* **2016**, *3*, 828–835.

(241) Kuwahara, M.; Suzuki, O.; Taketoshi, N.; Yamakawa, Y.; Yagi, T.; Fons, P.; Tsutsumi, K.; Suzuki, M.; Fukaya, T.; Tominaga, J.; *et al.* Measurements of Temperature Dependence of Optical and Thermal Properties of Optical Disk Materials. *Jpn. J. Appl. Phys.* **2006**, *45*, 1419–1421.

(242) Octon, T. J.; Nagareddy, V. K.; Russo, S.; Craciun, M. F.; Wright, C. D. Fast High-Responsivity Few-Layer MoTe2Photodetectors. *Adv. Opt. Mater.* **2016**, *4*, 1750–1754.

(243) Furchi, M. M.; Polyushkin, D. K.; Pospischil, A.; Mueller, T. Mechanisms of Photoconductivity in Atomically Thin MoS2. *Nano Lett.* **2014**, *14*, 6165–6170.

(244) Alexe, M.; Hesse, D. Tip-Enhanced Photovoltaic Effects in Bismuth Ferrite. *Nat. Commun.* **2011**, *2*, 255–256.

(245) Buscema, M.; Barkelid, M.; Zwiller, V.; Van Der Zant, H. S. J.; Steele, G. A.; Castellanos-Gomez, A. Large and Tunable Photothermoelectric Effect in Single-Layer MoS2. *Nano Lett.* **2013**, *13*, 358–363.

(246) Hu, C.; Wang, X.; Miao, P.; Zhang, L.; Song, B.; Liu, W.; Lv, Z.; Zhang, Y.; Sui, Y.; Tang, J.; *et al.* Origin of the Ultrafast Response of the Lateral Photovoltaic Effect in Amorphous MoS2/Si Junctions. *ACS Appl. Mater. Interfaces* **2017**, *9*, 18362–18368.

(247) Xu, X.; Gabor, N. M.; Alden, J. S.; Van Der Zande, A. M.; McEuen, P. L. Photo-Thermoelectric Effect at a Graphene Interface Junction. *Nano Lett.* **2010**, *10*, 562–566.

(248) Park, Y.; Choong, V.; Gao, Y.; Hsieh, B. R.; Tang, C. W. Work Function of Indium Tin Oxide Transparent Conductor Measured by Photoelectron Spectroscopy. *Appl. Phys. Lett.* **1996**, *68*, 2699–2701.

(249) Tong, H.; Yang, Z.; Yu, N. N.; Zhou, L. J.; Miao, X. S. Work Function Contrast and Energy Band Modulation between Amorphous and Crystalline Ge2Sb2Te5films. *Appl. Phys. Lett.* **2015**, *107*, 082101.

(250) Woo, W. S.; Won, S. S.; Ahn, C. W.; Chae, S. A.; Ullah, A.; Kim, I. W. Photovoltaic Effect of Lead-Free (Na0.82K0.18)0.5Bi4.5Ti4O15 Ferroelectric Thin Film Using Pt and Indium Tin Oxide Top Electrodes. **2017**, *034107*, 0–8.

(251) Harshan, V. N.; Kotru, S. Influence of Work-Function of Top Electrodes on the Photovoltaic Characteristics of Pb0.95La0.05Zr0.54Ti0.46O3 Thin Film Capacitors. *Appl. Phys. Lett.* **2012**, *100*, 10–14.

(252) Sun, Z.; Pan, Y.; Zhou, J.; Sa, B.; Ahuja, R. Origin of P-Type Conductivity in Layered NGeTe • mSb 2Te 3 Chalcogenide Semiconductors. *Phys. Rev. B - Condens. Matter Mater. Phys.* **2011**, *83*, 3–6.

(253) Heo, Y. W.; Tien, L. C.; Norton, D. P.; Pearton, S. J.; Kang, B. S.; Ren, F.; LaRoche, J. R. Pt/ZnO Nanowire Schottky Diodes. *Appl. Phys. Lett.* **2004**, *85*, 3107–3109.

(254) Keem, K.; Kim, H.; Kim, G. T.; Lee, J. S.; Min, B.; Cho, K.; Sung, M. Y.; Kim, S. Photocurrent in ZnO Nanowires Grown from Au Electrodes. *Appl. Phys. Lett.* **2004**, *84*, 4376–4378.

(255) Kolobov, A. V.; Kim, D. J.; Giussani, A.; Fons, P.; Tominaga, J.; Calarco, R.; Gruverman, A. Ferroelectric Switching in Epitaxial GeTe Films. *APL Mater.* **2014**, *2*, 066101.

(256) Wang, W.C. Optical Detectors, "Http://Depts.Washington.Edu/Mictech/Optics/Sensors/Detector."

(257) Wang, Z.; Rao, M.; Midya, R.; Joshi, S.; Jiang, H.; Lin, P.; Song, W.; Asapu, S.; Zhuo, Y.; Li, C.; *et al.* Threshold Switching of Ag or Cu in Dielectrics: Materials, Mechanism, and Applications. *Adv. Funct. Mater.* **2018**, *28*, 1704862.

(258) Lu, L.; Dong, W.; Behera, J. K.; Chew, L.; Simpson, R. E. Inter-Diffusion of Plasmonic Metals and Phase Change Materials. *J. Mater. Sci.* **2019**, *54*, 2814–2823.

(259) Casari, C. S.; Tommasini, M.; Tykwinski, R. R.; Milani, A. Carbon-Atom Wires: 1-D Systems with Tunable Properties. *Nanoscale* **2016**, *8*, 4414–4435.

(260) Sheng, Y.; Rong, Y.; He, Z.; Fan, Y.; Warner, J. H. Uniformity of Large-Area Bilayer Graphene Grown by Chemical Vapor Deposition. *Nanotechnology* **2015**, *26*.